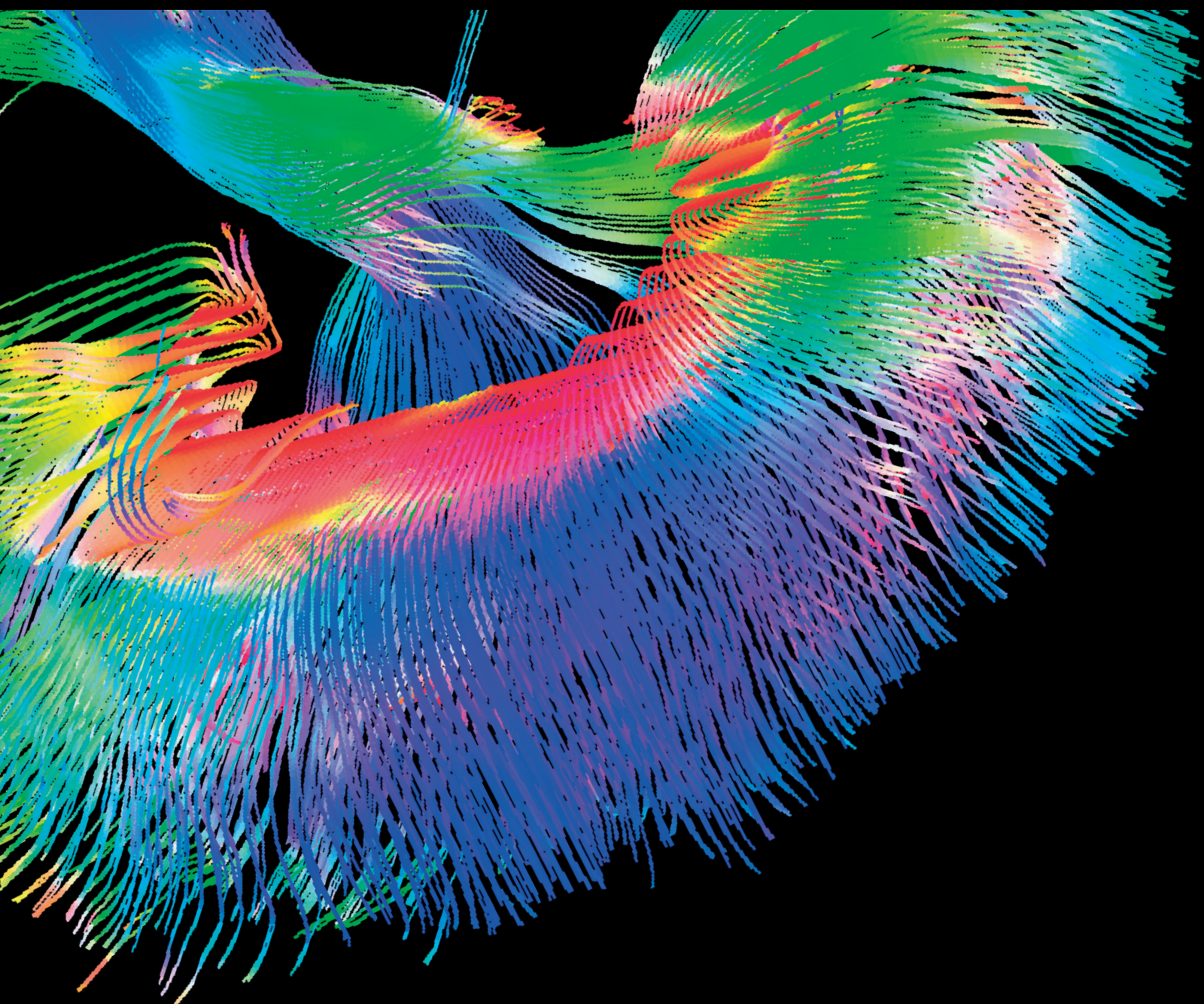


Contrast Media & Molecular Imaging

In Vivo Imaging of Inflammation and Infection

Special Issue Editor in Chief: Anne Roivainen

Guest Editors: Xiang-Guo Li, Cristina Nanni, Weibo Cai, and Sarah Ohrndorf





In Vivo Imaging of Inflammation and Infection

Contrast Media & Molecular Imaging

In Vivo Imaging of Inflammation and Infection

Special Issue Editor in Chief: Anne Roivainen

Guest Editors: Xiang-Guo Li, Cristina Nanni, Weibo Cai,
and Sarah Ohrndorf



Copyright © 2018 Hindawi. All rights reserved.

This is a special issue published in “Contrast Media & Molecular Imaging.” All articles are open access articles distributed under the Creative Commons Attribution License, which permits unrestricted use, distribution, and reproduction in any medium, provided the original work is properly cited.

Editorial Board

Ali Azhdarinia, USA
Peter Bannas, Germany
Giorgio Biasiotto, Italy
André L. B. de Barros, Brazil
Dinesh K. Deelchand, USA
Paul Edison, UK
Guillermina Ferro-Flores, Mexico
María L. García-Martín, Spain
Hao Hong, USA

Alexey P. Kostikov, Canada
Françoise Kraeber-Bodéré, France
Gaurav Malviya, UK
Barbara Palumbo, Italy
Giancarlo Pascali, Australia
Maria Joao Ribeiro, France
Laurent M. Riou, France
Anne Roivainen, Finland
Pedro Rosa-Neto, Canada

Giuseppe Rubini, Italy
Barbara Salvatore, Italy
Ralf Schirmacher, Canada
Giorgio Treglia, Switzerland
Reza Vali, Canada
Changning Wang, USA
Luc Zimmer, France

Contents

In Vivo Imaging of Inflammation and Infection

Anne Roivainen , Xiang-Guo Li , Cristina Nanni, Weibo Cai , and Sarah Ohrndorf
Editorial (2 pages), Article ID 3817871, Volume 2018 (2018)

A Comparative ^{68}Ga -Citrate and ^{68}Ga -Chloride PET/CT Imaging of *Staphylococcus aureus* Osteomyelitis in the Rat Tibia

Petteri Lankinen, Tommi Noponen, Anu Autio, Pauliina Luoto, Janek Frantzèn , Eliisa Löyttyniemi, Antti J. Hakanen, Hannu T. Aro , and Anne Roivainen 
Research Article (10 pages), Article ID 9892604, Volume 2018 (2018)

Imaging and Methotrexate Response Monitoring of Systemic Inflammation in Arthritic Rats Employing the Macrophage PET Tracer [^{18}F]Fluoro-PEG-Folate

Durga M. S. H. Chandrupatla , Gerrit Jansen, Elise Mantel, Philip S. Low, Takami Matsuyama, René P. Musters, Albert D. Windhorst, Adriaan A. Lammertsma , Carla F. M. Molthoff , and Conny J. van der Laken 
Research Article (10 pages), Article ID 8092781, Volume 2018 (2018)

Prospective of ^{68}Ga Radionuclide Contribution to the Development of Imaging Agents for Infection and Inflammation

Irina Velikyan 
Review Article (24 pages), Article ID 9713691, Volume 2018 (2018)

Comparison of ^{68}Ga -DOTA-Siglec-9 and ^{18}F -Fluorodeoxyribose-Siglec-9: Inflammation Imaging and Radiation Dosimetry

Helena Virtanen, Johanna M. U. Silvola, Anu Autio, Xiang-Guo Li, Heidi Liljenbäck, Sanna Hellberg, Riikka Siitonen, Mia Stähle, Meeri Käkälä, Anu J. Airaksinen, Kerttuli Helariutta, Tuula Tolvanen, Tibor Z. Veres, Antti Saraste, Juhani Knuuti, Sirpa Jalkanen, and Anne Roivainen
Research Article (10 pages), Article ID 7645070, Volume 2017 (2018)

In Vivo PET Imaging of Adenosine 2A Receptors in Neuroinflammatory and Neurodegenerative Disease

Anna Vuorimaa, Eero Rissanen, and Laura Airas
Review Article (15 pages), Article ID 6975841, Volume 2017 (2018)

Integrating a ^{19}F MRI Tracer Agent into the Clinical Scale Manufacturing of a T-Cell Immunotherapy

Charles F. O'Hanlon, Tamara Fedczyna, Shannon Eaker, William D. Shingleton, and Brooke M. Helfer
Research Article (7 pages), Article ID 9548478, Volume 2017 (2018)

Head-to-Head Comparison of ^{68}Ga -Citrate and ^{18}F -FDG PET/CT for Detection of Infectious Foci in Patients with *Staphylococcus aureus* Bacteraemia

Soile P. Salomäki, Jukka Kemppainen, Ulla Hohenthal, Pauliina Luoto, Olli Eskola, Pirjo Nuutila, Marko Seppänen, Laura Pirilä, Jarmo Oksi, and Anne Roivainen
Clinical Study (8 pages), Article ID 3179607, Volume 2017 (2018)

Intensity of ^{18}F -FDG PET Uptake in Culture-Negative and Culture-Positive Cases of Chronic Osteomyelitis

Petteri Lankinen, Marko Seppänen, Kimmo Mattila, Markku Kallajoki, Juhani Knuuti, and Hannu T. Aro
Research Article (9 pages), Article ID 9754293, Volume 2017 (2018)

Kinetic Modelling of Infection Tracers [^{18}F]FDG, [^{68}Ga]Ga-Citrate, [^{11}C]Methionine, and [^{11}C]Donepezil in a Porcine Osteomyelitis Model

Lars Jødal, Svend B. Jensen, Ole L. Nielsen, Pia Afzelius, Per Borghammer, Aage K. O. Alstrup, and Søren B. Hansen
Research Article (18 pages), Article ID 9256858, Volume 2017 (2018)

TSPO PET Imaging: From Microglial Activation to Peripheral Sterile Inflammatory Diseases?

Bérenger Largeau, Anne-Claire Dupont, Denis Guilloteau, Maria-João Santiago-Ribeiro, and Nicolas Arlicot
Review Article (17 pages), Article ID 6592139, Volume 2017 (2018)

Correlation of ^{18}F -FDG PET/MRE Metrics with Inflammatory Biomarkers in Patients with Crohn's Disease: A Pilot Study

Liran Domachevsky, Haim Leibovitzh, Irit Avni-Biron, Lev Lichtenstein, Natalia Goldberg, Meital Nidam, David Groshar, Hanna Bernstine, and Ofer Ben-Bassat
Clinical Study (9 pages), Article ID 7167292, Volume 2017 (2018)

Editorial

In Vivo Imaging of Inflammation and Infection

Anne Roivainen ^{1,2,3} **Xiang-Guo Li** ^{1,4} **Cristina Nanni**,⁵ **Weibo Cai** ⁶
and **Sarah Ohrndorf**⁷

¹Turku PET Centre, University of Turku, 20521 Turku, Finland

²Turku PET Centre, Turku University Hospital, 20521 Turku, Finland

³Turku Center for Disease Modeling, University of Turku, 20521 Turku, Finland

⁴Turku PET Centre, Åbo Akademi University, 20521 Turku, Finland

⁵University of Bologna, Bologna, Italy

⁶University of Wisconsin-Madison, Madison, WI, USA

⁷Charité Universitätsmedizin, Berlin, Germany

Correspondence should be addressed to Anne Roivainen; anne.roivainen@utu.fi

Received 17 April 2018; Accepted 17 April 2018; Published 17 May 2018

Copyright © 2018 Anne Roivainen et al. This is an open access article distributed under the Creative Commons Attribution License, which permits unrestricted use, distribution, and reproduction in any medium, provided the original work is properly cited.

Inflammation is a significant component of several chronic diseases involving the cardiovascular, metabolic, musculo-skeletal, and nervous systems. Timely identification and localization of inflammation is critical for the adequate treatment of patients. Notably, also, infection always has inflammatory components. Molecular imaging such as positron emission tomography (PET) may reveal molecular and cellular changes and provide sensitive detection of inflammatory and/or infectious foci at an early stage of disease. In general, specific imaging of inflammatory processes may be a demanding task because of increased blood flow and enhanced vascular permeability causing unspecific uptake of imaging agents. Although several radiopharmaceuticals have been developed, no agent has been found with the optimal characteristics for imaging inflammation, and thus, there is still room for new, better agents and development of quantification methods.

This special issue consists of totally 11 articles (147 pages) including three review articles, six research articles, and two clinical studies. Nine articles are dealing with PET, one with magnetic resonance imaging (MRI), and one with PET-MRI. One of the research article deals with the modeling of PET, and the rest are preclinical/translational studies.

To perform diagnosis with PET, appropriate radiopharmaceuticals are needed. The radiopharmaceuticals are compounds possessing positron-emitting radionuclides, and

gallium-68 (⁶⁸Ga) is one of the most frequently used radionuclides in clinical PET. The review article “Prospective of ⁶⁸Ga Radionuclide Contribution to the Development of Imaging Agents for Infection and Inflammation” by Velikyan provides an overview of ⁶⁸Ga-labelled compounds for imaging of inflammation and infection in both pre-clinical and clinical settings. ⁶⁸Ga can be conveniently obtained from commercially available generators, which facilitates the implementation of ⁶⁸Ga-radiopharmaceutical research in many medical centers and in major human diseases including infection and inflammation.

In neuroinflammatory diseases such as multiple sclerosis (MS), there are clear clinical evidences for upregulation of the adenosine subtype 2A receptor (A_{2A}). PET imaging of A_{2A} has become an approach to monitor functional changes and the treatment responses in the brain in the neuro-inflammatory conditions. The review article “In Vivo PET Imaging of Adenosine 2A Receptors in Neuroinflammatory and Neurodegenerative Disease” by Vuorimaa et al. presents the progress in the research of PET imaging of A_{2A}. So far, five PET ligands have entered into clinical trials, and each of them has their strengths and shortcomings regarding A_{2A} imaging.

Another important target for PET imaging of inflammation is 18 kDa translocator protein (TSPO). In the paper “TSPO PET Imaging: from Microglial Activation to

Peripheral Sterile Inflammatory Diseases?” by Largeau et al., the authors discuss the exciting findings so far observed in the research of TSPO-targeted imaging. Furthermore, the challenges related to TSPO expression under physiological conditions and radioligand metabolism have been presented.

Fluorine-18 is a frequently used radionuclide for PET imaging, and its nonradioactive isotope fluorine-19 (^{19}F) is very useful in MRI applications. In the work “Integrating a ^{19}F MRI Tracer Agent into the Clinical Scale Manufacturing of a T-Cell Immunotherapy” by O’Hanlon et al., the authors report the scaling-up production of ^{19}F -labelled T cells. The engineered T cells are originally used for immunotherapy. Upon incorporation of the cell sense agent into the T cells, it becomes possible to monitor the *in vivo* migration of the ^{19}F -labelled T cells with MRI in the setting of treatment. Therefore, ^{19}F -labelling is expected to have an added value in the development of cell-based therapeutics.

Osteomyelitis is an infectious bone disease, and PET imaging of osteomyelitis is often challenging, in particular in the cases of altered bone structures. In the work “A Comparative ^{68}Ga -Citrate and ^{68}Ga -Chloride PET/CT Imaging of *Staphylococcus aureus* Osteomyelitis in the Rat Tibia” by Lankinen et al., the authors have confirmed that ^{68}Ga -citrate is a more appropriate radiopharmaceutical than ^{68}Ga -chloride for PET imaging of osteomyelitis in their experimental settings in rats.

In addition to ^{68}Ga -citrate, there are a number of other PET tracers that have been used for osteomyelitis imaging. In the work “Kinetic Modelling of Infection Tracers [^{18}F]FDG, [^{68}Ga]Ga-Citrate, [^{11}C]Methionine, and [^{11}C]Donepezil in a Porcine Osteomyelitis Model” by Jødal et al., with the aid of kinetic modelling, the authors conclude that [^{18}F]FDG is an applicable tracer in general for PET imaging of osteomyelitis models in pigs.

In a clinical setting for osteomyelitis PET imaging, Salomäki et al. compare the imaging performance of ^{68}Ga -citrate and [^{18}F]FDG in their paper “Head-to-Head Comparison of ^{68}Ga -Citrate and ^{18}F -FDG PET/CT for Detection of Infectious Foci in Patients with *Staphylococcus aureus* Bacteraemia.” The results suggest that ^{68}Ga -citrate and [^{18}F]FDG have comparable performance in detection of osteomyelitis in general, but [^{18}F]FDG shows higher intensity in soft tissues.

In another clinical study, Lankinen et al. use [^{18}F]FDG to image osteomyelitis in their work “Intensity of ^{18}F -FDG PET Uptake in Culture-Negative and Culture-Positive Cases of Chronic Osteomyelitis.” The results suggest that [^{18}F]FDG can reveal osteomyelitis even in cases when microbiological culturing is still negative.

Regarding PET imaging of inflammation, vascular adhesion protein-1 (VAP-1) is one of the ideal targets. VAP-1 stays in its intracellular storage granules but rapidly relocates to endothelial cell surfaces upon inflammation. Virtanen et al. have studied two radiolabelled VAP-1 ligands in rats with skin inflammation and in mice with atherosclerosis, as described in their paper “Comparison of ^{68}Ga -DOTA-Siglec-9 and ^{18}F -Fluorodeoxyribose-Siglec-9: Inflammation Imaging and Radiation Dosimetry.”

In inflammation, folate receptors are often upregulated, which provides an alternative way for medical imaging and

treatment. In the contribution “Imaging and Methotrexate Response Monitoring of Systemic Inflammation in Arthritic Rats Employing the Macrophage PET Tracer [^{18}F]Fluoro-PEG-Folate” by Chandrupatla et al., the authors found out with the aid of ^{18}F -labelled folate imaging that activated macrophages are reduced in the liver and spleen upon methotrexate treatment.

Crohn’s disease is a chronic inflammatory disease that can affect the entire gastrointestinal track. To increase the accuracy in assessing Crohn’s disease, Domachevsky et al. have added an apparent diffusion coefficient and a metabolic inflammatory volume to the magnetic resonance index of the activity score, and this has been described in their paper “Correlation of ^{18}F -FDG PET/MRE Metrics with Inflammatory Biomarkers in Patients with Crohn’s Disease: A Pilot Study.”

This special issue presents some new evidences of pre-clinical and clinical PET imaging of inflammation and infection, in addition to the overviews highly relevant to this field. We hope that this issue will provoke further research on these topics.

Acknowledgments

Thanks are due to all the authors for their excellent contributions and the reviewers for their kind cooperation and critical comments in achieving this special issue.

Anne Roivainen
Xiang-Guo Li
Cristina Nanni
Weibo Cai
Sarah Ohrndorf

Research Article

A Comparative ^{68}Ga -Citrate and ^{68}Ga -Chloride PET/CT Imaging of *Staphylococcus aureus* Osteomyelitis in the Rat Tibia

Petteri Lankinen,¹ Tommi Noponen,² Anu Autio,³ Pauliina Luoto,³ Janek Frantzèn ,⁴ Eliisa Löyttyniemi,⁵ Antti J. Hakanen,⁶ Hannu T. Aro ,^{1,7} and Anne Roivainen ,^{3,8,9}

¹Department of Orthopaedics and Traumatology, Turku University Hospital, Turku, Finland

²Department of Clinical Physiology and Nuclear Medicine, Turku University Hospital and University of Turku, Turku, Finland

³Turku PET Centre, University of Turku, Turku, Finland

⁴Division of Clinical Neurosciences, Department of Neurosurgery, Turku University Hospital, Turku, Finland

⁵Department of Biostatistics, University of Turku, Turku, Finland

⁶Department of Clinical Microbiology, Turku University Hospital and Medical Microbiology and Immunology, University of Turku, Turku, Finland

⁷Orthopaedic Research Unit, Department of Orthopaedic Surgery and Traumatology, University of Turku, Turku, Finland

⁸Turku PET Centre, Turku University Hospital, Turku, Finland

⁹Turku Center for Disease Modeling, University of Turku, Turku, Finland

Correspondence should be addressed to Anne Roivainen; anne.roivainen@utu.fi

Received 22 September 2017; Accepted 18 January 2018; Published 25 February 2018

Academic Editor: Ralf Schirmmacher

Copyright © 2018 Petteri Lankinen et al. This is an open access article distributed under the Creative Commons Attribution License, which permits unrestricted use, distribution, and reproduction in any medium, provided the original work is properly cited.

There may be some differences in the *in vivo* behavior of ^{68}Ga -chloride and ^{68}Ga -citrate leading to different accumulation profiles. This study compared ^{68}Ga -citrate and ^{68}Ga -chloride PET/CT imaging under standardized experimental models. *Methods.* Diffuse *Staphylococcus aureus* tibial osteomyelitis and uncomplicated bone healing rat models were used ($n = 32$). Two weeks after surgery, PET/CT imaging was performed on consecutive days using ^{68}Ga -citrate or ^{68}Ga -chloride, and tissue accumulation was confirmed by *ex vivo* analysis. In addition, peripheral quantitative computed tomography and conventional radiography were performed. Osteomyelitis was verified by microbiological analysis and specimens were also processed for histomorphometry. *Results.* In PET/CT imaging, the SUV_{max} of ^{68}Ga -chloride and ^{68}Ga -citrate in the osteomyelitic tibias (3.6 ± 1.4 and 4.7 ± 1.5 , resp.) were significantly higher ($P = 0.0019$ and $P = 0.0020$, resp.) than in the uncomplicated bone healing (2.7 ± 0.44 and 2.5 ± 0.49 , resp.). In osteomyelitic tibias, the SUV_{max} of ^{68}Ga -citrate was significantly higher than the uptake of ^{68}Ga -chloride ($P = 0.0017$). In animals with uncomplicated bone healing, no difference in the SUV_{max} of ^{68}Ga -chloride or ^{68}Ga -citrate was seen in the operated tibias. *Conclusions.* This study further corroborates the use of ^{68}Ga -citrate for PET imaging of osteomyelitis.

1. Introduction

Deep bone infections are one of the most challenging conditions to treat in orthopedics and trauma surgery. By nature, these infections are highly challenging for diagnostic imaging, especially when bone structures have been altered by trauma, surgery, or a previous pathological condition. Standard diagnostic tools such as conventional radiographs, magnetic resonance imaging (MRI), computed tomography (CT), and conventional nuclear medicine methods are known

to have major limitations in the early diagnosis of deep bone infections [1–5]. Positron emission tomography (PET) imaging with 2-deoxy-2- ^{18}F -fluoro-*D*-glucose (^{18}F -FDG) has been shown to have a high diagnostic accuracy for confirming or excluding the diagnosis of chronic osteomyelitis [3, 6, 7]. In the clinical setting, the use of ^{18}F -FDG-PET for differential diagnosis involves a risk of possible false positive findings due to the early bone healing process, which involves an inflammatory phase. This phase represents a highly activated state of cell metabolism and glucose consumption [8] and can

thus possibly mimic a similar ^{18}F -FDG-PET tracer uptake pattern to that occurring during infection. In an experimental study using a rabbit osteomyelitis model, bone infection could be distinguished from bone healing by means of ^{18}F -FDG PET 3 weeks after surgery [9]. In a previous rat study, we reported elevated uptake of ^{18}F -FDG in healing bone but a significantly lower uptake of ^{68}Ga -chloride in tibias with uncomplicated healing defects, whereas no statistical difference was seen between the tracers in osteomyelitic tibias [10]. Thus, in patients with postsurgical and posttraumatic bone healing, ^{68}Ga could be more promising than ^{18}F -FDG in the discrimination of bacterial infection from the unspecific uptake caused by the physiological inflammatory processes of normal bone healing.

^{67}Ga -citrate has been used in scintigraphy for the evaluation of infectious processes for several decades. The accumulation of gallium in inflammatory or infectious sites is partly due to the increased capillary permeability associated with inflammatory reactions; gallium exits the vascular network and is trapped in the extravascular compartment [11]. As an iron analogue, it binds to circulating transferrin and, via transferrin receptors, accesses cells and evolves to a highly stable state [12]. As a tracer, gallium is able to bind to bacterial siderophores and activated lactoferrin in neutrophils [13], with an uptake by macrophages also having been demonstrated [14–16]. In addition, a direct bacterial uptake pattern has been reported [17]. In general, different radionuclides such as ^{68}Ga (positron emitter used for PET) and ^{67}Ga (gamma emitter used for single-photon emission computed tomography (SPECT)) vary only according to their physical properties, with their chemical and physiological behavior being comparable. However, there may be some differences between ^{68}Ga -chloride and ^{68}Ga -citrate in regard to their *in vivo* behavior.

The purpose of this study was to compare ^{68}Ga -citrate and ^{68}Ga -chloride PET/CT imaging under standardized experimental models of uncomplicated bone healing and *Staphylococcus aureus* osteomyelitis. In addition, *ex vivo* measurements of tissue radioactivity concentration in normal bone healing and osteomyelitic tissues were performed to verify the uptake and biodistribution of ^{68}Ga -citrate.

2. Materials and Methods

2.1. Animals. Thirty-two skeletally mature male Sprague-Dawley rats (Harlan, Horst, The Netherlands) with a mean weight of 412.6 ± 64.2 g were used in these experiments. The rats were allowed to acclimatize to their new environment before surgery. All animal experiments were approved by the National Animal Experiment Board in Finland and the Regional State Administrative Agency for Southern Finland and were conducted in accordance with the European Union directive.

2.2. Experimental Design. In each animal, the left tibia was operated on and the right contralateral tibia served as an intact control. For the comparative ^{68}Ga -citrate and ^{68}Ga -chloride PET/CT imaging, animals with induced osteomyelitis ($n = 8$) and animals with normal bone healing ($n = 8$)

were imaged with both tracers on consecutive days (Figure 1). Bone structural changes caused by infection were evaluated by peripheral quantitative computed tomography (pQCT), which was performed after the PET/CT imaging. The operated tibias were harvested and samples were retrieved for quantitative microbiological analyses and semiquantitative histopathologic analyses. For the *ex vivo* measurements of tissue radioactivity concentration, the accumulation of ^{68}Ga -citrate was studied in animals with induced osteomyelitis ($n = 8$) and animals with normal bone healing ($n = 8$). All studies were performed 2 weeks after surgery, that is, after induction of osteomyelitis or creation of a healing bone defect.

2.3. Induction of Infection. The diffuse rat osteomyelitis model (stage IVA in the Cierny-Mader classification; osteomyelitis secondary to a contiguous focus of infection in the Waldvogel classification) was adopted for this study [10, 18–20]. The rats were anaesthetized with a mixture of fentanyl, fluanisone (Hypnorm, Janssen Pharmaceutica, Beerse, Belgium), and midazolam (Midazolam Hameln 5 mg/ml, Hameln Pharmaceuticals GmbH, Hameln, Germany). The left hind leg was shaved, disinfected, and covered with sterile sheets. Using sterile surgical conditions, a small cortical bone defect (diameter 1.0 mm) was created into the proximal medial metaphysis of the right tibia using a high speed dental drill. Local bone marrow was removed with saline lavage. As described earlier [10, 18], osteomyelitis was induced by injecting into the medullary cavity a volume of 0.05 ml of 5% wt/vol sodium morrhuate (Scleromate, Glenwood, Englewood, NJ, USA), which was immediately followed by a 0.05 ml volume of the bacterial inoculum (3×10^8 colony-forming unit [CFU]/ml of *S. aureus*). The drilling hole was sealed with bone wax (Braun, Aesculap AG & Co., Tuttlingen, Germany) to prevent bacterial leakage and provide a foreign body for infection [20]. Finally, the skin wound was cleaned with a 40 ml sterile saline lavage without antibiotics and closed in layers. In control animals, a cortical defect of equal size was drilled, but the sodium morrhuate, bacterial suspension, and bone wax were not used. Before wound closure, the surgical field was lavaged with 40 ml sterile saline containing 150 mg cefuroxime sodium (Zinacef, GlaxoSmithKline, Verona, Italy). Bacitracin and neomycin sulfate powder (Bacibact, Orion Oyj, Espoo, Finland) were applied to the sutured skin wound and it was covered with an aerosol-based plastic film (HansaPlast, Beiersdorf AG, Hamburg, Germany). Anaesthesia was reversed by a subcutaneous injection of naloxone (Narcanti, Du Pont Pharmaceuticals Ltd., Letchworth, UK). After surgery, the animals were closely monitored and standard postoperative pain medication was given for the first 3 postoperative days (0.5 mg/kg of buprenorphine subcutaneously every 12 hours, Temgesic® 0.3 mg/ml, Schering-Plough, Brussels, Belgium). The animals were housed individually for 2 days, after which they were returned to their normal housing in groups of two. All the animals had an uneventful postoperative recovery, and their activity was not limited within the individual cages.

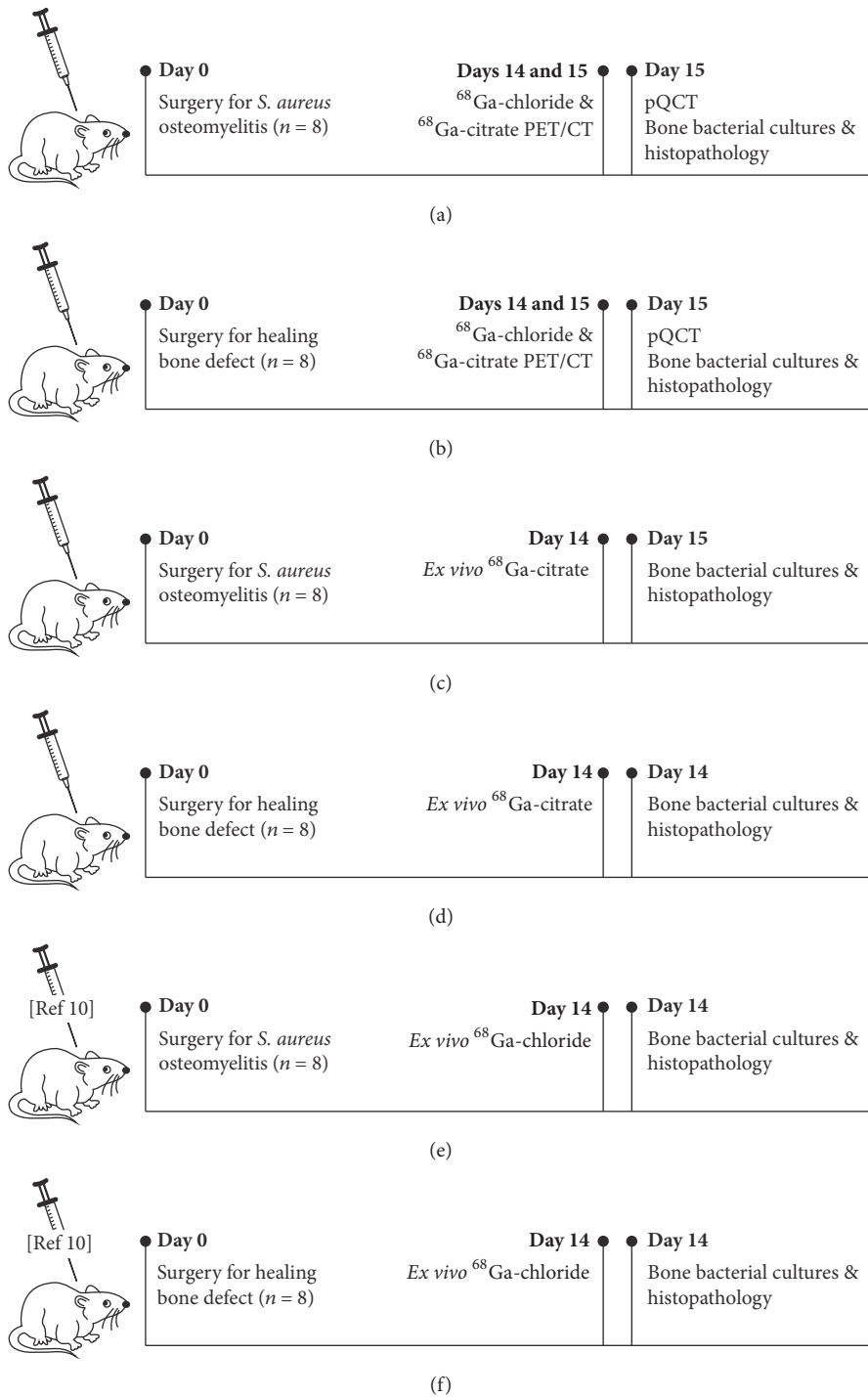


FIGURE 1: Schematic illustration of experimental design and timing of performed analysis methods.

2.4. ^{68}Ga -Citrate and ^{68}Ga -Chloride PET/CT. Comparative ^{68}Ga -citrate and ^{68}Ga -chloride PET/CT were performed 2 weeks after the surgery in which either osteomyelitis was induced or a cortical bone defect was created (Figure 1).

To prepare the ^{68}Ga -chloride injection, ^{68}Ga from $^{68}\text{Ge}/^{68}\text{Ga}$ generator (Eckert & Ziegler, Valencia, CA, USA) was eluted with 0.1 M hydrochloric acid and neutralized with

1 M sodium hydroxide before use. ^{68}Ga -citrate was prepared by mixing the ^{68}Ga -eluate with sodium citrate as previously described [21]. Radiochemical purity was evaluated by the instant thin layer chromatography-silica-gel technique using methanol/acetic acid (9 : 1) as a mobile phase.

PET/CT imaging was performed with a Discovery VCT (General Electric Medical Systems, Milwaukee, WI, USA)

operating in 3-dimensional mode. This is a combined 64-slice CT and PET scanner with 24 rings of bismuth germanate detectors; it acquires 47 imaging planes with an axial field-of-view of 15.7 cm. The transaxial crystal size of the PET scanner is 4.7 mm, and the spatial resolution in 3D mode is 5.12 mm in full width at half maximum with a 1 cm offset from the center of the field-of-view [22]. In a pilot study, two rats in the osteomyelitis group underwent 180 min dynamic scanning starting immediately after an i.v. injection of ^{68}Ga -citrate. The protocols for PET imaging were designed according to the observed patterns of tracer accumulation. Dynamic PET imaging consisting of 4×5 min frames was started 120 minutes after the injection of ^{68}Ga -citrate and 90 minutes after the injection of ^{68}Ga -chloride. Dynamic PET imaging was performed to avoid the potential effects of animal movement during the scanning period. CT was performed before PET, using the following technical parameters: helical scan mode, helical slice thickness of 3.75 mm, detector coverage of 20 mm, pitch factor of 0.531:1, voltage of 100 kVp, current of 80 mA, rotation time of 1 s, "large body" scan field-of-view, and display field-of-view 50. PET images were reconstructed using an ordered subsets expectation maximization algorithm and the CT images were reconstructed using a CT attenuation correction (CTAC) and bone kernels. The CT data were used for attenuation correction (CTAC images) and anatomical reference (bone images) when fused with the PET images.

The animals fasted for 4 h prior to tracer injection and were sedated for PET/CT imaging as in the surgical procedure. On average, 29.1 ± 1.8 MBq of ^{68}Ga -citrate (mean \pm standard deviation [SD]) and 28.8 ± 2.4 MBq of ^{68}Ga -chloride were injected into the tail vein of the animal in a volume of 0.5–1.0 ml. Quantitative analysis of tracer uptake was performed for a standardized circular region of interest (ROI diameter, 3.0 mm) in the operated left tibia and the corresponding region in the contralateral intact right tibia. The levels of ^{68}Ga -citrate and ^{68}Ga -chloride accumulation were reported as the maximum standardized uptake value (SUV_{max}). The SUV_{max} was calculated as the maximum radioactivity concentration within the ROI divided by the relative injected radioactivity dose expressed per kg of body weight. In addition, SUV ratios, that is, operated bone-to-intact bone, were calculated.

2.5. pQCT. Each animal underwent pQCT scanning following the PET imaging. Under fentanyl-fluanisone sedation, the operated limbs were placed in a holder for standard positioning. Imaging was performed using a Stratec XCT Research M pQCT device with software version 5.20 (Norland Stratec Medizintechnik GmbH, Birkenfeld, Germany). After an initial scout view for positioning, the proximal tibias were imaged with six consecutive cross-sectional images using a slice distance of 0.75 mm. A voxel size of $0.07 \times 0.07 \times 0.50$ mm was used. The pQCT images were analysed for the presence of osteomyelitic destruction and reactive new bone formation.

After pQCT imaging, the animals were killed with an intravenous administration of sodium pentobarbital.

2.6. Microbiological Analyses. The presence of infection was confirmed with bacterial cultures at the time of killing. Using sterile techniques, the bone defect area was exposed and swab cultures were taken from subfascial soft tissues. The proximal tibia was aseptically cross-sectioned using a high speed circular saw to obtain three (proximal, middle, and distal) bone specimens from the site of bone infection. The proximal and middle segments were used for histological analysis and the distal bone segment was used for quantitative bacterial culture.

All swab specimens were cultured for 18–20 hours at 35°C on blood agar plates. After snap-freezing in liquid nitrogen and homogenization with a mortar and pestle, the distal bone segment was vortexed in saline for 5 min, and ten serial 10-fold dilutions were performed to determine the CFU of *S. aureus* per gram of bone. The dilutions were cultured for 18–20 hours at 35°C on blood agar plates. The aseptically harvested bone cement blocks were cultured on blood agar and immediately placed in BBL™ Brain Heart Infusion broth (Becton, Dickinson and Company, Sparks, MD, USA) and incubated for up to 5 days at 35°C . The turbidity of broth samples was observed every day, and positive cultures (i.e., opaque tubes) were plated onto blood agar plates and incubated for 18–20 hours at 35°C . Negative broth samples (i.e., clear tubes) were similarly cultured after 2 and 5 days of incubation.

The isolated pathogens were identified on the basis of their morphology and with the Slidex® Staph Plus latex agglutination test (bioMérieux, Marcy l'Etoile, France) [23]. *S. aureus* (American Type Culture Collection [ATCC] strain 29213) was used as the positive control and *Enterococcus faecalis* (ATCC strain 29212) was used as the negative control.

2.7. Semiquantitative Histopathologic Analysis. The proximal and middle bone specimens were processed for histology. The proximal specimen was fixed in 70% ethanol, embedded in isobornyl methacrylate (Technovit 1200 VLC, Kulzer, Germany), and stained with a modified van Gieson method. The middle bone segment was decalcified, embedded in paraffin, and stained with hematoxylin and eosin. Histological changes in the periosteum, cortical bone, and medullary canal were classified according to the histopathological scoring system presented by Petty and coworkers [10, 18, 24, 25]. Two observers classified the histological sections, with the results presented being their mutual agreement of the interpretation.

2.8. Ex Vivo Measurement of ^{68}Ga -Citrate Accumulation. As a separate substudy, the accumulation of ^{68}Ga -citrate at 2 weeks after operation was studied *ex vivo* in animals with induced osteomyelitis ($n = 8$) and control animals with a healing bone defect ($n = 8$) (Figure 1). The animals fasted for 4 h prior to tracer injection. Under sedation obtained by a subcutaneous injection of midazolam, fluanisone, and fentanyl citrate, a dose of 33.0 ± 3.2 MBq of ^{68}Ga -citrate was injected via the tail vein of the animal in a volume of 0.5–1.0 ml. After tracer accumulation (90 min for ^{68}Ga -citrate), a blood sample was obtained via intracardiac

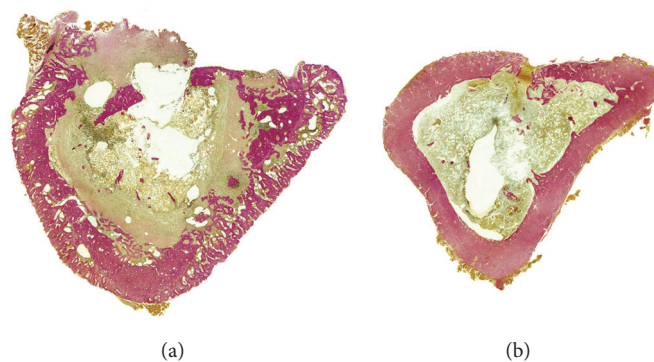


FIGURE 2: Histological sections of osteomyelitic (a) and control (b) rat tibias at 2 weeks after surgery. The osteomyelitic changes were characterised by a wide circumferential periosteal reaction, focally enlarged haversian canals filled with fragmented polymorphonuclear leukocytes and occasional microabscesses, and major infiltration of the bone marrow by polymorphonuclear leukocytes. In some cases, a devitalized bone fragment was seen in the unhealed cortical window. In the control animals, periosteal reaction was minimal and there was modest endosteal new bone close to the cortical defect, indicating healing of the cortical defect. Modified van Gieson stain at $\times 10$ magnification.

puncture, and the animals were sacrificed by intracardiac administration of sodium pentobarbital (Mebunat, Orion, Espoo, Finland). Quantitative bacterial culture was performed on bone tissue specimens removed from the distal tibia to confirm the presence of osteomyelitis. In addition to tissue specimens excised from calf muscles, a 15 mm long segment of the operated proximal tibia (including the site of the bone defect) and a corresponding segment of the contralateral tibia were resected for analysis of tracer accumulation. The radioactivity of blood, muscle, and bone specimens was measured with a gamma counter (1480 Wizard 3^{''}; PerkinElmer/Wallac, Turku, Finland) cross-calibrated with a dose calibrator (VDC-202, Veenstra Instruments, Joure, The Netherlands). The radioactivity concentration was expressed as SUV [(tissue radioactivity/tissue weight)/(total given radioactivity/rat body weight)], and the SUV ratios (operated bone-to-muscle, operated bone-to-blood and operated bone-to-intact bone) were calculated.

We used previously published results of *ex vivo* ^{68}Ga -chloride accumulation that utilized the same study protocol and identical animal model [10] to make comparisons with the accumulation of ^{68}Ga -citrate (Figure 1).

2.9. Statistical Analysis. Data are expressed as mean \pm SD. Histological osteomyelitic changes (periosteal reaction, cortical bone, and medullary canal) were compared between the groups with a Wilcoxon rank sum test. The comparisons of SUV ratios between ^{68}Ga -citrate and ^{68}Ga -chloride, and between the osteomyelitis and bone healing groups, were performed with a hierarchical linear mixed model for repeated measures, including one within-factor (tracer) and one between-factor analysis (group). The model also included interaction between the factors, which indicated whether a significant mean difference between the groups was different between the two different tracers. Pairwise comparisons between tracers for specific study questions were programmed into the model. SUV_{max} was analysed separately for both tracers, using similar methods.

All tests performed were two-sided, with a significance level set at 0.05. The analyses were performed using SAS version 9.3 (SAS Institute Inc., Cary, NC, USA).

3. Results

3.1. Confirmation of Staphylococcal Infection and Histological Appearance of Osteomyelitis. The inoculated pathogen was cultured from the homogenized bone specimens in all animals with induced osteomyelitis. In 14 out of 16 osteomyelitic animals (87.5%), the swab cultures taken from subfascial soft tissues were positive for the inoculated *S. aureus*, indicating the extension of infection outside the bone. None of the animals had an infected draining sinus. No bacteria could be cultured from the homogenized bone specimens retrieved from the control animals. Similarly, all swab cultures from the soft tissues of control animals were negative.

The *S. aureus* group of animals showed histologically severe osteomyelitis in all cases (histologic score 2.5 ± 0.4 ; Figure 2). Histological appearance was characterised by a nearly circumferential periosteal reaction, reactive new bone formation, occasional sequester formation, and drastic infiltration of polymorphonuclear leukocytes with occasional microabscesses. The control group with healing cortical-defects showed healing of the defect by endosteal new bone formation, with no signs of infection (score 0.2 ± 0.3 ; Figure 2). Histological appearance was characterised by closure of the cortical defect with only a limited number of inflammatory cell infiltrations. There was a significant difference in the mean histological score between the two groups ($P = 0.0065$).

3.2. ^{68}Ga -Citrate and ^{68}Ga -Chloride PET/CT Imaging. On the basis of the dynamic imaging, the accumulation kinetics of ^{68}Ga -chloride and ^{68}Ga -citrate at the site of infection was found rather stable at 90–120 min postinjection (Figure 3). PET/CT imaging demonstrated intense accumulation of both ^{68}Ga -chloride and ^{68}Ga -citrate in osteomyelitic tibias in

TABLE 1: *Ex vivo* analysis of tracer accumulation reported as SUV.

	⁶⁸ Ga-citrate		⁶⁸ Ga-chloride [10]	
	Osteomyelitis	Bone healing	Osteomyelitis	Bone healing
Blood	1.0 ± 0.12	0.85 ± 0.41	1.4 ± 0.17	1.2 ± 0.15
Muscle, operated side	0.14 ± 0.054	0.12 ± 0.055	0.075 ± 0.032	0.055 ± 0.039
Muscle, control side	0.14 ± 0.081	0.13 ± 0.087	0.10 ± 0.057	0.071 ± 0.033
Bone, operated side	0.70 ± 0.13	0.19 ± 0.093	0.48 ± 0.19	0.28 ± 0.10
Bone, intact control	0.42 ± 0.081	0.18 ± 0.088	0.24 ± 0.044	0.31 ± 0.11
Operated bone-to-muscle	7.0 ± 4.9	1.7 ± 0.67	6.7 ± 1.2	5.6 ± 1.8
Operated bone-to-blood	0.70 ± 0.13	0.23 ± 0.033	0.36 ± 0.055	0.25 ± 0.074
Operated bone-to-intact bone	1.7 ± 0.21	1.1 ± 0.13	1.9 ± 0.56	0.92 ± 0.21

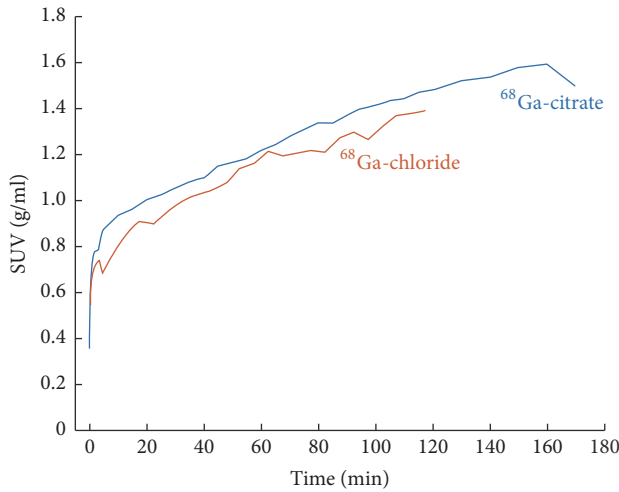


FIGURE 3: Time-activity curves for ⁶⁸Ga-citrate and ⁶⁸Ga-chloride accumulation at the site of induced osteomyelitis in rat tibia as determined by *in vivo* PET/CT imaging. The line represents the mean value of two animals. The radioactivity concentration, expressed in SUV, has been decay-corrected to the time of injection.

comparison with the contralateral intact bone or animals with uncomplicated bone healing (Figure 4).

The SUV_{max} of ⁶⁸Ga-chloride and ⁶⁸Ga-citrate in the osteomyelitic tibias (3.6 ± 1.4 and 4.7 ± 1.5 , respectively, $P = 0.0017$ between them) were significantly higher ($P = 0.0019$ and $P = 0.0020$, respectively) than in the tibias with uncomplicated bone healing (2.7 ± 0.44 and 2.5 ± 0.49 , respectively, $P = 0.60$ between them; Figure 5).

Furthermore, the corresponding SUV_{max} ratios were significantly higher in the osteomyelitic animals (osteomyelitis-to-intact bone ratio 1.8 ± 0.32 and 2.2 ± 0.76 , respectively) than in the animals with healing bone-defects (operated-to-intact bone ratio 1.2 ± 0.18 and 1.4 ± 0.25 , respectively) for both ⁶⁸Ga-chloride and ⁶⁸Ga-citrate ($P = 0.012$ and $P = 0.0011$, respectively) (Figure 4). In the animals with healing bone-defects, no statistically significant difference was found between the SUV_{max} ratios ($P = 0.22$, Figure 5).

3.3. Osteomyelitic Changes Determined Using pQCT. In pQCT imaging, the group of animals with *S. aureus*

(52/52A/80) infection showed signs consistent with bone infection, characterised by cortical bone destruction with circumferential periosteal reaction, reactive endosteal new bone, and sequestrum formation. Animals with healing bone-defects showed diminution of the defect, representing cortical bone healing with no signs of infection.

3.4. Ex Vivo Analysis of ⁶⁸Ga-Citrate Accumulation and Comparison with Previously Published ⁶⁸Ga-Chloride Results. The *ex vivo* measurements of retrieved tissues correlated closely with the results of the *in vivo* PET imaging (Table 1). In the *ex vivo* analysis of ⁶⁸Ga-citrate accumulation, an intense uptake was seen in osteomyelitic tibias in comparison with the contralateral intact bone ($P < 0.0001$; Table 1). In the control group, there was no statistically significant difference in ⁶⁸Ga-citrate uptake between the operated and contralateral bones.

The accumulation of ⁶⁸Ga-citrate was significantly ($P < 0.0001$) higher in the osteomyelitic group than in the control group of animals with healing bone-defects (Table 1). In the control group, there was no statistically significant difference in ⁶⁸Ga-citrate uptake between the operated bone and contralateral bone.

There was no statistically significant difference in ⁶⁸Ga-citrate accumulation in retrieved samples from blood, muscle, heart, lungs, spleen, kidney, and liver between the animals with induced osteomyelitis and animals with healing bone-defects.

Corresponding with the *in vivo* PET results, a significantly ($P = 0.0027$) higher ⁶⁸Ga-citrate SUV-uptake was found in osteomyelitic tibias in comparison with ⁶⁸Ga-chloride uptake. Similarly, a significant increase ($P = 0.0026$) in ⁶⁸Ga-citrate uptake was seen in the healthy control tibias of the osteomyelitic animals in comparison with ⁶⁸Ga-chloride uptake.

4. Discussion

The purpose of this study was to compare the feasibility of ⁶⁸Ga-citrate and ⁶⁸Ga-chloride PET/CT imaging under standardized experimental models of *S. aureus* osteomyelitis and uncomplicated bone healing. There is a clinical need for more specific and early detection of bacterial infection

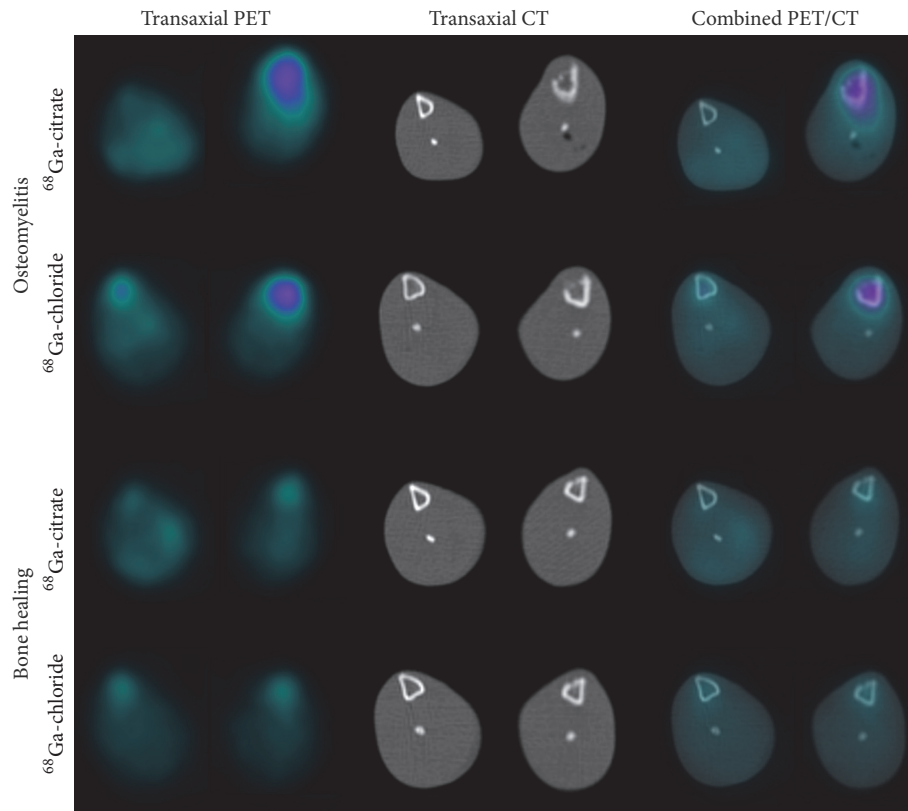


FIGURE 4: Representative transaxial PET, CT, and combined PET/CT images of ^{68}Ga -citrate and ^{68}Ga -chloride accumulation at the site of induced osteomyelitis and healing bone-defects at 2 weeks after surgery. In each animal, the left tibia (on the right) underwent surgery for induction of infection or the creation of a surgical defect to represent uncomplicated bone healing, with the contralateral intact bone (on the left) serving as the control.

after bone surgery. A tracer capable of differentiating between the physiological healing processes occurring in low-grade inflammation and early bacterial infection would therefore be highly beneficial. ^{18}F -FDG is a gold standard for PET imaging, but it is not specific for infection and inflammation. There are high expectations for novel tracers for the imaging of infection, with studies applying them in both patients and experimental models, with the objective of increasing the specificity of PET imaging [13, 26–30]. However, to date, none of the published novel imaging agents for infection imaging have been accepted for widespread clinical use. Only a few ^{68}Ga -labelled radiopharmaceuticals are in everyday use, although their potential applications are under extensive research [13, 31–34].

Nanni and coworkers [35] published promising results on the evaluation of bone infections with ^{68}Ga -citrate PET/CT. It has been shown that the image qualities of ^{68}Ga (β^+ decay 90%, $E\beta^+_{\text{max}}$ 2.91 MeV, $T_{1/2}$ 68 minutes) and ^{18}F tracers (β^+ decay 97%, $E\beta^+_{\text{max}}$ 0.64 MeV, $T_{1/2}$ 110 minutes) are almost equal [32, 35, 36]. ^{68}Ga has a rather high positron energy and it could be expected that this would result in a lower spatial resolution in comparison with ^{18}F . However, both computational analyses and experimental measurements have demonstrated that the image qualities are equal [37, 38].

Another advantage of ^{68}Ga over ^{18}F is the lower effective dose of ionizing radiation [38, 39].

When ^{68}Ga -chloride is neutralized with 1M sodium hydroxide, ^{68}Ga is rapidly hydrolyzed. Depending on the pH and concentration, in an aqueous solution ^{68}Ga occurs in a form of soluble anion called gallate, $^{68}\text{Ga}(\text{OH})_4^-$, and/or the insoluble neutral hydroxide $^{68}\text{Ga}(\text{OH})_3$. After rapid i.v. administration to the vascular system, the radioactivity can be distributed in the blood circulation as free ^{68}Ga or ^{68}Ga bound to transferrin, ferritin, or lactoferrin [40]. The free ^{68}Ga can be directly taken up by siderophores, which are low molecular weight chelates produced by bacteria, and which have a high affinity for gallium. The citrate is only a weak chelator *in vivo*, and after i.v. injection of ^{68}Ga -citrate, ^{68}Ga is rapidly released, hydrolyzed, and bound to transferrin and other plasma proteins. However, it is assumed that only a soluble gallate $^{67}\text{Ga}(\text{OH})_4^-$ is formed *in vivo* because the citrate is able to prevent precipitation of $^{67}\text{Ga}(\text{OH})_3$ [41].

The accumulation of gallium in inflammatory or infectious sites is partly due to the increased capillary permeability associated with inflammatory reactions; gallium exits the vascular network and is trapped in the extravascular compartment [11]. As an iron analogue, it binds to circulating transferrin, and via transferrin receptors, accesses cells and

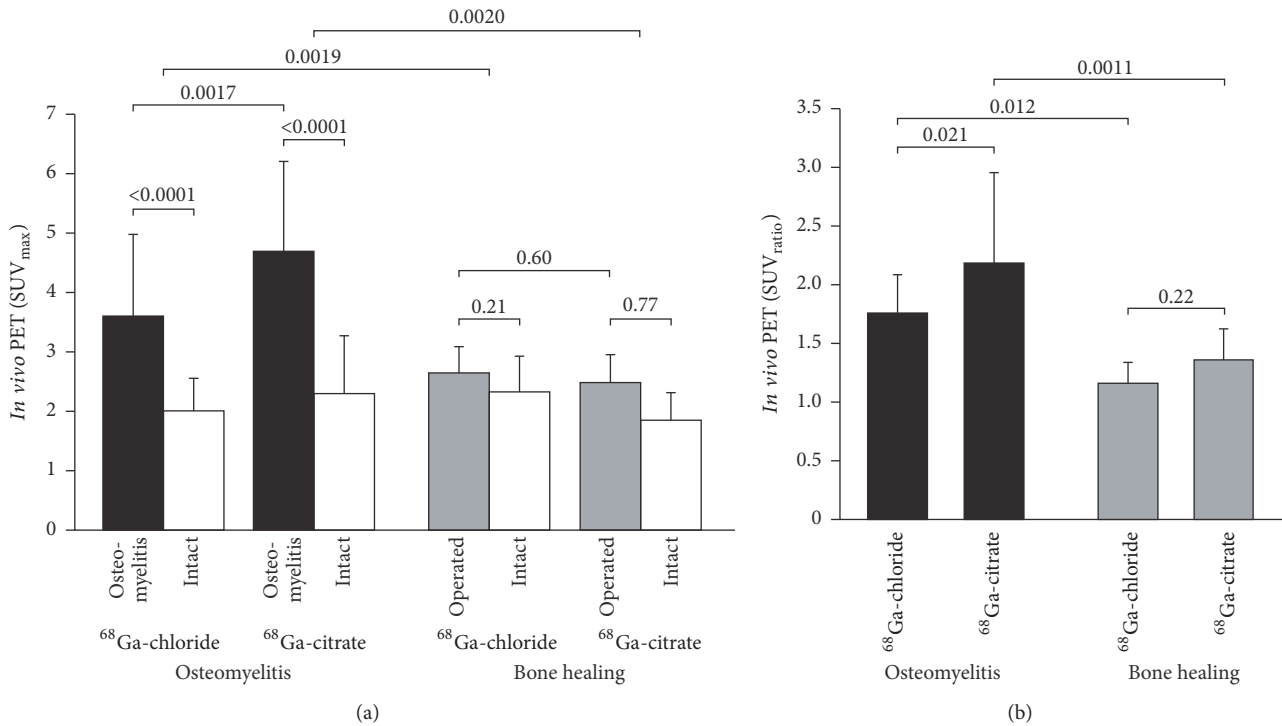


FIGURE 5: Quantification of ^{68}Ga -citrate and ^{68}Ga -chloride PET/CT imaging at 2 weeks after surgery. Bar graphs represent mean SUV_{max} values ($\pm\text{SD}$) (a) and SUV_{max} ratios, that is, operated bone-to-intact bone (b) ($n = 8$).

evolves to a highly stable state [12]. Gallium is able to bind to activated lactoferrin in neutrophils, and to bacterial siderophores [13], and uptake in macrophages has also been demonstrated [15, 16]. Also, a direct bacterial uptake pattern of gallium has been reported [17].

In our previous study, we evaluated the uptake patterns of ^{68}Ga -chloride and ^{18}F -FDG in *S. aureus* osteomyelitis and uncomplicated bone healing at 2 weeks after surgery [10]. ^{68}Ga -chloride was initially chosen for this further study, as a promising accumulation was seen in dynamic PET imaging when it was used as a control in a ^{68}Ga -labelled oligonucleotide study [34]. Additionally, ^{68}Ga -chloride was readily available at the Turku PET Centre through a relatively simple cyclotron independent manufacturing process. The accumulation of ^{68}Ga -chloride in the infected bone area was high 90 minutes after intravenous injection into rats, and therefore allowed rapid infection imaging. The accumulation kinetics of ^{68}Ga -chloride and ^{68}Ga -citrate at the site of infected bone appeared similar and rather stable during 90–120 min (Figure 3). According to *ex vivo* gamma counting of excised tissue samples, the operated bone-to-intact bone ratio of ^{68}Ga -chloride was significantly higher than that of ^{68}Ga -citrate. By *in vivo* PET/CT, however, the difference between tracers was the other way around; the corresponding SUV ratio with ^{68}Ga -citrate was higher. The difference between *ex vivo* and *in vivo* PET results may at least partly be explained by the different accumulation times. The 20 min

^{68}Ga -citrate PET acquisition started 120 min after injection while accumulation time after ^{68}Ga -chloride injection was shorter, 90 min. Also, *ex vivo* analyses were performed 90 min after ^{68}Ga -chloride or ^{68}Ga -citrate injection.

5. Conclusions

Our results revealed that ^{68}Ga -citrate may be superior to ^{68}Ga -chloride for PET imaging of osteomyelitis in postoperative situations and further support its use for such imaging.

Abbreviations

^{18}F -FDG:	2-Deoxy-2- ^{18}F -fluoro- <i>D</i> -glucose
CFU:	Colony-forming unit
CT:	Computed tomography
MRI:	Magnetic resonance imaging
PET:	Positron emission tomography
pQCT:	Peripheral quantitative computed tomography
ROI:	Region of interest
SUV_{max} :	Maximum standardized uptake value
SD:	Standard deviation.

Ethical Approval

The study protocol was approved by the National Animal Experiment Board in Finland and the Regional State Administrative Agency for Southern Finland and carried out in compliance with the relevant European Union directives.

Conflicts of Interest

The authors declare that they have no conflicts of interest.

Authors' Contributions

Anne Roivainen, Hannu T. Aro, Antti J. Hakanen, and Petteri Lankinen designed the study. Petteri Lankinen, Anu Autio, Pauliina Luoto, and Tommi Noponen carried out the experimental aspects of the study. Petteri Lankinen, Janek Frantzèn, Anne Roivainen, Tommi Noponen, and Eliisa Löyttyniemi carried out the analytical aspects of the study, including statistical analysis and modeling. Petteri Lankinen, Hannu T. Aro, and Anne Roivainen drafted the manuscript. All authors read and approved the final manuscript.

Acknowledgments

The authors thank Henri Sipilä for preparing tracers and Mia Stähle, Riikka Siitonen, and Timo Kattelus for making images. The studies were conducted within the Finnish Centre of Excellence in Cardiovascular and Metabolic Diseases supported by the Academy of Finland, the University of Turku, the Turku University Hospital, and Åbo Akademi University. This study was also funded by the State Research Funding (ERVA no. 13856), the Jane and Aatos Erkko Foundation, and Academy of Finland (no. 258814).

References

- [1] M. T. Dinh, C. L. Abad, and N. Safdar, "Diagnostic accuracy of the physical examination and imaging tests for osteomyelitis underlying diabetic foot ulcers: Meta-analysis," *Clinical Infectious Diseases*, vol. 47, no. 4, pp. 519–527, 2008.
- [2] N. Prandini, E. Lazzeri, B. Rossi, P. Erba, M. G. Parisella, and A. Signore, "Nuclear medicine imaging of bone infections," *Nuclear Medicine Communications*, vol. 27, no. 8, pp. 633–644, 2006.
- [3] M. F. Termaat, P. G. H. M. Rajmakers, H. J. Scholten, F. C. Barker, P. Patka, and H. J. T. M. Haarman, "The accuracy of diagnostic imaging for the assessment of chronic osteomyelitis: a systematic review and meta-analysis," *The Journal of Bone and Joint Surgery—American Volume*, vol. 87, no. 11, pp. 2464–2471, 2005.
- [4] T. K. Chacko, H. Zhuang, K. Z. Nakhoda, B. Moussavian, and A. Alavi, "Applications of fluorodeoxyglucose positron emission tomography in the diagnosis of infection," *Nuclear Medicine Communications*, vol. 24, no. 6, pp. 615–624, 2003.
- [5] H. P. Ledermann, A. Kaim, G. Bongartz, and W. Steinbrich, "Pitfalls and limitations of magnetic resonance imaging in chronic posttraumatic osteomyelitis," *European Radiology*, vol. 10, no. 11, pp. 1815–1823, 2000.
- [6] F. de Winter, D. Vogelaers, F. Gemmel, and R. Dierckx, "Promising role of 18-F-fluoro-D-deoxyglucose positron emission tomography in clinical infectious diseases," *European Journal of Clinical Microbiology & Infectious Diseases*, vol. 21, no. 4, pp. 247–257, 2002.
- [7] F. De Winter, C. Van De Wiele, D. Vogelaers, K. De Smet, R. Verdonk, and R. A. Dierckx, "Fluorine-18 fluorodeoxyglucose-positron emission tomography: A highly accurate imaging modality for the diagnosis of chronic musculoskeletal infections," *The Journal of Bone & Joint Surgery*, vol. 83, no. 5, pp. 651–24, 2001.
- [8] T. A. Einhorn, "The cell and molecular biology of fracture healing," *Clinical Orthopaedics and Related Research*, no. 355, supplement, pp. S7–S21, 1998.
- [9] J. K. Koort, T. J. Mäkinen, J. Knuuti, J. Jalava, and H. T. Aro, "Comparative ¹⁸F-FDG PET of experimental *Staphylococcus aureus* osteomyelitis and normal bone healing," *Journal of Nuclear Medicine*, vol. 45, no. 8, pp. 1406–1411, 2004.
- [10] T. J. Mäkinen, P. Lankinen, T. Pöyhönen, J. Jalava, H. T. Aro, and A. Roivainen, "Comparison of ¹⁸F-FDG and ⁶⁸Ga PET imaging in the assessment of experimental osteomyelitis due to *Staphylococcus aureus*," *European Journal of Nuclear Medicine and Molecular Imaging*, vol. 32, no. 11, pp. 1259–1268, 2005.
- [11] T. El-Maghraby, H. Moustafa, and E. Pauwels, "Nuclear medicine methods for evaluation of skeletal infection among other diagnostic modalities," *The Quarterly Journal of Nuclear Medicine and Molecular Imaging*, vol. 50, no. 3, pp. 167–192, 2006.
- [12] M. Chianelli, S. J. Mather, J. Martin-Comin, and A. Signore, "Radiopharmaceuticals for the study of inflammatory processes: A review," *Nuclear Medicine Communications*, vol. 18, no. 5, pp. 437–455, 1997.
- [13] A. Roivainen, S. Jalkanen, and C. Nanni, "Gallium-labelled peptides for imaging of inflammation," *European Journal of Nuclear Medicine and Molecular Imaging*, vol. 39, no. 1, pp. S68–S77, 2012.
- [14] J. M. Silvola, I. Laitinen, H. J. Sipilä et al., "Uptake of ⁶⁸gallium in atherosclerotic plaques in LDLR^{-/-} ApoB^{100/100} mice," *European Journal of Nuclear Medicine and Molecular Imaging Research*, vol. 1, 14, no. 1, pp. 1–8, 2011.
- [15] L. R. Bernstein, "Mechanisms of therapeutic activity for gallium," *Pharmacological Reviews*, vol. 50, no. 4, pp. 665–682, 1998.
- [16] D. C. Swartzendruber, B. Nelson, and R. L. Hayes, "Gallium-67 localization in lysosomal-like granules of leukemic and nonleukemic murine tissues," *Journal of the National Cancer Institute*, vol. 46, no. 5, pp. 941–952, 1971.
- [17] S. Menon, H. N. Wagner Jr., and M. F. Tsan, "Studies on gallium accumulation in inflammatory lesions: II. Uptake by *Staphylococcus aureus*: concise communication," *Journal of Nuclear Medicine*, vol. 19, no. 1, pp. 44–47, 1978.
- [18] P. Lankinen, T. J. Mäkinen, T. A. Pöyhönen et al., "⁶⁸Ga-DOTAVAP-P1 PET imaging capable of demonstrating the phase of inflammation in healing bones and the progress of infection in osteomyelitic bones," *European Journal of Nuclear Medicine and Molecular Imaging*, vol. 35, no. 2, pp. 352–364, 2008.
- [19] T. O'Reilly and J. T. Mader, "Rat model of bacterial osteomyelitis of the tibia," in *Handbook of animal models of infection experimental models in antimicrobial chemotherapy*, O. Zak and M. A. Sande, Eds., pp. 561–575, Academic Press Ltd., London, UK, 1999.
- [20] D. R. Nelson, T. B. Buxton, Q. N. Luu, and J. P. Rissing, "The promotional effect of bone wax on experimental *Staphylococcus aureus* osteomyelitis," *The Journal of Thoracic and Cardiovascular Surgery*, vol. 99, no. 6, pp. 977–980, 1990.
- [21] V. Kumar, D. K. Boddeti, S. G. Evans, and S. Angelides, "⁶⁸Ga-Citrate-PET for diagnostic imaging of infection in rats and for intra-abdominal infection in a patient," *Current Radiopharmaceuticals*, vol. 5, no. 1, pp. 71–75, 2012.

- [22] M. Teräs, T. Tolvanen, J. J. Johansson, J. J. Williams, and J. Knuuti, "Performance of the new generation of whole-body PET/CT scanners: discovery STE and Discovery VCT," *European Journal of Nuclear Medicine and Molecular Imaging*, vol. 34, no. 10, pp. 1683–1692, 2007.
- [23] A. Van Griethuysen, M. Bes, J. Etienne, R. Zbinden, and J. Kluytmans, "International multicenter evaluation of latex agglutination tests for identification of *Staphylococcus aureus*," *Journal of Clinical Microbiology*, vol. 39, no. 1, pp. 86–89, 2001.
- [24] P. Lankinen, K. Lehtimäki, A. J. Hakanen, A. Roivainen, and H. T. Aro, "A comparative ^{18}F -FDG PET/CT imaging of experimental *Staphylococcus aureus* osteomyelitis and *Staphylococcus epidermidis* foreign-body-associated infection in the rabbit tibia," *European Journal of Nuclear Medicine and Molecular Imaging Research*, vol. 2, no. 1, pp. 1–10, 2012.
- [25] W. Petty, S. Spanier, J. J. Shuster, and C. Silverthorne, "The influence of skeletal implants on incidence of infection. Experiments in a canine model," *The Journal of Bone & Joint Surgery*, vol. 67, no. 8, pp. 1236–1244, 1985.
- [26] M. Vorster, A. Maes, C. V. D. Wiele, and M. Sathekge, "Gallium-68 PET: A powerful generator-based alternative to infection and inflammation imaging," *Seminars in Nuclear Medicine*, vol. 46, no. 5, pp. 436–447, 2016.
- [27] M. Vorster, A. Maes, C. Van Dewiele, and M. Sathekge, "Gallium-68: A systematic review of its nononcological applications," *Nuclear Medicine Communications*, vol. 34, no. 9, pp. 834–854, 2013.
- [28] F. Gemmel, N. Dumarey, and M. Welling, "Future Diagnostic Agents," *Seminars in Nuclear Medicine*, vol. 39, no. 1, pp. 11–26, 2009.
- [29] S. J. Goldsmith and S. Vallabhajosula, "Clinically proven radiopharmaceuticals for infection imaging: mechanisms and applications," *Seminars in Nuclear Medicine*, vol. 39, no. 1, pp. 2–10, 2009.
- [30] M. Patel, Y. Rojavin, A. Jamali, S. Wasielewski, and C. Salgado, "Animal Models for the Study of Osteomyelitis," *Seminars in Plastic Surgery*, vol. 23, no. 02, pp. 148–154, 2009.
- [31] P. Spang, C. Herrmann, and F. Roesch, "Bifunctional Gallium-68 Chelators: Past, Present, and Future," *Seminars in Nuclear Medicine*, vol. 46, no. 5, pp. 373–394, 2016.
- [32] I. Velikyan, "Continued rapid growth in ^{68}Ga applications: Update 2013 to June 2014," *Journal of Labelled Compounds and Radiopharmaceuticals*, 2015.
- [33] A. Autio, T. Ujula, P. Luoto, S. Salomäki, S. Jalkanen, and A. Roivainen, "PET imaging of inflammation and adenocarcinoma xenografts using vascular adhesion protein 1 targeting peptide ^{68}Ga -DOTAVAP-P1: Comparison with ^{18}F -FDG," *European Journal of Nuclear Medicine and Molecular Imaging*, vol. 37, no. 10, pp. 1918–1925, 2010.
- [34] A. Roivainen, T. Tolvanen, S. Salomäki et al., " ^{68}Ga -labeled oligonucleotides for in vivo imaging with PET," *Journal of Nuclear Medicine*, vol. 45, no. 2, pp. 347–355, 2004.
- [35] C. Nanni, C. Errani, and L. Boriani, " ^{68}Ga -citrate PET/CT for evaluating patients with infections of the bone: preliminary results," *Journal of Nuclear Medicine*, vol. 51, no. 12, pp. 1932–1936, 2010.
- [36] A. Sánchez-Crespo, P. Andreo, and S. A. Larsson, "Positron flight in human tissues and its influence on PET image spatial resolution," *European Journal of Nuclear Medicine and Molecular Imaging*, vol. 31, no. 1, pp. 44–51, 2004.
- [37] I. Velikyan, "Positron emitting [^{68}Ga]Ga-based imaging agents: Chemistry and diversity," *Medicinal Chemistry*, vol. 7, no. 5, pp. 345–379, 2011.
- [38] I. Velikyan, "Prospective of ^{68}Ga -Radiopharmaceutical development," *Theranostics*, vol. 10, 1, no. 4, pp. 47–80, 2013.
- [39] U. Eberlein and M. Lassmann, "Dosimetry of [^{68}Ga]-labeled compounds," *Applied Radiation and Isotopes*, vol. 76, pp. 70–74, 2013.
- [40] W. J. Oyen, O. C. Boerman, C. J. Van Der Laken, R. A. Claessens, J. W. Van Der Meer, and F. H. Corstens, "The uptake mechanisms of inflammation-and infection-localizing agents," *European Journal of Nuclear Medicine and Molecular Imaging*, vol. 23, no. 4, pp. 459–465, 1996.
- [41] M. A. Green and M. J. Welch, "Gallium radiopharmaceutical chemistry," *International Journal of Radiation Applications and Instrumentation. Part B. Nuclear Medicine and Biology*, vol. 16, no. 5, pp. 435–448, 1989.

Research Article

Imaging and Methotrexate Response Monitoring of Systemic Inflammation in Arthritic Rats Employing the Macrophage PET Tracer [¹⁸F]Fluoro-PEG-Folate

Durga M. S. H. Chandrupatla ¹, Gerrit Jansen,¹ Elise Mantel,¹ Philip S. Low,² Takami Matsuyama,³ René P. Musters,⁴ Albert D. Windhorst,⁵ Adriaan A. Lammertsma ⁵, Carla F. M. Molthoff ⁵ and Conny J. van der Laken ¹

¹Amsterdam Rheumatology and Immunology Center, Location VUmc, VU University Medical Center, Amsterdam, Netherlands

²Department of Chemistry, Purdue University, West Lafayette, IN, USA

³Department of Immunology, Graduate School of Medical and Dental Sciences, Kagoshima University, Kagoshima 890-8544, Japan

⁴Department of Physiology, VU University Medical Center, Amsterdam, Netherlands

⁵Department of Radiology & Nuclear Medicine, VU University Medical Center, Amsterdam, Netherlands

Correspondence should be addressed to Conny J. van der Laken; j.vanderlaken@vumc.nl

Received 22 September 2017; Revised 22 December 2017; Accepted 24 January 2018; Published 21 February 2018

Academic Editor: Cristina Nanni

Copyright © 2018 Durga M. S. H. Chandrupatla et al. This is an open access article distributed under the Creative Commons Attribution License, which permits unrestricted use, distribution, and reproduction in any medium, provided the original work is properly cited.

Background. In rheumatoid arthritis, articular inflammation is a hallmark of disease, while the involvement of extra-articular tissues is less well defined. Here, we examined the feasibility of PET imaging with the macrophage tracer [¹⁸F]fluoro-PEG-folate, targeting folate receptor β (FR β), to monitor systemic inflammatory disease in liver and spleen of arthritic rats before and after methotrexate (MTX) treatment. **Methods.** [¹⁸F]Fluoro-PEG-folate PET scans (60 min) were acquired in saline- and MTX-treated (1 mg/kg, 4x) arthritic rats, followed by tissue resection and radiotracer distribution analysis. Liver and spleen tissues were stained for ED1/ED2-macrophage markers and FR β expression. **Results.** [¹⁸F]Fluoro-PEG-folate PET and ex vivo tissue distribution studies revealed a significant ($p < 0.01$) 2-fold lower tracer uptake in both liver and spleen of MTX-treated arthritic rats. Consistently, ED1- and ED2-positive macrophages were significantly ($p < 0.01$) decreased in liver (4-fold) and spleen (3-fold) of MTX-treated compared with saline-treated rats. Additionally, FR β -positive macrophages were also significantly reduced in liver (5-fold, $p < 0.005$) and spleen (3-fold, $p < 0.01$) of MTX- versus saline-treated rats. **Conclusions.** MTX treatment reduced activated macrophages in liver and spleen, as markers for systemic inflammation in these organs. Macrophage PET imaging with [¹⁸F]fluoro-PEG-folate holds promise for detection of systemic inflammation in RA as well as therapy (MTX) response monitoring.

1. Introduction

Rheumatoid arthritis (RA) is a chronic inflammatory disease involving mainly the synovium of the joints, although other tissue/organ involvement has been recognized [1, 2]. Extra-articular manifestations occur in active and severe RA, including skin, eye, heart, lung, renal, nervous, and gastrointestinal systems [3, 4]. Therefore, early detection and treatment of systemically affected organs in RA could benefit in achieving predefined low disease activity and remission [5, 6]. To this end, in a preclinical setting, animal models

of arthritis may serve a valuable tool for imaging (extra) articular and nonarticular inflammation and for monitoring the response to therapeutic interventions.

Many experimental animal models have been exploited to unravel the pathophysiology of inflammatory arthritis [7–12]. However, in most of these studies the primary research focus was on disease pathways and immune cells of the synovium rather than extra-articular manifestations. Also, depending on the modality and time frame of arthritis induction, extra-articular manifestations were not monitored or underreported.

Macrophages are known to play central role in RA disease progression [13]. Several studies have shown a direct correlation between disease remission and lower numbers of macrophage infiltration incidents into the synovium [14–16]. In patients, tissue resident macrophages in macrophage-rich organs such as liver and spleen may also be involved in extra-articular inflammation in RA [17]. Recent studies indicated that up to 50% of RA patients were reported with abnormal liver symptoms, including elevated alkaline phosphatase and small foci of necrosis and fatty liver [18]. Moreover, liver resident macrophages in an animal model were implicated in regulating chronic inflammation of arthritis through interacting with synovial phagocytes [19]. Not limiting to liver, spleen has also been reported in systemic inflammation in RA. Studies have shown manifestations of spleen enlargement and histological changes in either early or longstanding RA [20, 21].

Macrophage Positron Emission Tomography (PET) has been proposed as a noninvasive modality to monitor disease activity and therapy response in the whole body [22]. Beyond the prototypical macrophage tracer [^{11}C]-PK11195, targeting the translocator protein (TSPO) on activated macrophages, second-generation TSPO tracers showed improved properties over [^{11}C]-PK11195 to visualize arthritis [23]. Other interesting macrophage PET tracers to visualize arthritis are 4- ^{18}F -fluorophenylfolate, [^{68}Ga]-DOTA-folate [24], and [^{18}F]fluoro-PEG-folate [25]. These folate-based tracers bind with high affinity to folate receptor β (FR β) expressed on activated macrophages [26–28]. FR β is also of interest from a therapeutic perspective as it can bind and internalize antifolates and folate-conjugated antiarthritic therapeutics [26–31].

Recently we reported that the macrophage tracer [^{18}F]fluoro-PEG-folate allowed visualizing arthritis in the inflamed knee joints of arthritic rats and also was able to monitor the response to the anchor drug in RA therapy, methotrexate (MTX) [32]. In the present study we extend on these observations by exploiting [^{18}F]fluoro-PEG-folate PET to monitor potential systemic inflammation in liver and spleen of arthritic rats before and after MTX therapy, hypothesizing that MTX therapy also impacts systemic inflammatory effects in the organs. These studies were complemented with histological and immunofluorescence assessment of macrophage infiltration in liver and spleen.

2. Materials and Methods

2.1. Animals. The European community council directives 2010/63/EU for laboratory animal care and the Dutch law on animal experimentation criteria were fulfilled for performing the animal experiments. Wistar rats (male, 150–200 grams, Charles River International Inc., Sulzfeld, Germany) were provided with standard food, water (*ad libitum*), and conditions as described previously [32]. The local committee on animal experimentation of the VU University Medical Center (DEC PET13-07) validated and approved experimental protocols.

2.2. Arthritic Induction and Therapeutic Interventions. Wistar rats were immunized [33] and arthritis was induced via

4x intra-articular (i.a.) methylated bovine serum albumin (mBSA) injections, 4 or 5 days apart in the arthritic (right) knee with the contralateral (left, nonarthritic) knee serving as control knee essentially as described before [33]. Rats were anesthetized during immunization and arthritic induction using inhalation anesthetics (isoflurane: 2–2.5% and oxygen: 1 L/min).

After the last i.a. injection the rats ($n = 4/\text{group}$) were treated 4x (d0, d7, d14, and d21) either with saline (500 μL , intraperitoneal (i.p.) injection) or with MTX (VU University Medical Centers' Pharmacy) (i.p.) at 1.0 mg/kg. Healthy rats (nonarthritic) ($n = 3$) did not receive either arthritic induction or therapeutic interventions [32].

Six days after the last saline or MTX treatment, [^{18}F]fluoro-PEG-folate PET scans were performed, immediately after which rats were sacrificed and tissues were excised for further processing and various analyses described hereafter.

2.3. [^{18}F]Fluoro-PEG-Folate and PET. [^{18}F]fluoro-PEG-folate was synthesized as previously described [25], with a radiochemical purity of >97% and mean specific activity of $49.7 \pm 2.1 \text{ GBq}/\mu\text{mol}$. Saline- and MTX-treated arthritic rats were anesthetized using inhalation anaesthetics (isoflurane: 2–2.5% and oxygen: 1 L/min). The jugular vein was cannulated with a polyurethane 3-French cannula (0.7 mm \times 19 mm, BD Angiocath, Breda, Netherlands). During all procedures body temperature, heartbeat, respiratory rate, and blood oxygen saturation were monitored continuously using a rectal temperature probe and a pulse oxygen meter with SpO₂ sensor. Anesthetized rats ($n = 2$, from saline- and MTX-treated groups) were positioned in a high resolution research tomograph (HRRT) (Siemens/CTI, Knoxville, TN, USA) and [^{18}F]fluoro-PEG-folate ($20.5 \pm 3.4 \text{ MBq}$) was administered i.v. through the cannula and a dynamic PET scan was acquired for 60 min. Next, PET scans were normalized (for scatter, random, attenuation, decay, and dead time) and reconstructed as described before [25]. AMIDE software (version 0.9.2) [34] was used to analyse the images and data were expressed as standardized uptake values (SUV). The last frame was used to manually draw fixed size ellipsoidal shaped ROI over the area of liver and spleen (dimensions: $4 \times 4 \times 4 \text{ mm}^3$) and arthritic and contralateral knees (dimensions: $7 \times 4 \times 7 \text{ mm}^3$). The ROI for knees was drawn on top of the knee area [25] whereas, for liver and spleen, first a dotted line was drawn to represent the organ and then ROI was drawn approximately at the same spot in the saline- and MTX-treated rats. Through projecting ROIs onto the dynamic image sequence the time activity curve (TAC) was generated. TACs were expressed as standardized uptake values (SUV), that is, mean ROI radioactivity concentration normalized to injected dose and body weight.

2.4. Ex Vivo Tissue Distribution Studies. Rats (saline ($n = 4$), MTX ($n = 4$)) were sacrificed sixty minutes after [^{18}F]fluoro-PEG-folate tracer administration [33]. Upon sacrificing, the knees, liver, and spleen were excised, rinsed, dipped dry, weighed, and the amount of radioactivity determined using an LKB 1282 Compugamma CS gamma counter (LKB,

Wallac, Turku, Finland). Tissue radioactivity was expressed as percentage of the injected dose per gram tissue (%ID/g).

2.5. Histopathology and Immunohistochemistry. The liver and spleen sections from all rats ($n = 3$ for healthy rats and $n = 4$ for saline- and MTX-treated rats) were fixed in 4% neutral buffered paraformaldehyde for 24 h before embedding in paraffin wax. Sections of $5 \mu\text{m}$ were cut and stained initially with haematoxylin and eosin and then with an ED1 (homologous to human CD68), ED2 (homologous to human CD163), or isotype control antibody [32]. ED2/CD163 serves as marker for M2-type (anti-inflammatory) macrophages. Images were captured using a Leica 4000B microscope and Leica digital camera DC500 (Microsystems B.V. Rijswijk, Netherlands).

2.6. FR β Immunofluorescence and Microscopy (Frozen Rat Tissue). At the end of the study, liver and spleen tissues were collected from healthy rats ($n = 3$) and saline- and MTX-treated rats ($n = 4$) and snap frozen in liquid nitrogen and stored at -80°C . Tissues were embedded in appropriate media (OCT; SKU4583, Tissue-Tek, Netherlands) and were cut using cryotome (-20°C) (Leica, Netherlands) and placed on Superfrost (4951PLUS4, ThermoFisher, Netherlands) glass slides for immunofluorescence (IF) staining. Sections of $8 \mu\text{m}$ were cut and stained with haematoxylin and eosin, and staining for FR β -positive macrophages was performed with a mouse anti-rat FR β antibody [29] or isotype control antibody.

For immunostaining, liver and spleen tissue sections were first brought to room temperature (RT) for 30 min, fixed in acetone (439126, Sigma-Aldrich, Netherlands) for 10 min at -20°C , and air-dried for 10 min at RT. A DAKO pen was used to mark the sections (S2002, DAKO, Santa Carla, CA, USA) which were subsequently washed 3x with PBS on a shaker. Next, sections were incubated with 100% fetal bovine serum (FBS) for 30 min at RT to avoid nonspecific binding and washed again in PBS (3×5 min). Thereafter, sections were incubated with mouse anti-rat FR β IgM (final concentration $1 \mu\text{g}/\text{ml}$) or isotype control IgM (ab35768, Abcam, Cambridge, UK; final concentration $1 \mu\text{g}/\text{ml}$) in 10% FBS/PBS for 24 hours at 4°C or with 10% FBS/PBS. After washing (3×5 min in PBS on a shaker), sections were incubated with goat-anti-mouse Alexa 488 ((final concentration $1 \mu\text{g}/\text{ml}$) (A21042) ThermoFisher Scientific, Netherlands) in 10% FBS/PBS, washed (3×5 min in PBS on a shaker), air-dried, and mounted with $2 \mu\text{l}$ of MOWIOL mounting medium (81381, Merck, Zwijndrecht, The Netherlands). The 2D IF slides were imaged with a Zeiss Axiovert 200 M Marianas™ inverted microscope (40x oil-immersion lens). The microscope, camera, and data processing were controlled by SlideBook™ software (SlideBook version 6 (Intelligent Imaging Innovations, Denver, CO)) as described previously [35].

2.7. Quantification of Macrophages. The identity of all stained slides was hidden from and counted by two independent observers for FR β and ED1- and ED2-positive macrophages. For quantification, representative areas of liver and spleen sections were divided into 4 regions and counted at 400x magnification for FR β and ED1- and ED2-positive

macrophages in the saline- and MTX-treated rats. The average numbers of macrophages per area from all four regions were combined and depicted as total numbers of FR β , ED1, or ED2 macrophages.

2.8. Statistical Analysis. Statistical analysis was performed using SPSS (version 15) for Windows (SPSS Inc., Chicago, IL, USA). Mann–Whitney (exact) tests were performed to analyse differences in tracer uptake (tissue distribution) macrophage infiltration in saline- versus MTX-treated groups. A p value < 0.05 was considered as statistically significant. All results are presented as mean \pm standard deviation (SD).

3. Results and Discussion

3.1. Arthritis Induction and MTX Therapeutic Interventions. Upon arthritic induction all rats showed macroscopic thickening of the arthritic knee compared with the contralateral control knee (data not shown). As shown earlier, arthritis induction was well tolerated and allowed a window for therapeutic intervention with MTX, which was also well tolerated and not associated with any adverse effects [32].

3.2. [^{18}F]Fluoro-PEG-Folate PET. In a recent study we showed that imaging with the macrophage tracer [^{18}F]fluoro-PEG-folate could visualize decreased accumulation of the tracer in the knee joints of arthritic rats treated with MTX. In the present study, we particularly focussed on macrophage-rich organs such as liver and spleen for their potential involvement in systemic inflammation and the impact of MTX therapy upon this. The coronal PET images visualized higher tracer uptake in liver and spleen of the saline-treated arthritic rats (Figure 1(a)) compared to the MTX-treated rats (Figure 1(b)). Standard uptake values (SUV) of [^{18}F]fluoro-PEG-folate were quantified for liver and spleen with ROIs (colored ellipsoid) demonstrating decreased liver (1.5-fold) (Figure 1(c)) and spleen (2-fold) (Figure 1(d)) tracer uptake in MTX-treated compared to saline-treated rats. The relatively high uptake in the intestinal area, kidney, and bladder was due to the known clearance of the folate tracer [25, 32]. The MTX treatment results showed that, beyond knee joints, folate tracer binding is also inhibited by methotrexate in the extra-articular tissues, liver, and spleen, which suggests local anti-inflammatory effects on macrophage activity as part of systemic inflammation in these organs. These results are consistent with data from another arthritic rat model wherein [$^{99\text{m}}\text{Tc}$]-EC20 folate scans also showed increased tracer uptake in liver and spleen [36] as compared to healthy rats. The increased tracer uptake in liver and spleen in arthritic rats coincided with increased tissue FR levels as measured by [^3H]folic acid binding studies. Notably, a clinical study with [^{18}F]-FDG, an indicator of active metabolism, in patients with collagen vascular disease-associated arthritis also showed significantly increased tracer uptake in the spleen, pointing to its inflammatory involvement [37]. In a clinical study in RA patients with [$^{99\text{m}}\text{Tc}$]-EC20 folate, articular inflammation as well as liver and spleen involvement were demonstrated [38], further corroborating systemic inflammatory effects in arthritis.

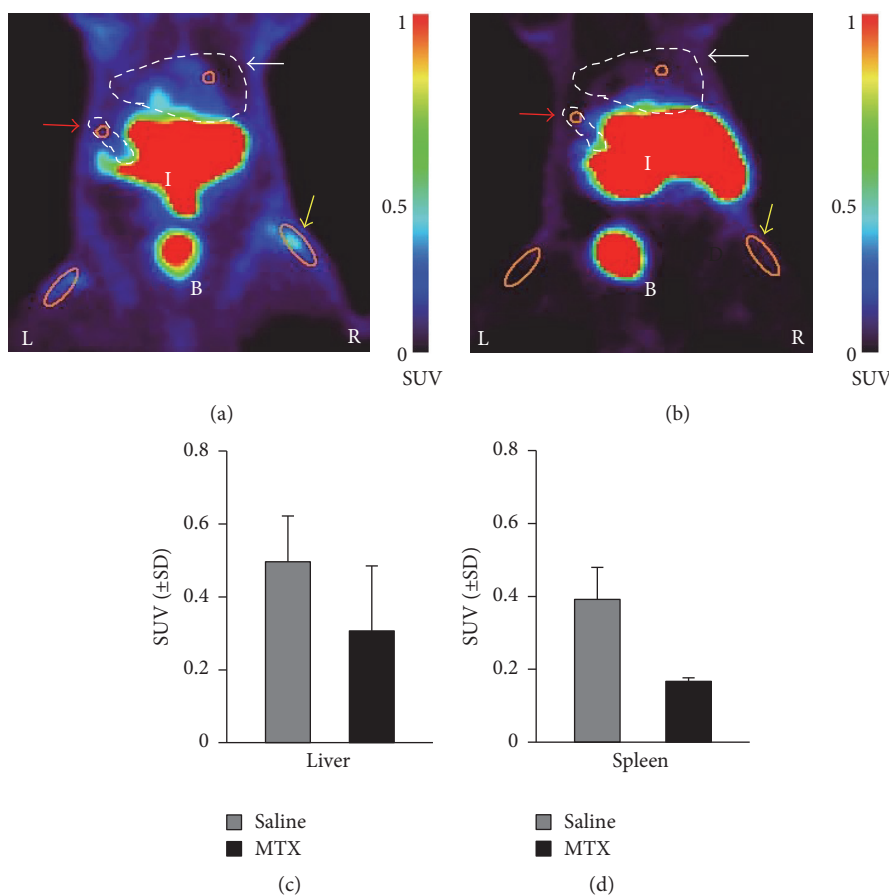


FIGURE 1: Representative coronal PET images of [^{18}F]fluoro-PEG-folate in (a) saline-treated ($n = 2$) and (b) MTX-treated ($n = 2$) rats. *Orange ellipsoid*: ROI drawn around the synovium of the knee joint, liver (white arrow), spleen (red arrow), and arthritic (right (R); yellow arrow) and contralateral knees (left (L)) depicted on each image. Spleen and liver areas are indicated by dashed lines. Standardized uptake value (SUV) scale bar from minimum 0 to maximum 1 represents the uptake of the tracer. Clearance organs intestine (I) and bladder (B) are also depicted. [^{18}F]Fluoro-PEG-folate uptake is expressed as SUV (\pm SD) in (c) liver and (d) spleen of the saline- and MTX-treated group.

3.3. Ex Vivo Tissue Distribution Studies. To further establish the usefulness of therapeutic monitoring of systemic inflammation via [^{18}F]fluoro-PEG-folate PET and regular MTX treatment (the anchor drug in RA), ex vivo tissue distribution studies were performed on selected tissues 60 minutes after tracer injection. In excised liver and spleen sections of MTX-treated rats, tracer uptake was significantly 3- and 16-fold lower ($p < 0.01$ and $p < 0.001$), respectively, compared to the saline-treated rats (Figure 2). For comparison, previously reported tracer uptake in liver and spleen of healthy rats was ~ 1.4 -fold lower [32] than in arthritic rats also pointing at presence of systemic inflammation/macrophage activity in liver and spleen. The markedly lower tracer uptake (5-fold, $p < 0.01$) in the MTX-treated arthritic rat knees [32] is depicted as a reference (Figure 2). Plasma levels of [^{18}F]fluoro-PEG-folate were low and comparable between both groups. Uptake of [^{18}F]fluoro-PEG-folate in kidney (2.92 ± 0.33 versus $3.34 \pm 0.63\%$ ID/g) and intestine (1.06 ± 0.49 versus $0.84 \pm 0.56\%$ ID/g) is not significantly altered after MTX therapy. This is consistent with the notion that kidney constitutively expresses another FR isoform (i.e., FR α , implicated in renal retention of folates) [32].

It is of importance to note that tissue distributions data were obtained 6 days after the last MTX administration; thus it is unlikely that lowered tracer uptake is due to FR β blocking by MTX as residual plasma levels of MTX will be very low (< 10 nM) at that stage [32]. Moreover, [^{18}F]fluoro-PEG-folate binding affinity towards FR β outweighs MTX by at least 2-3 orders of magnitude [25, 27].

Together, PET and tissue distribution data illustrate that MTX treatment has a marked effect on macrophage tracer uptake in liver and spleen of arthritic rats.

3.4. Effect of MTX on Systemic Macrophage Infiltration. To extend on the PET and ex vivo tissue distribution data with [^{18}F]fluoro-PEG-folate, the level of macrophage infiltration was examined in saline-treated and MTX-treated rats. Macrophage numbers were quantified in liver and spleen sections of saline-treated versus MTX-treated rats by immunohistochemical assessment of the abundance of total ED1-positive macrophages and ED2-positive macrophages, the latter, as CD163 homologue, serving as a proposed marker for anti-inflammatory macrophages. Figures 3 and 4 show representative images of ED1- and ED2-positive macrophages

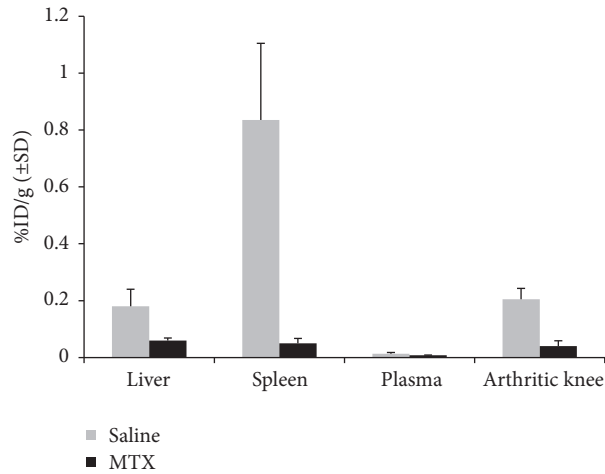


FIGURE 2: Ex vivo tissue distribution of [¹⁸F]fluoro-PEG-folate in liver, spleen, plasma, and arthritic knee of saline-treated (*n* = 4) and MTX-treated (*n* = 4) rats at 60 min after tracer injection. Results expressed as mean percentage injected dose per gram (%ID/g). Error bars indicate SD. *p* < 0.01 and *p* < 0.001.

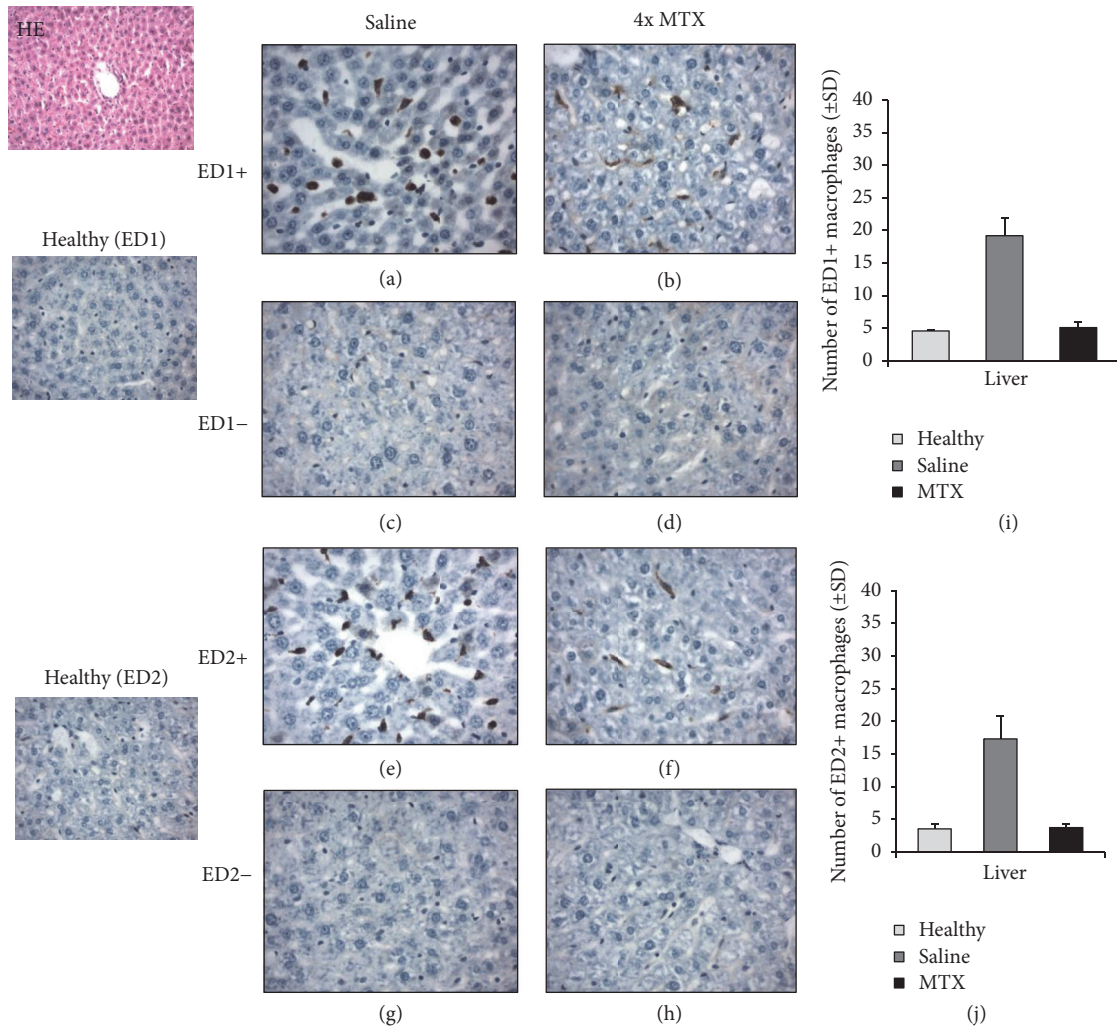


FIGURE 3: Representative immunohistochemical (HE) images of ED1⁺ and ED2⁺ macrophages in liver sections of healthy (*n* = 3) (ED1 and ED2), saline-treated (*n* = 4), and MTX-treated (*n* = 4) rats. ((a), (b)) Images represent ED1⁺ macrophages in the liver of saline-treated and MTX-treated rats, respectively. ((c), (d)) Isotype control stained liver sections of saline-treated and MTX-treated rats, respectively. ((e), (f)) Images of ED2⁺ macrophages in the liver of saline-treated and MTX-treated rats, respectively. ((g), (h)) Images of isotype control stained liver sections of saline-treated and MTX-treated rats, respectively. ((i), (j)) Bar graph representations of quantifications of ED1⁺ and ED2⁺ macrophages in liver of healthy, saline-treated, and MTX-treated rats. Values depict mean numbers of macrophages counted in predefined areas of the liver. Error bars indicate SD. *p* < 0.01.

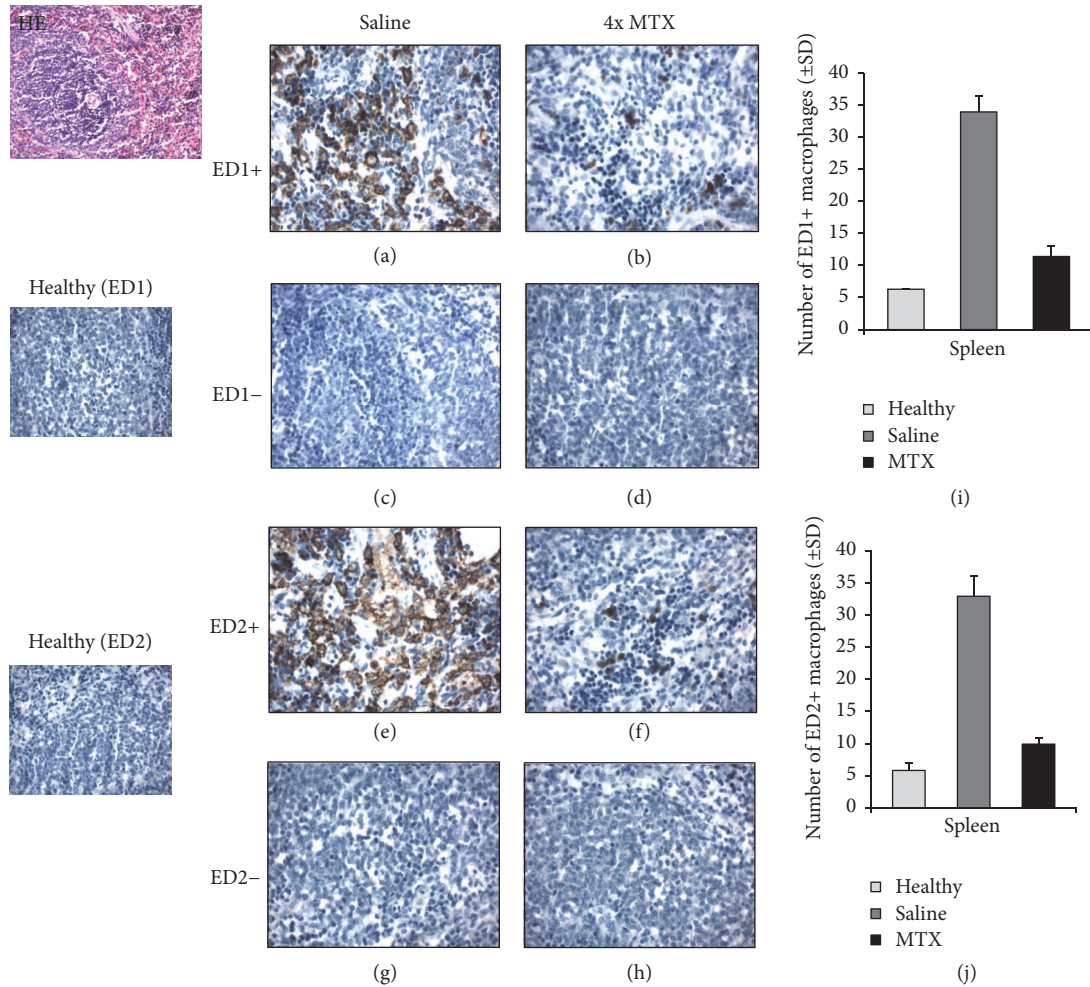


FIGURE 4: Representative immunohistochemical (HE) images of ED1⁺ and ED2⁺ macrophages in spleen sections of healthy ($n = 3$) (ED1 and ED2), saline-treated ($n = 4$), and MTX-treated ($n = 4$) rats. ((a), (b)) Images represent ED1⁺ macrophages in the spleen of saline-treated and MTX-treated rats, respectively. ((c), (d)) Isotype control stained spleen sections of saline-treated and MTX-treated rats, respectively. ((e), (f)) Images of ED2⁺ macrophages in the spleen of saline-treated and MTX-treated rats, respectively. ((g), (h)) Images of isotype control stained spleen sections of saline-treated and MTX-treated rats, respectively. ((i), (j)) Bar graph representations of quantifications of ED1⁺ and ED2⁺ macrophages in spleen of healthy, saline-treated, and MTX-treated rats. Values depict mean numbers of macrophages counted in predefined areas of the spleen. Error bars indicate SD. $p < 0.01$.

in liver and spleen sections. In liver and spleen of arthritic rats the numbers of ED1- and ED2-positive macrophages were ~5-fold higher ($p < 0.01$) than those of healthy rats.

For both ED1- and ED2-positive macrophages in liver and spleen, a marked decrease in macrophage infiltration is noted for MTX treatment compared to saline-treated rats. This was confirmed by a significantly (4-fold, $p < 0.01$) lower numbers of ED1- and ED2-positive macrophages in the liver of MTX-treated rats (Figures 3(i) and 3(j)), compared to saline-treated rats. Similarly, spleen sections of MTX-treated rats revealed significantly (3-fold, $p < 0.01$) lower quantifications of ED1- and ED2-positive macrophages, compared to saline-treated rats (Figures 4(i) and 4(j)). Antibody control stained liver and spleen sections were clearly negative for both ED1- and ED2-positive macrophages (Figures 3(c), 3(d), 3(g), 3(h), 4(c), 4(d), 4(g), and 4(h)). It is of interest to note that MTX impacted the infiltration of both ED1 and ED2 macrophage

in liver and spleen of arthritic rats. For ED2 macrophages this may be counterintuitive given their assigned anti-inflammatory phenotype [13]. However, in the context of RA, recent evidence suggests that M2 macrophages can be skewed to produce proinflammatory cytokines [39], which can shift the balance of M2 to a more M1 phenotype. An alternative explanation could be that the MTX impacts circulating proinflammatory subsets of FR β expressing circulating monocytes [40] to suppress overall infiltration and polarization of macrophages in arthritic knees, liver, and spleen. Unravelling the exact mechanism of action of how MTX impairs macrophage infiltration awaits further research.

3.5. Effect of MTX on FR β -Positive Macrophages. FR β -positive synovial macrophages were shown to be highly infiltrated in the synovium of RA patients [27]. Given that [¹⁸F]fluoro-PEG-folate binds to FR β [25], we examined the

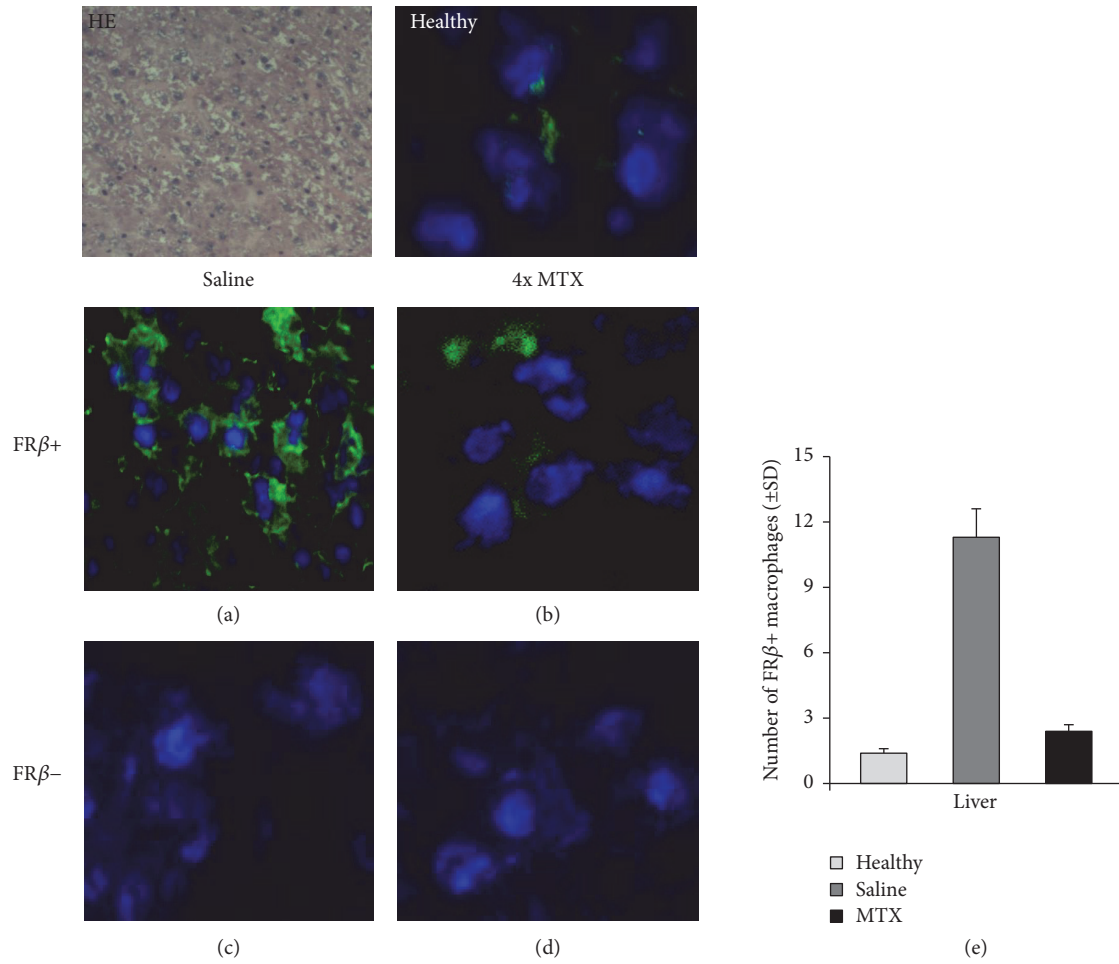


FIGURE 5: Representative immunofluorescence images of FRβ⁺ macrophages in liver sections of healthy ($n = 3$) and saline- ($n = 4$) and MTX-treated ($n = 4$) rats. ((a), (b)) Images represent FRβ⁺ macrophages in the liver of saline-treated and MTX-treated rats, respectively. ((c), (d)) Isotype control stained liver sections of saline-treated and MTX-treated rats, respectively. (e) Bar graph representation of quantifications of FRβ⁺ macrophages in liver of saline-treated and MTX-treated rats. Values depict mean numbers of macrophages counted in predefined areas of the liver. Error bars indicate SD (blue color: DAPI (nucleus staining); green color: FRβ staining). $p < 0.01$.

expression of FRβ in liver and spleen sections of saline-treated and MTX-treated arthritic rats to verify the data of the PET and tissue distribution studies. In liver and spleen of arthritic rats the number of FRβ-positive macrophages was significantly ($p < 0.01$) higher than those of healthy rats.

Representative immunofluorescence images of FRβ expression in cryosections of liver (Figures 5(a)–5(d)) and spleen (Figures 6(a)–6(d)) after saline and MTX therapeutic interventions revealed a markedly lower FRβ expression in both liver and spleen of MTX-treated versus saline-treated rats. This was confirmed by quantitative assessments showing significant 5-fold ($p < 0.005$) and 3-fold ($p < 0.01$) lower numbers of FRβ-positive macrophages in the liver (Figure 5(e)) and spleen (Figure 6(e)) of MTX-treated rats. The FRβ levels in MTX-treated rats approximated FRβ-positive macrophages in liver and spleen of healthy rats. Antibody control stained liver and spleen sections were negative (Figures 5(c), 5(d), 6(c), and 6(d)). Results for FRβ staining were consistent with ED1 and ED2 stainings (Figures 3 and 4). Together, these results underscore that macrophage

infiltration in liver and spleen is implicated in inflammation and response to therapy, similar to that shown for RA synovium in patients [14–16].

In addition to MTX, antiarthritic effects elicited through FRβ targeting have been reported for folate-conjugated immunotoxins [29] and various folate-conjugated drugs [30, 41, 42]. Since FRβ is primarily expressed on activated macrophages [27, 28], microenvironmental conditions in liver and spleen will be of importance for FRβ expression and macrophage polarization. FRβ expression has been reported on both M1- and M2-type macrophages [43], and in rat RA synovium FRβ expression has been also observed on a mixed M1- and M2-type [44]. As indicated above, in the RA microenvironment with circulating complex IgG autoantibodies and/or ACPA antibodies, FRβ expressing activated macrophages can release proinflammatory cytokines [39, 45] and thus be a bona fide target. More detailed investigations on the specific polarization and phenotypic properties of FRβ-expressing tissue macrophages in liver and spleen may assist optimal targeting of this receptor for imaging and therapeutic

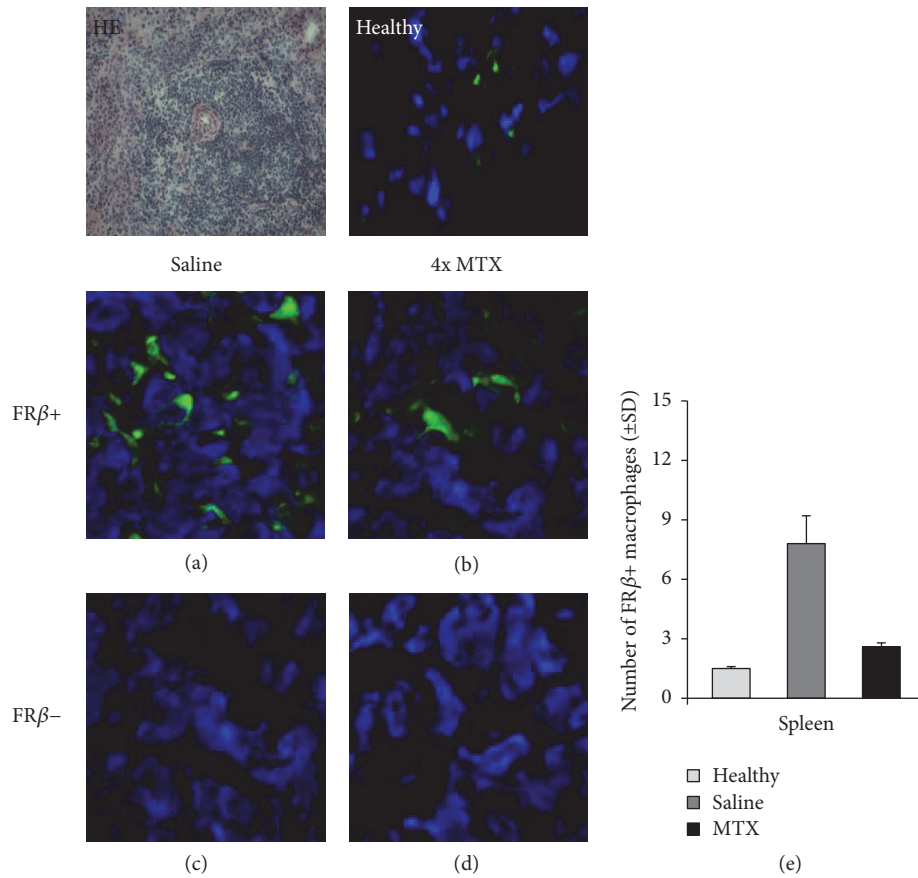


FIGURE 6: Representative immunofluorescence images of $FR\beta^+$ macrophages in spleen sections of healthy ($n = 3$) and saline- ($n = 4$) and MTX-treated ($n = 4$) rats. ((a), (b)) Images represent $FR\beta^+$ macrophages in the spleen of saline-treated and MTX-treated rats, respectively. ((c), (d)) Isotype control stained spleen sections of saline-treated and MTX-treated rats, respectively. (e) Bar graph representation of quantifications of $FR\beta^+$ macrophages in spleen of saline-treated and MTX-treated rats. Values depict mean numbers of macrophages counted in predefined areas of the spleen. Error bars indicate SD. (blue color: DAPI (nuclear staining); green color: $FR\beta$ staining). $p < 0.01$.

exploitations. These premises do not only hold for arthritis but also for cancer [46].

4. Conclusion

MTX treatment reduced activated macrophages in liver and spleen, as markers for systemic inflammation in these organs. Macrophage PET imaging with [^{18}F]fluoro-PEG-folate holds promise for detection of systemic inflammation in RA as well as therapy (MTX) response monitoring.

Abbreviations

RA: Rheumatoid arthritis
 mBSA: Methylated bovine serum albumin
 MTX: Methotrexate
 HRRT: High resolution research tomography
 PEG: Polyethylene glycol
 SD: Standard deviation
 %ID/g: Percentage of the injected dose per gram
 i.a.: Intra-articular
 $FR\beta$: Folate Receptor β

ROI: Region of interest

EC20: A folate-linked chelator of ^{99m}Tc .

Conflicts of Interest

The authors declare that they have no conflicts of interest regarding the publication of this article.

Authors' Contributions

Durga M. S. H. Chandrupatla contributed to the acquisition, analysis, and interpretation of the data and drafted the manuscript. Elise Mantel was involved in all in vitro studies. Carla F. M. Molthoff, Gerrit Jansen, and Conny J. van der Laken were involved in the design of the study, contributed to the interpretation of the data, and critically revised the manuscript. Adriaan A. Lammertsma contributed to the interpretation of the PET data and critically revised the manuscript. Philip S. Low synthesized the PET tracer precursor and assisted with revision of the manuscript. Albert D. Windhorst synthesized the folate PET tracer and performed quality controls on the tracer. Takami Matsuyama

provided the mouse anti-rat-folate receptor β antibody and staining protocol and critically revised the manuscript. René P. Musters was involved in the acquisition and interpretation of the immunofluorescence data and critically revised the manuscript. All authors read and approved the final manuscript.

Acknowledgments

The authors gratefully acknowledge Mariska Verlaan and Ricardo Vos for their excellent technical support with the PET scans and animal experiments. Rolph van Kooij and Martien Mooijer are thanked for [^{18}F]fluoro-PEG-folate tracer synthesis and planning. This study was supported by VU University Medical Center (Cancer Center Amsterdam) (CCA-PV13/87).

References

- [1] J. S. Smolen, D. Aletaha, and I. B. McInnes, "Rheumatoid arthritis," *The Lancet*, vol. 388, no. 10055, pp. 2023–2038, 2016.
- [2] E. Choy, "Understanding the dynamics: Pathways involved in the pathogenesis of rheumatoid arthritis," *Rheumatology*, vol. 51, supplement 5, pp. v3–v11, 2012.
- [3] M. Cojocaru, I. M. Cojocaru, I. Silosi, C. D. Vrabie, and R. Tanasescu, "Extra-articular Manifestations in Rheumatoid Arthritis," *Maedica*, vol. 5, no. 4, pp. 286–291, 2010.
- [4] I. B. McInnes and G. Schett, "The pathogenesis of rheumatoid arthritis," *The New England Journal of Medicine*, vol. 365, no. 23, pp. 2205–2219, 2011.
- [5] Y. P. M. Goekoop-Ruiterman, J. K. de Vries-Bouwstra, C. F. Allaart et al., "Clinical and radiographic outcomes of four different treatment strategies in patients with early rheumatoid arthritis (the best study): a randomized, controlled trial," *Arthritis & Rheumatology*, vol. 52, no. 11, pp. 3381–3390, 2005.
- [6] M. F. Bakker, J. W. G. Jacobs, S. M. M. Verstappen, and J. W. J. Bijlsma, "Tight control in the treatment of rheumatoid arthritis: efficacy and feasibility," *Annals of the Rheumatic Diseases*, vol. 66, no. 3, pp. iii56–iii60, 2007.
- [7] G. Kollias, P. Papadaki, F. Apparailly et al., "Animal models for arthritis: Innovative tools for prevention and treatment," *Annals of the Rheumatic Diseases*, vol. 70, no. 8, pp. 1357–1362, 2011.
- [8] P. Li and E. M. Schwarz, "The TNF- α transgenic mouse model of inflammatory arthritis," *Springer Seminars in Immunopathology*, vol. 25, no. 1, pp. 19–33, 2003.
- [9] A. D. Christensen, C. Haase, A. D. Cook, and J. A. Hamilton, "K/BxN serum-transfer arthritis as a model for human inflammatory arthritis," *Frontiers in Immunology*, vol. 7, article no. 213, 2016.
- [10] R. C. Schimmer, D. J. Schrier, C. M. Flory et al., "Streptococcal cell wall-induced arthritis: requirements for IL-4, IL-10, IFN- γ , and monocyte chemoattractant protein-1," *The Journal of Immunology*, vol. 160, no. 3, pp. 1466–1471, 1998.
- [11] L. Bevaart, M. J. Vervoordeldonk, and P. P. Tak, "Evaluation of therapeutic targets in animal models of arthritis: how does it relate to rheumatoid arthritis?" *Arthritis & Rheumatology*, vol. 62, no. 8, pp. 2192–2205, 2010.
- [12] B. D. Fischer, A. Adeyemo, M. E. O'Leary, and A. Bottaro, "Animal models of rheumatoid pain: Experimental systems and insights," *Arthritis Research & Therapy*, vol. 19, no. 1, article no. 146, 2017.
- [13] I. A. Udalova, A. Mantovani, and M. Feldmann, "Macrophage heterogeneity in the context of rheumatoid arthritis," *Nature Reviews Rheumatology*, vol. 12, no. 8, pp. 472–485, 2016.
- [14] Z. N. Jahangier, J. W. G. Jacobs, M. C. Kraan et al., "Pretreatment macrophage infiltration of the synovium predicts the clinical effect of both radiation synovectomy and intra-articular glucocorticoids," *Annals of the Rheumatic Diseases*, vol. 65, no. 10, pp. 1286–1292, 2006.
- [15] M. D. Smith, M. C. Kraan, J. Slavotinek et al., "Treatment-induced remission in rheumatoid arthritis patients is characterized by a reduction in macrophage content of synovial biopsies," *Rheumatology*, vol. 40, no. 4, pp. 367–374, 2001.
- [16] J. J. Haringman, D. M. Gerlag, A. H. Zwinderman et al., "Synovial tissue macrophages: a sensitive biomarker for response to treatment in patients with rheumatoid arthritis," *Annals of the Rheumatic Diseases*, vol. 64, no. 6, pp. 834–838, 2005.
- [17] L. C. Davies, S. J. Jenkins, J. E. Allen, and P. R. Taylor, "Tissue-resident macrophages," *Nature Immunology*, vol. 14, no. 10, pp. 986–995, 2013.
- [18] C. Selmi, M. De Santis, and M. E. Gershwin, "Liver involvement in subjects with rheumatic disease," *Arthritis Research & Therapy*, vol. 13, no. 3, article 226, 2011.
- [19] Y. Kakinuma, T. Kimura, and Y. Watanabe, "Possible Involvement of Liver Resident Macrophages (Kupffer Cells) in the Pathogenesis of Both Intrahepatic and Extrahepatic Inflammation," *Canadian Journal of Gastroenterology and Hepatology*, vol. 2017, Article ID 2896809, 10 pages, 2017.
- [20] K. Nishiya, N. Hisakawa, T. Hosokawa, K. Hashimoto, and T. Doi, "Enlarged spleen detected by abdominal ultrasonography in patients with RA," *Annals of the Rheumatic Diseases*, vol. 59, no. 9, pp. 751–752, 2000.
- [21] J. M. Pena, J. Garcia-Alegria, M. Crespo, J. Gijon, and J. J. Vazquez, "Spontaneous rupture of the spleen in RA," *Annals of the Rheumatic Diseases*, vol. 43, no. 3, pp. 411–414, 1984.
- [22] S. T. G. Bruijnen, Y. Y. J. Gent, A. E. Voskuyl, O. S. Hoekstra, and C. J. Van Der Laken, "Present role of positron emission tomography in the diagnosis and monitoring of peripheral inflammatory arthritis: A systematic review," *Arthritis Care & Research*, vol. 66, no. 1, pp. 120–130, 2014.
- [23] Y. Y. J. Gent, K. Weijers, C. F. M. Molthoff et al., "Promising potential of new generation translocator protein tracers providing enhanced contrast of arthritis imaging by positron emission tomography in a rat model of arthritis," *Arthritis Research & Therapy*, vol. 16, no. 2, article R70, 2014.
- [24] S. A. Kularatne, M.-J. Bélanger, X. Meng et al., "Comparative analysis of folate derived PET imaging agents with [^{18}F]-2-fluoro-2-deoxy-d-glucose using a rodent inflammatory paw model," *Molecular Pharmaceutics*, vol. 10, no. 8, pp. 3103–3111, 2013.
- [25] Y. Y. J. Gent, K. Weijers, C. F. M. Molthoff et al., "Evaluation of the novel folate receptor ligand [^{18}F]fluoro-PEG-folate for macrophage targeting in a rat model of arthritis," *Arthritis Research & Therapy*, vol. 15, no. 2, article R37, 2013.
- [26] N. Nakashima-Matsushita, T. Homma, S. Yu et al., "Selective expression of folate receptor β and its possible role in methotrexate transport in synovial macrophages from patients with rheumatoid arthritis," *Arthritis & Rheumatology*, vol. 42, no. 8, pp. 1609–1616, 1999.
- [27] J. W. van der Heijden, R. Oerlemans, B. A. C. Dijkmans et al., "Folate receptor beta as a potential delivery route for novel folate antagonists to macrophages in the synovial tissue of

- rheumatoid arthritis patients," *Arthritis & Rheumatology*, vol. 60, no. 1, pp. 12–21, 2009.
- [28] W. Xia, A. R. Hilgenbrink, E. L. Matteson, M. B. Lockwood, J.-X. Cheng, and P. S. Low, "A functional folate receptor is induced during macrophage activation and can be used to target drugs to activated macrophages," *Blood*, vol. 113, no. 2, pp. 438–446, 2009.
- [29] T. Nagai, A. Kyo, K. Hasui, S. Takao, and T. Matsuyama, "Efficacy of an immunotoxin to folate receptor beta in the intra-articular treatment of antigen-induced arthritis," *Arthritis Research & Therapy*, vol. 14, no. 3, article R106, 2012.
- [30] Y. Lu, N. Parker, P. J. Kleindl et al., "Antiinflammatory activity of a novel folic acid targeted conjugate of the mTOR inhibitor everolimus," *Molecular Medicine*, vol. 21, pp. 584–596, 2015.
- [31] R. Nagayoshi, M. Nakamura, K. Ijiri, H. Yoshida, S. Komiya, and T. Matsuyama, "LY309887, antifolate via the folate receptor suppresses murine type II collagen-induced arthritis," *Clinical and Experimental Rheumatology*, vol. 21, no. 6, pp. 719–725, 2003.
- [32] D. M. S. H. Chandrupatla, G. Jansen, R. Vos et al., "In-vivo monitoring of anti-folate therapy in arthritic rats using [18F]fluoro-PEG-folate and positron emission tomography," *Arthritis Research & Therapy*, vol. 19, no. 1, article no. 114, 2017.
- [33] D. M. S. H. Chandrupatla, K. Weijers, Y. Y. J. Gent et al., "Sustained macrophage infiltration upon multiple intra-articular injections: An improved rat model of rheumatoid arthritis for PET guided therapy evaluation," *BioMed Research International*, vol. 2015, Article ID 509295, 11 pages, 2015.
- [34] A. M. Loening and S. S. Gambhir, "AMIDE: a free software tool for multimodality medical image analysis," *Molecular Imaging*, vol. 2, no. 3, pp. 131–137, 2003.
- [35] S. E. Verbrugge, M. Al, Y. G. Assaraf et al., "Multifactorial resistance to aminopeptidase inhibitor prodrug CHR2863 in myeloid leukemia cells: Down-regulation of carboxylesterase 1, drug sequestration in lipid droplets and pro-survival activation ERK/Akt/mTOR," *Oncotarget*, vol. 7, no. 5, pp. 5240–5257, 2016.
- [36] M. J. Turk, G. J. Breur, W. R. Widmer et al., "Folate-targeted imaging of activated macrophages in rats with adjuvant-induced arthritis," *Arthritis & Rheumatology*, vol. 46, no. 7, pp. 1947–1955, 2002.
- [37] T. Okabe, H. Shibata, K. Shizukuishi, T. Yoneyama, T. Inoue, and U. Tateishi, "F-18 FDG uptake patterns and disease activity of collagen vascular diseases-associated arthritis," *Clinical Nuclear Medicine*, vol. 36, no. 5, pp. 350–354, 2011.
- [38] E. L. Matteson, V. J. Lowe, F. G. Prendergast et al., "Assessment of disease activity in rheumatoid arthritis using a novel folate targeted radiopharmaceutical Folatescan," *Clinical and Experimental Rheumatology*, vol. 27, no. 2, pp. 253–259, 2009.
- [39] C. Clavel, L. Ceccato, F. Anquetil, G. Serre, and M. Sebbag, "Among human macrophages polarised to different phenotypes, the M-CSF-oriented cells present the highest pro-inflammatory response to the rheumatoid arthritis-specific immune complexes containing ACPA," *Annals of the Rheumatic Diseases*, vol. 75, no. 12, pp. 2184–2191, 2016.
- [40] J. Shen, A. R. Hilgenbrink, W. Xia et al., "Folate receptor- β constitutes a marker for human proinflammatory monocytes," *Journal of Leukocyte Biology*, vol. 96, no. 4, pp. 563–570, 2014.
- [41] Y. Lu, T. W. Stinnette, E. Westrick et al., "Treatment of experimental adjuvant arthritis with a novel folate receptor-targeted folic acid-aminopterin conjugate," *Arthritis Research & Therapy*, vol. 13, no. 2, article no. R56, 2011.
- [42] Y. Yi, "Folate receptor-targeted diagnostics and therapeutics for inflammatory diseases," *Immune Network*, vol. 16, no. 6, pp. 337–343, 2016.
- [43] A. Puig-Kröger, E. Sierra-Filardi, A. Domínguez-Soto et al., "Folate receptor β is expressed by tumor-associated macrophages and constitutes a marker for M2 anti-inflammatory/regulatory Macrophages," *Cancer Research*, vol. 69, no. 24, pp. 9395–9403, 2009.
- [44] Y. Tsuneyoshi, M. Tanaka, T. Nagai et al., "Functional folate receptor beta-expressing macrophages in osteoarthritis synovium and their M1/M2 expression profiles," *Scandinavian Journal of Rheumatology*, vol. 41, no. 2, pp. 132–140, 2012.
- [45] L. T. C. Vogelpoel, I. S. Hansen, T. Rispen et al., "Fc gamma receptor-TLR cross-talk elicits pro-inflammatory cytokine production by human M2 macrophages," *Nature Communications*, vol. 5, article no. 5444, 2014.
- [46] J. Shen, K. S. Putt, D. W. Visscher et al., "Assessment of folate receptor- β expression in human neoplastic tissues," *Oncotarget*, vol. 6, no. 16, pp. 14700–14709, 2015.

Review Article

Prospective of ^{68}Ga Radionuclide Contribution to the Development of Imaging Agents for Infection and Inflammation

Irina Velikyan ^{1,2,3}

¹Section of Nuclear Medicine and PET, Department of Surgical Sciences, Uppsala University, Uppsala, Sweden

²Preclinical PET Platform, Department of Medicinal Chemistry, Uppsala University, Uppsala, Sweden

³PET Centre, Centre for Medical Imaging, Uppsala University Hospital, 75185 Uppsala, Sweden

Correspondence should be addressed to Irina Velikyan; irina.velikyan@akademiska.se

Received 17 September 2017; Revised 19 November 2017; Accepted 10 December 2017; Published 4 January 2018

Academic Editor: Xiang-Guo Li

Copyright © 2018 Irina Velikyan. This is an open access article distributed under the Creative Commons Attribution License, which permits unrestricted use, distribution, and reproduction in any medium, provided the original work is properly cited.

During the last decade, the utilization of ^{68}Ga for the development of imaging agents has increased considerably with the leading position in the oncology. The imaging of infection and inflammation is lagging despite strong unmet medical needs. This review presents the potential routes for the development of ^{68}Ga -based agents for the imaging and quantification of infection and inflammation in various diseases and connection of the diagnosis to the treatment for the individualized patient management.

1. Introduction

The blossom of ^{68}Ga utilization is reflected in the continuous rapid growth of the number of basic and clinical research publications as well as clinical trials and clinical practice [1–3]. The potential scope of ^{68}Ga -based imaging agents is rather extensive including ligands specifically targeting receptors, enzymes, and antigens; hapten and effector molecules involved in pretargeted imaging; small molecules with biological function to monitor glycolysis, hypoxia, cell proliferation, and angiogenesis; nontargeting particles of various sizes for imaging of ventilation and perfusion [4]. The leading clinical application area is oncology with targeted imaging of somatostatin receptors (SSTR), prostate specific membrane antigen (PSMA), integrin receptors, glucagon-like peptide 1 receptors (GLP1R), gastrin-releasing peptide receptors (GRPR), human epidermal growth factor receptor family (HER2), and pretargeted imaging of carcinoembryonic antigen (CEA) [1, 3, 5].

The scope of ^{68}Ga -based imaging agents for inflammation and infection is rather limited despite disease diversity and magnitude, and strong unmet medical need [1, 4, 6]. However, the research and development of ^{68}Ga -based tracers for the diagnosis and discrimination of inflammation and infection accelerated during last five years [7–19]. Such ^{68}Ga -based tracers with specific action could also considerably

contribute to drug development. Unfortunately, the failure rate of new therapeutic drugs, in general, is rather high and it is a costly process. PET offers advantages such as possibility of quantifying the target occupancy by the drug very early in the development in vivo in humans due to the microdosing concept thus facilitating stratification of candidate therapeutic drugs.

This review presents the status of the ^{68}Ga -based imaging agents for inflammation and infection and discusses the potential routes for the development of the agents and their connection to the treatment for the individualized patient management.

2. Infection and Inflammation

Infection is caused by the invasion of such pathogens as bacteria, virus, fungi, parasite, or prion. It is a significant cause of morbidity and mortality globally, especially in children causing more death than any other disease. Tuberculosis, malaria, and AIDS stand for about 50% of all lethal cases claiming 5 million lives and causing 300 million illnesses each year. Bacterial infection, for example, tuberculosis and multidrug resistant bacteria, presents diagnostic and therapeutic challenges [20, 21]. Inflammation is immune response to microbial invasion or an injury and can either be

related to the pathogens or be sterile. It can be classified as acute or chronic, and the latter has been investigated as the major cause of inflammatory autoimmune, cardiovascular, neurological, and cancerous diseases.

In order to control infectious diseases and provide efficient treatment, early diagnosis as well as discrimination between bacterial and sterile inflammation is crucial. The disease specificity of the diagnostic tools is a desirable characteristic. Currently available diagnostic means present some disadvantages. Clinical laboratory tests such as white blood cell (WBC) counts and C-reactive protein (CRP) cannot unambiguously distinguish between bacterial and viral infection and may result in unnecessary treatment with antibiotics [22]. Radiological imaging techniques such as magnetic resonance imaging (MRI), X-ray, computed tomography (CT), and ultrasound are morphological and rely on the anatomical changes that occur at later stage of the disease. Moreover, these methods are not specific to neither inflammation nor infection type. Detection of viral infection is even more challenging since it does not produce anatomic changes as bacterial infection does even when the viral infection is severe.

In contrast to morphological imaging techniques, functional methods such as gamma scintigraphy (Single Photon Emission Computed Tomography (SPECT) and planar gamma imaging) and Positron Emission Tomography (PET) provide fast, whole-body, and noninvasive real time evaluation of physiology and pathology on molecular level early in disease processes before noticeable changes in anatomical structure occur. The whole-body examination might be of great importance especially in cases of occult infection [23]. The respective examinations can be repeated in order to monitor the treatment outcome resulting in personalized medicine approach [24–27]. The advantages of PET over SPECT are intrinsic to the technology and are presented with higher examination throughput, considerably higher sensitivity, possibility of detection, and quantification of tracer picomolar amounts as well as tracer uptake kinetics recording and dynamic image reconstruction [28]. In recent years, the stand-alone PET scanners have been substituted with hybrid PET-CT scanners that offer both high sensitivity of functional PET and temporal/spatial resolution of morphological CT in one examination. The hybrid PET-MRI scanners have also entered market providing advantages of MRI over CT in higher soft tissue contrast and absence of radiation dose to the patient. PET has demonstrated efficiency and profitability in individualized patient diagnostics especially in oncology, and its impact on patient management has been recognized by Medicare and Medicaid Services [29].

2.1. Common Clinical Imaging Agents for Inflammation and Infection. There are a few radiopharmaceuticals used in clinical routine, and they are nonspecific in their action: ^{67}Ga -Citrate, $^{99\text{m}}\text{Tc}/^{111}\text{In}$ -white blood cells (WBC), and [^{18}F]-fluorodeoxyglucose ([^{18}F]FDG) [30]. They target components of inflammatory response to injury and infection and accumulate in the lesions as a result of an increased blood flow and enhanced vascular permeability. ^{67}Ga -Citrate presumably

transfers ^{67}Ga to transferrin and lactoferrin that accumulate at the inflammation site on the cells such as leukocytes and B-lymphocytes expressing respective receptors [31]. Moreover, ^{67}Ga can be accumulated in the macrophages, bacteria, and fungi via siderophores. Radiolabelled WBCs accumulate in the sites of leukocyte infiltration and do not discriminate infective from sterile inflammation [32]. [^{18}F]FDG accumulates in leukocytes, macrophages, monocytes, lymphocytes, and giant cells due to upregulation of glucose transporters [33].

^{67}Ga -Citrate has been in clinical use for imaging of infection and inflammation for over 40 years. It is applicable, for example, for the diagnosis of lung infections, acute/chronic osteomyelitis, tuberculosis, sarcoidosis, and retroperitoneal fibrosis [34]. However, the specificity of the agent is suboptimal with accumulation in malignancies and bone remodeling sites as well as bowel excretion pathway. Moreover, radiation doses to the healthy organs and tissues are unfavorable and the examination requires several visits to the hospital with an interval of 1–3 days between radiopharmaceutical administration and examination.

Radiolabelled autologous WBCs have been used for a wide range of infections such as peripheral osteomyelitis, postoperative infection, joint prosthesis infection, diabetic foot infection, cardiovascular infection, fever of unknown origin (FUO), opportunistic infection, central nervous system infection, musculoskeletal infection, and inflammatory bowel disease for over three decades. Various labelling techniques using ^{111}In -oxine, $^{99\text{m}}\text{Tc}$ -sulfur colloids, and $^{99\text{m}}\text{Tc}$ -exametazime (HMPAO) have been developed; however the radiopharmaceutical preparation procedure is complicated and potentially hazardous for both personnel and patient [21, 30]. Moreover, the examination process is very demanding on the patient [35].

Most nuclear medicine applications worldwide (90%) stand for diagnostics with leading position for $^{99\text{m}}\text{Tc}$ -based radiopharmaceuticals, especially in cardiology [36]. The most essential contribution to the improvement of the patient management in oncology has been presented by [^{18}F]-fluorodeoxyglucose ([^{18}F]FDG)/PET-CT reflecting the elevation of glucose transporter expression in tumour cells, and providing nearly universal application in the evaluation of various fast growing cancer types. [^{18}F]FDG/PET-CT stands for over 90% of all PET-CT examinations [37, 38]. [^{18}F]FDG/PET is an established diagnostic means also in infection and inflammation, and the major indications for it are FUO, sarcoidosis, peripheral bone osteomyelitis, suspected spinal infection, metastatic infection, bacteremia, and vasculitis [33]. However, demand for the imaging agents towards disease specific targets in cancer and inflammation/infection is growing [39, 40] since [^{18}F]FDG fails to detect slowly growing tumours and to discriminate malignancy from sterile inflammation, infection, wound healing, tuberculosis, sarcoidosis, and reactive lymph nodes [41, 42]. Another disadvantage is high accumulation of [^{18}F]FDG in healthy organs such as brain and gut resulting in suboptimal image contrast and consequently potential risk for lesion detection failure.

TABLE 1: Positron-emitting, gamma-emitting, and therapeutic radionuclides, their physical characteristics, and production mode. Adapted from [4].

Radionuclide	Half-life	E_{\max} (keV)	Radiation	Production
<i>Positron emitters</i>				
^{18}F	110 min	634	β^+ (97%)	Accelerator
^{64}Cu	12.8 h	656	β^+ (19%)	Accelerator
^{68}Ga	67.6 min	1899, 770	β^+ (89%)	Generator
^{89}Zr	78.4 h	900	β^+ (23%)	Accelerator
^{124}I	4.17 d	2100	β^+ (23%)	Accelerator
<i>Gamma emitters</i>				
^{67}Ga	78.26 h	91, 93, 185, 296, 388	γ	Accelerator
$^{99\text{m}}\text{Tc}$	6.0 h	141	γ	Generator
^{111}In	67.9 h	245, 172 (0.5–25)	γ , Auger electrons	Accelerator
^{123}I	13.3 h	159	γ	Accelerator
<i>Therapeutic radionuclides</i>				
^{177}Lu	6.71 d	113, 208.4 (598)	γ (β^-)	Reactor

2.2. *Unmet Medical Need.* Noninvasive and specific diagnosis of many inflammatory diseases such as sarcoidosis, osteomyelitis, inflammatory bowel disease, and rheumatoid arthritis as well as early and accurate diagnosis of deep-seated infectious diseases such as septic arthritis, abscesses, endocarditis, and infections of prosthetics and implants would benefit patients [20]. Introduction of specific imaging agents disclosing cellular mechanisms of various diseases on molecular level would allow improvement in patient management and treatment outcome. There is a strong need for specific imaging agents not only for the accurate and quantitative diagnosis but also for the prognosis, treatment selection, planning, and adjustment as well as response monitoring as, for example, requirement for a certain antibiotic and treatment duration. Moreover, the imaging could guide surgical procedures and monitor implants of medical devices or transplanted organs [43]. Such imaging guided treatment would decrease the cost, side effects, and overtreatment avoiding immune suppression effects in inflammation and possibly reducing the problem of antimicrobial resistance by the termination of an accomplished successful treatment as early as possible. There are potential challenges in targeting both components of inflammatory response and microbes specifically: discrimination between infectious and sterile inflammation; discrimination between acute and chronic inflammation; discrimination between various infectious microorganisms; discrimination between pathogenic bacteria and microbiota; targeting specific types of bacteria; difficulty of accessing bacteria aggregated in a biofilm; and quantification of reproducing bacteria.

Health care requires further improvement of efficiency, safety, and quality of treatment with patient personalized approach that would allow early diagnosis which is a crucial factor in the reduction of mortality and patient management cost [81]. The concept of individualized patient management on molecular level with regard to both diagnostics and therapy is based on discoveries and success in genomics, proteomics, and biotechnology. Those achievements also accelerate the development of various imaging agents, and

the application of molecular imaging diagnostic techniques is expanding very fast globally contributing considerably to the realization of personalized medicine.

3. Advantages of ^{68}Ga : Nuclide Properties and Chemistry

Such radionuclides as ^{11}C , ^{18}F , ^{64}Cu , ^{68}Ga , ^{89}Zr , $^{99\text{m}}\text{Tc}$, ^{111}In , and ^{124}I are used in various radiopharmaceuticals for diagnostic imaging with PET and SPECT (Table 1). With regard to PET, ^{18}F stands for 41%, ^{11}C stands for 31%, and ^{64}Cu , ^{68}Ga , ^{89}Zr , and ^{124}I stand for 28% of the radiopharmaceuticals [82]. With regard to SPECT, $^{99\text{m}}\text{Tc}$ and ^{111}In stand, respectively, for 42% and 29% of the radiopharmaceuticals. As mentioned above in the field of inflammation and infection gamma emitting ^{67}Ga , $^{99\text{m}}\text{Tc}$, ^{111}In , and positron-emitting ^{18}F are commonly in use. The choice of a radionuclide depends on various aspects of production and application: availability, production mode, and cost of the radionuclide; nuclear characteristics and decay mode of the radionuclide; labelling chemistry pathways and duration; radiation dose to subjects; relevance of the physical half-life of the radionuclide to the pharmacokinetic time frame of the imaging agent. Within the group of gamma emitters used for SPECT, the production via generator system is an advantage that contributes to the leading position of $^{99\text{m}}\text{Tc}$ due to ready accessibility and lower cost. Moreover, the single and lower gamma energy of $^{99\text{m}}\text{Tc}$ results in higher image resolution as compared to ^{67}Ga and ^{111}In and shorter half-life of $^{99\text{m}}\text{Tc}$ reduces radiation dose to the patient (Table 2).

The advantages of PET such as higher spatial resolution, sensitivity, and accurate signal quantification are crucial, especially in the case of small size lesions. Furthermore, dynamic scanning allows modeling and investigation of the mechanism of the interaction between the imaging agent and target. Even though ^{68}Ga has a relatively high positron energy, the resolution of the images is comparable to that of ^{18}F , since it is the scanner detector resolution (4–6 mm)

TABLE 2: Effective doses for some PET and SPECT imaging agents. Reproduced from [6].

Agent	Examination time	Effective dose, [mSv]
[¹¹¹ In]In-DTPA-octreotide/SPECT	24–48 h	10.8
[⁶⁸ Ga]Ga-DOTA-TOC/PET	30–60 min	2.3
[¹⁸ F]FDG/PET	60–120 min	5.6
[^{99m} Tc]-BPAMD/SPECT	2–6 h	6
[^{99m} Tc]-MDP/SPECT	2–6 h	3–4
[⁶⁸ Ga]Ga-BPAMD/PET	30–60 min	3–4

which is the limiting factor [4, 83, 84]. The 68-min half-life of ⁶⁸Ga is not compatible with ligands of slow pharmacokinetics, for example, antibodies. Thus other positron emitters such as ¹²⁴I, ⁸⁹Zr, and ⁶⁴Cu with longer half-lives allowing 2–4 days required for the clearance of the agent for the blood circulation and washout for the nontarget tissue are more relevant. The relatively short half-life of ⁶⁸Ga presents advantage in cases when repetitive examinations on the same day are of interest [85]. The high fraction of positron emission is another advantage of ⁶⁸Ga (89%) as compared to ⁶⁴Cu (19%) and ¹²⁴I (23%). Comparison of some clinically used imaging agents demonstrates the lower effective dose that patient is exposed to when using ⁶⁸Ga-based agent as compared to the agents comprising ¹⁸F, ^{99m}Tc, and ¹¹¹In (Table 2) [6, 86, 87]. Moreover, the duration of patient examinations is shorter for ⁶⁸Ga-agents than that for SPECT agents, and to some extent for [¹⁸F]FDG. In summary, the use of ⁶⁸Ga would be beneficial in terms of accessibility, high sensitivity and resolution, quantification, dynamic scanning, fast scanning protocol, repetitive examinations, and low radiation burden.

The chemical form in aqueous solution is Ga(III) cation which provides robust coordination chemistry. ⁶⁸Ga-labelling can be direct or chelator mediated. The direct labelling utilizes the chelating ability of macromolecules, for example, lactoferrin and transferrin comprising Tyr, His, and Asp AA residues that can chelate Ga(III) in the presence of synergetic bicarbonate ion. Low molecular weight ligands can form stable complexes of variable lipophilicity and charge for nontargeting imaging. The chelator mediated ⁶⁸Ga-labelling requires presence of a bifunctional chelator (BFC) for the subsequent, straightforward, and side specific coordination with Ga(III). Considerable number of chelators was successfully developed [4, 6, 88–95]. The most commonly used are DOTA and NOTA based chelators. The former requires heating under over 60°C for the complexation with ⁶⁸Ga, while the latter can chelate ⁶⁸Ga at ambient temperature which might be crucial in case of temperature sensitive ligands, and it also allows for cold kit type radiopharmaceutical preparation under radiopharmacy practice [96]. DOTA presents an advantage in the context of radiotheranostics since it can form stable complexes with ⁶⁸Ga for PET diagnostics and ¹⁷⁷Lu for radiotherapy.

The chelator or prosthetic group mediated labelling most commonly results in agents comprising biologically active vector molecule, chelator/prosthetic group moiety, and

radionuclide. Very often pharmacokinetic modifiers (PKM) are incorporated in order to modulate pharmacokinetics and agent organ distribution and improve in vivo stability as well as separate the binding site from the bulky chelator/prosthetic group moiety which may deteriorate the biological activity of the vector molecule. Considerable number of publications reveal strong influence of even slight modifications in any of the agent structural components, and the accurate prediction of pharmacokinetics and pharmacodynamics of a new agent is not straightforward [97]. Nevertheless, vast experience and knowledge have been intensively gathered during last two decades providing possibility for more efficient and effective development. The labelling chemistry of ⁶⁸Ga is well characterized and is relevant to small molecules, macromolecules, and particles.

Ga(III) as a chemical element presents a unique advantage over other radionuclides as it has properties closely resembling those of Fe(III) which is involved in many biochemical processes including inflammation. Moreover, Fe(III) is an essential nutrient and limiting factor of microbial life [98]. Stable Ga(III) has been used in treatment of various diseases including cancer, infection, and inflammation [99–101]. The ability of Ga(III) to bind iron proteins, for example, lactoferrin and transferrin as well as siderophores, and enzymes can be utilized in the imaging agent development.

4. Biomarkers and Radiopharmaceutical Development

The development of imaging agents relies strongly on the advances, experience, and knowledge of the research of biomarkers, for example, receptors and antigens; transport systems; substances involved in angiogenesis, glycolysis, hypoxia, proliferation, and apoptosis; and enzyme activity. Targeting biomarkers that are specific for a given disease is one the major aims of an agent development for both diagnostic imaging and therapy. The knowledge and access to respective vector molecules have considerably expanded due to the achievements in proteomics and genomics. Infection, inflammation, and fibrosis are closely interrelated processes and corresponding biomarkers might present practical interest in developing respective imaging agents. Favorable characteristics of a target in general include expression upregulation, absence of expression in normal tissue, and internalization or stable binding of the respective ligand for the longitudinal accumulation of the latter [102].

5. Imaging Inflammation

Inflammatory response is a complex process involving immune system cells (T- and B-lymphocytes, NK cells, macrophages, monocytes, neutrophils, eosinophils, and mast cells) and products of their (patho)physiological activity, for example, cytokines involved in the cell signaling. Various functions of the cells and their products as well as their receptors provide a broad range of potential imaging targets [103–107]. Targeting the white blood cells of the immune system such as macrophages, monocytes, lymphocytes, and neutrophils for the detection of their upregulation and trafficking, secretion of cytokines and chemokines, and phagocytosis has been investigated both clinically and preclinically. Receptors such as SSTR, NCA-90, integrins, folate, bombesin, vascular cell adhesion protein-1, and interleukins expressed by activated T-cells, CXCR2 expressed on neutrophils, and CXCR4 overexpressed by leukocytes have demonstrated potential for *in vivo* targeted imaging [108]. Respective ligands and substrates can be considered for radiolabelling. Cytokines including interferons, lymphokines, interleukins, and chemokines bind to various receptors, for example, IL1 and IL2 receptor types, IFN, CD40, CD37, CD30, CD4, CCR5, and IL1-17R receptor family. Folate, CD64, NCA90, and CD15 receptors expressed on macrophages, leukocytes, and granulocytes can serve as targets. Not only do molecules of such super families as chemokine, integrin, selectin, and immunoglobulin participate in the cell emigration cascade, but also enzymes on the surface of endothelial cells and leukocytes contribute to the leukocyte extravasation [109]. Receptors on the endothelial wall, for example, for binding of IL1 and TNF α , are another category of the targets. These are only few examples of targets for potential imaging agent development (Table 3). Many targets were utilized in oncology [28] and their translation to inflammation is feasible.

5.1. Targeting Cell Receptors with Antibodies. Radiolabelled (^{99m}Tc , ^{111}In , and ^{123}I) anti-CD2, anti-CD5, anti-CD25, anti-CD45 antibodies and their fragments were used for the imaging of T-lymphocyte infiltration in various inflammatory diseases [110]. Typically for antibody slow pharmacokinetics, the time delay between the administration and examination stretches up to 24 hours. Interleukin-8 labelled with ^{99m}Tc was studied in rabbits with induced acute pyogenic osteomyelitis [111] and induced acute colitis [112]. The agent was found suitable for the scintigraphic evaluation of the respective diseases. CD163 receptor expressed in monocytes and activated macrophages was targeted with an anti-CD163 antibody labelled with ^{68}Ga in rats with acute collagen-induced arthritis [45]. The agent demonstrated specific binding and thus potential for studies of inflammatory diseases.

5.2. Targeting Angiogenesis. Angiogenesis plays an important role in wound healing, chronic inflammation, and tumour growth [113]. The family of vascular endothelial growth factors (VEGF) and integrins play crucial role in the angiogenesis cascade. Integrin receptors are overexpressed on the surface of vascular endothelial cells during angiogenesis in malignancies, tissue healing, and inflammation. The largest

group is radiolabelled peptide ligands comprising arginine-glycine-aspartic acid (RGD) sequence and peptidomimetics targeting $\alpha_v\beta_3$ integrin receptors. Various analogues were developed introducing cyclization and multimerization; variety of chelate/coligand moieties; PKM such as carbohydrate and polyethylene glycol chains [114–121]. Various RGD analogues labelled with ^{18}F , ^{68}Ga , and ^{99m}Tc were used in oncological clinical trials [122]. The majority of them comprised ^{18}F ; however, advantages of ^{68}Ga such as accessibility of the radionuclide, more straightforward and efficient labelling chemistry, lower radiation dose, and better image contrast rendered more extensive development of ^{68}Ga -based analogues [123–127].

The imaging agents tested in cancer systems can be relevant for the imaging of inflammation related diseases. The imaging and evaluation of synovial angiogenesis in patients with rheumatoid arthritis was accomplished using [^{68}Ga]Ga-PRGD $_2$ [46]. The elevated agent uptake was detected in the sites of active inflammation, rich neovasculature, and physiological integrin receptor expression, while no tracer accumulation was detected in axillary lymph nodes with reactive hyperplasia and strenuous skeletal muscles. [^{68}Ga]Ga-PRGD $_2$ /PET-CT was found useful for the evaluation of synovial angiogenesis and follow-up of the treatment response.

[^{68}Ga]Ga-NOTA-c(RGDyK) was developed for the imaging of myocardial infarction (MI) and follow-up of the response to the therapeutic intervention and demonstrated promising results preclinically [47]. The uptake in the MI lesions was enhanced and correlated with the vascular endothelial growth factor expression. Dynamic [^{68}Ga]Ga-NOTA-c(RGDyK)/PET scanning with subsequent kinetic modeling studies in rats with forelimb ischemia showed higher uptake and distribution volume in the ischemic area as compared to that of sham operation and control regions [48]. Monitoring myocardial repair and angiogenesis after ischemic injury was found plausible using [^{68}Ga]Ga-NODAGA-RGD and [^{68}Ga]Ga-TRAP-(RGD) $_3$ in rat model [49]. Elevated uptake of [^{68}Ga]Ga-DOTA-E-[c(RGDfK)] $_2$ was observed in the infarcted area while no accumulation was detected in the noninfarcted myocardium of the same rats [50]. The uptake of [^{68}Ga]Ga-DOTA-RGD in atherosclerotic plaques was studied *in vivo* in atherosclerotic mice with promising results [52]. Elevated uptake of [^{68}Ga]Ga-NODAGA-RGD in injured myocardium as compared to viable ischemic areas in pig model presumably indicated increased expression of $\alpha_v\beta_3$ receptors associated with injury repair in the presence of coronary stenosis [51].

Although targeting VEGF receptors were studied in the context of cancerous diseases, chronic inflammation can also be considered. A ligand consisting of a single chain (scVEGF, 3–112 amino acids of human VEGF $_{121}$) [128, 129] was labelled with ^{68}Ga and the resulting agent showed distinct uptake in the tumour xenografts in mice; however high kidney uptake needed to be addressed [130, 131].

5.3. Targeting Selectins. P-selectin is expressed on the active endothelium surface and platelets and operates the migration of leukocytes in response to inflammatory cytokines.

TABLE 3: ^{68}Ga -based imaging agents for inflammation and infection investigated preclinically and clinically.

Target/mechanism	Imaging agent	Disease/microorganism (study type)
<i>Inflammation</i>		
P-selectin	^{68}Ga]Ga-Fuoidan	Atherosclerotic plaques (preclinical [44])
Anti-CD163	^{68}Ga]Ga-anti-CD163-antibody	Acute collagen-induced arthritis (preclinical [45])
Integrins	^{68}Ga]Ga-PRGD ₂	Rheumatoid arthritis (clinical [46])
Integrins	^{68}Ga]Ga-NOTA-c(RGDyK) ^{68}Ga]Ga-NODAGA-RGD ^{68}Ga]Ga-TRAP-(RGD) ₃ ^{68}Ga]Ga-DOTA-E-[c(RGDfK)] ₂	Myocardial infarction (preclinical [47–51])
Integrins	^{68}Ga]Ga-NODAGA-RGD	Atherosclerotic plaques (preclinical [52])
VAP-1	^{68}Ga]Ga-Siglec	Synovial inflammation; inflammatory lung injury; atherosclerotic lesions; skin/muscle inflammation (preclinical [53–56])
VAP-1	^{68}Ga]Ga-DOTAVAP-P1, ^{68}Ga]Ga-DOTAVAP-PEG-P1	Skin/muscle inflammation (preclinical [57])
CXCR4	^{68}Ga]Ga-pentixafor	Ischemic heart; atherosclerotic plaques (clinical [58, 59])
FR	^{68}Ga]Ga-DOTA-PEG-FA ^{68}Ga]Ga-DOTA-folate	Inflammation/implant (preclinical [60, 61])
SSTR	^{68}Ga]Ga-DOTA-TOC	Sarcoidosis, idiopathic pulmonary fibrosis, Graves' disease, Hashimoto's disease, coronary artery plaque, atherosclerotic inflammation (clinical [62–65])
Mannose receptors	^{68}Ga]Ga-NOTA-MSA	Myocarditis (preclinical [66])
A β plaques	^{68}Ga -labelled styrylpyridines, benzofuran, curcumin	Neuroinflammation, Alzheimer's disease (preclinical [67–69])
<i>Infection</i>		
Antibiotics/inhibitor	^{68}Ga]Ga-ciprofloxacin	<i>Staphylococcus aureus</i> (preclinical [70])
Antimicrobial/membrane	^{68}Ga]Ga-NOTA-UBI29-41 ^{68}Ga]Ga-NOTA-UBI30-41	<i>Staphylococcus aureus</i> (preclinical [71, 72])
Antimicrobial/membrane	^{68}Ga]Ga-DOTA-TBIA101	<i>E. coli</i> (preclinical [73, 74])
Antimicrobial/membrane	^{68}Ga]Ga-GF-17 and ^{68}Ga]Ga-RAWVAVR-NH2	<i>E. coli</i> and <i>S. aureus</i> (preclinical [75])
Siderophores	^{68}Ga]Ga-TAFC, ^{68}Ga]Ga-FC, ^{68}Ga]Ga-FOXE	Invasive pulmonary aspergillosis (preclinical [15, 16, 76])
Leukocytes	^{68}Ga]Ga-citrate	Osteomyelitis, diskitis, intra-abdominal infection, tuberculosis, interstitial nephritis (clinical [18, 19, 77–80])
Leukocytes	^{68}Ga]Ga-Apo-transferrin	<i>Staphylococcus aureus</i> (preclinical [14])

E-selectin binding peptide labelled with $^{99\text{m}}\text{Tc}$ accumulated in acute osteomyelitic lesions in rats presumably by interaction with activated vascular endothelium [132]. An analogue of P-selectin natural ligand, fuoidan, labelled with ^{68}Ga could discriminate active and inactive atherosclerotic plaques in mice [44].

5.4. *Targeting Vascular Adhesion Protein-1*. Vascular adhesion protein-1 (VAP-1) and CD73 are endothelial surface enzymes involved in the recruitment of leukocytes and their movement from the blood into the tissue [109]. Endothelial activation that takes place during inflammation can be utilized for specific targeting imaging. Several peptide analogues

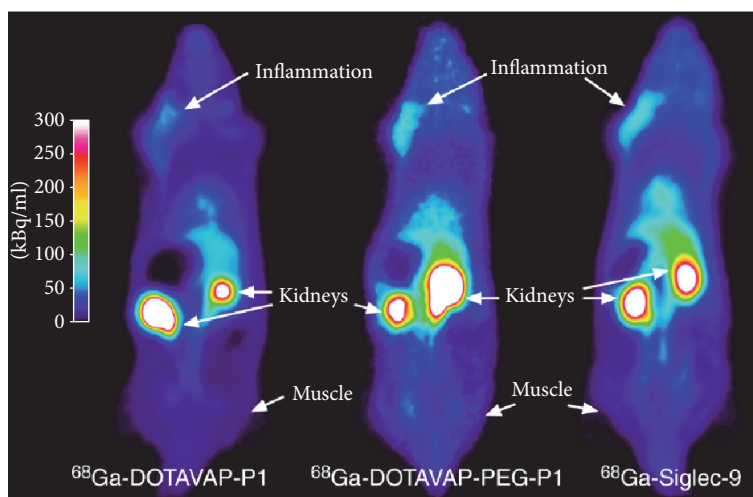


FIGURE 1: PET images of the distribution of [^{68}Ga]Ga-DOTAVAP-P1, [^{68}Ga]Ga-DOTAVAP-PEG-P1, and [^{68}Ga]Ga-DOTA-Siglec-9 in turpentine-induced rat model of sterile inflammation. All three peptide analogues showed target-to-nontarget ratio above 6 with rapid accumulation in the inflammation site and renal clearance. Adapted from [57].

labelled with ^{68}Ga were designed for the visualization of VAP-1 and showed promising results in animals with induced infection and sterile inflammation [7–13, 133]. The binding was proven specific and it was possible to differentiate inflammation from infection. [^{68}Ga]Ga-Siglec targeting VAP-1 demonstrated preclinical potential for imaging of synovial inflammation in patients with rheumatic diseases [53]. The same agent was utilized for respiratory distress syndrome (ARDS, an inflammatory lung injury) imaging in a porcine model [54]. Imaging VAP-1 with [^{68}Ga]Ga-Siglec was found promising also for the detection of inflamed atherosclerotic lesions [55] and inflammatory response induced by catheter implantation and staphylococcal infection [56]. ^{68}Ga -Siglec and two more peptide analogues with affinity to VAP-1 ([^{68}Ga]Ga-DOTAVAP-P1, [^{68}Ga]Ga-DOTAVAP-PEG-P1, and [^{68}Ga]Ga-DOTA-Siglec-9) were investigated in rat model of sterile skin/muscle inflammation (Figure 1) [57]. They showed distinct uptake in the affected sites.

5.5. Targeting Chemokines. Cytokines are produced by macrophages, B-lymphocytes, T-lymphocytes, and mast cells and act through receptors modulating, for example, immune response to infection and inflammation. Cytokines include chemokines, interleukins, interferons, and lymphokines that can be classified in broad families exhibiting diverse functions, for example, IL-1 and IL-6 superfamilies and TNF/TNF receptor superfamily. Therapeutics targeting cytokines are in clinical use, for example, inhibiting TNF or IL-6 in rheumatic diseases.

Chemokine receptors are physiologically expressed on B-lymphocytes, T-lymphocytes, macrophages, neutrophils, eosinophils, monocytes, and hematopoietic stem cells [134]. Imaging agents targeting CXCR4 are based on inhibitors (AMD3100) or small peptides (NFB, T140, pentixafor, and TN14003) and comprise ^{18}F , ^{67}Ga , ^{68}Ga , or ^{64}Cu [135–148]. They were developed and studied for the imaging of

various cancerous diseases: lung, breast, prostate cancers, acute myeloid leukemia, and glioblastoma.

The application of CXCR4 targeting agents was extended beyond oncology. Clinical case/image reports [149, 150] were published on the utilization of [^{68}Ga]Ga-pentixafor for detection and quantification of CXCR4 receptor density in ischemic heart diseases reflecting the role of the receptor in inflammatory and progenitor cell recruitment [58, 59]. The same agent was successfully used in the assessment of macrophage infiltration in atherosclerotic plaques in rabbit disease model [151].

5.6. Targeting Folate Receptors. Folate receptors (FRs) are overexpressed on a variety of cancer cells and activated macrophages, but not on normal cells [152, 153]. The enhanced expression of FR was found in lung macrophages during acute inflammation [154]. The majority of the nuclear imaging agents based on folic acid or pteric acid [155] were developed for diagnosis of cancers overexpressing FR receptors such as breast, cervical, ovarian, colorectal, nasopharyngeal, renal, and endometrial cancers. Various ^{68}Ga -labelled agents demonstrated accumulation in cell cultures and mice bearing folate-receptor positive human nasopharyngeal carcinoma cell line (KB) xenografts [6, 156–162]. [^{68}Ga]Ga-DOTA-PEG-FA comprising folic acid was investigated for the detection and quantification of inflammatory response to medical implants using mice with subcutaneously implanted polylactic acid and poly(N-isopropylacrylamide) particles as a model [60]. The agent was accumulated in the area of the implant most probably reflecting interaction of [^{68}Ga]Ga-DOTA-PEG-FA with folate receptor expressed on activated macrophages. Another folic acid based agent, [^{68}Ga]Ga-DOTA-folate, was successfully tested in an inflammatory paw rat model (Figure 2) [61]. Distinct accumulation in inflamed hand and foot joints of rheumatoid arthritis of a $^{99\text{m}}\text{Tc}$ -labelled folate analogue was observed in a patient, while no

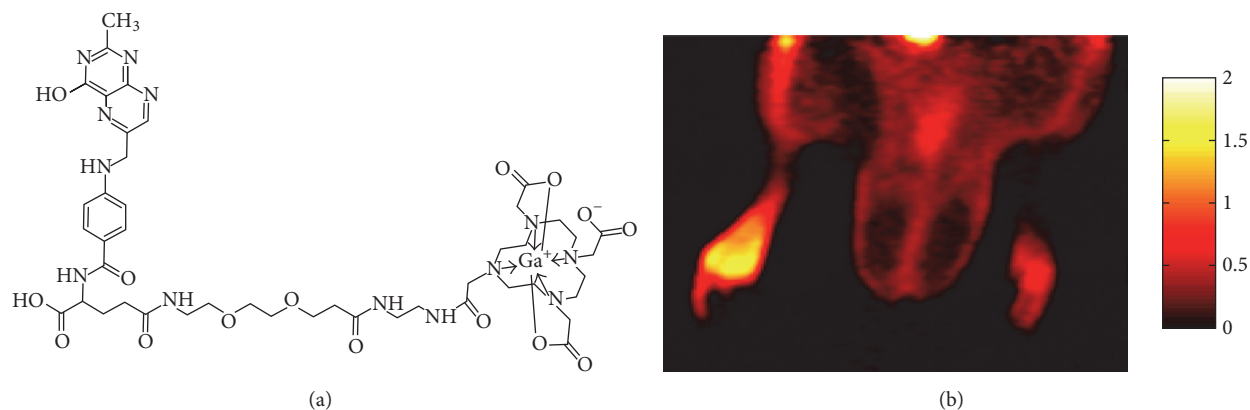


FIGURE 2: Accumulation of [^{68}Ga]Ga-DOTA-folate (a) in the site of inflammation of rat inflammatory paw model induced by subcutaneously injected Complete Freund's Adjuvant (b). Adapted from [61].

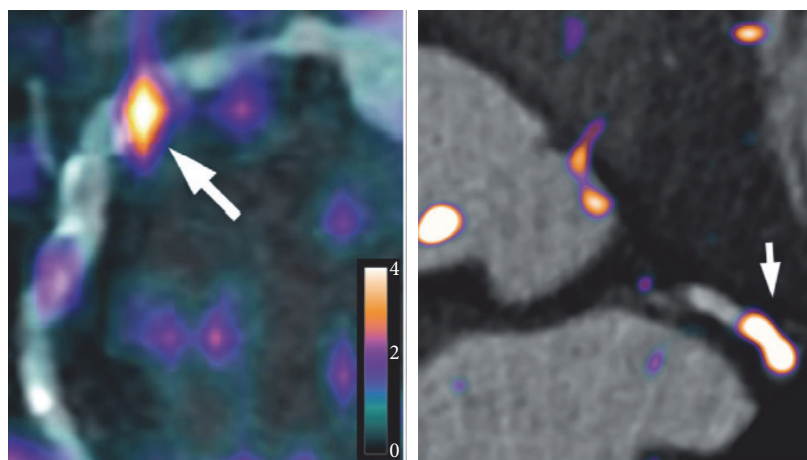


FIGURE 3: Intense atherosclerotic inflammation (white arrows) was detected by [^{68}Ga]Ga-DOTA-TATE in a patient with acute coronary syndrome. Adapted from [65].

uptake was detected in a nonarthritis patient's hands and feet [163].

5.7. Targeting Somatostatin Receptors. Somatostatin receptor (SSTR) ligand analogues have found an extensive application in diagnosis and radiotherapy of neuroendocrine tumours. The elevated expression of SSTRs is known also in small cell lung cancer, breast cancer, renal cell carcinoma, prostate cancer, and malignant lymphoma. A number of somatostatin ligand analogues labelled with gamma- and positron-emitting radionuclides were used clinically for oncological cases [85, 164–174]. ^{68}Ga -labelled somatostatin analogues demonstrated superior performance in terms of higher specificity and sensitivity, detection rate, shorter examination time, and quantification possibility and have become a golden standard for the detection of neuroendocrine tumours (NETs) taking over that title from [^{111}In]pentetretotide (OctreoScan[®]) and demonstrating specificity and sensitivity of over 90% [27, 175–180]. ^{68}Ga -labelled agents for the imaging of NETs demonstrated advantages

also over other radionuclides and tracers such as [^{18}F]FDG [174], ^{123}I -metaiodobenzylguanidine ([^{123}I]MIBG) [181, 182], [^{18}F]DOPA [183], [$^{99\text{m}}\text{Tc}$]-dicarboxy propane diphosphonate [184], and [^{18}F]NaF.

SSTR are also overexpressed on activated macrophages and T-lymphocytes. ^{68}Ga -labelled analogues were used in inflammation related diseases such as idiopathic pulmonary fibrosis [62], Graves' and Hashimoto's diseases [63], coronary artery plaque imaging and characterization [64], and atherosclerotic inflammation with excellent macrophage specificity (Figure 3) [65]. Promising diagnostic potential of a $^{99\text{m}}\text{Tc}$ -labelled analogue was demonstrated in patients with rheumatoid arthritis and secondary Sjogren's syndrome, and the method was suggested for the assistance in anti-TNF alpha antibody treatment planning [185]. [^{68}Ga]Ga-DOTA-TOC/PET-CT was found superior to ^{67}Ga -Citrate/SPECT in detection of sarcoidosis lesions [186]. A clinical study demonstrated correlation between uptake of [^{68}Ga]Ga-DOTA-TOC and SSTR₂ mRNA expression and recorded the information in a database [187] providing tools for accurate quantification

and evaluation of disease progression and treatment response in cancerous and inflammatory diseases involving SSTRs. Preclinical study using atherosclerotic mice demonstrated superior targeting properties of [^{68}Ga]Ga-DOTA-NOC as compared to [^{18}F]FDR-NOC [188], overall confirming the potential of SSTR targeting for atherosclerotic plaque imaging.

5.8. Imaging Neuroinflammation. Despite difficulty of designing ^{68}Ga -labelled molecules capable of blood-brain barrier penetration, several agents were suggested for the imaging of neuroinflammation, in particular A β plaques deposited on blood vessels [67–69]. Bivalent styrylpyridines labelled with ^{68}Ga demonstrated high specificity and affinity for A β plaques using postmortem Alzheimer's disease (AD) brain sections [67]. Benzofuran derivative comprising ^{68}Ga showed promising results in terms of binding specificity and affinity investigated in vitro in sections of Tg2576 mice [68]. Although the synthesis of a ^{68}Ga -labelled Pittsburgh compound analogue was successful, the in vitro binding to amyloid deposits was limited [69]. The common disadvantage of these agents is poor blood-brain barrier penetration; nevertheless the exploration of more successful analogues continues. Curcumin functions as an antioxidant, antimicrobial, anti-inflammatory, and anticancer agent. Diacetyl-curcumin and bis(dehydroxy)curcumin labelled with ^{68}Ga demonstrated in vitro binding to β -amyloid fibrils and lung cancer cells [189]. Potential application of the agents could include diagnostic imaging of Alzheimer's disease and various cancers.

6. Imaging Infection

Infection imaging can be indirect utilizing targets involved in the immune response, namely, inflammation, as presented in the inflammation targets section above or direct utilizing pathogen related targets. The direct imaging is especially crucial in cases where inflammatory response is absent. The difference in biochemistry and structure between bacterial and human cells might exclude physiological uptake by human tissue making it easier to meet the favorable characteristics of an imaging agent. However, discrimination between the various infectious microorganisms, pathogenic bacteria, and microbiota, targeting specific bacteria type as well as difficulty of accessing bacteria aggregated in a biofilm makes the task very challenging [190, 191]. The specific targeting of infection would require accumulation of the radioactive signal in the pathogen. The radiolabelled targeting agents for infection can be roughly divided into several groups: antibiotics based; antimicrobial protein and peptide based; siderophore and other metabolisable compound based; and antigen-specific antibodies and antibody fragments (Table 3).

6.1. Radiolabelled Antibiotics. Antimicrobials act on the processes that are specific to microbes, for example, bacteria and fungi, and thus corresponding imaging agents might distinguish infection from inflammation [191]. They might require internalization or may bind to the cell surface dependent on

their biological action mechanism [191–193]. The possibility of antibiotic resistance development exists also in the case of imaging agents even though the amount of such agents would be subnanomolar [194, 195]. Another complication is possible nonspecific uptake of antibiotics based agents by leucocytes [196]. Considerable number of various antibiotic analogues have been labelled with $^{99\text{m}}\text{Tc}$, ^{111}In , ^{131}I , ^{11}C , and ^{18}F [102] and evaluated preclinically and clinically with $^{99\text{m}}\text{Tc}$ -ciprofloxacin becoming a commercial product (Infecton) [21, 197, 198]. However, the further improvement of specificity is desirable [191]. Antibiotics are accessible and cheap, and they demonstrate high sensitivity [102, 191] making the development of ^{68}Ga -labelled analogues very attractive given the earlier mentioned advantages that ^{68}Ga as a radionuclide in combination with PET provides. Two ^{68}Ga -labelled analogues based on ciprofloxacin demonstrated potential for discrimination between bacterial infection and inflammation in rats infected with *Staphylococcus aureus* [70].

6.2. Radiolabelled Antimicrobial Proteins and Peptides. Antimicrobial proteins and peptides, for example, serprocidins, cathelicidins, and defensins produced by the cells of immune system, target microbial membrane lipids and impose microbicidal effect [35, 43]. They present a large group of potential candidates for microbial imaging including bacteria, fungi, parasites, and viruses. Antimicrobial peptides have demonstrated higher specificity for infection than antibiotic analogues. They accumulate at infection but not sterile inflammation sites. The most thoroughly studied antimicrobial peptide, ubiquicidin UBI [29–41] labelled with $^{99\text{m}}\text{Tc}$ [199], demonstrated promising results in human clinical trials [200, 201]. It has the potential for quantification of viable infecting microorganisms and consequently for monitoring the efficacy of antimicrobial therapy in patients.

Fragments of an antimicrobial peptide ubiquicidin conjugated to NOTA and labelled with ^{68}Ga , [^{68}Ga]Ga-NOTA-UBI29-41, and [^{68}Ga]Ga-NOTA-UBI30-41 demonstrated possibility for the distinction between infection and inflammation in a rabbit model [71, 72]. Antimicrobial peptide fragments GF-17 and RAWVAWR-NH2 of, respectively, human cathelicidin LL-37 and human lysozyme active against *E. coli* and *S. aureus* were labelled with ^{68}Ga and their biodistribution in normal rats demonstrated fast clearance from liver [75]. Antimicrobial depsipeptide based agent, [^{68}Ga]Ga-DOTA-TBIA101, targeting bacterial lipopolysaccharides detected muscular *E. coli*-infection in mice (Figure 4) [73]. The agent was also studied in healthy rabbits and various disease model rabbits such as sterile inflammation, *Staphylococcus aureus* infection, and *Mycobacterium tuberculosis* [74]. The clearance of [^{68}Ga]Ga-DOTA-TBIA101 from blood and normal tissue was fast, and enhanced uptake in sterile inflammation and *Mycobacterium tuberculosis* sites was observed. The improvement of the bacterial selectivity will require modification of the agent structure.

6.3. Radiolabelled Siderophores. Bacteria and fungi produce various siderophores for harvesting iron which is essential for their survival and growth [34, 98, 191]. Siderophores

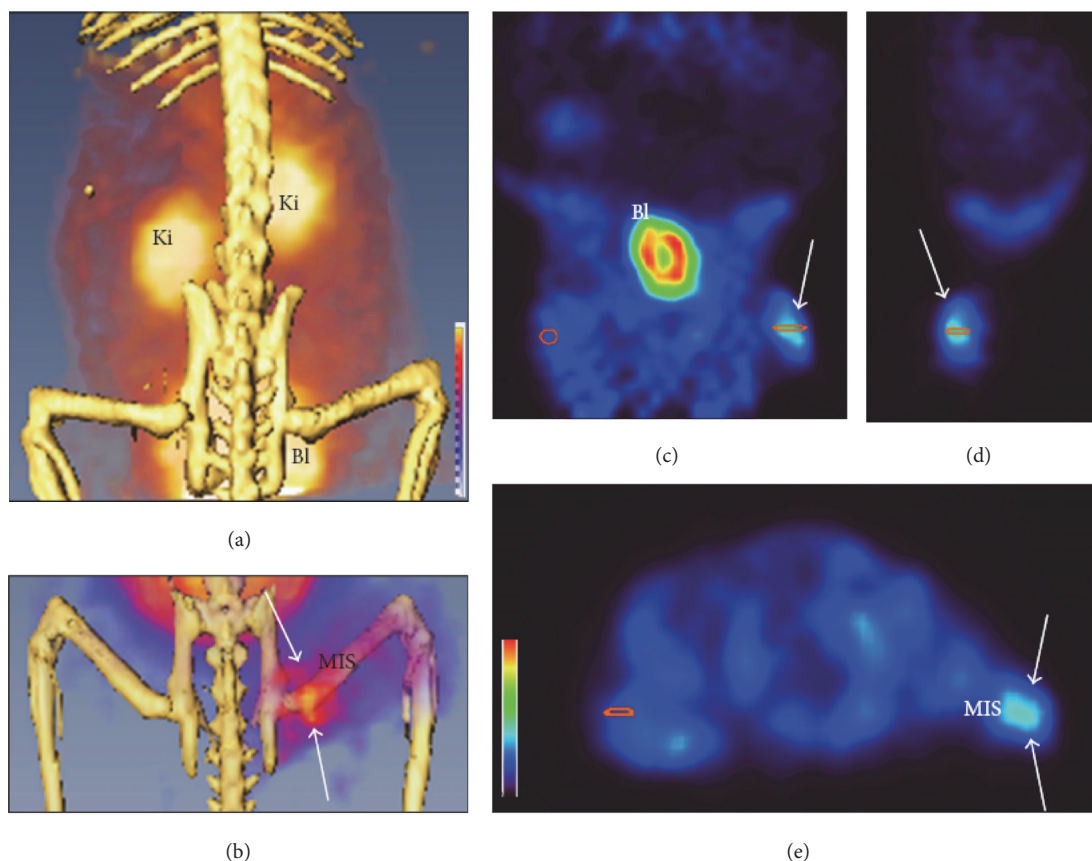


FIGURE 4: Left panel presents maximum intensity projection images of [^{68}Ga]Ga-DOTA-TBIA101 distribution in a healthy mouse (a) and a mouse with muscular infection site (MIS) in the right hind muscle tissue (white arrows). Right panel presents coronal (c), sagittal (d), and axial (e) images with uptake in the MIS (white arrow) and absence of the uptake in the contralateral muscle tissue. Ki and Bl stand, respectively, for kidney and bladder. Reproduced from [73].

can also play a critical role in the development of biofilms by microbes. They are low molecular weight compounds specifically chelating Fe(III), and Ga(III) can form stable complexes with them mimicking Fe(III) [202, 203].

Desferri-triacetylfusarinine C (TAFC) and desferri-ferricrocin (FC) labelled with ^{68}Ga were used for the imaging of invasive pulmonary aspergillosis (IPA) caused by *Aspergillus fumigatus* [15]. [^{68}Ga]Ga-TAFC demonstrated superior characteristics in terms of specific target binding, metabolic stability, and fast blood clearance in a rat model of *A. fumigatus* infection. Seven analogues were developed in another study with TAFC and ferrioxamine E (FOXE) showing favorable binding, clearance, elimination, and stability characteristics [16] as well as lung uptake in rat of invasive aspergillosis model wherein the uptake extent was correlated with disease severity [17]. [^{68}Ga]Ga-triacetylfusarinine C and [^{68}Ga]Ga-ferrioxamine E were investigated in rat model of *A. fumigatus* and demonstrated rapid uptake in the lungs (Figure 5) [76].

6.4. Radiolabelled Metabolisable Agents. Mammalian microbiota consumes (poly)saccharides, in particular maltose and maltodextrins [204]. The transport mechanism is specific

to bacteria and is absent in mammalian cells making it possible to utilize these (poly)saccharides for imaging agent development. Maltodextrin functionalized with a fluorescent dye was internalized through the bacteria-specific maltodextrin transport pathway and discriminated between active bacteria and inflammation in vivo [192]. Maltose labelled with ^{18}F localized specifically bacterial infection in mice [205]. Potential to label polysaccharides directly with ^{68}Ga might be utilized extensively.

As mentioned above, the chemical properties of Ga(III) provide the potential for direct labelling of polysaccharides. Dextran was labelled directly and resulting complex demonstrated sufficient stability in human serum; however the feasibility of the bacterial imaging was not demonstrated [206].

Trapping of nucleosides that are substrates of thymidine kinase occurring within bacteria was explored using ^{18}F and ^{125}I labelled analogues of uracil [207]. Promising results were obtained in seven bacterial species in mice. Another study, in the context of therapeutic bacteria development, demonstrated possibility of detecting *Salmonella* vectors within tumours using ^{18}F -labelled uracil [208]. However,

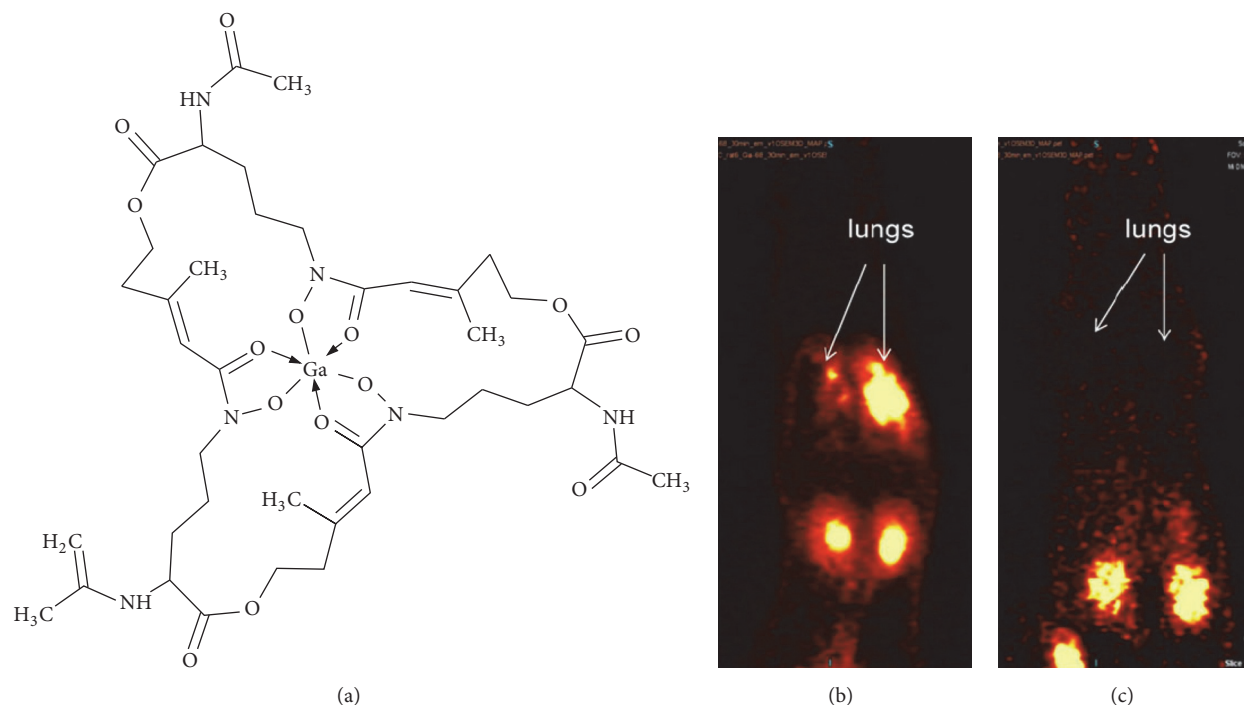


FIGURE 5: Molecular structure of [^{68}Ga]Ga-triacetylfusarinine C (a) used for the in vivo imaging of a rat with *Aspergillus fumigatus* infection (b) and negative control of noninfected rat (c). White arrows point at the infected (b) and normal (c) lungs. Adapted from [76].

the development of ^{68}Ga -labelled nucleosides that would maintain their biological activity is challenging and few examples known from the literature confirm that [4, 6].

7. ^{68}Ga -Citrate

As mentioned above ^{68}Ga /PET provides a number of advantages over ^{67}Ga /SPECT and following publications demonstrate it in clinical and preclinical studies. [^{68}Ga]Ga-citrate demonstrated high diagnostic accuracy of 90% of osteomyelitis and diskitis in clinical studies (Figure 6) [18, 19]. This study demonstrates that [^{68}Ga]Ga-citrate can be employed for monitoring the response to treatment. [^{68}Ga]Ga-citrate was used clinically to follow-up surgical intervention in patients with acute osteomyelitis and intra-abdominal infection [77]. The agent was also used to successfully visualize lung malignancy and tuberculosis in patients; however in case of high prevalence of granulomatous diseases the distinction between malignant and benign lung lesions was unclear [78, 79]. Another clinical study conducted head-to-head comparison of [^{68}Ga]Ga-citrate (Figure 7) and [^{18}F]FDG in patients with *Staphylococcus aureus* bacteremia [80]. The detection rate of osteomyelitis was similar, and further investigation of [^{68}Ga]Ga-citrate applicability in cases of osteomyelitis induced by other pathogens as well as for monitoring healing process is warranted.

Comparative study of [^{68}Ga]Ga-citrate and [^{67}Ga]Ga-citrate was performed in healthy and infection model rats [77]. The performance of [^{68}Ga]Ga-citrate was found superior in terms of image contrast in the lower abdomen and

extremities. Potential of [^{68}Ga]Ga-citrate for the differentiation of acute interstitial nephritis from acute tubular necrosis was studied in rat model of the disease and it was demonstrated that the kidney uptake correlated with the extent of mononuclear cell infiltration accompanying inflammation [209]. ^{68}Ga -labelled *Apo*-transferrin demonstrated bacterial infection detection capacity in rat model with *Staphylococcus aureus* wherein the infection site was visualized 1 h after administration of the agent [14].

7.1. Radiolabelled Antibodies and Antibody Fragments. Human immunoglobulin (HIG) binds to bacteria but also accumulates at the sites of fungal and viral infection as well as sterile inflammation due to binding to leukocytes. The improved specificity for bacteria was achieved for the fragments of HIG. It is feasible to develop specific antibodies to various antigens present on the bacterial cell surface [102]. Monoclonal antibodies labelled with $^{99\text{m}}\text{Tc}$ were used for infection imaging via granulocytes targeting NCA-95 [210]. Various cytokines of interleukin family (IL-1, IL-8) labelled with ^{123}I or $^{99\text{m}}\text{Tc}$ demonstrated accumulation in the sites of infection in various animal models [111, 112, 211–214]. Registered antigranulocyte radiopharmaceuticals such as LeuTech[®], Scintimun[®], and Leukoscan[®] are based on $^{99\text{m}}\text{Tc}$ -labelled antibodies. This experience can be translated to ^{68}Ga ; however either the size of the antibodies must be reduced or pretargeting techniques must be applied in order to overcome the discrepancy between the short physical half-life of ^{68}Ga and slow pharmacokinetics of antibodies.

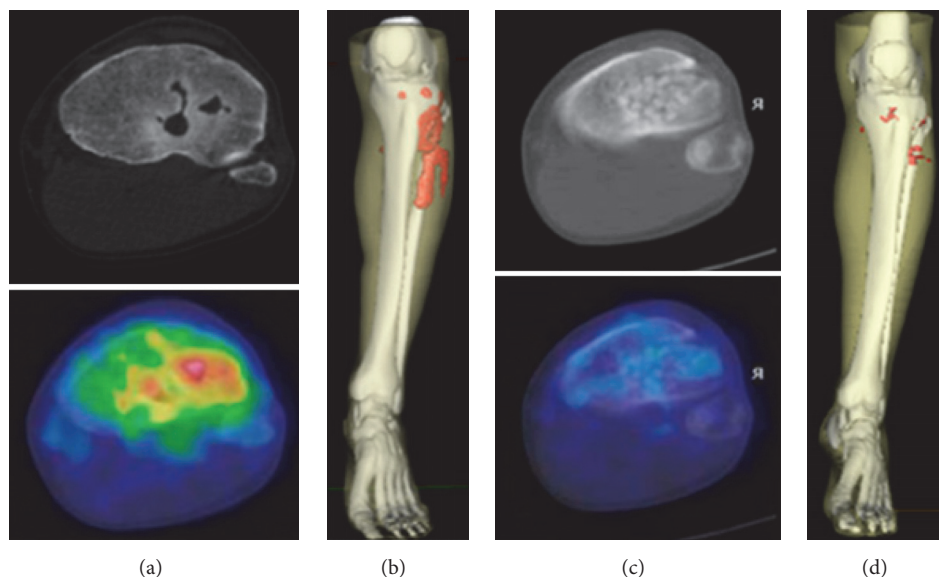


FIGURE 6: [^{68}Ga]Ga-citrate PET/CT examination of a patient affected by acute osteomyelitis before (left panel) and after (right panel) surgical curettage showing uptake in the transaxial (a, c) and 3D reconstruction images (b, d; red area). Absence of the uptake after the therapy confirms complete response to the treatment. Adapted from [19].

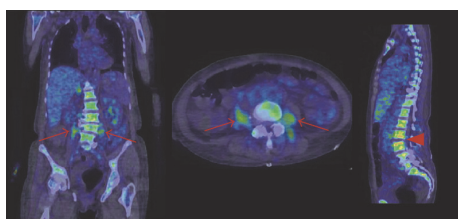


FIGURE 7: Vertebral osteomyelitis (spondylodiscitis; red arrowheads) and abscesses in the iliopsoas and paravertebral area (red arrows) were detected by [^{68}Ga]Ga-citrate in a patient admitted to the hospital with back pain and general symptoms. The PET acquisition was performed 88 min after administration of 245 MBq of [^{68}Ga]Ga-citrate. Adapted from [80].

7.2. Radiolabelled Biotin. Biotin is a growth factor utilized in many bacteria. An ^{111}In -labelled analogue of biotin was successfully utilized for diagnosis of vertebral infections in a clinical study [215]. It would be rational to explore the relevance of ^{68}Ga -labelled analogues given the advantages of ^{68}Ga over ^{111}In and promising [^{68}Ga]Ga-DOTA-Biotin analogues [216, 217] developed for monitoring survival of transplanted avidin-coated islets.

8. Miscellaneous

Stable Ga(III) complex with thiosemicarbazones demonstrated antimicrobial effect against *P. aeruginosa* and *C. albicans* due to most probably both displacement of essential Fe(III) with Ga(III) and thiosemicarbazones [101]. Substitution of the stable Ga(III) by radioactive ^{68}Ga might result in a specific infection imaging agent.

Selective imaging of Enterobacteriaceae using 2- ^{18}F -fluoro-deoxy-sorbitol (^{18}F -FDS) was demonstrated in a murine

myositis model [218]. The uptake of ^{18}F -FDS was correlated with bacterial burden; moreover the agent differentiated infection from sterile inflammation. Given the potential of ^{68}Ga for the labelling of small biologically active molecules [4] it might be plausible to develop a respective analogue with added value of the advantages that ^{68}Ga offers including simpler production chemistry, lowered radiation dose, repetitive examination, and accessibility at clinical centers without cyclotrons and remote from [^{18}F]-FDG distribution sites. As mentioned above, the poor access to bacteria aggregated in a biofilm might make the imaging task challenging. Several peptide candidates with affinity for *S. aureus* biofilm were designed and labelled with ^{68}Ga [219]. The resulting agents demonstrated binding in vitro; however it was not possible to block the binding with excess of the cold peptide.

Ionic ^{68}Ga was found superior to [^{18}F]-FDG in infection detection in the rat model with diffuse osteomyelitis [220]. In another study, the uptake of ionic ^{68}Ga was observed in the aortic plaques of atherosclerotic mice, specifically at the sites rich in macrophages [221]. However, the slow blood clearance of ionic ^{68}Ga presents a limitation.

Chronic inflammation is the major reason of fibrosis [222]. ^{68}Ga -labelled SST analogue ([^{68}Ga]Ga-DOTA-NOC) demonstrated uptake in pathogenic areas in patients affected by idiopathic pulmonary fibrosis with potential for monitoring response to treatment and drug development [62]. Another clinical study using [^{68}Ga]Ga-pentixafor also showed potential of the agent for monitoring disease activity and response to treatment in idiopathic pulmonary fibrosis [223]. Peptide based agents, CNO2A-PEG₂-c[CPGRVMHGLHLGDDEGPG] and [^{68}Ga]Ga-NODAGA-PEG₂-c[CPGRVMHGLHLGDDEGPG] for the imaging and quantification of fibrosis by PET were developed and characterized preclinically showing fast clearance from normal

tissue and blood and binding specificity [89]. Dosimetry calculations demonstrated possibility of six examinations per year in humans assuring disease monitoring in longitudinal studies and routine clinical setup [224].

Several hyaluronan conjugates of oligonucleotides targeting CD44 positive cells were developed and tested in healthy rats, sham-operated rats, and rats with myocardial infarction [225]. The uptake of the agents was higher for the latter group and varied dependent on the difference in the oligonucleotide structure.

TLR2 and TLR4 expression levels in neutrophils were found higher in individuals with bacterial and viral infections than those in control samples. There is a possibility that IL-4, IL-8, IL-10, IL-12, and TNF- α might serve as biomarkers for infections and that IL-2, IL-8, or IL-10 is potentially able to distinguish between bacterial and viral infections [22].

Mannosylated human serum albumin labelled with ^{68}Ga via NOTA chelator moiety (^{68}Ga]-Ga-NOTA-MSA) was tested in a rat model of myocarditis targeting mannose receptors expressed on macrophages infiltrating myocardium [66]. The uptake in the diseased myocardium was considerably higher than that of the normal one and it was precluded by administration of excess of nonlabelled MSA indicating binding specificity. The tracer build-up was also observed in the organs of macrophage accumulation.

^{68}Ga]-Ga-DOTA was investigated for the quantification of increased blood flow which is one of the key events in inflammation [226]. The uptake kinetics of ^{68}Ga]-Ga-DOTA in the site of inflammation in rats with induced inflammation correlated well with that of ^{15}O -water, suggesting high relevance ^{68}Ga]-Ga-DOTA.

9. Pretargeted Imaging

The half-life of ^{68}Ga is shorter than that of ^{64}Cu , ^{67}Ga , $^{99\text{m}}\text{Tc}$, ^{89}Zr , ^{111}In , and $^{123,124,125}\text{I}$ and thus in contrast to the latter it is not compatible with slow pharmacokinetics of large molecules such as antibodies and glycoproteins. The range of antigen-specific antibodies relevant to inflammation and infection is broad and a number of $^{99\text{m}}\text{Tc}$ -labelled antibodies were used clinically [20, 21, 227]. The respective range of ^{68}Ga -based agents could be similar. The solution to overcome the incompatibility of half-life time frames could be either the reduction of the antibody size or the application of the pretargeting concept.

The history of the pretargeting concept spans three decades, predominantly in the field of oncology [228–230]. It was developed to improve image contrast and dosimetry in immunoimaging and radioimmunotherapy when using radiolabelled antibody ligands with slow pharmacokinetics [231]. The arsenal of antibodies is vast and diverse encouraging extensive investment into development of techniques that would allow their exploration to the fullest. Pretargeting considers at least two major steps wherein a functionalized antibody is first administered for target localization and clearance from blood and normal tissue and thereafter a radiolabelled small molecule capable of binding to the functionalized

antibody due to high affinity or covalent interaction is administered. The key properties of the radiolabelled molecules are fast pharmacokinetic and clearance. Several techniques have been developed for the realization of pretargeting concept including avidin/streptavidin-biotin systems [216, 217, 232, 233]; bispecific antibodies (bsmAb) with haptens [232, 234–254]; antibody-oligonucleotide conjugates with complementary oligonucleotides [255]; biorthogonal systems allowing covalent chemical reactions *in vivo* (Figure 8).

The high affinity of biotin to avidin and streptavidin proteins was utilized clinically and preclinically in pretargeting approach for the imaging and therapy of pancreatic adenocarcinoma [232], glioblastoma [256], and lymphoma [257]. However, this pretargeting technique may require three steps in order to eliminate the excess of antibody-(strept)avidin conjugate, circulating in the blood and not bound to the target, by adding clearing agent. Another application of the technique was monitoring transplantation of islets of Langerhans in the treatment for type 1 diabetes mellitus, wherein the cells or cell mimetics were conjugated to (strept)avidin prior to the transplantation [216, 217]. Several analogues of biotin comprising DOTA chelate moiety for labelling with ^{68}Ga and ethylene glycol linker of various length demonstrated the influence of the latter on the affinity towards avidin.

Particular example of hapten molecules is the ones comprising histamine-succinyl-glycine (HSG) motif and chelate moiety [251–253, 258] for the complexation with ^{68}Ga . Several analogues were developed for the imaging of carcinoembryonic antigen (CEA) pretargeted with anti-CEA bsmAb [254, 259, 260], and two clinical studies of medullary thyroid carcinoma and breast carcinoma positive for CEA using ^{68}Ga -labelled hapten molecules and bsmAb were initiated [261].

Biorthogonal reactions are fast, regioselective, requiring small reagent concentration, and occurring under mild conditions often in aqueous solution and temperature below 37°C [262, 263]. Amongst various biorthogonal reaction types, the cycloaddition of tetrazines and various dienophiles referred to as inverse-electron-demand Diels-Alder (IEDDA) reaction is the most successful in the context of pretargeting. Antibodies functionalized with *trans*-cyclooctene (TCO) and a radiolabelled tetrazine that can interact *in vivo* based on IEDDA reaction were studied [264–267]. In particular, ^{68}Ga -labelled tetrazine dextran demonstrated favorable pharmacokinetics in a healthy mouse [264]. However, the proof of concept is to be performed in a xenografted animal. Accumulation of anti-TAG72 [265] and anti-A33 [266] antibodies functionalized with TCO in mouse xenografts was visualized, respectively, by an ^{111}In and ^{64}Cu -labelled tetrazine analogues. Anti-CA19.9 antibody-TCO in combination with ^{177}Lu -labelled tetrazine demonstrated radiotherapeutic effect in pancreatic cancer murine model [267].

The pretargeted imaging techniques may contribute to the expansion of immuno-PET with ^{68}Ga providing the intrinsic advantages of ^{68}Ga and PET. As mentioned above, most of the developed radiolabelled counterparts of pretargeting techniques have demonstrated promising results. There are

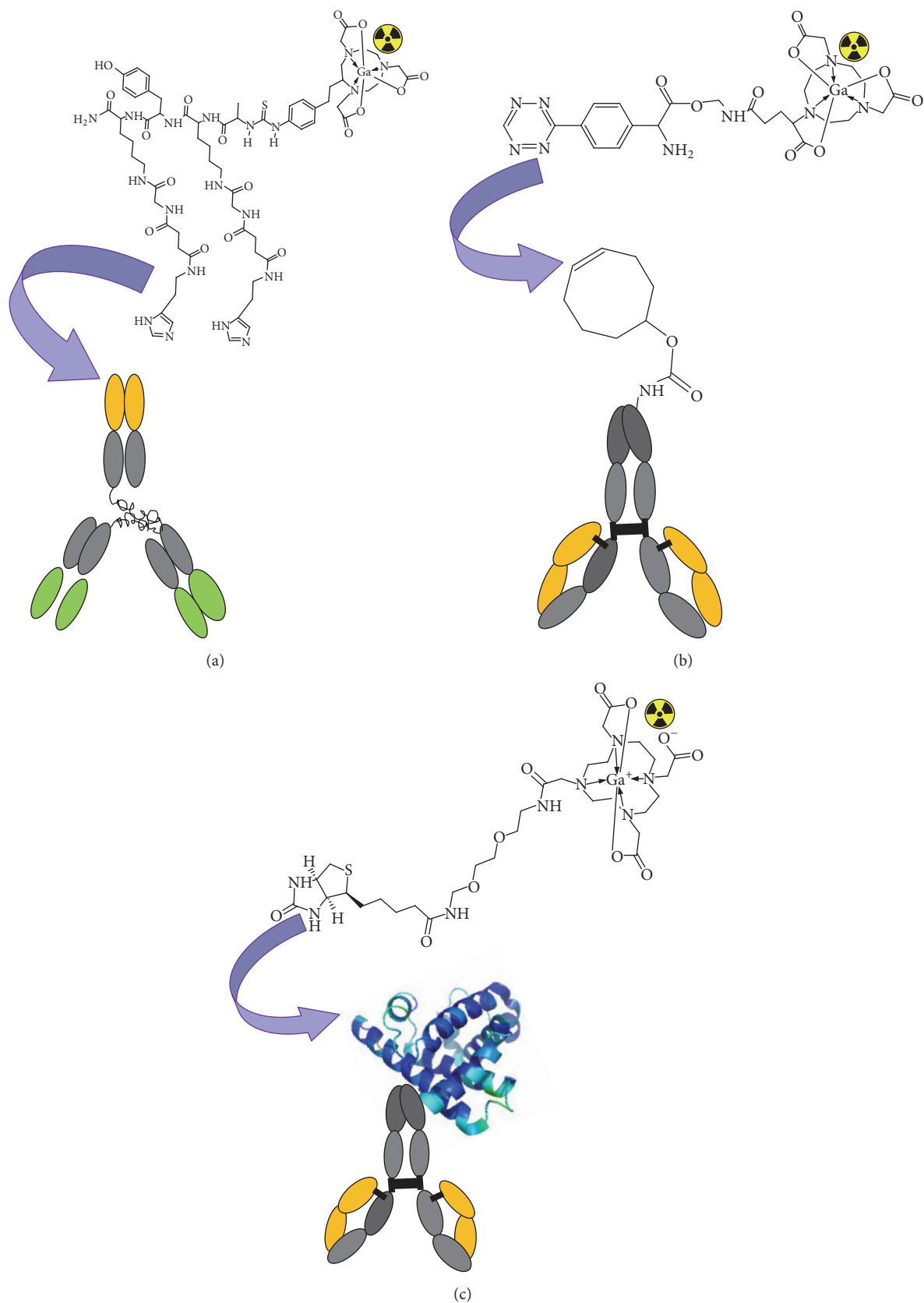


FIGURE 8: Schematic presentation of pretargeting techniques: (a) bispecific antibodies engineered to specifically bind with radiolabelled hapten molecules; (b) bioorthogonal click chemistry for fast and specific covalent binding between, for example, a *trans*-cyclooctene functionalized antibody and a radiolabelled tetrazine; (c) interaction between antibody-(strept)avidin conjugate and radiolabelled biotin utilizing extremely high affinity of (strept)avidin and biotin.

a considerable number of potential antibody biomarkers that could be considered for the imaging of infection and inflammation.

10. Theranostics Potential

Theranostics [268] embraces realization of personalized medicine by conducting diagnosis on individual basis and providing possibility of predicting the efficacy of a specific treatment and following up the response to the treatment enabling adjustment of the latter very early in the process. In the context of nuclear medicine wherein the radiopharmaceuticals targeted at biomarkers specific to a disease can carry either diagnostic radionuclides or therapeutic ones, the concept can be denoted as radiotheranostics [28]. The targeted molecular imaging such as PET can offer noninvasive diagnosis specific to the disease, for example, tumour-type specific, and provide accurate localization of the lesions. The strongest advantage of PET is the potential for quantification of the target, for example, receptor expression, investigation of the uptake kinetics, and estimation of the dosimetry. These characteristics of PET allow for individualized treatment selection and planning, monitoring of treatment response, and detection of recurrent disease. The individualized patient management provides such advantages as optimization of the treatment regimen for the improved response and exclusion of futile treatments, minimization of risks and toxicity with overall outcome of reduced cost and patient distress. The importance of individualized patient management was demonstrated by clinical studies wherein the influence of dose of the administered radiopharmaceutical, targeted at receptors overexpressed in cancer lesions, on the diagnostic outcome was investigated in the same patient [85, 269, 270]. ^{68}Ga -labelled SST analogues [26–28, 271] and Affibody molecules [5, 272–274] used, respectively, in NENs and breast cancer patients are the most prominent examples of (radio)theranostics involving ^{68}Ga /PET wherein ^{68}Ga -labelled analogues were used not only for localization of the lesions, but also for staging, patient stratification, prognosis, therapy selection, and monitoring of the response to the treatment of NETs and other cancer types [2–4, 6, 85, 176, 275–277].

The methodology can be translated to inflammation and infection allowing for accurate and specific selection of treatment regimen and for follow-up and evaluation of the response to therapy, resulting in improved treatment efficacy and decreased cost and side effects. The accommodation of both imaging function and antibiotic function in the same molecule is a novel example of a theranostic agent [278]. A series of siderophores conjugated with DOTA moiety for the radiolabelling and with antibiotics for the treatment of bacterial infection were investigated preclinically. The accumulation of the intravenously administered ampicillin conjugate in the site of subcutaneously injected *P. aeruginosa* in mice was clearly and focally visualized within 0.6 h with retention for at least 24 h. These results obtained using analogues carrying dye for optical imaging can be translated to ^{68}Ga -labelled counterparts for PET.

11. Conclusions

The medical need for specific agents for noninvasive, quantitative, and whole-body imaging of inflammation and infection has not been met yet despite decades of research. However, the prerequisites in terms of identification of potential targets, design and synthesis of the respective ligands, and imaging technologies are evolving very fast. The potential of accurate and quantitative lesion localization as well as monitoring of the treatment response promises personalized patient management.

The use of ^{68}Ga in oncology is established proving the strong potential of ^{68}Ga for the promotion of PET technology for effective and efficient diagnostics and personalized medicine. The experience of oncological ^{68}Ga -based agents is getting translated to inflammation and infection. Pretargeted imaging technology opens wide possibilities based on antibody biomarkers.

Conflicts of Interest

The author declares that there are no conflicts of interest regarding the publication of this article.

References

- [1] I. Velikyan, “Continued rapid growth in Ga applications: update 2013 to June 2014,” *Journal of Labelled Compounds & Radiopharmaceuticals*, pp. 99–121, 2015.
- [2] I. Velikyan, “ ^{68}Ga -based radiopharmaceuticals: Production and application relationship,” *Molecules*, vol. 20, no. 7, pp. 12913–12943, 2015.
- [3] M. Fani, P. Peitl, and I. Velikyan, “Current status of radiopharmaceuticals for the theranostics of neuroendocrine neoplasms,” *Pharmaceuticals*, vol. 10, no. 1, article no. 30, 2017.
- [4] I. Velikyan, “Positron emitting [^{68}Ga]Ga-based imaging agents: Chemistry and diversity,” *Medicinal Chemistry*, vol. 7, no. 5, pp. 345–379, 2011.
- [5] J. Sörensen, I. Velikyan, D. Sandberg et al., “Measuring HER2-receptor expression in metastatic breast cancer using [^{68}Ga]ABY-025 Affibody PET/CT,” *Theranostics*, vol. 6, no. 2, pp. 262–271, 2016.
- [6] I. Velikyan, “Prospective of ^{68}Ga -Radiopharmaceutical development,” *Theranostics*, vol. 4, no. 1, pp. 47–80, 2014.
- [7] P. Lankinen, T. J. Mäkinen, T. A. Pöyhönen et al., “ ^{68}Ga -DOTAVAP-P1 PET imaging capable of demonstrating the phase of inflammation in healing bones and the progress of infection in osteomyelitic bones,” *European Journal of Nuclear Medicine and Molecular Imaging*, vol. 35, no. 2, pp. 352–364, 2008.
- [8] T. Ujula, M. Huttunen, P. Luoto et al., “Matrix metalloproteinase 9 targeting peptides: Syntheses, ^{68}Ga -labeling, and preliminary evaluation in a rat melanoma xenograft model,” *Bioconjugate Chemistry*, vol. 21, no. 9, pp. 1612–1621, 2010.
- [9] A. Autio, T. Ujula, P. Luoto, S. Salomäki, S. Jalkanen, and A. Roivainen, “PET imaging of inflammation and adenocarcinoma xenografts using vascular adhesion protein 1 targeting peptide ^{68}Ga -DOTAVAP-P1: Comparison with ^{18}F -FDG,” *European Journal of Nuclear Medicine and Molecular Imaging*, vol. 37, no. 10, pp. 1918–1925, 2010.

- [10] J. Silvola, A. Autio, P. Luoto, S. Jalkanen, and A. Roivainen, "Preliminary evaluation of novel ^{68}Ga -DOTAVAP-PEG-P2 peptide targeting vascular adhesion protein-1," *Clinical Physiology and Functional Imaging*, vol. 30, no. 1, pp. 75–78, 2010.
- [11] T. Ujula, S. Salomäki, P. Virsu et al., "Synthesis, ^{68}Ga labeling and preliminary evaluation of DOTA peptide binding vascular adhesion protein-1: a potential PET imaging agent for diagnosing osteomyelitis," *Nuclear Medicine and Biology*, vol. 36, no. 6, pp. 631–641, 2009.
- [12] A. Autio, T. Henttinen, H. J. Sipilä, S. Jalkanen, and A. Roivainen, "Mini-PEG spacing of VAP-1-targeting ^{68}Ga -DOTAVAP-P1 peptide improves PET imaging of inflammation," *EJNMMI Research*, vol. 1, no. 1, pp. 1–7, 2011.
- [13] K. Aalto, A. Autio, E. A. Kiss et al., "Siglec-9 is a novel leukocyte ligand for vascular adhesion protein-1 and can be used in PET imaging of inflammation and cancer," *Blood*, vol. 118, no. 13, pp. 3725–3733, 2011.
- [14] V. Kumar, D. K. Boddeti, S. G. Evans, F. Roesch, and R. Howman-Giles, "Potential use of ^{68}Ga -apo-transferrin as a PET imaging agent for detecting *Staphylococcus aureus* infection," *Nuclear Medicine and Biology*, vol. 38, no. 3, pp. 393–398, 2011.
- [15] M. Petrik, H. Haas, G. Dobrozemsky et al., " ^{68}Ga -siderophores for PET imaging of invasive pulmonary aspergillosis: Proof of principle," *Journal of Nuclear Medicine*, vol. 51, no. 4, pp. 639–645, 2010.
- [16] M. Petrik, H. Haas, M. Schrettel, A. Helbok, M. Blatzer, and C. Decristoforo, "In vitro and in vivo evaluation of selected ^{68}Ga -siderophores for infection imaging," *Nuclear Medicine and Biology*, vol. 39, no. 3, pp. 361–369, 2012.
- [17] M. Petrik, G. M. Franssen, H. Haas et al., "Preclinical evaluation of two ^{68}Ga -siderophores as potential radiopharmaceuticals for *Aspergillus fumigatus* infection imaging," *European Journal of Nuclear Medicine and Molecular Imaging*, vol. 39, no. 7, pp. 1175–1183, 2012.
- [18] A. Rizzello, D. Di Pierro, F. Lodi et al., "Synthesis and quality control of ^{68}Ga citrate for routine clinical PET," *Nuclear Medicine Communications*, vol. 30, no. 7, pp. 542–545, 2009.
- [19] C. Nanni, C. Errani, and L. Boriani, " ^{68}Ga -citrate PET/CT for evaluating patients with infections of the bone: preliminary results," *Journal of Nuclear Medicine*, vol. 51, no. 12, pp. 1932–1936, 2010.
- [20] S. S. Das, A. V. Hall, D. W. Wareham, and K. E. Britton, "Infection imaging with radiopharmaceuticals in the 21st century," *Brazilian Archives of Biology and Technology*, vol. 45, no. spe, pp. 25–37, 2002.
- [21] A. Signore and A. W. J. M. Glaudemans, "The molecular imaging approach to image infections and inflammation by nuclear medicine techniques," *Annals of Nuclear Medicine*, vol. 25, no. 10, pp. 681–700, 2011.
- [22] T. Yusa, K. Tateda, A. Ohara, and S. Miyazaki, "New possible biomarkers for diagnosis of infections and diagnostic distinction between bacterial and viral infections in children," *Journal of Infection and Chemotherapy*, vol. 23, no. 2, pp. 96–100, 2017.
- [23] A. Signore, A. W. J. M. Glaudemans, O. Gheysens, C. Lauri, and O. A. Catalano, "Nuclear Medicine Imaging in Pediatric Infection or Chronic Inflammatory Diseases," *Seminars in Nuclear Medicine*, vol. 47, no. 3, pp. 286–303, 2017.
- [24] I. Velikyan, "Molecular imaging and radiotherapy: Theranostics for personalized patient management," *Theranostics*, vol. 2, no. 5, pp. 424–426, 2012.
- [25] F. Rösch and R. P. Baum, "Generator-based PET radiopharmaceuticals for molecular imaging of tumours: On the way to THERANOSTICS," *Dalton Transactions*, vol. 40, no. 23, pp. 6104–6111, 2011.
- [26] R. P. Baum, H. R. Kulkarni, and C. Carreras, "Peptides and receptors in image-guided therapy: Theranostics for neuroendocrine neoplasms," *Seminars in Nuclear Medicine*, vol. 42, no. 3, pp. 190–207, 2012.
- [27] R. P. Baum and H. R. Kulkarni, "Theranostics: From molecular imaging using ^{68}Ga labeled tracers and PET/CT to personalized radionuclide therapy - the bad berka experience," *Theranostics*, vol. 2, no. 5, pp. 437–447, 2012.
- [28] I. Velikyan, "Radionuclides for Imaging and Therapy in Oncology," *Cancer Theranostics*, pp. 285–325, 2014.
- [29] J. Czernin and W. A. Weber, "Issues and controversies in nuclear medicine. Introduction," *Journal of Nuclear Medicine*, vol. 52, no. Supplement 2, pp. 1S–2S, 2011.
- [30] S. J. Goldsmith and S. Vallabhajosula, "Clinically proven radiopharmaceuticals for infection imaging: mechanisms and applications," *Seminars in Nuclear Medicine*, vol. 39, no. 1, pp. 2–10, 2009.
- [31] M. F. Tsan, "Mechanism of gallium-67 accumulation in inflammatory lesions," *Journal of Nuclear Medicine*, vol. 26, no. 1, pp. 88–92, 1985.
- [32] S. L. Kipper, "Radiolabelled leukocyte imaging of the abdomen," in *Nuclear Medicine Annual*, J. Freeman, Ed., pp. 81–126, Raven Press, New York, NY, USA, 1995.
- [33] F. Jamar, J. Buscombe, A. Chiti et al., "EANM/SNMMI guideline for ^{18}F -FDG use in inflammation and infection," *Journal of Nuclear Medicine*, vol. 54, no. 4, pp. 647–658, 2013.
- [34] C. J. Palestro, "The current role of gallium imaging in infection," *Seminars in Nuclear Medicine*, vol. 24, no. 2, pp. 128–141, 1994.
- [35] M. S. Akhtar, M. B. Imran, M. A. Nadeem, and A. Shahid, "Antimicrobial peptides as infection imaging agents: better than radiolabeled antibiotics," *International Journal of Peptides*, vol. 2012, Article ID 965238, 19 pages, 2012.
- [36] D. Delbeke and G. M. Segall, "Status of and trends in nuclear medicine in the United States," *Journal of Nuclear Medicine*, vol. 52, no. 2, 2011.
- [37] S. S. Gambhir, J. Czernin, J. Schwimmer, D. H. Silverman, R. E. Coleman, and M. E. Phelps, "A tabulated summary of the FDG PET literature," *Journal of Nuclear Medicine*, vol. 42, pp. 1S–93S, 2001.
- [38] M. J. Lindsay, B. A. Siegel, S. R. Tunis et al., "The National Oncologic PET Registry: Expanded Medicare coverage for PET under coverage with evidence development," *American Journal of Roentgenology*, vol. 188, no. 4, pp. 1109–1113, 2007.
- [39] F. Gemmel, H. Van Den Wyngaert, C. Love, M. M. Welling, P. Gemmel, and C. J. Palestro, "Prosthetic joint infections: radionuclide state-of-the-art imaging," *European Journal of Nuclear Medicine and Molecular Imaging*, vol. 39, no. 5, pp. 892–909, 2012.
- [40] J. Sörensen, "How does the patient benefit from clinical PET?" *Theranostics*, vol. 2, no. 5, pp. 427–436, 2012.
- [41] S. L. Rice, C. A. Roney, P. Daumar, and J. S. Lewis, "The next generation of positron emission tomography radiopharmaceuticals in oncology," *Seminars in Nuclear Medicine*, vol. 41, no. 4, pp. 265–282, 2011.
- [42] R. L. Wahl, J. M. Herman, and E. Ford, "The Promise and Pitfalls of Positron Emission Tomography and Single-Photon Emission Computed Tomography Molecular Imaging-Guided Radiation Therapy," *Seminars in Radiation Oncology*, vol. 21, no. 2, pp. 88–100, 2011.

- [43] A. W. J. M. Glaudemans, R. H. J. A. Slart, J. M. Van Dijk, M. Van Oosten, and G. M. Van Dam, "Molecular imaging of infectious and inflammatory diseases: A terra incognita," *Journal of Nuclear Medicine*, vol. 56, no. 5, pp. 659–661, 2015.
- [44] X. Li, W. Bauer, I. Israel et al., "Targeting p-selectin by gallium-68-labeled fucoidan positron emission tomography for noninvasive characterization of vulnerable plaques: Correlation with in vivo 17.6t mri," *Arteriosclerosis, Thrombosis, and Vascular Biology*, vol. 34, no. 8, pp. 1661–1667, 2014.
- [45] S. Eichendorff, P. Svendsen, D. Bender et al., "Biodistribution and PET Imaging of a Novel [⁶⁸Ga]-Anti-CD163-Antibody Conjugate in Rats with Collagen-Induced Arthritis and in Controls," *Molecular Imaging and Biology*, vol. 17, no. 1, pp. 87–93, 2014.
- [46] Z. Zhu, Y. Yin, K. Zheng et al., "Evaluation of synovial angiogenesis in patients with rheumatoid arthritis using 68Ga-PRGD2 PET/CT: A prospective proof-of-concept cohort study," *Annals of the Rheumatic Diseases*, vol. 73, no. 6, pp. 1269–1272, 2014.
- [47] J. S. Eo, J. C. Paeng, S. Lee et al., "Angiogenesis imaging in myocardial infarction using 68Ga-NOTA- RGD PET: Characterization and application to therapeutic efficacy monitoring in rats," *Coronary Artery Disease*, vol. 24, no. 4, pp. 303–311, 2013.
- [48] J. H. Kim, Y.-H. Kim, Y. J. Kim et al., "Quantitative positron emission tomography imaging of angiogenesis in rats with forelimb ischemia using 68Ga-NOTA-c(RGDyK)," *Angiogenesis*, vol. 16, no. 4, pp. 837–846, 2013.
- [49] I. Laitinen, J. Notni, K. Pohle et al., "Comparison of cyclic RGD peptides for $\alpha\beta3$ integrin detection in a rat model of myocardial infarction," *EJNMMI Research*, vol. 3, no. 1, pp. 1–9, 2013.
- [50] M. Kiugel, I. Dijkgraaf, V. Kytö et al., "Dimeric [⁶⁸Ga]DOTA-RGD Peptide Targeting $\alpha\beta3$ Integrin Reveals Extracellular Matrix Alterations after Myocardial Infarction," *Molecular Imaging and Biology*, vol. 16, no. 6, pp. 793–801, 2014.
- [51] M. Grönman, M. Tarkia, T. Kiviniemi et al., "Imaging of $\alpha\beta3$ integrin expression in experimental myocardial ischemia with [68Ga]NODAGA-RGD positron emission tomography," *Journal of Translational Medicine*, vol. 15, no. 1, p. 144, 2017.
- [52] J. Haukkala, I. Laitinen, P. Luoto et al., "68Ga-DOTA-RGD peptide: Biodistribution and binding into atherosclerotic plaques in mice," *European Journal of Nuclear Medicine and Molecular Imaging*, vol. 36, no. 12, pp. 2058–2067, 2009.
- [53] H. Virtanen, A. Autio, R. Siitonen et al., "68Ga-DOTA-Siglec-9 - a new imaging tool to detect synovitis," *Arthritis Research & Therapy*, vol. 17, no. 1, article no. 308, 2015.
- [54] J. Retamal, J. Sorensen, M. Lubberink et al., "Feasibility of (68) Ga-labeled Siglec-9 peptide for the imaging of acute lung inflammation: a pilot study in a porcine model of acute respiratory distress syndrome," *Am J Nucl Med Mol Imaging*, vol. 6, no. 1, pp. 18–31, 2016.
- [55] J. M. U. Silvola, H. Virtanen, R. Siitonen et al., "Leukocyte trafficking-associated vascular adhesion protein 1 is expressed and functionally active in atherosclerotic plaques," *Scientific Reports*, vol. 6, Article ID 35089, 2016.
- [56] H. Ahtinen, J. Kulkova, L. Lindholm et al., "68Ga-DOTA-Siglec-9 PET/CT imaging of peri-implant tissue responses and staphylococcal infections," *EJNMMI Research*, vol. 4, no. 1, article no. 45, pp. 1–11, 2014.
- [57] A. Autio, S. Jalkanen, and A. Roivainen, "Nuclear imaging of inflammation: Homing-associated molecules as targets," *EJNMMI Research*, vol. 3, no. 1, pp. 1–7, 2013.
- [58] J. T. Thackeray, T. Derlin, A. Haghikia et al., "Molecular Imaging of the Chemokine Receptor CXCR4 after Acute Myocardial Infarction," *JACC: Cardiovascular Imaging*, vol. 8, no. 12, pp. 1417–1426, 2015.
- [59] J. S. Schmid, A. Schirbel, A. K. Buck, S. Kropf, H.-J. Wester, and C. Lapa, "Pentixafor-Positron Emission Tomography/Computed Tomography Detects Chemokine Receptor CXCR4 Expression after Ischemic Stroke," *Circulation: Cardiovascular Imaging*, vol. 9, no. 9, Article ID e005217, 2016.
- [60] J. Zhou, G. Hao, H. Weng et al., "In vivo evaluation of medical device-associated inflammation using a macrophage-specific positron emission tomography (PET) imaging probe," *Bioorganic & Medicinal Chemistry Letters*, vol. 23, no. 7, pp. 2044–2047, 2013.
- [61] S. A. Kularatne, M.-J. Bélanger, X. Meng et al., "Comparative analysis of folate derived PET imaging agents with [18F]-2-fluoro-2-deoxy-d-glucose using a rodent inflammatory paw model," *Molecular Pharmaceutics*, vol. 10, no. 8, pp. 3103–3111, 2013.
- [62] V. Ambrosini, M. Zompatori, F. De Luca et al., "68Ga-DOTANOC PET/CT Allows Somatostatin Receptor Imaging in Idiopathic Pulmonary Fibrosis: Preliminary Results," *Journal of Nuclear Medicine*, vol. 51, no. 12, pp. 1950–1955, 2010.
- [63] T. Lincke, J. Singer, R. Kluge, O. Sabri, and R. Paschke, "Relative quantification of indium-111 pentetreotide and gallium-68 DOTATOC uptake in the thyroid gland and association with thyroid pathologies," *Thyroid*, vol. 19, no. 4, pp. 381–389, 2009.
- [64] A. Rominger, T. Saam, E. Vogl et al., "In vivo imaging of macrophage activity in the coronary arteries using 68Ga-DOTATATE PET/CT: correlation with coronary calcium burden and risk factors," *Journal of Nuclear Medicine*, vol. 51, no. 2, pp. 193–197, 2010.
- [65] J. M. Tarkin, F. R. Joshi, N. R. Evans et al., "Detection of Atherosclerotic Inflammation by 68Ga-DOTATATE PET Compared to [18F]FDG PET Imaging," *Journal of the American College of Cardiology*, vol. 69, no. 14, pp. 1774–1791, 2017.
- [66] S.-P. Lee, H.-J. Im, S. Kang et al., "Noninvasive imaging of myocardial inflammation in myocarditis using 68Ga-tagged mannoseylated human serum albumin positron emission tomography," *Theranostics*, vol. 7, no. 2, pp. 413–424, 2017.
- [67] Z. Zha, J. Song, S. R. Choi et al., "68Ga-Bivalent Polypegylated Styrylpyridine Conjugates for Imaging A β Plaques in Cerebral Amyloid Angiopathy," *Bioconjugate Chemistry*, vol. 27, no. 5, pp. 1314–1323, 2016.
- [68] H. Watanabe, M. Ono, S. Iikuni et al., "A 68Ga complex based on benzofuran scaffold for the detection of β -amyloid plaques," *Bioorganic & Medicinal Chemistry Letters*, vol. 24, no. 20, pp. 4834–4837, 2014.
- [69] D. Cressier, M. Dhilly, T. T. Cao Pham et al., "Gallium-68 Complexes Conjugated to Pittsburgh Compound B: Radiolabeling and Biological Evaluation," *Molecular Imaging and Biology*, vol. 18, no. 3, pp. 334–343, 2016.
- [70] D. Satpati, C. Arjun, R. Krishnamohan, G. Samuel, and S. Banerjee, "68Ga-labeled Ciprofloxacin Conjugates as Radiotracers for Targeting Bacterial Infection," *Chemical Biology & Drug Design*, vol. 87, no. 5, pp. 680–686, 2016.
- [71] T. Ebenhan, N. Chadwick, and M. M. Sathekge, "Peptide synthesis, characterization and 68Ga-radiolabeling of NOTA-conjugated ubiquitin fragments for prospective infection imaging with PET/CT," *Nuclear Medicine and Biology*, vol. 41, no. 5, pp. 390–400, 2014.

- [72] T. Ebenhan, J. R. Zeevaart, and J. D. Venter, "Preclinical evaluation of ^{68}Ga -labeled 1, 4, 7-triazacyclononane-1, 4, 7-triacetic acid-ubiquicidin as a radioligand for PET infection imaging," *Journal of Nuclear Medicine*, vol. 55, no. 2, pp. 308–314, 2014.
- [73] B. B. Mokalleng, T. Ebenhan, S. Ramesh et al., "Synthesis, ^{68}Ga -radiolabeling, and preliminary in vivo assessment of a depsipeptide-derived compound as a potential PET/CT infection imaging agent," *BioMed Research International*, vol. 2015, Article ID 284354, 2015.
- [74] T. Ebenhan, B. Mokalleng, J. Venter, H. Kruger, J. Zeevaart, and M. Sathekge, "Preclinical Assessment of a ^{68}Ga -DOTA-Functionalized Depsipeptide as a Radiodiagnostic Infection Imaging Agent," *Molecules*, vol. 22, no. 9, p. 1403, 2017.
- [75] S. Chopra, B. Singh, A. Koul, A. Mishra, and H. Wester, "Synthesis of DOTA conjugated GF-17 and RAWVAWR-NH₂ and radiolabeling with ^{68}Ga as a potential PET tracer for infection imaging," *J Nucl Med*, vol. 57, Supplement 2, p. 1115, 2016.
- [76] M. Petrik, H. Haas, P. Laverman et al., " ^{68}Ga -triacetylfusarinine C and ^{68}Ga -ferrioxamine e for aspergillus infection imaging: uptake specificity in various microorganisms," *Molecular Imaging and Biology*, vol. 16, no. 1, pp. 102–108, 2014.
- [77] V. Kumar and D. K. Boddeti, " ^{68}Ga -radiopharmaceuticals for PET imaging of infection and inflammation," *Recent Results in Cancer Research*, vol. 194, pp. 189–219, 2013.
- [78] M. Vorster, A. Maes, A. Jacobs et al., "Evaluating the possible role of ^{68}Ga -citrate PET/CT in the characterization of indeterminate lung lesions," *Annals of Nuclear Medicine*, vol. 28, no. 6, pp. 523–530, 2014.
- [79] M. Vorster, B. Mokalleng, M. M. Sathekge, and T. Ebenhan, "A modified technique for efficient radiolabeling of ^{68}Ga -citrate from a SnO₂-based $^{68}\text{Ge}/^{68}\text{Ga}$ generator for better infection imaging," *Hellenic Journal of Nuclear Medicine*, vol. 16, no. 3, pp. 193–198, 2013.
- [80] S. Salomaeki, J. Kemppainen, U. Hohenthal et al., "Head-to-head comparison of ^{68}Ga -Citrate and ^{18}F -FDG PET/CT for detection of infectious foci in patients with staphylococcus aureus bacteraemia," *Contrast Media & Molecular Imaging*, vol. 2017, p. 8, 2017.
- [81] L. Fass, "Imaging and cancer: a review," *Molecular Oncology*, vol. 2, no. 2, pp. 115–152, 2008.
- [82] A. Chopra, L. Shan, W. C. Eckelman et al., "Molecular imaging and contrast agent database (MICAD): Evolution and progress," *Molecular Imaging and Biology*, vol. 14, no. 1, pp. 4–13, 2012.
- [83] A. Sánchez-Crespo, P. Andreo, and S. A. Larsson, "Positron flight in human tissues and its influence on PET image spatial resolution," *European Journal of Nuclear Medicine and Molecular Imaging*, vol. 31, no. 1, pp. 44–51, 2004.
- [84] H. W. A. M. De Jong, L. Perk, G. W. M. Visser, R. Boellaard, G. A. M. S. Van Dongen, and A. A. Lammertsma, "High resolution PET imaging characteristics of ^{68}Ga , ^{124}I and ^{89}Zr compared to ^{18}F ," in *Proceedings of the Nuclear Science Symposium Conference Record, 2005 IEEE*, pp. 1624–1627, Puerto Rico, October 2005.
- [85] I. Velikyan, A. Sundin, B. Eriksson et al., "In vivo binding of [^{68}Ga]-DOTATOC to somatostatin receptors in neuroendocrine tumours - impact of peptide mass," *Nuclear Medicine and Biology*, vol. 37, no. 3, pp. 265–275, 2010.
- [86] U. Eberlein and M. Lassmann, "Dosimetry of [^{68}Ga]-labeled compounds," *Applied Radiation and Isotopes*, vol. 76, pp. 70–74, 2013.
- [87] C. Pettinato, A. Sarnelli, M. Di Donna et al., " ^{68}Ga -DOTANOC: Biodistribution and dosimetry in patients affected by neuroendocrine tumors," *European Journal of Nuclear Medicine and Molecular Imaging*, vol. 35, no. 1, pp. 72–79, 2008.
- [88] B. P. Burke, G. S. Clemente, and S. J. Archibald, "Recent advances in chelator design and labelling methodology for ^{68}Ga radiopharmaceuticals," *Journal of Labelled Compounds and Radiopharmaceuticals*, vol. 57, no. 4, pp. 239–243, 2014.
- [89] I. Velikyan, U. Rosenström, S. Estrada et al., "Synthesis and preclinical evaluation of ^{68}Ga -labeled collagelin analogs for imaging and quantification of fibrosis," *Nuclear Medicine and Biology*, vol. 41, no. 9, pp. 728–736, 2014.
- [90] M. F. Ferreira, G. Pereira, J. P. André, and et al C., "Ga[NO₂A-N-(α -amino)propionate] chelates: Synthesis and evaluation as potential tracers for ^{68}Ga PET," *Dalton Transactions*, vol. 43, no. 21, pp. 8037–8047, 2014.
- [91] J. Notni, J. Šimeček, and H.-J. Wester, "Phosphinic acid functionalized polyazacycloalkane chelators for radiodiagnostics and radiotherapeutics: Unique characteristics and applications," *ChemMedChem*, vol. 9, no. 6, pp. 1107–1115, 2014.
- [92] J. Šimeček, O. Zemek, P. Hermann, J. Notni, and H. J. Wester, "Tailored gallium(III) chelator NOPO: synthesis, characterization, bioconjugation, and application in preclinical Ga- ^{68}Ga -PET imaging," *Molecular Pharmaceutics*, 2013.
- [93] D. Parker, B. P. Waldron, and D. S. Yufit, "Crystallographic and solution NMR structural analyses of four hexacoordinated gallium(III) complexes based on ligands derived from 6-amino-perhydro-1,4-diazepine," *Dalton Transactions*, vol. 42, no. 22, pp. 8001–8008, 2013.
- [94] B. P. Waldron, D. Parker, C. Burchardt, D. S. Yufit, M. Zimny, and F. Roesch, "Structure and stability of hexadentate complexes of ligands based on AAZTA for efficient PET labelling with gallium- 68 ," *Chemical Communications*, vol. 49, no. 6, pp. 579–581, 2013.
- [95] D. Parker and B. P. Waldron, "Conformational analysis and synthetic approaches to polydentate perhydro-diazepine ligands for the complexation of gallium(III)," *Organic & Biomolecular Chemistry*, vol. 11, no. 17, pp. 2827–2838, 2013.
- [96] I. Velikyan, H. Maecke, and B. Langstrom, "Convenient preparation of ^{68}Ga -based PET-radiopharmaceuticals at room temperature," *Bioconjugate Chemistry*, vol. 19, no. 2, pp. 569–573, 2008.
- [97] J. Erchevyi, R. Cescato, B. Waser, J. E. Rivier, and J. C. Reubi, "N-Imidazolebenzyl-histidine substitution in somatostatin and in its octapeptide analogue modulates receptor selectivity and function," *Journal of Medicinal Chemistry*, vol. 54, no. 17, pp. 5981–5987, 2011.
- [98] R. Saha, N. Saha, R. S. Donofrio, and L. L. Bestervelt, "Microbial siderophores: A mini review," *Journal of Basic Microbiology*, vol. 53, no. 4, pp. 303–317, 2013.
- [99] V. Nikolova, S. Angelova, N. Markova, and T. Dudev, "Gallium as a Therapeutic Agent: A Thermodynamic Evaluation of the Competition between Ga³⁺ and Fe³⁺ Ions in Metalloproteins," *The Journal of Physical Chemistry B*, vol. 120, no. 9, pp. 2241–2248, 2016.
- [100] C. R. Chitambar, "Gallium and its competing roles with iron in biological systems," *Biochimica et Biophysica Acta (BBA) - Molecular Cell Research*, vol. 1863, no. 8, pp. 2044–2053, 2016.
- [101] J. A. Lessa, M. A. Soares, and R. G. dos Santos, "Gallium(III) complexes with 2-acetylpyridine-derived thiosemicarbazones: antimicrobial and cytotoxic effects and investigation on the interactions with tubulin," *BioMetals*, vol. 26, pp. 151–165, 2013.

- [102] M. van Oosten, M. Hahn, L. M. A. Crane et al., "Targeted imaging of bacterial infections: Advances, hurdles and hopes," *FEMS Microbiology Reviews*, vol. 39, no. 6, pp. 892–916, 2015.
- [103] M. Vorster, A. Maes, C. V. D. Wiele, and M. Sathekge, "Gallium-68 PET: A Powerful Generator-based Alternative to Infection and Inflammation Imaging," *Seminars in Nuclear Medicine*, vol. 46, no. 5, pp. 436–447, 2016.
- [104] M. Kircher and C. Lapa, "Novel Noninvasive Nuclear Medicine Imaging Techniques for Cardiac Inflammation," *Current Cardiovascular Imaging Reports*, vol. 10, no. 2, article no. 6, 2017.
- [105] D. A. Hammoud, "Molecular imaging of inflammation: Current status," *Journal of Nuclear Medicine*, vol. 57, no. 8, pp. 1161–1165, 2016.
- [106] D. R. Brenner, D. Scherer, K. Muir et al., "A review of the application of inflammatory biomarkers in epidemiologic cancer research," *Cancer Epidemiology, Biomarkers & Prevention*, vol. 23, no. 9, pp. 1729–1751, 2014.
- [107] M. D. Turner, B. Nedjai, T. Hurst, and D. J. Pennington, "Cytokines and chemokines: at the crossroads of cell signalling and inflammatory disease," *Biochimica et Biophysica Acta (BBA) - Molecular Cell Research*, vol. 1843, no. 11, pp. 2563–2582, 2014.
- [108] L. Werner, H. Guzner-Gur, and I. Dotan, "Involvement of CXCR4/CXCR7/CXCL12 interactions in inflammatory bowel disease," *Theranostics*, vol. 3, no. 1, pp. 40–46, 2013.
- [109] S. Jalkanen and M. Salmi, "VAP-1 and CD73, endothelial cell surface enzymes in leukocyte extravasation," *Arteriosclerosis, Thrombosis, and Vascular Biology*, vol. 28, no. 1, pp. 18–26, 2008.
- [110] G. Malviya, F. Galli, I. Sonni, and A. Signore, "Imaging T-lymphocytes in inflammatory diseases: A nuclear medicine approach," *The Quarterly Journal of Nuclear Medicine and Molecular Imaging*, vol. 58, no. 3, pp. 237–257, 2014.
- [111] S. Gratz, H. J. Rennen, O. C. Boerman, W. J. Oyen, and P. Burma, "(99m)Tc-interleukin-8 for imaging acute osteomyelitis," *Journal of Nuclear Medicine*, vol. 42, no. 8, pp. 1257–1264, 2001.
- [112] S. Gratz, H. J. Rennen, O. C. Boerman, W. J. Oyen, and F. H. Corstens, "Rapid imaging of experimental colitis with (99m)Tc-interleukin-8 in rabbits," *Journal of Nuclear Medicine*, vol. 42, no. 6, pp. 917–923, 2001.
- [113] C. Alkim, H. Alkim, A. R. Koksall, S. Boga, and I. Sen, "Angiogenesis in inflammatory bowel disease," *International Journal of Inflammation*, vol. 2015, Article ID 970890, 2015.
- [114] I. S. Alam, T. H. Witney, G. Tomasi et al., "Radiolabeled RGD tracer kinetics annotates differential $\alpha\beta 3$ integrin expression linked to cell intrinsic and vessel expression," *Molecular Imaging and Biology*, vol. 16, no. 4, pp. 558–566, 2014.
- [115] J. Notni, K. Pohle, and H.-J. Wester, "Be spoiled for choice with radiolabelled RGD peptides: Preclinical evaluation of ^{68}Ga -TRAP(RGD) $_3$," *Nuclear Medicine and Biology*, vol. 40, no. 1, pp. 33–41, 2013.
- [116] J. Oxboel, M. Brandt-Larsen, C. Schjoeth-Eskesen et al., "Comparison of two new angiogenesis PET tracers ^{68}Ga -NODAGA-E[c(RGDyK)] $_2$ and ^{64}Cu -NODAGA-E[c(RGDyK)] $_2$; in vivo imaging studies in human xenograft tumors," *Nuclear Medicine and Biology*, vol. 41, no. 3, pp. 259–267, 2014.
- [117] J. Šimeček, J. Notni, T. G. Kapp, H. Kessler, and H.-J. Wester, "Benefits of NOPO as chelator in gallium-68 peptides, exemplified by preclinical characterization of ^{68}Ga -NOPO-c(RGDfK)," *Molecular Pharmaceutics*, vol. 11, no. 5, pp. 1687–1695, 2014.
- [118] M. Trajkovic-Arsic, P. Mohajerani, A. Sarantopoulos et al., "Multimodal molecular imaging of integrin $\alpha\beta 3$ for in vivo detection of pancreatic cancer," *Journal of Nuclear Medicine*, vol. 55, no. 3, pp. 446–451, 2014.
- [119] H. Cai and P. S. Conti, "RGD-based PET tracers for imaging receptor integrin $\alpha\beta 3$ expression," *Journal of Labelled Compounds and Radiopharmaceuticals*, vol. 56, no. 5, pp. 264–279, 2013.
- [120] I. Dijkgraaf, S. Y. A. Terry, W. J. McBride et al., "Imaging integrin $\alpha\text{-v}\beta\text{-3}$ expression in tumors with an ^{18}F -labeled dimeric RGD peptide," *Contrast Media & Molecular Imaging*, vol. 8, no. 3, pp. 238–245, 2013.
- [121] P. A. Knetsch, M. Petrik, C. Rangger et al., "[^{68}Ga]NS3-RGD and [^{68}Ga]Oxo-DO3A-RGD for imaging $\alpha\beta 3$ integrin expression: Synthesis, evaluation, and comparison," *Nuclear Medicine and Biology*, vol. 40, no. 1, pp. 65–72, 2013.
- [122] Z. Liu and F. Wang, "Development of RGD-based radiotracers for tumor imaging and therapy: Translating from bench to bedside," *Current Molecular Medicine*, vol. 13, no. 10, pp. 1487–1505, 2013.
- [123] H. Choi, J. H. Phi, J. C. Paeng et al., "Imaging of integrin $\alpha\beta 3$ expression using ^{68}Ga -RGD positron emission tomography in pediatric cerebral infarct," *Molecular Imaging*, vol. 12, no. 4, pp. 213–217, 2013.
- [124] H.-J. Yoon, K. W. Kang, I. K. Chun et al., "Correlation of breast cancer subtypes, based on estrogen receptor, progesterone receptor, and HER2, with functional imaging parameters from ^{68}Ga -RGD PET/CT and ^{18}F -FDG PET/CT," *European Journal of Nuclear Medicine and Molecular Imaging*, vol. 41, no. 8, pp. 1534–1543, 2014.
- [125] R. P. Baum, H. R. Kulkarni, D. Müller et al., "First-in-human study demonstrating tumor-angiogenesis by PET/CT imaging with ^{68}Ga -NODAGA-THERANOST, a high-affinity peptidomimetic for $\alpha\beta 3$ integrin receptor targeting," *Cancer Biotherapy and Radiopharmaceuticals*, vol. 30, no. 4, pp. 152–159, 2015.
- [126] R. Haubner, A. Finkenstedt, A. Stegmayr et al., "[^{68}Ga]NODAGA-RGD – Metabolic stability, biodistribution, and dosimetry data from patients with hepatocellular carcinoma and liver cirrhosis," *European Journal of Nuclear Medicine and Molecular Imaging*, vol. 43, no. 11, pp. 2005–2013, 2016.
- [127] V. López-Rodríguez, C. Galindo-Sarco, F. O. García-Pérez, G. Ferro-Flores, O. Arrieta, and M. A. Ávila-Rodríguez, "PET-based human dosimetry of the dimeric $\alpha\beta 3$ integrin ligand ^{68}Ga -DOTA-E-[c(RGDfK)] $_2$, a potential tracer for imaging tumor angiogenesis," *Journal of Nuclear Medicine*, vol. 57, no. 3, pp. 404–409, 2016.
- [128] M. V. Backer, Z. Levashova, V. Patel et al., "Molecular imaging of VEGF receptors in angiogenic vasculature with single-chain VEGF-based probes," *Nature Medicine*, vol. 13, no. 4, pp. 504–509, 2007.
- [129] M. V. Backer, Z. Levashova, R. Levenson, F. G. Blankenberg, and J. M. Backer, "Cysteine-containing fusion tag for site-specific conjugation of therapeutic and imaging agents to targeting proteins," *Methods in Molecular Biology (Clifton, N.J.)*, vol. 494, pp. 275–294, 2008.
- [130] M. Eder, A. V. Krivoshein, M. Backer, J. M. Backer, U. Haberkorn, and M. Eisenhut, "scVEGF-PEG-HBED-CC and scVEGF-PEG-NOTA conjugates: comparison of easy-to-label recombinant proteins for [^{68}Ga]PET imaging of VEGF receptors in angiogenic vasculature," *Nuclear Medicine and Biology*, vol. 37, no. 4, pp. 405–412, 2010.
- [131] E. Blom, I. Velikyan, A. Monazzam, P. Razifar et al., "Synthesis and characterization of scVEGF-PEG-[^{68}Ga]NOTA and scVEGF-PEG-[^{68}Ga]DOTA PET tracers," *Journal of Labelled*

- Compounds and Radiopharmaceuticals*, vol. 54, no. 11, pp. 685–692, 2011.
- [132] S. Gratz, M. Béhé, and O. C. Boerman, “ ^{99m}Tc -E-selectin binding peptide for imaging acute osteomyelitis in a novel rat model,” *Nuclear Medicine Communications*, vol. 22, no. 9, pp. 1003–1013, 2001.
- [133] S. B. Jensen, M. Käkälä, L. Jødal et al., “Exploring the radiosynthesis and in vitro characteristics of $[68\text{Ga}]\text{Ga}$ -DOTA-Siglec-9,” *Journal of Labelled Compounds and Radiopharmaceuticals*, vol. 60, no. 9, pp. 439–449, 2017.
- [134] B. A. Teicher and S. P. Fricker, “CXCL12 (SDF-1)/CXCR4 pathway in cancer,” *Clinical Cancer Research*, vol. 16, no. 11, pp. 2927–2931, 2010.
- [135] O. Jacobson, I. D. Weiss, D. O. Kiesewetter, J. M. Farber, and X. Chen, “PET of tumor CXCR4 expression with 4-18F-T140,” *Journal of Nuclear Medicine*, vol. 51, no. 11, pp. 1796–1804, 2010.
- [136] A. Aghanejad, A. R. Jalilian, Y. Fazaeli et al., “Synthesis and evaluation of $[67\text{Ga}]\text{-AMD3100}$: A novel imaging agent for targeting the chemokine receptor CXCR4,” *Scientia Pharmaceutica*, vol. 82, no. 1, pp. 29–42, 2014.
- [137] O. Jacobson, I. D. Weiss, L. P. Szajek et al., “PET imaging of CXCR4 using copper-64 labeled peptide antagonist,” *Theranostics*, vol. 1, pp. 251–262, 2011.
- [138] O. Jacobson, I. D. Weiss, L. P. Szajek et al., “Improvement of CXCR4 tracer specificity for PET imaging,” *Journal of Controlled Release*, vol. 157, no. 2, pp. 216–223, 2012.
- [139] H. J. Wester, U. Keller, M. Schottelius et al., “Disclosing the CXCR4 expression in lymphoproliferative diseases by targeted molecular imaging,” *Theranostics*, vol. 5, no. 6, pp. 618–630, 2015.
- [140] E. Gourni, O. Demmer, M. Schottelius et al., “PET of CXCR4 expression by a 68Ga -labeled highly specific targeted contrast agent,” *Journal of Nuclear Medicine*, vol. 52, no. 11, pp. 1803–1810, 2011.
- [141] O. Demmer, I. Dijkgraaf, U. Schumacher et al., “Design, synthesis, and functionalization of dimeric peptides targeting chemokine receptor CXCR4,” *Journal of Medicinal Chemistry*, vol. 54, no. 21, pp. 7648–7662, 2011.
- [142] O. Demmer, E. Gourni, U. Schumacher, H. Kessler, and H.-J. Wester, “PET Imaging of CXCR4 Receptors in Cancer by a New Optimized Ligand,” *ChemMedChem*, vol. 6, no. 10, pp. 1789–1791, 2011.
- [143] U. Hennrich, L. Seyler, M. Schäfer et al., “Synthesis and in vitro evaluation of 68Ga -DOTA-4-FBn-TN14003, a novel tracer for the imaging of CXCR4 expression,” *Bioorganic & Medicinal Chemistry*, vol. 20, no. 4, pp. 1502–1510, 2012.
- [144] G. P. C. George, E. Stevens, O. Åberg et al., “Preclinical evaluation of a CXCR4-specific 68Ga -labelled TN14003 derivative for cancer PET imaging,” *Bioorganic & Medicinal Chemistry*, vol. 22, no. 2, pp. 796–803, 2014.
- [145] S. Poty, E. Gourni, P. Désogère et al., “AMD3100: A Versatile Platform for CXCR4 Targeting 68Ga -Based Radiopharmaceuticals,” *Bioconjugate Chemistry*, vol. 27, no. 3, pp. 752–761, 2016.
- [146] K. Philipp-Abbrederis, K. Herrmann, S. Knop et al., “In vivo molecular imaging of chemokine receptor CXCR4 expression in patients with advanced multiple myeloma,” *EMBO Molecular Medicine*, vol. 7, no. 4, pp. 477–487, 2015.
- [147] Z. Wang, M. Zhang, L. Wang et al., “Prospective study of 68Ga -NOTA-NFB: Radiation dosimetry in healthy volunteers and first application in glioma patients,” *Theranostics*, vol. 5, no. 8, pp. 882–889, 2015.
- [148] I. M. Jackson, P. J. Scott, and S. Thompson, “Clinical Applications of Radiolabeled Peptides for PET,” *Seminars in Nuclear Medicine*, vol. 47, no. 5, pp. 493–523, 2017.
- [149] C. Lapa, T. Reiter, R. A. Werner et al., “[68Ga]Pentixafor-PET/CT for Imaging of Chemokine Receptor 4 Expression after Myocardial Infarction,” *JACC: Cardiovascular Imaging*, vol. 8, no. 12, pp. 1466–1468, 2015.
- [150] C. Rischpler, S. G. Nekolla, H. Kossmann et al., “Upregulated myocardial CXCR4-expression after myocardial infarction assessed by simultaneous 68Ga -pentixafor PET/MRI,” *Journal of Nuclear Cardiology*, vol. 23, no. 1, pp. 131–133, 2016.
- [151] F. Hyafil, J. Pelisek, I. Laitinen et al., “Imaging the Cytokine Receptor CXCR4 in atherosclerotic plaques with the radiotracer 68Ga -Pentixafor for PET,” *Journal of Nuclear Medicine*, vol. 58, no. 3, pp. 499–506, 2017.
- [152] Y. Yi, “Folate receptor-targeted diagnostics and therapeutics for inflammatory diseases,” *Immune Network*, vol. 16, no. 6, pp. 337–343, 2016.
- [153] C. M. Paulos, M. J. Turk, G. J. Breur, and P. S. Low, “Folate receptor-mediated targeting of therapeutic and imaging agents to activated macrophages in rheumatoid arthritis,” *Advanced Drug Delivery Reviews*, vol. 56, no. 8, pp. 1205–1217, 2004.
- [154] W. Han, R. Zaynagetdinov, F. E. Yull et al., “Molecular imaging of folate receptor β -positive macrophages during acute lung inflammation,” *American Journal of Respiratory Cell and Molecular Biology*, vol. 53, no. 1, pp. 50–59, 2015.
- [155] B. Kühle, C. Müller, and T. L. Ross, “A Novel 68Ga -Labeled pteric acid-based PET tracer for tumor imaging via the folate receptor,” *Recent Results in Cancer Research*, vol. 194, pp. 257–267, 2013.
- [156] C. Brand, V. A. Longo, M. Groaning, W. A. Weber, and T. Reiner, “Development of a New Folate-Derived 68Ga -Based PET Imaging Agent,” *Molecular Imaging and Biology*, vol. 19, no. 5, pp. 754–761, 2017.
- [157] M. Fani, X. Wang, G. Nicolas et al., “Development of new folate-based PET radiotracers: Preclinical evaluation of 68Ga -DOTA-folate conjugates,” *European Journal of Nuclear Medicine and Molecular Imaging*, vol. 38, no. 1, pp. 108–119, 2011.
- [158] C. J. Mathias, M. R. Lewis, D. E. Reichert et al., “Preparation of 66Ga - and 68Ga -labeled Ga(III) -deferoxamine-folate as potential folate-receptor-targeted PET radiopharmaceuticals,” *Nuclear Medicine and Biology*, vol. 30, no. 7, pp. 725–731, 2003.
- [159] S.-M. Kim, N. Choi, S. Hwang et al., “Folate receptor-specific positron emission tomography imaging with folic acid-conjugated tissue inhibitor of metalloproteinase-2,” *Bulletin of the Korean Chemical Society*, vol. 34, no. 11, pp. 3243–3248, 2013.
- [160] M. Fani, M.-L. Tamma, G. P. Nicolas et al., “In vivo imaging of folate receptor positive tumor xenografts using novel 68Ga -NODAGA-folate conjugates,” *Molecular Pharmaceutics*, vol. 9, no. 5, pp. 1136–1145, 2012.
- [161] C. Müller and R. Schibli, “Prospects in folate receptor-targeted radionuclide therapy,” *Frontiers in Oncology*, vol. 3, Article ID Article 249, 2013.
- [162] A. Jain, A. Mathur, U. Pandey et al., “Synthesis and evaluation of a 68Ga labeled folic acid derivative for targeting folate receptors,” *Applied Radiation and Isotopes*, vol. 116, pp. 77–84, 2016.
- [163] W. Xia, A. R. Hilgenbrink, E. L. Matteson, M. B. Lockwood, J.-X. Cheng, and P. S. Low, “A functional folate receptor is induced during macrophage activation and can be used to target drugs to activated macrophages,” *Blood*, vol. 113, no. 2, pp. 438–446, 2009.

- [164] E. P. Krenning, W. A. P. Breeman, P. P. M. Kooij et al., "Localisation of endocrine-related tumours with radioiodinated analogue of somatostatin," *The Lancet*, vol. 1, no. 8632, pp. 242–244, 1989.
- [165] E. P. Krenning, D. J. Kwekkeboom, W. H. Bakker et al., "Somatostatin receptor scintigraphy with [¹¹¹In-DTPA-d-Phe¹]- and [¹²³I-Tyr³]-octreotide: the Rotterdam experience with more than 1000 patients," *European Journal of Nuclear Medicine and Molecular Imaging*, vol. 20, no. 8, pp. 716–731, 1993.
- [166] A. Stahl, G. Meisetschläger, M. Schottelius et al., "[¹²³I]Mtr-TOCA, a radioiodinated and carbhydrated analogue of octreotide: Scintigraphic comparison with [¹¹¹In]octreotide," *European Journal of Nuclear Medicine and Molecular Imaging*, vol. 33, no. 1, pp. 45–52, 2006.
- [167] R. Lebtahi, J. le Cloirec, C. Houzard et al., "Detection of neuroendocrine tumors: ^{99m}Tc-P829 scintigraphy compared with ¹¹¹In-pentetreotide scintigraphy," *Journal of Nuclear Medicine*, vol. 43, no. 7, pp. 889–895, 2002.
- [168] C. Decristoforo, T. Maina, B. Nock, M. Gabriel, P. Cordopatis, and R. Moncayo, "99mTc-demotate 1: First data in tumour patients - Results of a pilot/phase I study," *European Journal of Nuclear Medicine and Molecular Imaging*, vol. 30, no. 9, pp. 1211–1219, 2003.
- [169] C. Decristoforo, S. J. Mather, W. Cholewinski, E. Donnemiller, G. Riccabona, and R. Moncayo, "(99m)Tc-EDDA/HYNIC-TOC: A new (99m)Tc-labelled radiopharmaceutical for imaging somatostatin receptor-positive tumours: First clinical results and intra-patient comparison with ¹¹¹In-labelled octreotide derivatives," *European Journal of Nuclear Medicine and Molecular Imaging*, vol. 27, no. 9, pp. 1318–1325, 2000.
- [170] A. Hubalewska-Dydejczyk, K. Fröss-Baron, R. Mikołajczak et al., "99mTc-EDDA/HYNIC-octreotate scintigraphy, an efficient method for the detection and staging of carcinoid tumours: Results of 3 years' experience," *European Journal of Nuclear Medicine and Molecular Imaging*, vol. 33, no. 10, pp. 1123–1133, 2006.
- [171] M. Bangard, M. Béhé, S. Guhlke et al., "Detection of somatostatin receptor-positive tumours using the new 99mTc-tricine-HYNIC-D-Phe¹-Tyr³-octreotide: First results in patients and comparison with ¹¹¹In-DTPA-D-Phe¹-octreotide," *European Journal of Nuclear Medicine and Molecular Imaging*, vol. 27, no. 6, pp. 628–637, 2000.
- [172] A. Helisch, G. J. Förster, H. Reber et al., "Pre-therapeutic dosimetry and biodistribution of ⁸⁶Y-DOTA-Phe¹-Tyr³-octreotide versus ¹¹¹In-pentetreotide in patients with advanced neuroendocrine tumours," *European Journal of Nuclear Medicine and Molecular Imaging*, vol. 31, no. 10, pp. 1386–1392, 2004.
- [173] M. Henze, J. Schuhmacher, P. Hipp et al., "PET imaging of somatostatin receptors using [⁶⁸Ga]DOTA-D-Phe¹-Tyr³-Octreotide: First results in patients with meningiomas," *Journal of Nuclear Medicine*, vol. 42, no. 7, pp. 1053–1056, 2001.
- [174] I. Kayani, J. B. Bomanji, A. Groves et al., "Functional imaging of neuroendocrine tumors with combined PET/CT using ⁶⁸Ga-DOTATATE (Dota-DPhe¹, Tyr³-octreotate) and ¹⁸F-FDG," *Cancer*, vol. 112, no. 11, pp. 2447–2455, 2008.
- [175] A. Al-Nahhas, "Nuclear medicine imaging of neuroendocrine tumours," *Clinical Medicine*, vol. 12, no. 4, pp. 377–380, 2012.
- [176] V. Ambrosini, S. Nicolini, P. Caroli et al., "PET/CT imaging in different types of lung cancer: an overview," *European Journal of Radiology*, vol. 81, no. 5, pp. 988–1001, 2012.
- [177] V. Ambrosini, D. Campana, P. Tomassetti, and S. Fanti, "⁶⁸Ga-labelled peptides for diagnosis of gastroenteropancreatic NET," *European Journal of Nuclear Medicine and Molecular Imaging*, vol. 39, no. 1, pp. S52–S60, 2012.
- [178] K. E. Oberg, J.-C. Reubi, D. J. Kwekkeboom, and E. P. Krenning, "Role of somatostatins in gastroenteropancreatic neuroendocrine tumor development and therapy," *Gastroenterology*, vol. 139, no. 3, pp. 753–753, 2010.
- [179] K. Öberg, "Gallium-68 somatostatin receptor PET/CT: Is it time to replace ¹¹¹Indium DTPA octreotide for patients with neuroendocrine tumors?" *Endocrine Journal*, vol. 42, no. 1, pp. 3–4, 2012.
- [180] R. Srirajakanthan, I. Kayani, A. M. Quigley, J. Soh, M. E. Caplin, and J. Bomanji, "The role of ⁶⁸Ga-DOTATATE PET in patients with neuroendocrine tumors and negative or equivocal findings on ¹¹¹In-DTPA-octreotide scintigraphy," *Journal of Nuclear Medicine*, vol. 51, no. 6, pp. 875–882, 2010.
- [181] A. Kroiss, D. Putzer, and C. Uprimny, "Functional imaging in pheochromocytoma and neuroblastoma with ⁶⁸Ga-DOTA-Tyr³-octreotide positron emission tomography and ¹²³I-metaiodobenzylguanidine," *European Journal of Nuclear Medicine and Molecular Imaging*, vol. 38, no. 5, pp. 865–873, 2011.
- [182] M. Naji, C. Zhao, S. J. Welsh et al., "⁶⁸Ga-DOTA-TATE PET vs. ¹²³I-MIBG in identifying malignant neural crest tumours," *Molecular Imaging and Biology*, vol. 13, no. 4, pp. 769–775, 2011.
- [183] V. Ambrosini, P. Tomassetti, P. Castellucci et al., "Comparison between ⁶⁸Ga-DOTA-NOC and ¹⁸F-DOPA PET for the detection of gastro-entero-pancreatic and lung neuro-endocrine tumours," *European Journal of Nuclear Medicine and Molecular Imaging*, vol. 35, no. 8, pp. 1431–1438, 2008.
- [184] D. Putzer, M. Gabriel, B. Henninger et al., "Bone metastases in patients with neuroendocrine tumor: ⁶⁸Ga-DOTA-Tyr³-octreotide PET in comparison to CT and bone scintigraphy," *Journal of Nuclear Medicine*, vol. 50, no. 8, pp. 1214–1221, 2009.
- [185] L. K. Anzola-Fuentes, M. Chianelli, F. Galli et al., "Somatostatin receptor scintigraphy in patients with rheumatoid arthritis and secondary Sjögren's syndrome treated with Infliximab: a pilot study," *EJNMMI Research*, vol. 6, no. 1, article no. 49, 2016.
- [186] T. Nobashi, Y. Nakamoto, T. Kubo et al., "The utility of PET/CT with ⁶⁸Ga-DOTATOC in sarcoidosis: comparison with ⁶⁷Ga-scintigraphy," *Annals of Nuclear Medicine*, vol. 30, no. 8, pp. 544–552, 2016.
- [187] C. Boy, T. A. Heusner, T. D. Poeppel et al., "⁶⁸Ga-DOTATOC PET/CT and somatostatin receptor (sst1-sst5) expression in normal human tissue: Correlation of sst2 mRNA and SUV max," *European Journal of Nuclear Medicine and Molecular Imaging*, vol. 38, no. 7, pp. 1224–1236, 2011.
- [188] P. Rinne, S. Hellberg, M. Kiugel et al., "Comparison of Somatostatin Receptor 2-Targeting PET Tracers in the Detection of Mouse Atherosclerotic Plaques," *Molecular Imaging and Biology*, vol. 18, no. 1, pp. 99–108, 2016.
- [189] M. Asti, E. Ferrari, S. Croci et al., "Synthesis and characterization of ⁶⁸Ga-labeled curcumin and curcuminoid complexes as potential radiotracers for imaging of cancer and alzheimers disease," *Inorganic Chemistry*, vol. 53, no. 10, pp. 4922–4933, 2014.
- [190] A. Signore, I. Santino, and A. W. J. M. Glaudemans, "In vivo imaging of microorganisms," *Clinical and Translational Imaging*, vol. 4, no. 3, pp. 161–162, 2016.
- [191] S. Auletta, F. Galli, C. Lauri, D. Martinelli, I. Santino, and A. Signore, "Imaging bacteria with radiolabelled quinolones,

- cephalosporins and siderophores for imaging infection: a systematic review," *Clinical and Translational Imaging*, vol. 4, no. 4, pp. 229–252, 2016.
- [192] X. Ning, S. Lee, Z. Wang et al., "Maltodextrin-based imaging probes detect bacteria in vivo with high sensitivity and specificity," *Nature Materials*, vol. 10, no. 8, pp. 602–607, 2011.
- [193] J. Ady and Y. Fong, "Imaging for infection: From visualization of inflammation to visualization of microbes," *Surgical Infections*, vol. 15, no. 6, pp. 700–707, 2014.
- [194] J. M. Sierra, D. Rodriguez-Puig, A. Soriano, J. Mensa, C. Piera, and J. Vila, "Accumulation of 99mTc-ciprofloxacin in *Staphylococcus aureus* and *Pseudomonas aeruginosa*," *Antimicrobial Agents and Chemotherapy*, vol. 52, no. 7, pp. 2691–2692, 2008.
- [195] D. I. Andersson and D. Hughes, "Microbiological effects of sublethal levels of antibiotics," *Nature Reviews Microbiology*, vol. 12, no. 7, pp. 465–478, 2014.
- [196] N. Dumarey, D. Blocklet, T. Appelboom, L. Tant, and A. Schoutens, "Infecton is not specific for bacterial osteo-articular infective pathology," *European Journal of Nuclear Medicine and Molecular Imaging*, vol. 29, no. 4, pp. 530–535, 2002.
- [197] K. E. Britton, D. W. Wareham, S. S. Das et al., "Imaging bacterial infection with 99mTc-ciprofloxacin (Infecton)," *Journal of Clinical Pathology*, vol. 55, no. 11, pp. 817–823, 2002.
- [198] G. Ferro-Flores, M. A. Avila-Rodríguez, and F. O. García-Pérez, "Imaging of bacteria with radiolabeled ubiquicidin by SPECT and PET techniques," *Clinical and Translational Imaging*, vol. 4, no. 3, pp. 175–182, 2016.
- [199] P. S. Hiemstra, M. T. van den Barselaar, M. Roest, P. H. Nibbering, and R. van Furth, "Ubiquicidin, a novel murine microbicidal protein present in the cytosolic fraction of macrophages," *Journal of Leukocyte Biology*, vol. 66, no. 3, pp. 423–428, 1999.
- [200] M. S. Akhtar, A. Qaisar, J. Irfanullah et al., "Antimicrobial peptide 99mTc-ubiquicidin 29–41 as human infection-imaging agent: clinical trial," *Journal of Nuclear Medicine*, vol. 46, no. 4, pp. 567–573, 2005.
- [201] M. Assadi, K. Vahdat, I. Nabipour et al., "Diagnostic value of 99mTc-ubiquicidin scintigraphy for osteomyelitis and comparisons with 99mTc-methylene diphosphonate scintigraphy and magnetic resonance imaging," *Nuclear Medicine Communications*, vol. 32, no. 8, pp. 716–723, 2011.
- [202] T. Emery, "Exchange of Iron by Gallium in Siderophores," *Biochemistry*, vol. 25, no. 16, pp. 4629–4633, 1986.
- [203] M. Petrik, C. Zhai, H. Haas, and C. Decristoforo, "Siderophores for molecular imaging applications," *Clinical and Translational Imaging*, vol. 5, no. 1, pp. 15–27, 2017.
- [204] H. J. Flint, E. A. Bayer, M. T. Rincon, R. Lamed, and B. A. White, "Polysaccharide utilization by gut bacteria: potential for new insights from genomic analysis," *Nature Reviews Microbiology*, vol. 6, no. 2, pp. 121–131, 2008.
- [205] G. Gowrishankar, M. Namavari, E. B. Jouannot et al., "Investigation of 6-[18F]-fluoromaltose as a novel PET tracer for imaging bacterial infection," *PLoS ONE*, vol. 9, no. 9, Article ID e107951, 2014.
- [206] N. Gholipour, M. Akhlaghi, A. M. Kheirabadi et al., "Chelator-free radiolabeling of dextran with 68Ga for PET studies," *Journal of Radioanalytical and Nuclear Chemistry*, vol. 311, no. 3, pp. 1811–1817, 2017.
- [207] C. Bettogowda, C. A. Foss, I. Cheong et al., "Imaging bacterial infections with radiolabeled 1-(2*D*-deoxy-2*L*-fluoro- β -D-arabinofuranosyl)-5-iodouracil," *Proceedings of the National Academy of Sciences of the United States of America*, vol. 102, no. 4, pp. 1145–1150, 2005.
- [208] S. A. Soghomonyan, M. Doubrovin, J. Pike et al., "Positron emission tomography (PET) imaging of tumor-localized *Salmonella* expressing HSV1-TK," *Cancer Gene Therapy*, vol. 12, no. 1, pp. 101–108, 2005.
- [209] C. Palestro, K. Nichols, S. Sheikh-Fayyaz, S. Dewey, P. Singhal, and K. Bhargava, "Can Gallium-68 PET differentiate acute interstitial nephritis from acute tubular necrosis?" *Journal of Nuclear Medicine*, vol. 57, Supplement 2, p. 551, 2016.
- [210] A. J. Morguet, D. L. Munz, V. Ivančević et al., "Immunoscintigraphy using technetium-99m-labeled anti-NCA-95 antigranulocyte antibodies as an adjunct to echocardiography in subacute infective endocarditis," *Journal of the American College of Cardiology*, vol. 23, no. 5, pp. 1171–1178, 1994.
- [211] C. van der Laken, O. Boerman, W. Oyen et al., "In Vivo Expression of Interleukin-1 Receptors during Various Experimentally Induced Inflammatory Conditions," *The Journal of Infectious Diseases*, vol. 177, no. 5, pp. 1398–1401, 1998.
- [212] C. J. Van Der Laken, O. C. Boerman, W. J. G. Oyen, M. T. P. Van De Ven, J. W. M. Van Der Meer, and F. H. M. Corstens, "Scintigraphic detection of infection and inflammation: New developments with special emphasis on receptor interaction," *European Journal of Nuclear Medicine and Molecular Imaging*, vol. 25, no. 5, pp. 535–546, 1998.
- [213] C. J. van der Laken, O. C. Boerman, W. J. G. Oyen, M. T. P. van de Ven, J. W. M. van der Meer, and F. H. M. Corstens, "Imaging of infection in rabbits with radioiodinated interleukin-1 (α and β), its receptor antagonist and a chemotactic peptide: a comparative study," *European Journal of Nuclear Medicine and Molecular Imaging*, vol. 25, no. 4, pp. 347–352, 1998.
- [214] C. J. Van Der Laken, O. C. Boerman, W. J. G. Oyen, M. T. P. Van De Ven, F. H. M. Corstens, and J. W. M. Van Der Meer, "The kinetics of radiolabelled interleukin-8 in infection and sterile inflammation," *Nuclear Medicine Communications*, vol. 19, no. 3, pp. 271–282, 1998.
- [215] E. Lazzeri, P. Erba, M. Perri et al., "Scintigraphic imaging of vertebral osteomyelitis with 111In-biotin," *The Spine Journal*, vol. 33, no. 7, pp. E198–E204, 2008.
- [216] E. Blom, B. Långström, and I. Velikyán, "68Ga-labeling of biotin analogues and their characterization," *Bioconjugate Chemistry*, vol. 20, no. 6, pp. 1146–1151, 2009.
- [217] O. Eriksson, F. Carlsson, E. Blom et al., "Preclinical evaluation of a 68Ga-labeled biotin analogue for applications in islet transplantation," *Nuclear Medicine and Biology*, vol. 39, no. 3, pp. 415–421, 2012.
- [218] E. A. Weinstein, A. A. Ordonez, V. P. DeMarco et al., "Imaging Enterobacteriaceae infection in vivo with ¹⁸F-fluorodeoxyisobutyl positron emission tomography," *Science Translational Medicine*, vol. 6, no. 259, p. 259ra146, 2014.
- [219] K. M. Nielsen, M. H. Kyneb, A. K. O. Alstrup et al., "68Ga-labeled phage-display selected peptides as tracers for positron emission tomography imaging of *Staphylococcus aureus* biofilm-associated infections: Selection, radiolabelling and preliminary biological evaluation," *Nuclear Medicine and Biology*, vol. 43, no. 10, pp. 593–605, 2016.
- [220] T. J. Mäkinen, P. Lankinen, T. Pöyhönen, J. Jalava, H. T. Aro, and A. Roivainen, "Comparison of 18F-FDG and 68Ga PET imaging in the assessment of experimental osteomyelitis due to *Staphylococcus aureus*," *European Journal of Nuclear Medicine and Molecular Imaging*, vol. 32, no. 11, pp. 1259–1268, 2005.
- [221] J. M. U. Silvola, I. Laitinen, H. J. Sipilä et al., "Uptake of ⁶⁸Ga in atherosclerotic plaques in LDLR^{-/-}ApoB^{100/100} mice," *EJN-MMI Research*, vol. 1, no. 1, pp. 1–8, 2011.

- [222] T. A. Wynn, "Cellular and molecular mechanisms of fibrosis," *The Journal of Pathology*, vol. 214, no. 2, pp. 199–210, 2008.
- [223] T. Derlin, D. Jonigk, J. Bauersachs, and F. M. Bengel, "Molecular Imaging of Chemokine Receptor CXCR4 in Non-Small Cell Lung Cancer Using 68Ga-Pentixafor PET/CT: Comparison With 18F-FDG," *Clinical Nuclear Medicine*, 2016.
- [224] I. Velikyan, U. Rosenström, T. N. Bulenga, O. Eriksson, and G. Antoni, "Feasibility of multiple examinations using 68Ga-labelled collagen analogues: Organ distribution in rat for extrapolation to human organ and whole-body radiation dosimetry," *Pharmaceuticals*, vol. 9, no. 2, article no. 31, 2016.
- [225] S. Jadhav, M. Käkälä, J. Mäkilä et al., "Synthesis and in Vivo PET Imaging of Hyaluronan Conjugates of Oligonucleotides," *Bioconjugate Chemistry*, vol. 27, no. 2, pp. 391–403, 2016.
- [226] A. Autio, A. Saraste, N. Kudomi et al., "Assessment of blood flow with (68) Ga-DOTA PET in experimental inflammation: a validation study using (15) O-water," *American Journal of Nuclear Medicine and Molecular Imaging*, vol. 4, no. 6, pp. 571–579, 2014.
- [227] G. Davies, A. Rolle, A. Maurer et al., "Towards translational immunoPET/MR imaging of invasive pulmonary aspergillosis: the Humanised Monoclonal Antibody JF5 detects in vivo," *Theranostics*, vol. 7, no. 14, pp. 3398–3414, 2017.
- [228] D. Goodwin, C. Meares, G. David et al., "Monoclonal antibodies as reversible equilibrium carriers of radiopharmaceuticals," *International Journal of Radiation Applications and Instrumentation. Part B: Nuclear Medicine and Biology*, vol. 13, no. 4, pp. 383–391, 1986.
- [229] D. A. Goodwin, C. F. Mears, M. McTigue, and G. S. David, "Monoclonal antibody hapten radiopharmaceutical delivery," *Nuclear Medicine Communications*, vol. 7, no. 8, pp. 569–580, 1986.
- [230] S. E. Halpern and R. O. Dillman, "Problems associated with radioimmunodetection and possibilities for future solutions," *J Biol Response Mod*, vol. 6, no. 3, pp. 235–262, 1987.
- [231] H. Hong, J. Sun, and W. Cai, "Radionuclide-based cancer imaging targeting the carcinoembryonic antigen," *Biomarker Insights*, vol. 3, pp. 435–451, 2008.
- [232] G. J. Förster, E. B. Santos, P. M. Smith-Jones, P. Zanzonico, and S. M. Larson, "Pretargeted radioimmunotherapy with a single-chain antibody/streptavidin construct and radiolabeled DOTA-biotin: Strategies for reduction of the renal dose," *Journal of Nuclear Medicine*, vol. 47, no. 1, pp. 140–149, 2006.
- [233] Z. Yao, M. Zhang, H. Kobayashi et al., "Improved targeting of radiolabeled streptavidin in tumors pretargeted with biotinylated monoclonal antibodies through an avidin chase," *Journal of Nuclear Medicine*, vol. 36, no. 5, pp. 837–841, 1995.
- [234] C.-H. Chang, R. M. Sharkey, E. A. Rossi et al., "Molecular Advances in Pretargeting Radioimmunotherapy with Bispecific Antibodies I Supported in part by USPHS Grant R01-CA-84379 from the NIH and Department of Energy Grant DE-FG01-00NE22941 (both to R. M. S.), I," *Mol Cancer Ther*, vol. 1, no. 7, pp. 553–563, 2002.
- [235] R. M. Sharkey, E. A. Rossi, W. J. McBride, C.-H. Chang, and D. M. Goldenberg, "Recombinant Bispecific Monoclonal Antibodies Prepared by the Dock-and-Lock Strategy for Pretargeted Radioimmunotherapy," *Seminars in Nuclear Medicine*, vol. 40, no. 3, pp. 190–203, 2010.
- [236] R. M. Sharkey, E. A. Rossi, C.-H. Chang, and D. M. Goldenberg, "Improved cancer therapy and molecular imaging with multivalent, multispecific antibodies," *Cancer Biotherapy and Radiopharmaceuticals*, vol. 25, no. 1, pp. 1–12, 2010.
- [237] D. M. Goldenberg, R. M. Sharkey, G. Paganelli, J. Barbet, and J. Chatal, "Antibody pretargeting advances cancer radioimmunodetection and radioimmunotherapy," *Journal of Clinical Oncology*, vol. 24, no. 5, pp. 823–834, 2006.
- [238] O. C. Boerman, F. G. van Schaijk, W. J. G. Oyen, and F. H. M. Corstens, "Pretargeted radioimmunotherapy of cancer: progress step by step," *Journal of Nuclear Medicine*, vol. 44, no. 3, pp. 400–411, 2003.
- [239] J. Schuhmacher, S. Kaul, G. Klivényi et al., "Immunoscintigraphy with positron emission tomography: Gallium-68 chelate imaging of breast cancer pretargeted with bispecific anti-MUC1/anti-Ga chelate antibodies," *Cancer Research*, vol. 61, no. 9, pp. 3712–3717, 2001.
- [240] J. Schuhmacher, G. Klivényi, S. Kaul et al., "Pretargeting of human mammary carcinoma xenografts with bispecific anti-MUC1/anti-Ga chelate antibodies and immunoscintigraphy with PET," *Nuclear Medicine and Biology*, vol. 28, no. 7, pp. 821–828, 2001.
- [241] C. Somasundaram, S. Matzku, J. Schuhmacher, and M. Zöller, "Development of a bispecific monoclonal antibody against a gallium-67 chelate and the human melanoma-associated antigen p97 for potential use in pretargeted immunoscintigraphy," *Cancer Immunology, Immunotherapy*, vol. 36, no. 5, pp. 337–345, 1993.
- [242] E. A. Rossi, D. L. Rossi, R. Stein, D. M. Goldenberg, and C.-H. Chang, "A bispecific antibody-IFN α 2b immunocytokine targeting CD20 and HLA-DR is highly toxic to human lymphoma and multiple myeloma cells," *Cancer Research*, vol. 70, no. 19, pp. 7600–7609, 2010.
- [243] R. M. Sharkey, H. Karacay, S. Litwin et al., "Improved therapeutic results by pretargeted radioimmunotherapy of non-Hodgkin's lymphoma with a new recombinant, trivalent, anti-CD20, bispecific antibody," *Cancer Research*, vol. 68, no. 13, pp. 5282–5290, 2008.
- [244] G. L. Griffiths, C.-H. Chang, W. J. McBride et al., "Reagents and methods for PET using bispecific antibody pretargeting and 68Ga-radiolabeled bivalent hapten-peptide-chelate conjugates," *Journal of Nuclear Medicine*, vol. 45, no. 1, pp. 30–39, 2004.
- [245] J. Watine, M. Miédougé, and B. Friedberg, "Carcinoembryonic antigen as an independent prognostic factor of recurrence and survival in patients resected for colorectal liver metastases: A systematic review," *Diseases of the Colon & Rectum*, vol. 44, no. 12, pp. 1791–1799, 2001.
- [246] M. J. Goldstein and E. P. Mitchell, "Carcinoembryonic antigen in the staging and follow-up of patients with colorectal cancer," *Cancer Investigation*, vol. 23, no. 4, pp. 338–351, 2005.
- [247] D. V. Gold, D. M. Goldenberg, H. Karacay et al., "A novel bispecific, trivalent antibody construct for targeting pancreatic carcinoma," *Cancer Research*, vol. 68, no. 12, pp. 4819–4826, 2008.
- [248] J. Schuhmacher, G. Klivényi, R. Matys et al., "Multistep tumor targeting in nude mice using bispecific antibodies and a gallium chelate suitable for immunoscintigraphy with positron emission tomography," *Cancer Research*, vol. 55, no. 1, pp. 115–123, 1995.
- [249] G. Klivényi, J. Schuhmacher, E. Patzelt et al., "Gallium-68 chelate imaging of human colon carcinoma xenografts pretargeted with bispecific anti-CD44(V6)/anti-gallium chelate antibodies," *Journal of Nuclear Medicine*, vol. 39, no. 10, pp. 1769–1776, 1998.
- [250] M. Zoller, J. Schuhmacher, J. Reed, W. Maier-Borst, and S. Matzku, "Establishment and characterization of monoclonal

- antibodies against an octahedral gallium chelate suitable for immunoscintigraphy with PET," *Journal of Nuclear Medicine*, vol. 33, no. 7, pp. 1366–1372, 1992.
- [251] R. M. Sharkey, T. M. Cardillo, E. A. Rossi et al., "Signal amplification in molecular imaging by pretargeting a multivalent, bispecific antibody," *Nature Medicine*, vol. 11, no. 11, pp. 1250–1255, 2005.
- [252] D. M. Goldenberg and R. M. Sharkey, "Novel radiolabeled antibody conjugates," *Oncogene*, vol. 26, no. 25, pp. 3734–3744, 2007.
- [253] D. M. Goldenberg, E. A. Rossi, R. M. Sharkey, W. J. McBride, and C.-H. Chang, "Multifunctional antibodies by the dock-and-lock method for improved cancer imaging and therapy by pretargeting," *Journal of Nuclear Medicine*, vol. 49, no. 1, pp. 158–163, 2008.
- [254] R. Schoffelen, R. M. Sharkey, D. M. Goldenberg et al., "Pretargeted immuno-positron emission tomography imaging of carcinoembryonic antigen-expressing tumors with a bispecific antibody and a⁶⁸Ga- And18F-labeled hapten peptide in mice with human tumor xenografts," *Molecular Cancer Therapeutics*, vol. 9, no. 4, pp. 1019–1027, 2010.
- [255] E. S. Bos, W. H. Kuijpers, M. Meesters-Winters et al., "In vitro evaluation of DNA-DNA hybridization as a two-step approach in radioimmunotherapy of cancer," *Cancer Research*, vol. 54, no. 13, pp. 3479–3486, 1994.
- [256] G. Paganelli, M. Bartolomei, M. Ferrari et al., "Pre-Targeted Locoregional Radioimmunotherapy with," *Cancer biotherapy and radiopharmaceuticals*, vol. 16, no. 3, pp. 227–235, 2001.
- [257] A. Forero, P. L. Weiden, J. M. Vose et al., "Phase I trial of a novel anti-CD20 fusion protein in pretargeted radioimmunotherapy for B-cell non-Hodgkin lymphoma," *Blood*, vol. 104, no. 1, pp. 227–236, 2004.
- [258] D. M. Goldenberg, C.-H. Chang, E. A. Rossi, W. J. McBride, and R. M. Sharkey, "Pretargeted molecular imaging and radioimmunotherapy," *Theranostics*, vol. 2, no. 5, pp. 523–540, 2012.
- [259] H. Karacay, R. M. Sharkey, W. J. McBride, E. A. Rossi, C.-H. Chang, and D. M. Goldenberg, "Optimization of hapten-peptide labeling for pretargeted immunoPET of bispecific antibody using generator-produced ⁶⁸Ga," *Journal of Nuclear Medicine*, vol. 52, no. 4, pp. 555–559, 2011.
- [260] J. R. Oh and B. C. Ahn, "False-positive uptake on radioiodine whole-body scintigraphy: physiologic and pathologic variants unrelated to thyroid cancer," *American Journal of Nuclear Medicine and Molecular Imaging*, vol. 2, no. 2, pp. 141–150, 2012.
- [261] E. Frampas, C. Rousseau, C. Bodet-Milin, J. Barbet, J.-F. Chatal, and F. Kraeber-Bodéré, "Improvement of radioimmunotherapy using pretargeting," *Frontiers in Oncology*, vol. 3, Article ID 00159, 2013.
- [262] C. S. McKay and M. G. Finn, "Click chemistry in complex mixtures: Bioorthogonal bioconjugation," *Chemistry & Biology*, vol. 21, no. 9, pp. 1075–1101, 2014.
- [263] B. L. Oliveira, Z. Guo, and G. J. Bernardes, "Inverse electron demand Diels–Alder reactions in chemical biology," *Chemical Society Reviews*, vol. 46, no. 16, pp. 4895–4950, 2017.
- [264] B. Nichols, Z. Qin, J. Yang, D. R. Vera, and N. K. Devaraj, "⁶⁸Ga chelating bioorthogonal tetrazine polymers for the multistep labeling of cancer biomarkers," *Chemical Communications*, vol. 50, no. 40, pp. 5215–5217, 2014.
- [265] R. Rossin, P. R. Verkerk, S. M. van den Bosch et al., "In vivo chemistry for pretargeted tumor imaging in live mice," *Angewandte Chemie International Edition*, vol. 49, no. 19, pp. 3375–3378, 2010.
- [266] B. M. Zeglis, K. K. Sevak, T. Reiner et al., "A pretargeted PET imaging strategy based on bioorthogonal diels-alder click chemistry," *Journal of Nuclear Medicine*, vol. 54, no. 8, pp. 1389–1396, 2013.
- [267] J. L. Houghton, R. Membreno, D. Abdel-Atti et al., "Establishment of the in vivo efficacy of pretargeted radioimmunotherapy utilizing inverse electron demand diels-alder click chemistry," *Molecular Cancer Therapeutics*, vol. 16, no. 1, pp. 124–133, 2017.
- [268] J. Funkhouser, "Reinventing pharma: the theranostic revolution," *Current Drug Discovery*, pp. 17–19, 2002.
- [269] J. Sorensen, I. Velikyan, A. Wennborg et al., "Measuring HER2-expression in metastatic breast cancer using ⁶⁸Ga-ABY025 PET/CT," *European Journal of Nuclear Medicine and Molecular Imaging*, vol. 41, pp. S226–S226, 2014.
- [270] I. Velikyan, A. Wennborg, J. Feldwisch et al., "GMP compliant preparation of a ⁶⁸Gallium-labeled Affibody analogue for breast cancer patient examination: first-in-man," *Eur J Nucl Med Mol Imaging*, vol. 41, pp. S228–S229, 2014.
- [271] K. Öberg, "Molecular imaging radiotherapy: Theranostics for personalized patient management of neuroendocrine tumors (NETs)," *Theranostics*, vol. 2, no. 5, pp. 448–458, 2012.
- [272] I. Velikyan, A. Wennborg, J. Feldwisch, H. Lindman, J. Carlsson, and J. Sorensen, "Good manufacturing practice production of [⁶⁸Ga]Ga-ABY-025 for HER2 specific breast cancer imaging," *American Journal of Nuclear Medicine and Molecular Imaging*, vol. 6, no. 2, pp. 135–153, 2016.
- [273] M. Sandström, K. Lindskog, I. Velikyan et al., "Biodistribution and radiation dosimetry of the anti-HER2 Affibody molecule ⁶⁸Ga-ABY-025 in breast cancer patients," *Journal of Nuclear Medicine*, vol. 57, no. 6, pp. 867–871, 2016.
- [274] D. Sandberg, V. Tolmachev, I. Velikyan et al., "Intra-image referencing for simplified assessment of HER2-expression in breast cancer metastases using the Affibody molecule ABY-025 with PET and SPECT," *European Journal of Nuclear Medicine and Molecular Imaging*, vol. 44, no. 8, pp. 1337–1346, 2017.
- [275] H. Zhang, M. A. Moroz, I. Serganova et al., "Imaging expression of the human somatostatin receptor subtype-2 reporter gene with ⁶⁸Ga-DOTATOC," *Journal of Nuclear Medicine*, vol. 52, no. 1, pp. 123–131, 2011.
- [276] M. Naji and A. Al-Nahhas, "⁶⁸Ga-labelled peptides in the management of neuroectodermal tumours," *European Journal of Nuclear Medicine and Molecular Imaging*, vol. 39, no. 1, pp. S61–S67, 2012.
- [277] I. Velikyan, "The diversity of ⁶⁸Ga-Based imaging agents," *Recent Results in Cancer Research*, vol. 194, pp. 101–131, 2013.
- [278] K. Ferreira, H.-Y. Hu, V. Fetz et al., "Multivalent siderophore-dotam conjugates as theranostics for imaging and treatment of bacterial infections," *Angewandte Chemie International Edition*, vol. 56, no. 28, pp. 8272–8276, 2017.

Research Article

Comparison of ^{68}Ga -DOTA-Siglec-9 and ^{18}F -Fluorodeoxyribose-Siglec-9: Inflammation Imaging and Radiation Dosimetry

Helena Virtanen,¹ Johanna M. U. Silvola,¹ Anu Autio,¹ Xiang-Guo Li,^{2,3} Heidi Liljenbäck,^{1,4} Sanna Hellberg,¹ Riikka Siitonen,¹ Mia Ståhle,¹ Meeri Käkälä,¹ Anu J. Airaksinen,³ Kerttuli Helariutta,³ Tuula Tolvanen,⁵ Tibor Z. Veres,⁶ Antti Saraste,^{1,5} Juhani Knuuti,^{1,5} Sirpa Jalkanen,⁶ and Anne Roivainen^{1,4,5}

¹Turku PET Centre, University of Turku, Turku, Finland

²Turku PET Centre, Åbo Akademi University, Turku, Finland

³Laboratory of Radiochemistry, Department of Chemistry, University of Helsinki, Helsinki, Finland

⁴Turku Centre for Disease Modeling, University of Turku, Turku, Finland

⁵Turku PET Centre, Turku University Hospital, Turku, Finland

⁶MediCity Research Laboratory, University of Turku, Turku, Finland

Correspondence should be addressed to Anne Roivainen; anne.roivainen@utu.fi

Received 27 July 2017; Accepted 13 November 2017; Published 31 December 2017

Academic Editor: Gaurav Malviya

Copyright © 2017 Helena Virtanen et al. This is an open access article distributed under the Creative Commons Attribution License, which permits unrestricted use, distribution, and reproduction in any medium, provided the original work is properly cited.

Sialic acid-binding immunoglobulin-like lectin 9 (Siglec-9) is a ligand of inflammation-inducible vascular adhesion protein-1 (VAP-1). We compared ^{68}Ga -DOTA- and ^{18}F -fluorodeoxyribose- (FDR-) labeled Siglec-9 motif peptides for PET imaging of inflammation. *Methods.* Firstly, we examined ^{68}Ga -DOTA-Siglec-9 and ^{18}F -FDR-Siglec-9 in rats with skin/muscle inflammation. We then studied ^{18}F -FDR-Siglec-9 for the detection of inflamed atherosclerotic plaques in mice and compared it with previous ^{68}Ga -DOTA-Siglec-9 results. Lastly, we estimated human radiation dosimetry from the rat data. *Results.* In rats, ^{68}Ga -DOTA-Siglec-9 (SUV, 0.88 ± 0.087) and ^{18}F -FDR-Siglec-9 (SUV, 0.77 ± 0.22) showed comparable ($P = 0.29$) imaging of inflammation. In atherosclerotic mice, ^{18}F -FDR-Siglec-9 detected inflamed plaques with a target-to-background ratio (1.6 ± 0.078) similar to previously tested ^{68}Ga -DOTA-Siglec-9 ($P = 0.35$). Human effective dose estimates for ^{68}Ga -DOTA-Siglec-9 and ^{18}F -FDR-Siglec-9 were 0.024 and 0.022 mSv/MBq, respectively. *Conclusion.* Both tracers are suitable for PET imaging of inflammation. The easier production and lower cost of ^{68}Ga -DOTA-Siglec-9 present advantages over ^{18}F -FDR-Siglec-9, indicating it as a primary choice for clinical studies.

1. Introduction

Inflammation plays role in several diseases, such as, rheumatoid arthritis, diabetes and atherosclerosis. The early detection of inflammatory foci is critical for the adequate treatment of patients, and quantitative PET imaging may provide a valuable tool for diagnosis and monitoring of the effects of therapeutic interventions. ^{18}F -FDG is the gold standard for PET, but not specific to inflammation. In addition, the high physiological accumulation of ^{18}F -FDG in heart and brain

makes it difficult to detect inflammatory foci close to these organs [1].

Vascular adhesion protein-1 (VAP-1) is an endothelial adhesion molecule, which is involved in leukocyte transendothelial migration from blood into the sites of inflammation. During inflammation VAP-1 translocates from intracellular storages on the endothelial cell surface where it contributes leukocyte-endothelial adhesion. Although VAP-1 plays important role in early phases of inflammation, its luminal expression on the endothelium will remain constant

TABLE 1: Characteristics of study animals.

	Sprague-Dawley skin inflammation rats	LDLR ^{-/-} ApoB ^{100/100} atherosclerotic mice	C57BL/6N control mice
Age (months)	2.2 ± 0.051	5.6 ± 0.96	2.1 ± 0.39
High fat diet (months)	ND	3.6 ± 1.0	ND
Female/male (no.)	0/16	15/4	6/7
Weight (g)	350 ± 22	27 ± 4.0	24 ± 2.2
<i>In vivo</i> PET (no.)	13	2	2
<i>Ex vivo</i> gamma counting (no.)	16	19	13
<i>Ex vivo</i> autoradiography (no.)	ND	12	10

LDLR^{-/-} ApoB^{100/100} = low-density lipoprotein receptor-deficient mouse expressing only apolipoprotein B100; ND = not done; no. = number of investigated animals.

if the inflammation continues, which suggest VAP-1 as a promising target for both anti-inflammatory therapy and molecular imaging of inflammation [2]. The role of VAP-1 in atherosclerotic inflammation is unclear. VAP-1 expression is upregulated in atherosclerotic plaques in human carotid arteries [3, 4] and in the aorta of hypercholesterolemic rabbits [5]. VAP-1 is also expressed in soluble form (sVAP-1), which associates with atherosclerosis [6, 7].

We previously showed that sialic acid-binding immunoglobulin-like lectin 9 (Siglec-9) is a VAP-1 ligand, and the radiolabeled peptide (CARLSLSWRGLTLCPSK) containing residues 283–297 from Siglec-9 can be used for PET imaging of inflammation [4, 8–11].

In this study, we examined the detection of skin/muscle inflammation in rats, comparing the utility of the Siglec-9 motif peptides ⁶⁸Ga-labeled 1,4,7,10-tetraazacyclododecane-N,N',N'',N'''-tetraacetic acid-conjugated ⁶⁸Ga-DOTA-Siglec-9 and ¹⁸F-labeled fluorodeoxyribose-conjugated ¹⁸F-FDR-Siglec-9 [9]. We also examined ¹⁸F-FDR-Siglec-9 uptake in inflamed atherosclerotic plaques of mice and compared it with previous ⁶⁸Ga-DOTA-Siglec-9 results [4]. Finally, we used the rat PET data to estimate the human radiation doses for ⁶⁸Ga-DOTA-Siglec-9 and ¹⁸F-FDR-Siglec-9.

2. Materials and Methods

2.1. Radiochemistry. ⁶⁸Ga-DOTA-Siglec-9 and ¹⁸F-FDR-Siglec-9 were produced as previously described [8, 9].

2.2. Animal Models. Twenty-four hours before the PET studies, Sprague-Dawley rats (weight, 350 ± 22 g; *n* = 16) were subcutaneously injected with turpentine oil (Sigma-Aldrich) to induce focal acute, sterile inflammation [12]. Before the injection, rats were shaved on the both forelegs. Inflamed area on the left foreleg contained both skin and muscle. The intact, contralateral side (right foreleg) was used as a control.

Six-month-old atherosclerotic low-density lipoprotein receptor-deficient mice (weight, 27 ± 4.1 g; *n* = 19) expressing only apolipoprotein B100 (LDLR^{-/-} ApoB^{100/100}, strain #003000; Jackson Laboratory, Bar Harbor, ME, USA) were fed for 4 months with a Western-type diet [13]. Two-month-old C57BL/6N mice (weight, 24 ± 2.2 g; *n* = 13) fed with a regular chow served as controls.

All animal experiments (Table 1) were approved by the national Animal Experiment Board in Finland and carried out in compliance with the EU directive.

2.3. Rat Studies. Rats were divided into two groups with Group 1 being intravenously (i.v.) given ⁶⁸Ga-DOTA-Siglec-9 (16 ± 2.9 MBq, *n* = 8) and Group 2 ¹⁸F-FDR-Siglec-9 (18 ± 5.1 MBq, *n* = 8). A 60 min dynamic PET acquisition was performed on a High Resolution Research Tomograph (HRRT; Siemens Medical Solutions, Knoxville, TN, USA). The PET data were reconstructed into 5 × 60 s and 11 × 300 s frames using an ordered-subsets expectation maximization 3D algorithm (OSEM3D). Quantitative PET image analysis was performed by defining regions of interest (ROIs) within the inflamed area (on the left foreleg), control area (on the right foreleg), kidneys, lungs, heart, liver, and urinary bladder using Carimas 2.8 software (Turku PET Centre). Results were expressed as standardized uptake values (SUV) and time-activity curves. SUV was calculated as a ratio of tissue radioactivity concentration (Bq/mL) and given radioactivity dose (Bq) divided by animal's body weight.

After PET imaging, rats were sacrificed and various tissues were excised and weighed, and their radioactivity levels were measured with a gamma counter (1480 Wizard 3^{II}, PerkinElmer, Turku, Finland). The *ex vivo* biodistribution results were expressed as a percentage of the injected radioactivity dose per gram of tissue (% ID/g) and target-to-background ratio.

The inflamed area and control area tissue samples were frozen, cut into sections, and stained with hematoxylin-eosin (H&E) for morphological evaluation.

Absorbed doses of ⁶⁸Ga-DOTA-Siglec-9 and ¹⁸F-FDR-Siglec-9 were calculated with the OLINDA/EXM version 1.0 software (organ level internal dose assessment and exponential modeling; Vanderbilt University, Nashville, TN, USA), which applies the MIRD schema (developed by the Medical Internal Radiation Dose committee of the Society of Nuclear Medicine) for radiation dose calculations in internal exposure. The software includes radionuclide information and selection of human body phantoms. The residence times derived from the rat data were integrated as the area under the time-activity curve. The residence times were converted into corresponding human values by multiplication with a factor

to scale the organ and body weights: $(W_{\text{Body, rat}}/W_{\text{Organ, rat}}) \times (W_{\text{Organ, human}}/W_{\text{Body, human}})$, where $W_{\text{Body, rat}}$ and $W_{\text{Body, human}}$ are the body weights of rat and human (a 70-kg male), respectively; and $W_{\text{Organ, rat}}$ and $W_{\text{Organ, human}}$ are the organ weights of rat and human (organ weights for a 70 kg male), respectively [14].

2.4. Mouse Studies. To detect luminal expression of VAP-1, mice were intravenously (i.v.) injected with a monoclonal rat anti-mouse VAP-1 antibody (7–88, 1 mg/kg diluted in saline) [15] 10 min before sacrifice. Aorta samples were frozen and cut into 8 μm longitudinal sections, incubated for 30 min at room temperature in the dark with a secondary goat anti-rat antibody (working dilution, 5 $\mu\text{g}/\text{mL}$ in phosphate-buffered saline (PBS) containing 5% normal mouse or human AB serum), conjugated to a fluorescent dye (Alexa Fluor 488; Invitrogen, Eugene, OR, USA), and rinsed twice in PBS for 5 min.

In PET studies, mice (19 atherosclerotic, 13 controls) were injected with 14 ± 4.4 MBq of ^{18}F -FDR-Siglec-9. Twenty-five minutes after ^{18}F -FDR-Siglec-9 injection, blood was drawn by cardiac puncture and the animals were killed. The thoracic aorta was excised and rinsed in saline to remove the blood. In addition, various other tissues were excised and patted dry. Samples of blood and urine were collected, and blood plasma was separated by centrifugation. All tissue samples were weighed, and their radioactivity levels were measured with a gamma counter (Triathler 3'', Hidex Oy, Turku, Finland). The results were expressed as % ID/g and target-to-background ratio.

Autoradiography was used to study the distribution of radioactivity in the aorta in more detail, as described previously [13]. After careful superimposition of the autoradiographs and H&E stained images, the count densities of 540 ROIs (185: plaques, 241: normal vessel walls, and 114: adventitia) were analyzed using Tina 2.1 software. The autoradiography results were calculated as the photostimulated luminescence per unit area (PSL/ mm^2) normalized for injected radioactivity dose, and as ratios between the atherosclerotic plaque, normal vessel wall, and adventitia.

A subset of mice (two atherosclerotic, two controls) were injected with 4.7 ± 1.1 MBq of ^{18}F -FDR-Siglec-9 and imaged with an Inveon Multimodality PET/CT (Siemens, Medical Solutions, Knoxville, TN, USA). Dynamic PET images were acquired for 60 min, followed by CT with a contrast agent (eXIATM160XL, Binitio Biomedical Inc., Ottawa, ON, Canada). The PET images were reconstructed with OSEM3D (frames 5×60 s, 3×300 s, 1×600 s, 2×1800 s).

Quantitative PET image analysis was performed by defining ROIs in the heart left ventricle (blood pool) and aortic arch as identified on the basis of the CT angiography by using the Inveon Research Workplace software (Siemens Medical Solutions, Knoxville, TN, USA). Time frames 10–20 min after injection were used for PET quantification, as previously reported in the same mouse model using ^{68}Ga -DOTA-Siglec-9 [4]. The results within ROIs were expressed as SUV and target-to-background ratio ($\text{SUV}_{\text{max, aortic arch}}/\text{SUV}_{\text{mean, blood}}$).

Finally, we compared ^{18}F -FDR-Siglec-9 results with previously reported ^{68}Ga -DOTA-Siglec-9 [4].

2.5. Statistical Analyses. All results are expressed as mean \pm SD. Paired 2-tailed Student's *t*-tests were applied for intra-animal comparisons. Nonpaired data were compared between two groups using *t*-tests and between multiple groups using ANOVA with Tukey's correction. A *P* value less than 0.05 was considered statistically significant.

3. Results

3.1. Radiochemistry. The specific radioactivity of ^{68}Ga -DOTA-Siglec-9 and ^{18}F -FDR-Siglec-9 was 70 ± 15 MBq/nmol and 83 ± 33 MBq/nmol, respectively, with radiochemical purity being $>95\%$ throughout the study.

3.2. Rat Studies. The turpentine oil caused focal soft-tissue inflammation with edema and leukocyte infiltration, predominantly neutrophils (Figure 1), and luminal VAP-1 as previously reported [8, 16].

The inflammatory focus was clearly visualized with both of the PET tracers and was demonstrated in the time-activity curves of the inflamed area, with the uptake kinetics of both tracers being comparable (Figure 2). In the inflamed area, the $\text{SUV}_{\text{mean, 10–60 min}}$ of ^{68}Ga -DOTA-Siglec-9 and ^{18}F -FDR-Siglec-9 was 0.88 ± 0.087 and 0.77 ± 0.22 , respectively ($P = 0.29$). The corresponding $\text{SUV}_{\text{max, 10–60 min}}$ values for ^{68}Ga -DOTA-Siglec-9 (1.1 ± 0.10) and ^{18}F -FDR-Siglec-9 (1.1 ± 0.097) were also close to each other ($P = 0.47$). Both tracers peaked about 10 min after the i.v. bolus injection, with a slow decrease thereafter. The inflammation-to-blood ratios_{10–60 min} of ^{68}Ga -DOTA-Siglec-9 (1.5 ± 0.33) and ^{18}F -FDR-Siglec-9 (1.7 ± 0.51) were also comparable ($P = 0.54$). Uptake in the heart, liver, kidneys, and urinary bladder was clearly visible with both tracers (Figure 2).

Ex vivo gamma counting at 60 min after injection demonstrated that ^{18}F -FDR-Siglec-9 uptake was significantly higher than ^{68}Ga -DOTA-Siglec-9 uptake in several organs, including inflamed and control areas. The difference was particularly notable in the liver, pancreas, heart, and kidneys (Table 2). Only in the spleen was the uptake of ^{68}Ga -DOTA-Siglec-9 significantly higher than that of ^{18}F -FDR-Siglec-9. Although the uptake of ^{18}F -FDR-Siglec-9 in inflamed area (0.19 ± 0.053 % ID/g) was significantly higher ($P = 0.013$) than that of ^{68}Ga -DOTA-Siglec-9 (0.12 ± 0.032 % ID/g), the inflammation-to-blood and inflamed-to-control area ratios (^{18}F -FDR-Siglec-9: 1.3 ± 0.16 and 2.0 ± 0.70 ; ^{68}Ga -DOTA-Siglec-9: 1.4 ± 0.42 and 2.5 ± 0.54) were similar ($P = 0.67$ and $P = 0.18$, resp.).

Extrapolation from the rat PET data suggested estimated human effective doses for a 70 kg man of 0.024 ± 0.0041 mSv/MBq for ^{68}Ga -DOTA-Siglec-9, and 0.022 ± 0.0042 mSv/MBq for ^{18}F -FDR-Siglec-9. The most critical organs were the urinary bladder wall with ^{68}Ga -DOTA-Siglec-9 (0.20 ± 0.087 mSv/MBq) and kidneys with ^{18}F -FDR-Siglec-9 (0.29 ± 0.13 mSv/MBq) (Tables 3 and 4).

TABLE 2: *Ex vivo* biodistribution (% ID/g) of ^{68}Ga -DOTA-Siglec-9 and ^{18}F -FDR-Siglec-9 at 60 min after injection in rats with skin/muscle inflammation.

Organ	^{68}Ga -DOTA-Siglec-9	^{18}F -FDR-Siglec-9	<i>P</i> value*
Control area	0.051 ± 0.0063	0.11 ± 0.056	0.015
Inflamed area	0.12 ± 0.032	0.19 ± 0.053	0.013
Adipose tissue, BAT	0.024 ± 0.026	0.049 ± 0.019	0.12
Adipose tissue, WAT	0.027 ± 0.014	0.017 ± 0.0041	0.090
Blood	0.099 ± 0.040	0.12 ± 0.023	0.33
Bone (femoral)	0.020 ± 0.0089	0.017 ± 0.010	0.67
Bone marrow	0.039 ± 0.012	0.056 ± 0.011	0.022
Brain	0.0062 ± 0.0049	0.010 ± 0.0030	0.083
Heart	0.030 ± 0.011	0.048 ± 0.010	0.0038
Kidneys	2.8 ± 1.8	14 ± 9.9	0.0053
Liver	0.32 ± 0.16	0.68 ± 0.12	0.00014
Lungs	0.079 ± 0.035	0.11 ± 0.028	0.059
Muscle	0.019 ± 0.0091	0.021 ± 0.0067	0.68
Pancreas	0.024 ± 0.0024	0.048 ± 0.011	0.00062
Plasma	0.13 ± 0.015	0.23 ± 0.087	0.087
Small intestine	0.060 ± 0.016	0.091 ± 0.029	0.051
Spleen	0.19 ± 0.110	0.060 ± 0.012	0.0048
Testis	0.035 ± 0.031	0.046 ± 0.022	0.45
Urine	24 ± 11	23 ± 14	0.93

% ID/g = percentage of injected radioactivity dose per gram of tissue; BAT=brown adipose tissue; WAT = white adipose tissue. *Unpaired, 2-tailed Student's *t*-test.

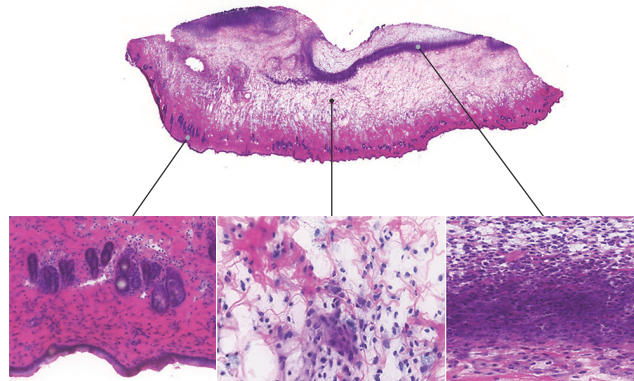


FIGURE 1: Inflammation of skin/muscle in a rat at 24 hours after subcutaneous injection of turpentine oil. Hematoxylin-eosin staining of a 10 μm cryosection reveals edema and leukocyte infiltration, predominantly neutrophils.

3.3. *Mouse Studies.* The $\text{LDLR}^{-/-}\text{ApoB}^{100/100}$ mice demonstrated atherosclerotic plaques, especially in the aortic arch, while the C57BL/6N mice showed no evidence of atherosclerosis. Furthermore, the $\text{LDLR}^{-/-}\text{ApoB}^{100/100}$ atherosclerotic lesions were VAP-1 positive, whereas normal vessel walls in the aortas of C57BL/6N mice were VAP-1-negative (Figure 3).

^{18}F -FDR-Siglec-9 PET/CT imaging of atherosclerotic mice showed plaques in the aortic arch, with a target-to-background ratio of 1.6 ± 0.078 at 10–20 min after injection (Figure 4(a)). This ratio was similar to that reported previously for ^{68}Ga -DOTA-Siglec-9 (1.7 ± 0.22 , $P = 0.35$).

According to *ex vivo* gamma counting, the aortic uptake of ^{18}F -FDR-Siglec-9 was significantly higher ($P = 0.0015$)

in the $\text{LDLR}^{-/-}\text{ApoB}^{100/100}$ mice (0.93 ± 0.38 % ID/g) than in the C57BL/6N mice (0.52 ± 0.23 % ID/g; Table 5) and comparable to the uptake of ^{68}Ga -DOTA-Siglec-9 (0.83 ± 0.33 % ID/g, $P = 0.38$).

Autoradiography of aortic cryosections further confirmed ^{18}F -FDR-Siglec-9 accumulation in atherosclerotic plaques, with a plaque-to-healthy vessel wall ratio of 1.9 ± 0.23 ($P < 0.001$) and plaque-to-adventitia ratio of 2.2 ± 0.53 ($P < 0.001$). In control mice, the uptake of ^{18}F -FDR-Siglec-9 in healthy vessel wall was similar to that in the atherosclerotic mice (Figure 4). However, the plaque-to-healthy vessel wall ratios were higher with ^{68}Ga -DOTA-Siglec-9 (2.1 ± 0.43) than with ^{18}F -FDR-Siglec-9 ($P = 0.038$).

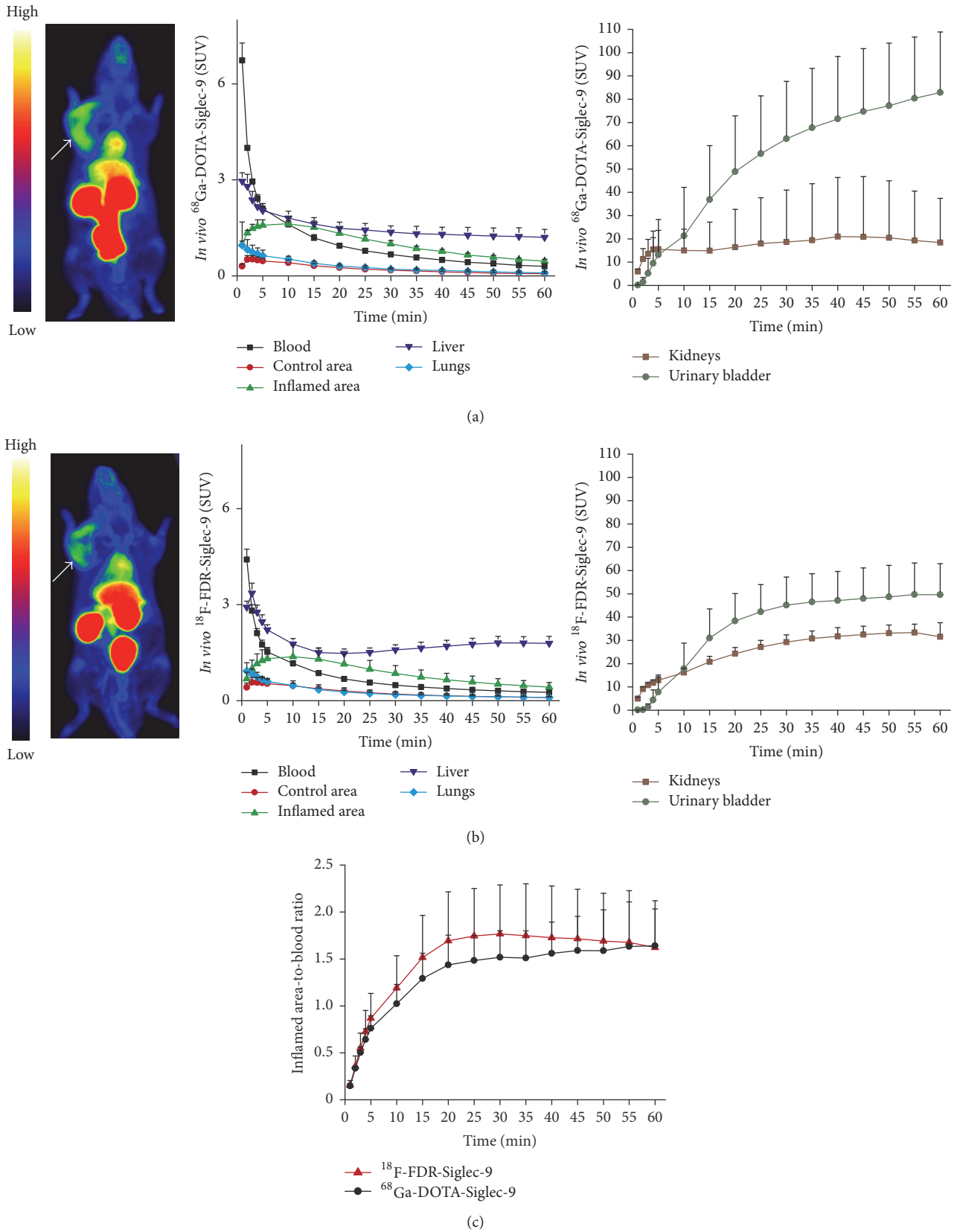


FIGURE 2: PET images and time-activity curves of rats with skin/muscle inflammation (arrow) imaged with (a) ^{68}Ga -DOTA-Siglec-9 ($n = 5$) or (b) ^{18}F -FDR-Siglec-9 ($n = 8$) and (c) comparison of their target-to-blood kinetics.

TABLE 3: Normalized number of disintegrations (hours) in source organs extrapolated from the rat PET data.

Organ	^{68}Ga -DOTA-Siglec-9	^{18}F -FDR-Siglec-9	<i>P</i> value*
Heart wall	0.0029 ± 0.00072	0.0026 ± 0.0010	0.55
Kidneys	0.093 ± 0.081	0.47 ± 0.21	0.0032
Liver	0.033 ± 0.0097	0.11 ± 0.043	0.0027
Lungs	0.0026 ± 0.0011	0.0029 ± 0.0011	0.62
Muscle	0.054 ± 0.0088	0.081 ± 0.042	0.17
Urinary bladder wall	0.17 ± 0.076	0.15 ± 0.070	0.70
Total body	1.3 ± 0.085	1.8 ± 0.32	0.0042

* Unpaired, 2-tailed Student's *t*-test.

TABLE 4: Human dose equivalent estimates (mSv/MBq) extrapolated from the rat PET data.

Organ	^{68}Ga -DOTA-Siglec-9	^{18}F -FDR-Siglec-9	<i>P</i> value*
Adrenals	0.014 ± 0.0012	0.020 ± 0.0029	0.0011
Brain	0.012 ± 0.00077	0.010 ± 0.0018	0.064
Breasts	0.011 ± 0.00064	0.0086 ± 0.0011	0.0036
Gallbladder wall	0.014 ± 0.00065	0.017 ± 0.0014	0.00022
Heart wall	0.0083 ± 0.0010	0.0085 ± 0.00045	0.52
Kidneys	0.15 ± 0.12	0.29 ± 0.13	0.070
Liver	0.012 ± 0.0024	0.021 ± 0.0061	0.014
Lower large intestine wall	0.015 ± 0.00077	0.014 ± 0.00091	0.067
Lungs	0.0044 ± 0.00054	0.0062 ± 0.00016	<0.0001
Muscle	0.0050 ± 0.00018	0.0074 ± 0.00025	<0.0001
Ovaries	0.015 ± 0.00064	0.014 ± 0.00083	0.14
Pancreas	0.014 ± 0.00085	0.018 ± 0.0015	0.00018
Red marrow	0.010 ± 0.00037	0.012 ± 0.00032	<0.0001
Osteogenic cells	0.017 ± 0.00094	0.016 ± 0.0019	0.43
Skin	0.010 ± 0.00054	0.0080 ± 0.00080	0.00019
Small intestine	0.014 ± 0.00047	0.015 ± 0.00049	0.0034
Spleen	0.014 ± 0.0011	0.018 ± 0.0022	0.00074
Stomach wall	0.013 ± 0.00065	0.014 ± 0.00041	0.0057
Testes	0.013 ± 0.00062	0.010 ± 0.0010	0.0012
Thymus	0.011 ± 0.00068	0.010 ± 0.0013	0.014
Thyroid	0.011 ± 0.00072	0.0094 ± 0.0014	0.017
Upper large intestine wall	0.014 ± 0.00046	0.015 ± 0.00045	0.0036
Urinary bladder wall	0.20 ± 0.087	0.081 ± 0.032	0.0037
Uterus	0.018 ± 0.0017	0.017 ± 0.0012	0.31
Total body	0.013 ± 0.00041	0.012 ± 0.00012	0.00073
Effective dose	0.024 ± 0.0041	0.022 ± 0.0042	0.58

* Unpaired, 2-tailed Student's *t*-test.

4. Discussion

VAP-1 targeted ligands are promising tools for PET imaging of inflammation. In this study, we compared the VAP-1 targeting tracers ^{68}Ga -DOTA-Siglec-9 and ^{18}F -FDR-Siglec-9 in the detection of experimental inflammation in rats and mice and also estimated the radiation burden to humans. We found that the uptake of both tracers was higher in skin/muscle inflammation than in healthy muscle, and in atherosclerotic rather than in nonatherosclerotic arterial walls. Both tracers resulted in a low radiation exposure, but the lower-cost and more straightforward radiolabeling procedures support the

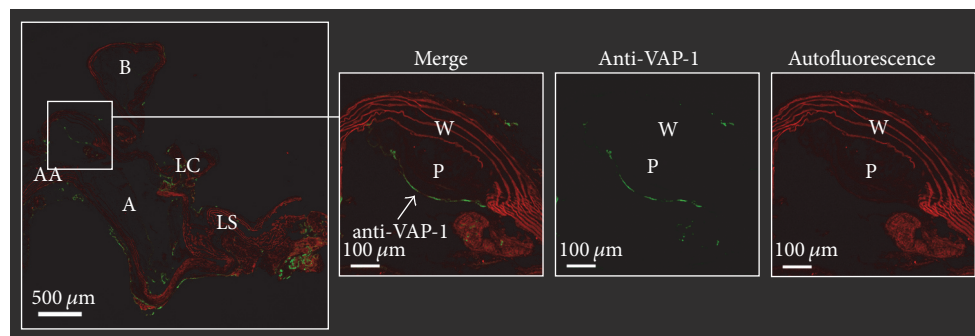
potential use of ^{68}Ga -DOTA-Siglec-9 for PET imaging of patients with inflammation.

The tested tracers have a similar amino acid sequence but a differently conjugated peptide structure (^{68}Ga -DOTA versus ^{18}F -FDR). We hypothesized that the ^{18}F -labeled tracer would provide improved visualization of inflammatory foci because it has a lower positron range (0.27 mm) than ^{68}Ga (1.05 mm). For PET imaging, ^{18}F ($t_{1/2} = 110$ min, $\beta^+_{\text{max}} = 640$ keV, $\beta^+ = 97\%$) is an ideal radionuclide, providing a high spatial resolution in the resulting images. ^{68}Ga ($t_{1/2} = 68$ min, $\beta^+_{\text{max}} = 1899$ keV, $\beta^+ = 89\%$) is a positron-emitting

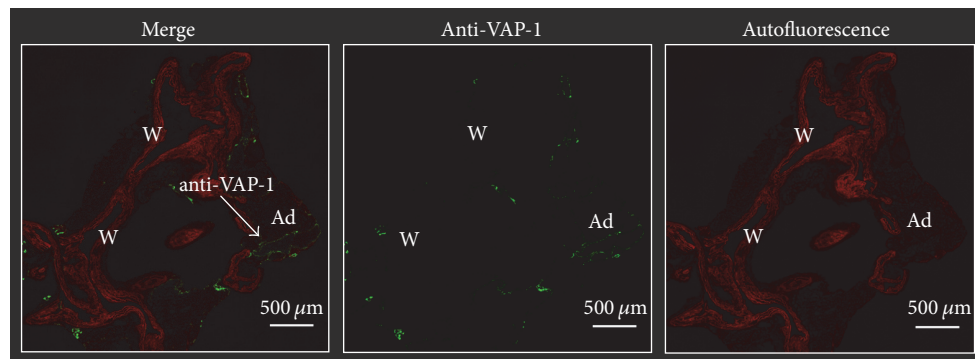
TABLE 5: *Ex vivo* biodistribution (% ID/g) of ^{18}F -FDR-Siglec-9 at 25 min after injection in atherosclerotic and control mice.

Organ	LDLR ^{-/-} ApoB ^{100/100} (n = 19)	C57BL/6N (n = 13)	P value*
Aorta	0.93 ± 0.38	0.52 ± 0.23	0.0014
Adipose tissue, BAT	0.57 ± 1.4	0.45 ± 0.13	0.16
Adipose tissue, WAT	0.72 ± 0.66	0.63 ± 0.37	0.67
Blood	3.2 ± 0.82	2.1 ± 0.59	0.00025
Brain	0.15 ± 0.060	0.11 ± 0.048	0.026
Heart	0.62 ± 0.28	0.34 ± 0.082	0.0019
Kidney	44 ± 26	43 ± 25	0.86
Liver	3.0 ± 0.97	3.5 ± 2.3	0.37
Lungs	2.4 ± 1.1	1.5 ± 0.45	0.011
Muscle	0.62 ± 0.20	0.43 ± 0.13	0.0056
Pancreas	0.82 ± 0.28	0.57 ± 0.18	0.011
Plasma	5.7 ± 1.4	3.8 ± 0.62	0.00015
Small intestine	1.6 ± 0.49	0.79 ± 0.29	<0.0001
Spleen	1.1 ± 0.28	0.62 ± 0.32	0.054
Thymus	0.69 ± 0.19	0.43 ± 0.089	<0.0001
Urine	470 ± 370	610 ± 340	0.27

% ID/g = percentage of injected radioactivity dose per gram of tissue; BAT = brown adipose tissue; WAT = white adipose tissue. *Unpaired, 2-tailed Student's *t*-test.



(a)



(b)

FIGURE 3: VAP-1 immunofluorescence of (a) atherosclerotic LDLR^{-/-} ApoB^{100/100} and (b) C57BL/6N control mice aortas. AA: ascending aorta, A: aortic arch, LC: left common carotid artery, LS: left subclavian artery, P: plaque, W: wall, and Ad: adipocyte.

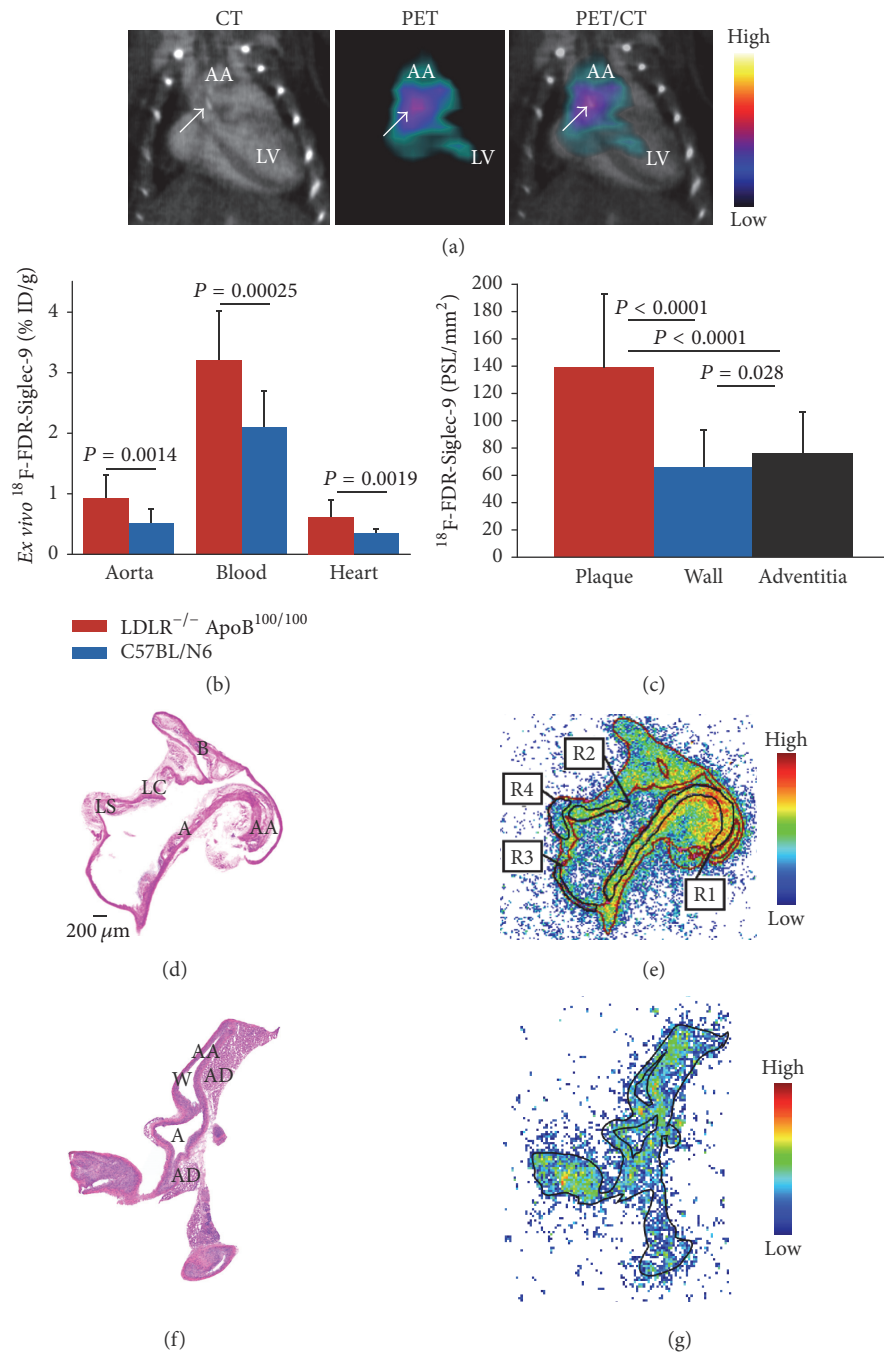


FIGURE 4: (a) The ^{18}F -FDR-Siglec-9 PET/CT detects atherosclerotic plaques in the aortic root with a target-to-background ratio ($\text{SUV}_{\text{max,aortic arch}}/\text{SUV}_{\text{mean,blood}}$) of 1.6. The blood radioactivity concentration was determined from heart left ventricle using contrast-enhanced CT as anatomical reference. Arrow shows calcified atherosclerotic plaques in the aortic arch (a). (b) Ex vivo biodistribution of ^{18}F -FDR-Siglec-9 in LDLR^{-/-} ApoB^{100/100} ($n = 19$) and C57BL/N6 ($n = 13$) mice. (c) Quantification of ^{18}F -FDR-Siglec-9 binding on the autoradiography of atherosclerotic mice aortas ($n = 12$, P values one-way ANOVA with Tukey's correction). (d) Representative hematoxylin-eosin staining of a longitudinally sectioned LDLR^{-/-} ApoB^{100/100} mouse aorta and (e) a superimposed autoradiograph (red lines represent the borders of the hematoxylin-eosin image). R1 and R2 are regions of interest in the plaque (excluding the media), R3 is in normal vessel wall (no lesion formation), and R4 is in adventitia (mainly adipose tissue around the aorta). (f) Hematoxylin-eosin staining of a longitudinally sectioned healthy C57BL/6N control mouse aorta. (g) Superimposed autoradiograph and hematoxylin-eosin staining (the black line represents the borders of the hematoxylin-eosin image). A: arch; AA: ascending aorta; B: brachiocephalic artery; LC: left common carotid artery; and LS: left subclavian artery. PSL/mm^2 = photostimulated luminescence/ mm^2 normalized for injected radioactivity dose.

radiometal that is particularly suitable for the labeling of chelate-conjugated peptides. While production of ^{18}F requires a cyclotron, ^{68}Ga is produced with an easily accessible low-cost $^{68}\text{Ge}/^{68}\text{Ga}$ -generator [17].

Although the inflammation detection characteristics of ^{68}Ga -DOTA-Siglec-9 and ^{18}F -FDR-Siglec-9 were similar, the uptake of ^{18}F -FDR-Siglec-9 was higher in several nontarget tissues, including the control area. We do not have a clear explanation for the distinctive distribution patterns, particularly in the liver, pancreas, heart, and kidneys, but suspect that they were at least partly due to the sugar moiety. Similar results have been observed with ^{68}Ga -DOTANOC and ^{18}F -FDR-NOC [18]. ^{68}Ga -DOTA-Siglec-9 and ^{18}F -FDR-Siglec-9 showed comparable *in vivo* imaging of inflammation in the rat model. The difference in the control area between the two tracers might at least partly be explained by the higher blood pool radioactivity of ^{18}F -FDR-Siglec-9. Although both ^{68}Ga -DOTA-Siglec-9 and ^{18}F -FDR-Siglec-9 clearly delineated inflamed area by *in vivo* PET, the ^{18}F -FDG uptake was higher ($\text{SUV}_{\text{mean}} 2.0 \pm 0.52$ at 90 min after injection) as reported in our previous rat studies with turpentine-induced inflammation [16].

As we earlier reported, the $\text{LDLR}^{-/-}\text{ApoB}^{100/100}$ mice expressed VAP-1 on endothelial cells lining the inflamed atherosclerotic lesions, while normal vessel walls in the aortas of C57BL/6N mice were VAP-1-negative [4]. In atherosclerotic mice, the aortic uptake of ^{18}F -FDR-Siglec-9 was comparable to the previously reported uptake of ^{68}Ga -DOTA-Siglec-9 [4]. With both tracers, the atherosclerotic lesions in mice were best detectable by *in vivo* PET/CT imaging at 10–20 min after injection. Autoradiography revealed that the plaque-to-healthy vessel wall ratios were slightly higher with ^{68}Ga -DOTA-Siglec-9 than with ^{18}F -FDR-Siglec-9, although both were close to the previously reported ratio for ^{18}F -FDG (2.3 ± 0.5) in a $\text{LDLR}^{-/-}\text{ApoB}^{100/100}$ model [13].

In general, *in vivo* PET imaging of such a small target as atherosclerotic lesion in mice aorta is very challenging. When size of the imaged structures is smaller than the spatial resolution of the scanner, spillover from adjacent tissues and partial volume effect may invalidate the quantification of PET data in addition to cardiac and respiratory movement artifacts. Although small-animal PET/CT image of atherosclerotic mouse showed hot spot in the lesion-rich aortic arch (Figure 4(a)), the *ex vivo* biodistribution showed that uptake in the whole thoracic aorta was much lower than the blood level (Figure 4(b)). Therefore, it is possible that the PET/CT imaging of atherosclerotic lesions is interfered with blood pool radioactivity. On the contrary, in the rat model, the size and location of focal skin/muscle inflammation as well as the blood radioactivity concentration were much more favorable for reliable PET imaging of inflamed area. The PET scanning protocols and quantification methods used in this study were based on our previous research to allow direct comparison of new and already existing results.

Extrapolated from rat PET data, the human radiation dose estimates for both ^{68}Ga -DOTA-Siglec-9 (0.024 ± 0.0041 mSv/MBq) and ^{18}F -FDR-Siglec-9 (0.022 ± 0.0042 mSv/MBq) were similar to those for other ^{68}Ga -labeled tracers

(e.g., ^{68}Ga -DOTANOC, 0.025 mSv/MBq) or ^{18}F -FDG (0.019 mSv/MBq) [19, 20].

5. Conclusion

VAP-1 targeted ^{68}Ga -DOTA-Siglec-9 and ^{18}F -FDR-Siglec-9 peptides are potential tracers for the PET imaging of inflammation. The human radiation dose estimates indicate a low radiation exposure with either of the investigated tracers. The present study further strengthens the concept of a VAP-1-based imaging strategy for the *in vivo* detection of inflammation by PET.

Conflicts of Interest

Sirpa Jalkanen owns stocks in Faron Pharmaceuticals Ltd. The remaining authors have no conflicts of interest to disclose.

Acknowledgments

The authors thank Erica Nyman, Marja-Riitta Kajaala, Liisa Lempiäinen, Aake Honkaniemi, Timo Kattelus, and Sari Mäki for technical assistance. This research was conducted within the Finnish Centre of Excellence in Cardiovascular and Metabolic Diseases supported by the Academy of Finland, University of Turku, Turku University Hospital, and Åbo Akademi University. The research leading to these results was further supported by funding from the Academy of Finland (no. 258814), the State Research Funding (no. 13856), the Finnish Foundation for Cardiovascular Research, and the Sigri Jusélius Foundation.

References

- [1] C. Wu, F. Li, G. Niu, and X. Chen, "PET imaging of inflammation biomarkers," *Theranostics*, vol. 3, no. 7, pp. 448–466, 2013.
- [2] M. Salmi and S. Jalkanen, "Ectoenzymes in leukocyte migration and their therapeutic potential," *Seminars in Immunopathology*, vol. 36, no. 2, pp. 163–176, 2014.
- [3] T. Anger, F. K. Pohle, L. Kandler et al., "VAP-1, Eotaxin3 and MIG as potential atherosclerotic triggers of severe calcified and stenotic human aortic valves: Effects of statins," *Experimental and Molecular Pathology*, vol. 83, no. 3, pp. 435–442, 2007.
- [4] J. M. U. Silvola, H. Virtanen, R. Siitonen et al., "Leukocyte trafficking-associated vascular adhesion protein 1 is expressed and functionally active in atherosclerotic plaques," *Scientific Reports*, vol. 6, Article ID 35089, 2016.
- [5] A. Bulgarelli, A. A. Martins Dias, B. Caramelli, and R. C. Maranhão, "Treatment with methotrexate inhibits atherogenesis in cholesterol-fed rabbits," *Journal of Cardiovascular Pharmacology*, vol. 59, no. 4, pp. 308–314, 2012.
- [6] K. Aalto, M. Maksimow, M. Juonala et al., "Soluble vascular adhesion protein-1 correlates with cardiovascular risk factors and early atherosclerotic manifestations," *Arteriosclerosis, Thrombosis, and Vascular Biology*, vol. 32, no. 2, pp. 523–532, 2012.
- [7] H.-Y. Li, M.-S. Lin, J.-N. Wei et al., "Change of serum vascular adhesion protein-1 after glucose loading correlates to carotid intima-medial thickness in non-diabetic subjects," *Clinica Chimica Acta*, vol. 403, no. 1-2, pp. 97–101, 2009.

- [8] K. Aalto, A. Autio, E. A. Kiss et al., "Siglec-9 is a novel leukocyte ligand for vascular adhesion protein-1 and can be used in PET imaging of inflammation and cancer," *Blood*, vol. 118, no. 13, pp. 3725–3733, 2011.
- [9] X.-G. Li, A. Autio, H. Ahtinen et al., "Translating the concept of peptide labeling with 5-deoxy-5-[¹⁸F]fluororibose into preclinical practice: ¹⁸F-labeling of Siglec-9 peptide for PET imaging of inflammation," *Chemical Communications*, vol. 49, no. 35, pp. 3682–3684, 2013.
- [10] H. Ahtinen, J. Kulkova, L. Lindholm et al., "⁶⁸Ga-DOTA-Siglec-9 PET/CT imaging of peri-implant tissue responses and staphylococcal infections," *EJNMMI Research*, vol. 4, no. 1, article no. 45, pp. 1–11, 2014.
- [11] H. Virtanen, A. Autio, R. Siitonen et al., "⁶⁸Ga-DOTA-Siglec-9 - a new imaging tool to detect synovitis," *Arthritis Research & Therapy*, vol. 17, no. 1, article no. 308, 2015.
- [12] S. Yamada, K. Kubota, R. Kubota, T. Ido, and N. Tamahashi, "High accumulation of fluorine-18-fluorodeoxyglucose in turpentine-induced inflammatory tissue," *Journal of Nuclear Medicine*, vol. 36, no. 7, pp. 1301–1306, 1995.
- [13] J. M. U. Silvola, A. Saraste, I. Laitinen et al., "Effects of age, diet, and type 2 diabetes on the development and FDG uptake of atherosclerotic plaques," *JACC: Cardiovascular Imaging*, vol. 4, no. 12, pp. 1294–1301, 2011.
- [14] K. Mikkola, C.-B. Yim, V. Fagerholm et al., "⁶⁴Cu- and ⁶⁸Ga-labelled [Nle¹⁴,Lys⁴⁰(Ahx-NODAGA)NH₂]-exendin-4 for pancreatic beta cell imaging in rats," *Molecular Imaging and Biology*, vol. 16, no. 2, pp. 255–263, 2014.
- [15] M. Merinen, H. Irjala, M. Salmi, I. Jaakkola, A. Hänninen, and S. Jalkanen, "Vascular adhesion protein-1 is involved in both acute and chronic inflammation in the mouse," *The American Journal of Pathology*, vol. 166, no. 3, pp. 793–800, 2005.
- [16] A. Autio, T. Ujula, P. Luoto, S. Salomäki, S. Jalkanen, and A. Roivainen, "PET imaging of inflammation and adenocarcinoma xenografts using vascular adhesion protein 1 targeting peptide ⁶⁸Ga-DOTAVAP-P1: Comparison with ¹⁸F-FDG," *European Journal of Nuclear Medicine and Molecular Imaging*, vol. 37, no. 10, pp. 1918–1925, 2010.
- [17] A. Sanchez-Crespo, "Comparison of Gallium-68 and Fluorine-18 imaging characteristics in positron emission tomography," *Applied Radiation and Isotopes*, vol. 76, pp. 55–62, 2013.
- [18] P. Rinne, S. Hellberg, M. Kiugel et al., "Comparison of somatostatin receptor 2-targeting pet tracers in the detection of mouse atherosclerotic plaques," *Molecular Imaging and Biology*, vol. 18, no. 1, pp. 99–108, 2016.
- [19] C. Pettinato, A. Sarnelli, M. Di Donna et al., "⁶⁸Ga-DOTANOC: Biodistribution and dosimetry in patients affected by neuroendocrine tumors," *European Journal of Nuclear Medicine and Molecular Imaging*, vol. 35, no. 1, pp. 72–79, 2008.
- [20] International Commission on Radiological Protection Publication 80. "Recalculated dose data for 19 frequently used radiopharmaceuticals from ICRP publication 53". *Annals of the ICRP* ICRP. vol. 28 pp. 47–83 1998.

Review Article

In Vivo PET Imaging of Adenosine 2A Receptors in Neuroinflammatory and Neurodegenerative Disease

Anna Vuorimaa,^{1,2} Eero Rissanen,^{1,2} and Laura Airas^{1,2}

¹Turku PET Centre, Turku University Hospital and University of Turku, Turku, Finland

²Division of Clinical Neurosciences, Turku University Hospital and University of Turku, Turku, Finland

Correspondence should be addressed to Anna Vuorimaa; annavuo@utu.fi

Received 10 August 2017; Accepted 18 October 2017; Published 20 November 2017

Academic Editor: Weibo Cai

Copyright © 2017 Anna Vuorimaa et al. This is an open access article distributed under the Creative Commons Attribution License, which permits unrestricted use, distribution, and reproduction in any medium, provided the original work is properly cited.

Adenosine receptors are G-protein coupled P1 purinergic receptors that are broadly expressed in the peripheral immune system, vasculature, and the central nervous system (CNS). Within the immune system, adenosine 2A (A_{2A}) receptor-mediated signaling exerts a suppressive effect on ongoing inflammation. In healthy CNS, A_{2A} receptors are expressed mainly within the neurons of the basal ganglia. Alterations in A_{2A} receptor function and expression have been noted in movement disorders, and in Parkinson's disease pharmacological A_{2A} receptor antagonism leads to diminished motor symptoms. Although A_{2A} receptors are expressed only at a low level in the healthy CNS outside striatum, pathological challenge or inflammation has been shown to lead to upregulation of A_{2A} receptors in extrastriatal CNS tissue, and this has been successfully quantitated using *in vivo* positron emission tomography (PET) imaging and A_{2A} receptor-binding radioligands. Several radioligands for PET imaging of A_{2A} receptors have been developed in recent years, and A_{2A} receptor-targeting PET imaging may thus provide a potential additional tool to evaluate various aspects of neuroinflammation *in vivo*. This review article provides a brief overview of A_{2A} receptors in healthy brain and in a selection of most important neurological diseases and describes the recent advances in A_{2A} receptor-targeting PET imaging studies.

1. Introduction

Adenosine is a highly bioactive molecule, which is stored inside cells as adenosine triphosphate (ATP) and transported to the extracellular space by transporter molecules or catabolized into adenosine extracellularly by ectoenzymes CD39 and CD73 [1, 2]. It is rapidly transported back into cells and degraded into inosine or phosphorylated back to adenosine monophosphate (AMP) by adenosine deaminase and adenosine kinase, respectively [1]. Within the central nervous system (CNS), neurons and glia release adenosine, and concentration of adenosine increases in the extracellular space following ATP release during inflammation or cellular trauma [3]. Adenosine is ubiquitous, but short-lived [4]. It confers its biological effects locally via four adenosine-binding purinergic P1 receptors: A_1 , A_{2A} , A_{2B} , and A_3 [1]. This leads to physiological regulation of a variety of important CNS functions, such as modulation of neuronal excitability, release and uptake of neurotransmitters, and modification of synaptic plasticity [5–9]. In addition, adenosine receptors

have a vasoactive function [10] and an important role in controlling inflammatory events [11]. In particular, signaling through the adenosine 2A (A_{2A}) receptor has been described as a potent regulator of inflammation [12]. In healthy CNS, A_{2A} receptor expression is the greatest in the neurons of the basal ganglia, where it is involved in motor control in conjunction with dopamine 2 (D_2) receptors, but under pathological conditions, A_{2A} receptor expression has been demonstrated also in brain areas outside the striatum [13]. Importantly, pharmacological targeting of A_{2A} receptors using antagonists or agonists may have important therapeutic implications in several CNS diseases [14]. A_{2A} receptor-binding radioligands have enabled *in vivo* positron emission tomography (PET) imaging of A_{2A} receptor expression. The human A_{2A} receptor PET studies have focused either on the striatal neuronal A_{2A} receptor expression, relevant to movement disorders [15, 16], or on A_{2A} receptor upregulation in the white matter in the context of neuroinflammatory disease [13]. This review will provide a brief overview of A_{2A} receptors in healthy brain and will describe their involvement

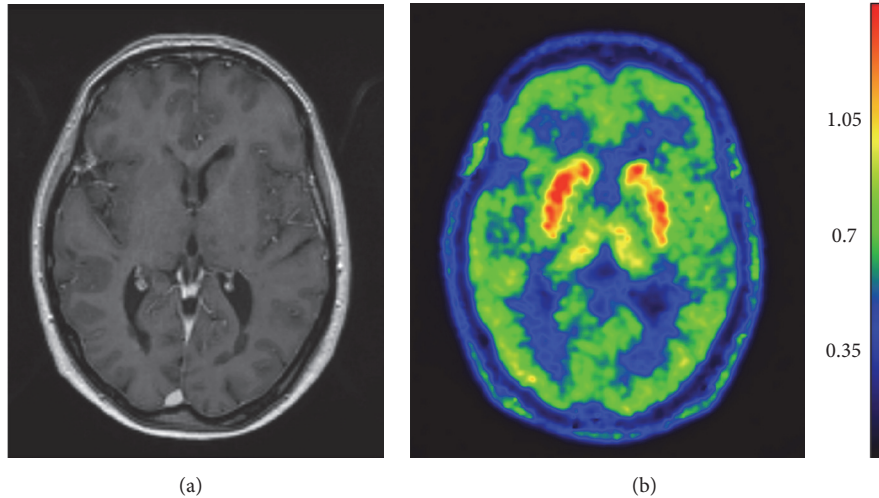


FIGURE 1: MRI and $[^{11}\text{C}]\text{TMSX}$ PET images of a healthy subject. Axial T1 gadolinium-enhanced weighted MR image (a) and corresponding parametric $[^{11}\text{C}]\text{TMSX}$ PET image (b). $[^{11}\text{C}]\text{TMSX}$ uptake is visualized as voxelwise distribution volume (V_T) denoted by the color scale on the right. Strong binding to A_{2A} receptors is seen in the striatum, where A_{2A} receptors are expressed on striatopallidal medium spiny neurons.

in a selection of most important neurological diseases, such as Parkinson's disease (PD), Huntington's disease (HD), stroke, and multiple sclerosis (MS). The role of *in vivo* PET imaging in advancing the understanding of the A_{2A} receptor biology within the CNS will be discussed.

2. A_{2A} Receptor Expression in Various CNS Compartments and Cell Types

2.1. Neurons. Adenosine receptors are far more abundant in the brain than in any other organ [17]. In healthy brain, A_{2A} receptor expression is most prominent in neurons of the basal ganglia (Figure 1) [18, 19]. A_{2A} receptors are also expressed in neurons in the neocortex and the limbic cortex [20–22], where they are predominantly present in nerve terminals, albeit with a density 20 times lower than that found in the basal ganglia [20]. The distribution of A_{2A} receptors is similar in rodents and humans [23, 24]. However, the level of extrastriatal A_{2A} receptor expression appears to be higher in humans than in rodents [18]. In the basal ganglia, the A_{2A} receptors are colocalized with dopamine 2 receptors in the striatopallidal gamma-aminobutyric acid (GABA)ergic neurons containing enkephalin [18, 25]. A_{2A} receptors are mostly localized postsynaptically [26] but are also found presynaptically on glutamatergic nerve terminals, where they contact the direct-pathway medium spiny neurons [27] and can form heteromers with A_1 receptors [9]. A_{2A} receptor antagonists have also been found to modify the N-methyl-D-aspartic acid (NMDA) receptor subunit composition in transgenic R6/2 mice [28]. The ability of A_{2A} receptors to control the release of glutamate in the cerebral cortex [8, 29, 30], hippocampus [21, 22, 31], and striatum [32–38] has led to the hypothesis that the reduction in glutamate release might be the explanation for the neuroprotective effects of A_{2A} receptor antagonism [39, 40]. The inhibition of glutamate release by A_{2A} receptor antagonism seems, however, strongly

time dependent in relation to lesion formation and animal age. Quinolinic acid (QA) induced glutamate release is almost completely blocked in rat striatum by pretreatment with A_{2A} receptor antagonist SCH58261 [39] but this effect of A_{2A} receptor antagonist is reversed two weeks after QA lesion, when SCH58261 significantly increases glutamate outflow [37]. Similarly, spontaneous outflow of glutamate in response to SCH58261 treatment in young rats is different from that in aged ones [35]. Future studies are awaited to confirm the usefulness of A_{2A} receptor antagonism in protection from glutamate-related neurotoxicity in various neurodegenerative conditions.

2.2. Endothelial Cells. Brain endothelial cells, together with astrocytes and pericytes, form the blood-brain barrier (BBB), a physical barrier that protects the CNS against blood pathogens and prevents immune cell infiltration [41]. Endothelial cells of the BBB are linked together with occludins, claudins, and junctional adhesion molecules (JAMs) that form the tight junctions that inhibit almost all the paracellular transportation through the BBB [42]. Although the BBB allows less passing than most endothelial barriers under normal circumstances, during CNS infection, trauma or autoimmunity immune cells from the periphery gain access to the CNS parenchyma [43]. One possible mediator controlling BBB permeability is the adenosine A_{2A} receptor [44].

A_{2A} receptors are expressed on human brain endothelial cells together with adenosine-forming enzymes, CD39 and CD73 [45–47]. A_{2A} receptor expression has also been described on mouse and rat brain endothelial cells [48]. Evidence from animal studies suggests that activation of the A_{2A} receptors promotes an increase in BBB permeability to macromolecules [48]. However, another study suggested that the increased production of adenosine via induction of the adenosine-generating ectoenzyme CD73 on primary human brain endothelial cells after interferon beta (IFN- β) treatment

leads to improved barrier function, but the target molecule of adenosine in this particular setting remains uncertain [49]. Activation of A_{2A} receptors with a broad-spectrum adenosine receptor agonist 5'-*N*-ethylcarboxamidoadenosine (NECA) or A_{2A} receptor-specific agonist Lexiscan (regadenoson, FDA approved for use as a pharmacological stress agent for radionuclide myocardial perfusion imaging) increased BBB permeability to macromolecules such as 10 kD dextrans (NECA and Lexiscan) and 70 kD dextrans (NECA) and antibodies to β -amyloid (NECA) *in vivo* [48]. Increase in barrier permeability after A_{2A} receptor agonist treatment was linked to changes in cell cytoskeleton structure, measured as decreased transendothelial cell electrical resistance (TEER) and actomyosin stress fiber formation, as well as decreased expression of tight junctions molecules, most strongly occludin [48]. Similar cytoskeletal changes were observed in primary human brain endothelial cells after treatment with A_{2A} receptor agonist [45]. Furthermore, A_{2A} receptor agonist treatment has been shown to promote paracellular transendothelial migration of lymphocytes through a model of human BBB [45]. In peripheral blood vessels the role of A_{2A} receptors in the control of vessel permeability remains less clear, as A_{2A} receptor agonists have been shown, depending on conditions, to either increase or decrease endothelial permeability [50–54].

2.3. A_{2A} Receptor in Choroid Plexus. In order for immune cells to gain access to the CNS, they need to cross either of the protective barriers between the periphery and CNS: the BBB or the blood-cerebrospinal fluid barrier (BCSFB). The BCSFB is formed by the choroid plexus and is made up of fenestrated capillaries, which are surrounded by parenchyma covered with epithelial cells that, like the BBB endothelial cells, are joined together by tight junctions [55, 56]. A_{2A} receptors are expressed on choroid plexus endothelial cells, where they seem to regulate lymphocyte migration into the CNS [57, 58]. This was also shown to contribute to the development of experimental autoimmune encephalomyelitis (EAE), the animal model of MS [57]. Here, ATP released from damaged cells within the CNS is hydrolyzed to adenosine by choroid-plexus-expressing ectoenzymes CD39 and CD73. Adenosine binds to the A_{2A} receptor and facilitates the lymphocyte entry via enhancing CX3CL1 expression at the choroid plexus [59]. Lack of A_{2A} receptors results in reduced lymphocyte entry [57].

2.4. A_{2A} Receptors in Glia. A role for A_{2A} receptors has been described in oligodendrocyte differentiation. A_{2A} receptor expression has been demonstrated on oligodendrocyte precursor cells [60], and A_{2A} receptor signaling seems to inhibit oligodendrocyte progenitor cell maturation, whereas A_1 receptor signaling promotes it [61, 62]. Under chronic inflammatory or neurodegenerative conditions, A_{2A} receptor expression has been demonstrated also in other CNS areas and cell types, such as microglia [63, 64] and astrocytes [65]. In several neurodegenerative CNS diseases astrogliaosis can contribute to the disease pathogenesis by contributing to cellular death. Interestingly, A_{2A} receptor antagonism

might contribute to control of astrogliaosis, as A_{2A} antagonists SCH58261 and KW6002 were shown to significantly inhibit signs of astrogliaosis in a primary cell culture of striatal rat astrocytes [66]. Similarly, A_{2A} receptor activation led to morphological changes in cultured microglia indicative of further microglial activation, a phenomenon which could be blocked using A_{2A} receptor antagonists [63]. Hence, astrocytes and microglia might provide the central link between A_{2A} receptor-mediated effects in neuroinflammatory and neurodegenerative diseases, which will be discussed in the next chapters.

3. A_{2A} Receptors in Neurodegenerative Disease

3.1. Parkinson's Disease. A_{2A} receptors are abundantly expressed on neurons in the striatum [18, 19], where they colocalize with dopamine 2 receptors on the GABAergic striatopallidal neurons of the “indirect pathway” [25, 67]. In the classical model, direct and indirect pathways work together in fine-tuning movement by exciting and inhibiting the cerebral motor cortex, respectively. Presently, it is acknowledged that complex interplay is likely to occur between these two pathways [68]. A_{2A} and D_2 receptors are functionally antagonistic, as A_{2A} receptor antagonist can exert a similar effect on motor control as D_2 agonists. This effect is explained by the receptors' opposing effect on adenylyl cyclase and by their ability to form heteromers [69, 70]. In PD, loss of dopaminergic input from substantia nigra leads to unbalance of the sensitive motor behavior controlling system. Initially effective solution to depletion of dopamine in PD has been dopamine replacement therapy by levodopa. However, in chronic levodopa treatment, patients start experiencing dyskinesias and symptoms of “wearing-off”; that is, there will be motor fluctuations as the effective time of the medication shortens [71]. Because A_{2A} receptor antagonists exert suppression similar to D_2 receptor activation on the medium spiny neurons of the indirect pathway, they have been studied as an add-on therapy to levodopa in PD [72].

PET imaging using A_{2A} receptor-binding radioligands has been used to evaluate striatal A_{2A} receptor expression in PD *in vivo*. Distribution volume ratio (DVR) of [11 C]TMSX ([7-*N*-methyl- 11 C]-(*E*)-8-(3,4,5-trimethoxystyryl)-1,3,7-trimethylxanthine) binding in the putamen was shown to be higher in PD patients with dyskinesias (disease duration: 11.1 ± 7.2 years) compared to healthy controls [16]. On the other hand, in drug-naïve patients (disease duration: 2.0 ± 1.2 years) there was no significant difference in [11 C]TMSX binding compared to healthy controls. [11 C]TMSX DVR was, however, increased in the putamen in a follow-up scan after approximately a year of induction of antiparkinsonian therapy compared to the baseline scans, despite the absence of clinical dyskinesias [16]. Similarly, using another A_{2A} receptor-binding radioligand, [11 C]SCH442416, and PET imaging, a significant increase was found in the binding potential in the putamen and the nucleus caudatus in PD patients with levodopa-induced dyskinesias (disease duration: 13.2 ± 5.6) compared to PD patients with levodopa

treatment without dyskinesias (disease duration: 6.2 ± 3.4) and to healthy controls [15].

3.2. Huntington's Disease. Brain pathology in HD is characterized by striatal atrophy with a selective loss of medium spiny neurons [73]. Interestingly, neuropathological studies have demonstrated a marked loss of striatal A_{2A} receptors in early stages of HD [23, 74], and similar loss of A_{2A} receptors is reported in transgenic mouse models of HD [75–77]. Moreover, expression of mutant Huntingtin was shown to lead to reduced A_{2A} receptor expression in cell cultures by regulating transcription of the A_{2A} receptor gene [78]. Finally, A_{2A} receptor gene (ADORA2A) rs 5751876 genotype was shown to affect the age of onset of HD in humans [79]. In transgenic HD animal models, blockade of A_{2A} receptors rescues cognitive performance impaired by the disease [80, 81]. A_{2A} receptor agonists on the other hand have shown to reverse motor deficits [77], whereas blockade of the receptor worsens motor performance [76, 82]. *In vivo* A_{2A} receptor-targeting PET imaging using [11 C]KF18446 has been used to demonstrate reduced A_{2A} receptor expression in an animal model of HD [83]. Here, the binding potential of [11 C]KF18446 was significantly decreased in the quinolinic acid-lesioned striatum. Thus, *in vivo* imaging of A_{2A} receptors in HD patients might provide insight into the pathologic changes in A_{2A} receptors in different stages of the disease. Moreover, PET imaging of A_{2A} receptors could be availed for interrogating treatment response to possible adenosine signaling targeting therapies in HD. To our knowledge, no A_{2A} receptor-targeting PET imaging has yet been performed in HD patients.

3.3. Alzheimer's Disease. A_{2A} receptors are upregulated in the frontal cortex and hippocampus in Alzheimer's disease (AD) [65, 84] and likewise in animal models of AD [5, 85]. *In vitro*, A_{2A} receptor antagonists prevent amyloid β ($A\beta$) induced neurotoxicity and synaptotoxicity [5, 86–88], whereas A_{2A} receptor agonists increase $A\beta$ production [89]. In various animal models of AD, blockade or genetic deletion of A_{2A} receptors enhances memory function [5, 90–92]. A_{2A} receptor activation is in fact sufficient to disrupt memory even in healthy rats [93, 94]. On the other hand, treatment of APP/PS1 mice with A_{2A} receptor antagonist was shown to increase $A\beta_{42}$ accumulation in cortical neurons (but not in the hippocampus) [95]. A_{2A} receptor activation specifically in the hippocampus was shown to impair memory, whereas in the nucleus accumbens it only induced locomotor activity instead [94]. Interestingly, activation of chimeric rhodopsin- A_{2A} receptor by light stimulated the cAMP-PKA pathway and increased CREB and c-Fos expression in the hippocampus but stimulated the MAPK signaling pathway in the nucleus accumbens [94]. Finally, Orr et al. showed that selective deletion of A_{2A} receptors from astrocytes enhanced memory in an AD animal model [65]. Even though A_{2A} receptor antagonism or deletion in animal models of AD mainly appears to exert neuroprotective effects, the causal relationship between adenosine signaling and amyloid deposition, as well as disease progression, remains unclear. More efficient therapies for halting or slowing down the course of the disease

in AD are sorely needed, and anti- A_{2A} therapy appears as an intriguing option in this field. Before this, however, additional evidence of the role of A_{2A} receptors in AD as well as in other neurodegenerative diseases would be needed. Imaging A_{2A} receptors in different stages of the disease and in studying treatment response to novel emerging therapies would shed more light on the understanding of the disease pathology. Still, to our knowledge, there are as yet no *in vivo* PET studies of A_{2A} receptor expression in AD or in animal models of AD.

4. A_{2A} Receptors in Multiple Sclerosis

4.1. Pathological Characteristics of Progressive Multiple Sclerosis. MS is traditionally considered an autoimmune disease, where an immune attack towards myelin leads to demyelination and bouts of neurological symptoms [96]. Neuropathological studies have demonstrated that, in addition to the active focal inflammation, there is also an ongoing neurodegenerative process, which starts already early on in the relapsing remitting multiple sclerosis (RRMS) phase of the disease, in both the gray matter and the white matter, and leads to gradual axonal damage, neuronal loss, and CNS atrophy [97]. With time, the RRMS disease advances to a secondary progressive phase (SPMS), with an alteration in neuropathological findings [98]. In addition to the focal inflammatory lesions, increased spreading of the inflammatory process into the so-called normal appearing white matter (NAWM) with involvement of brain resident glial cells is seen [98]. This inflammation can be measured *in vivo* using translocator protein-18 kDa (TSPO) PET imaging [99, 100]. The widespread microglial activation presumably contributes to the ongoing neurodegenerative process leading to clinical disease progression, but in general the mechanisms of neurodegeneration in progressive MS are presently relatively poorly understood. Importantly, better understanding and better alternatives for *in vivo* measurement of the pathological processes leading to disease progression would enhance therapeutic development for this undertreated condition [101].

4.2. Evidence of the Role of A_{2A} Receptors in Multiple Sclerosis Pathogenesis. Direct data on the role of A_{2A} receptors in MS is still scarce, but *in vivo* PET imaging studies using the A_{2A} receptor-binding radioligand [11 C]TMSX have demonstrated that A_{2A} receptor expression is increased in the NAWM of patients with SPMS compared to age- and sex-matched controls (Figure 2) [13]. Importantly, increased binding in the NAWM correlated with increased clinical disability score (EDSS) and decreased fractional anisotropy (FA) in diffusion tensor imaging (DTI) of SPMS patients, suggesting that the A_{2A} receptors have a likely role in the disease pathogenesis. In respective areas of normal appearing MS brain, increased microglial activation has been demonstrated using TSPO-binding radioligand [11 C]PK11195 and PET [99]. The identity of A_{2A} receptor-expressing cells in the context of MS is yet to be confirmed. It is nevertheless plausible to hypothesize that activated glia could be among the cell types expressing A_{2A} receptor in the SPMS NAWM, as A_{2A} receptor expression on

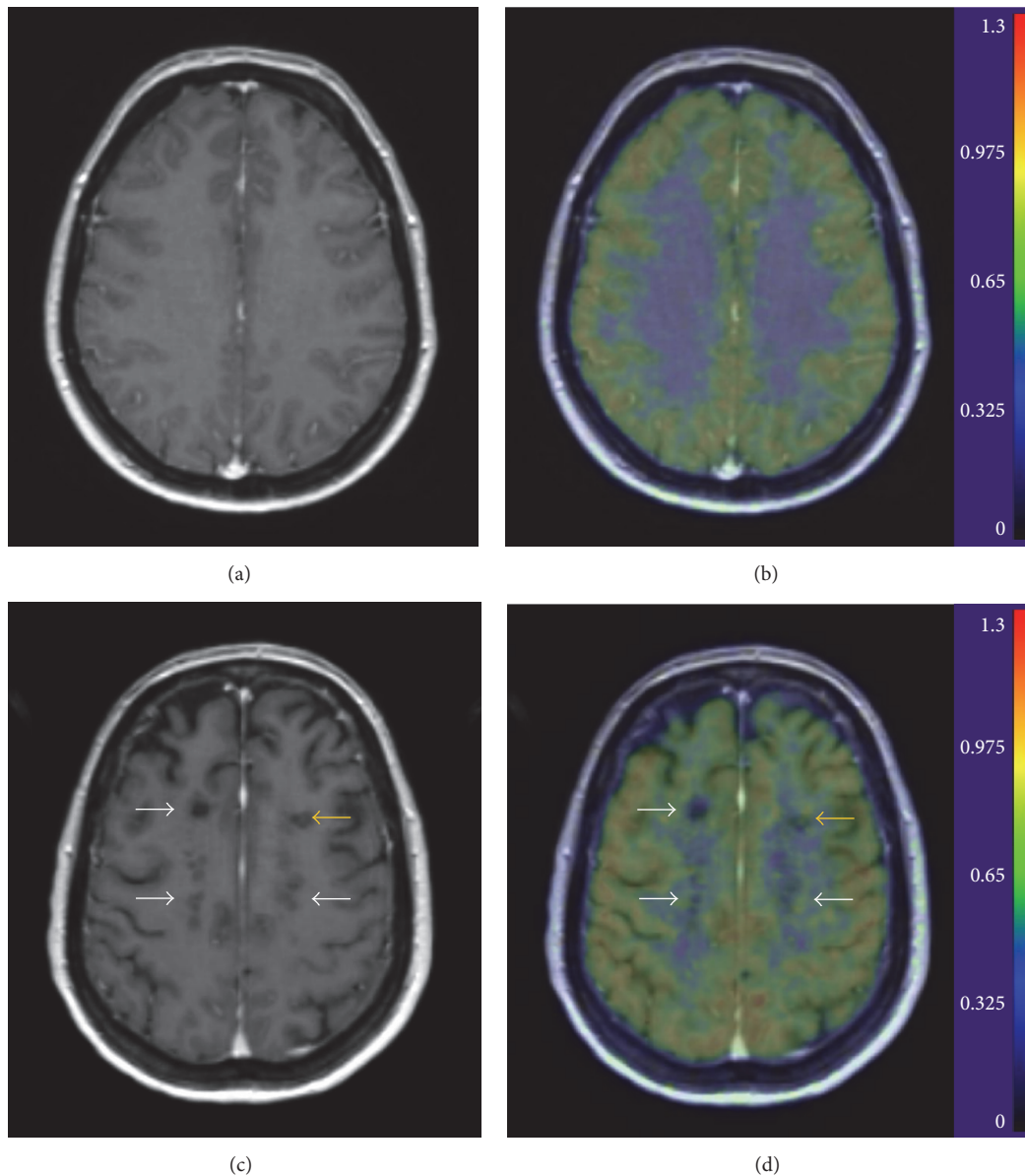


FIGURE 2: Brain MRI and $[^{11}\text{C}]\text{TMSX}$ PET images from a 45-year-old healthy female (a and b, resp.) and of a 48-year-old female with SPMS (disease duration: 6 years, EDSS 7.5) (c and d, resp.). The images represent axial views from gadolinium-enhanced T1 images (a and c) and parametric $[^{11}\text{C}]\text{TMSX}$ PET images with each voxel's intensity representing the distribution volume (V_T , ml/cm³) value of the ligand fused with the T1 image (b and d). A pattern of increased $[^{11}\text{C}]\text{TMSX}$ binding can be observed around the T1 hypointense lesions (white arrows) and within the mildly active plaque in the frontal white matter (yellow arrow) of the SPMS patient compared to the lower, homogeneous binding in the white matter of the healthy control. Figure reprinted with permission from Rissanen et al. (2013) [13].

activated glia has been demonstrated in other settings involving an inflammatory or neurodegenerative environment [63, 65, 102]. Interestingly, increased adenosine levels have been demonstrated in the cerebrospinal fluid and serum of MS patients compared to controls [103, 104]. Moreover, high consumption of coffee (caffeine is a nonspecific antagonist of A_1 and A_{2A} receptors) associates with decreased susceptibility risk of MS [105] and with reduced risk of progression of RRMS [106], also suggesting that A_{2A} receptor signaling might have a role in involvement of MS. No clinical trials targeting A_{2A} receptors in MS have been performed, but EAE

studies suggest that adenosine signaling might have a robust effect on CNS inflammation, as discussed below.

4.3. Evidence of the Role of A_{2A} Receptors in EAE. Treatment of EAE with A_{2A} receptor antagonists such as caffeine or SCH58261 has been shown to significantly reduce clinical scores in multiple mice and rat models of EAE [57, 58, 107–109]. Accordingly, infiltration of inflammatory cells is decreased in the cerebral cortex and spinal cord [58, 107, 109], and demyelination is reduced in these animals [107, 109]. Moreover, mice deficient in CD73 molecule, an ectoenzyme

that catalyzes ATP into adenosine, have significantly milder EAE disease and little immune cell infiltration [58]. This supports the notion that preventing stimulation of the A_{2A} receptors within the CNS helps ameliorate EAE.

Conversely and surprisingly, other studies show that genetic removal of A_{2A} receptors results in initial worsening of EAE, after which disease score returns to level of wild type controls [57, 102]. Here histopathology accordingly shows initial increased infiltration of CD4+ T lymphocytes and increased reactivity of microglial activation markers CD11b+/F480+ and Iba-1 in the brain and spinal cord [57, 110]. Interestingly, treatment with A_{2A} receptor agonists from time of immunization (day 0) reduces EAE scores [102, 111], but delayed treatment causes an opposite effect and exacerbates the disease. The opposite is seen with A_{2A} receptor antagonists: treatment with caffeine from day 0 leads to higher mean EAE scores and treatment from day 10 results in lower mean EAE scores [109].

5. A_{2A} Receptors in Ischemia and Stroke

Adenosine is excessively released from cells under ischemic conditions [3]. A_{2A} receptor expression in rat brain is increased in the striatum on neurons and microglia following cerebral ischemia [112]. A_{2A} receptors can be beneficially targeted under ischemic conditions, as A_{2A} receptor blockade by genetic deletion of the receptor or pharmacological inhibition protects against cerebral ischemia and ischemia-reperfusion injury in multiple animal studies [113–123]. The protective effect is possibly due to inhibition of glutamate outflow [30, 119]. Because global deletion of A_{2A} receptors seemed protective against ischemia, Yu et al. [124] tested the effect of selective deletion of A_{2A} receptors from bone marrow-derived cells (BMDC) and found that selective reconstitution of A_{2A} receptors on BMDCs reinstated the ischemic brain injury in global A_{2A} receptor knockout mice. Accordingly, selective lack of A_{2A} receptors in the BMDC compartment was sufficient to abolish the protective effect of A_{2A} receptor genetic deletion.

Although the literature on the beneficial effect of the A_{2A} receptor antagonists in ischemia is abundant, some studies suggest that the protective effect of the receptor blockade is lost following excessive reperfusion injury. A recent study suggests that, although A_{2A} receptor antagonists initially protect against transient ischemic injury, the protective effect is lost 7 days after ischemia despite chronic treatment with the antagonist (twice a day) [125]. Similarly, chronic 8-(3-chlorostyryl) caffeine treatment (s.c.) did not show any effect on infarct volume at 72 hours after permanent occlusion of the middle cerebral artery (MCAo) [126] and genetic deletion even worsened ischemic injury in young mice when assessed at 5 days after permanent occlusion of the common carotid artery [127]. Interestingly, A_{2A} receptor agonist CGS21680 (i.p.) was shown to reduce infarct volume (rat cortex but not striatum), microglial activation, and granulocyte infiltration into the brain following transient MCAo when assessed 7 days after ischemia [128].

6. A_{2A} Receptor-Binding Radioligands in Human PET Studies

PET imaging of A_{2A} receptors has been used in clinical research in humans but is not generally available or utilized in routine clinical practice. In the clinical diagnostics of neurodegenerative diseases, [123 I] β -CIT-SPECT (single-photon emission computed tomography) can be used for imaging dopamine transporter availability for differential diagnostics of early or atypical PD, [11 C]PIB for identifying amyloid pathology in early AD if routine morphological imaging is normal, and [18 F]FDG (2-deoxy-2-[fluorine-18]fluoro-D-glucose) for detecting hypometabolism and differentiating dementia with Lewy bodies (DLB) or frontotemporal lobe degeneration (FTD) from AD. In addition, [123 I] β -CIT-SPECT may aid in differentiating between DLB and AD. For imaging neuroinflammation, [18 F]FDG could theoretically be used for detecting hypermetabolism, but due to its unspecificity, it is of limited value in clinical practice compared to routine MRI imaging and cerebrospinal fluid (CSF) analyses. Thus, when imaging the detailed mechanisms of A_{2A} receptors in neuroinflammation, more specific probes, such as A_{2A} receptor-binding radioligands, are needed.

In the healthy CNS, human *in vivo* PET studies demonstrate greatest A_{2A} receptor ligand binding in the basal ganglia, whereas low radiotracer accumulation was shown in cortical areas and cerebellum [19, 129–131]. Subject age does not seem to affect striatal A_{2A} receptor radioligand binding [132]. Regarding evaluation of disease-related A_{2A} receptor expression *in vivo*, interest in PD therapy development has clearly been the driving force. Here, the main focus has been the variation in the A_{2A} receptor level within the striatum, according to disease stage and medication, as discussed above [15, 16, 133]. Several ligands for imaging the A_{2A} receptors have been developed and five of them, that is, [11 C]TMSX, [11 C]Preladenant, [11 C]SCH442416, [18 F]MNI-444, and [11 C]KW6002, have been tested in human subjects. Their chemical structures are presented in Figure 3. Below, we discuss the characteristics and the usability of these five radioligands.

6.1. [11 C]TMSX. [11 C]TMSX is a methylxanthine analog of KF17387. It is the most widely used A_{2A} receptor radioligand and its binding to A_{2A} receptors in humans has been described in the brain [134], myocardium [135, 136], and skeletal muscle [137, 138]. [11 C]TMSX (previously named KF18446) was first developed by Ishiwata et al. [139] in search of more A_{2A} receptor selective ligands after previously tested xanthine-type ligands had proven poor A_{2A} selectivity over A_1 and high nonspecific binding [140]. In the rat, [11 C]TMSX shows relatively low affinity for the A_{2A} receptor (Table 1) and about 270-fold selectivity to A_{2A} receptors over A_1 [139]. In human brain, A_{2A} receptor antagonist theophylline reduced [11 C]TMSX binding in the putamen by 4.5% and in the nucleus caudatus by 8%, but not in other areas outside of striatum [134]. Specific binding is highest in the striatum, with reported binding potential (BP) of 1.2–1.25 in the putamen [19] and DVR 1.67 in the striatum [141], followed

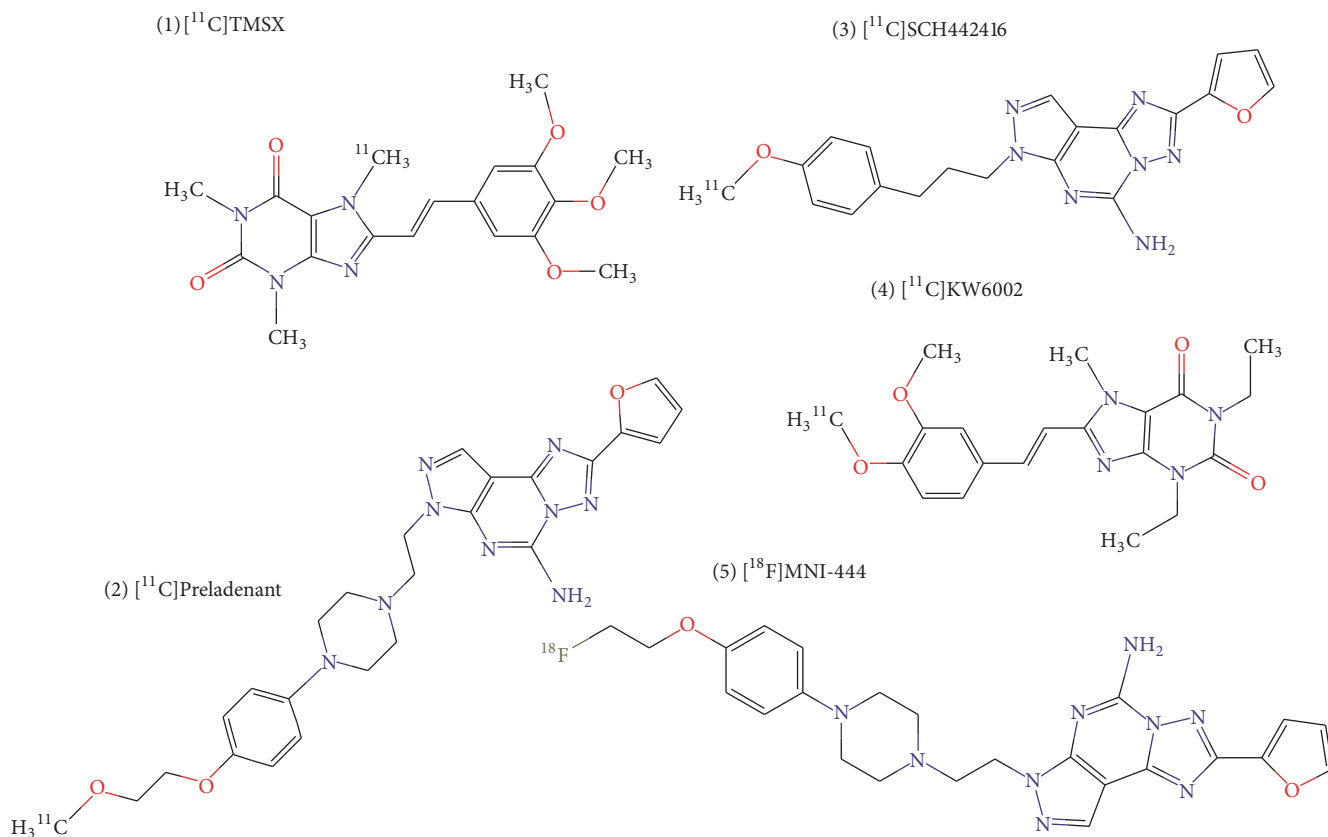


FIGURE 3: Chemical structures of A_{2A} receptor-binding radioligands. ((1) $[^{11}\text{C}]\text{TMSX}$, (2) $[^{11}\text{C}]\text{Preladenant}$, (3) $[^{11}\text{C}]\text{SCH442416}$, (4) $[^{11}\text{C}]\text{KW6002}$, (5) $[^{18}\text{F}]\text{MNI-444}$).

by lower binding in the thalamus, cerebellum, brainstem, and the cortex [19]. Both the centrum semiovale [142] and the cerebral cortex [132] have been used as reference for calculating TMSX binding. In addition, a semiautomated method using supervised clustering for the extraction of gray matter reference region has been developed [141].

Acquiring metabolite corrected plasma input function via arterial cannulation and repeated arterial sampling for the measurement of the radioligand activity and metabolism is considered the golden standard in brain PET image analyses especially with novel ligands without a priori knowledge of the ligand's kinetics and metabolism. However, this methodology can be unpleasant for the study subjects, may be prone to errors, and requires more expert personnel. Therefore, optional methods for obtaining plasma input function have been developed, including independent component analysis [142] and intersectional searching algorithm with averaging and clustering of PET data (robust EPISA) [150]. Importantly, plasma input methods can be affected by the fraction of radioactive metabolites. Using nonmetabolite corrected input has been reported to underestimate the $[^{11}\text{C}]\text{TMSX}$ distribution volume (V_T) by approximately 5% when compared with metabolite corrected plasma input [142]. Consequently, a noninvasive, validated method for obtaining metabolite corrected population-based plasma input function for $[^{11}\text{C}]\text{TMSX}$ has been developed and validated [141]. Dosing

and blood sampling under dimmed light is required due to $[^{11}\text{C}]\text{TMSX}$ photoisomerization.

6.2. $[^{11}\text{C}]\text{SCH442416}$. $[^{11}\text{C}]\text{SCH442416}$ (5-amino-7-(3-(4- $[^{11}\text{C}]\text{methoxy}$)phenylpropyl)-2-(2-furyl)pyrazolo[4,3-e]-1,2,4-triazolo[1,5-c]pyrimidine) was the first suitable non-anthine radioligand for the imaging of A_{2A} receptors. In a blocking study with vipadenant (an A_{2A} receptor antagonist), the highest radioligand binding measured as metabolite corrected V_T was seen in putamen ($V_T \sim 0.6 \text{ ml/cm}^3$), followed by caudate, nucleus accumbens, thalamus, and cerebellum ($V_T \sim 0.3 \text{ ml/cm}^3$) [149]. A_{2A} receptor blocking with vipadenant resulted in notable 3-4-fold reduction in total $[^{11}\text{C}]\text{SCH442416}$ binding (V_T) in striatal ROIs and also in about up to 2-fold reduction in cerebellum. Two later studies have shown very different specific binding potentials in the putamen when using the cerebellum as a reference region for the estimation of specific radioligand binding. Grachev et al. [148] reported the average binding potential (BP_{ND}) of five healthy subjects in the putamen as 2.47 ± 0.84 , whereas Ramlackhansingh et al. [15] reported the average BP_{ND} of six healthy controls (control group in a PD study) to be as low as 0.99 ± 0.21 . The intersubject variability was, however, fairly large in the aforementioned study (BP_{ND} 1.12–3.82 in the putamen) [148]. In both studies spectral analysis with metabolite corrected arterial plasma

TABLE 1: Currently available A_{2A} receptor binding radioligands.

	Affinity to A_{2A} (nM)/selectivity over other adenosine receptors	Characteristics of specific binding	$V_T(\text{putamen})$ with metabolite corrected arterial plasma input	A_{2A} receptor occupancy/blocking studies
[^{11}C]TMSX	$K_{i(\text{rat})} = 5.9/\text{selectivity over } A_1: 270\text{-fold}$ [139]	BP in anterior and posterior putamen: 1.25 ± 0.17 and 1.20 ± 0.16 , respectively (centrum semiovale as reference region) [19] DVR in striatum (clustered gray matter as reference region) 1.674 [141]	1.72 [134] 1.66–1.69 [19] 1.11 (striatum) [13]	Theophylline infusion reduced V_T in putamen by 4.5% and in the nucleus caudatus by 8%. No effect on other areas [134].
[^{11}C]Preladenant	$K_{i(\text{human})} = 1.1 K_{i(\text{rat})} = 2.5/\text{selectivity over (human) } A_1, A_{2B}, A_3: >1000\text{-fold}$ [143]	DVR in putamen 7.9 ± 2.3 (2 tissue model) 7.7 ± 1.9 (LGRM) (cerebellum as reference region) [129]	4.5 ± 1.3 [129]	Preladenant pretreatment reduced striatal V_T to level of extrastriatal binding in rhesus monkeys [144].
[^{18}F]MNI-444	$K_{i(\text{human recombinant})} = 2.8$ [145]	BP 4.7 ± 0.63 (cerebellum as reference region) [130]	3.26 ± 0.98 (with LGA) [130]	Preblocking with Tozadenant or Preladenant reduced total binding (SUV) to the level of extrastriatal (cerebellum) binding at the highest dose in rhesus monkeys. Also <15% reduction in cerebellar V_T with preblocking was observed [146].
[^{11}C]SCH442416	$K_{i(\text{human})} = 0.048/\text{selectivity over } A_1, A_{2B}, A_3 >20000\text{-fold}$ [147]	BP 0.99 ± 0.21 (cerebellum as reference region) [15] BP _{ND} 2.47 ± 0.84 (cerebellum as reference region) [148]	≈ 0.6 [149]	Preblocking with Preladenant led to dose-dependent A_{2A} receptor occupancy in the striatum (at 200 mg 88–105%), with corresponding decrease in [^{11}C]SCH442416 binding (BP _{ND}) [148]. Preblocking with vipadenant led to approximately 3–4-fold reduction [^{11}C]SCH442416 V_T in caudate and putamen and also to an up to 2-fold reduction in cerebellum. Dose-dependent receptor occupancy observed in putamen, caudate, nucleus accumbens, and cerebellum (on average from 74% to 95% with 2.5–100 mg dose), but not in thalamus [149].

input and cerebellum as a reference region were used for the quantification of specific radiotracer binding. Whether or not the region of interest (ROI) for cerebellum as reference region was defined in a similar manner in both studies—a possible source of discrepancy in the results—is not known. Finally, neither study reported the use of coffee or other caffeine-rich beverages prior to imaging session. In PET imaging studies using other A_{2A} ligands [13, 132], abstinence from caffeinated drinks has been required at least for 12 hours before the scan in order to rule out the possible blocking effect by caffeine.

6.3. [^{11}C]Preladenant. [^{11}C]Preladenant has high affinity for the A_{2A} receptor and >1000-fold selectivity to the A_{2A} over the other adenosine receptor subtypes [143]. First human study with [^{11}C]Preladenant was recently published [129]. Here, eight healthy male subjects were tested. Approximately 78% of Preladenant was unmetabolized at 60 minutes. In a rat study, 17% of the total radioactivity in the brain was due to radioactive metabolites at 60 minutes [151]. It will be thus necessary to take these radiometabolites into consideration in the kinetic modeling, with metabolite corrected input function. [^{11}C]Preladenant has a DVR of 7.9 ± 2.3 in the putamen and shows lower binding in the frontal cortex, thalamus, and cerebellum [129]. In rhesus monkeys, pretreatment with Preladenant before PET imaging with [^{11}C]Preladenant reduced striatal binding to extrastriatal levels but also reduced extrastriatal binding [144]. Cerebellum was nevertheless used as a reference region.

6.4. [^{18}F]MNI-444. [^{18}F]MNI-444 is the only [^{18}F]-labeled A_{2A} radioligand used in humans. It has relatively high affinity ($K_i = 2.8 \text{ nM}$) for the human recombinant A_{2A} receptor [145]. Reported BP_{ND} to putamen is 4.7 ± 0.63 , to globus pallidus 3.67 ± 0.69 , and to caudate 2.69 ± 0.74 [130]. Also in these studies, cerebellum was used as a reference region although a dose-independent reduction in cerebellar binding was found in preblocking with Tozadenant and Preladenant in the rhesus monkey [146].

6.5. [^{11}C]KW6002. In rodent and human studies, [^{11}C]KW6002 shows high binding in the striatum, but binding is also detected in the cerebellum and thalamus. In addition, preblocking with A_{2A} receptor antagonist KW6002 reduced [^{11}C]KW6002 binding to A_{2A} receptors in all studied brain regions [152, 153]. The authors concluded that the extrastriatal binding could be explained by binding to A_1 and A_{2B} receptors, although no effect of A_{2B} receptor antagonist on [^{11}C]KW6002 binding was found [153]. Due to its inadequate specificity, this ligand has not been further developed.

6.6. *Challenges in A_{2A} Receptor PET Imaging.* Even though the highest specific [^{11}C]TMSX binding occurs in putamen and caudate, there appears to be some specific, albeit lower, A_{2A} receptor binding in extrastriatal tissues such as cortical gray matter and cerebellum. The rate of specific binding, calculated as BP/V_T , has been reported to be as high as

53% in cerebellum and 37.8–42.7% in cerebral cortex for [^{11}C]TMSX [19]. Similarly, the previously mentioned blocking studies with newer A_{2A} receptor radioligands demonstrate the presence of some specific A_{2A} receptor binding in extrastriatal gray matter. Therefore, both cerebellum and cerebral cortex appear as less than optimal reference regions. Moreover, in diseases with widely spread pathology, such as MS, a common, anatomically defined reference region that is presumably free of disease pathology, inflammatory activity, and possible specific binding is difficult to find. Also, when studying diseases with predominant white matter affliction, such as MS, centrum semiovale is not a feasible reference region either, even though in healthy controls the A_{2A} receptor binding in central white matter is negligible. In order to overcome these issues, a method for supervised clustering of the reference region has been developed and validated for [^{11}C]TMSX based on the same algorithm used for [^{11}C]PK11195 studies (SuperPK software) [154]. Importantly, this method is based on predefined kinetic classes, where the shape of the time activity curve (TAC) in the gray matter reference region is considered to represent nonspecific binding as opposed to the high specific binding with different TAC shape [141].

7. Conclusion

There is increasing interest in the therapeutic development of A_{2A} receptor antagonists and agonists in a variety of neurological conditions. A_{2A} receptors are ubiquitously expressed in various areas of the CNS, but their significance in the context of the different CNS diseases still needs clarification. Pathological processes in CNS diseases are particularly difficult to investigate for reasons such as the difficulties in obtaining representative biopsies from the brain. PET imaging, on the other hand, provides an excellent opportunity to evaluate disease-specific pathology *in vivo*, by allowing quantitative study of the receptors of interest in an appropriate pathological environment *in situ*. With the increasing variety of A_{2A} receptor-binding PET ligands available for use in human *in vivo* PET imaging, there is good likelihood that PET imaging will improve our understanding of the involvement of A_{2A} receptors in the pathophysiology and pathogenesis of brain diseases, both in the neuronal compartment of the basal ganglia and in relation to inflammation, such as in progressive MS. Groups of patients can be studied cross sectionally at various stages of a given disease or, alternatively, PET imaging can be applied longitudinally to evaluate alterations in the A_{2A} receptor in the course of the disease or in response to treatment. PET imaging of neuroinflammation has relied heavily on TSPO-binding radioligands, but methodological challenges related to TSPO-imaging has directed the field to actively seek alternative imaging probes. A_{2A} receptor PET imaging provides one such alternative that is worth further exploring.

Conflicts of Interest

The authors declare that there are no conflicts of interest regarding the publication of this article.

Acknowledgments

This work was supported by the Finnish Academy, Sigrid Juselius Foundation, and the Finnish Parkinson Foundation.

References

- [1] B. B. Fredholm, A. P. Ijzerman, K. A. Jacobson, K. Klotz, and J. Linden, "International Union of Pharmacology. XXV. Nomenclature and classification of adenosine receptors," *Pharmacological Reviews*, vol. 53, no. 4, pp. 527–552, 2001.
- [2] B. B. Fredholm, Y. Chern, R. Franco, and M. Sitkovsky, "Aspects of the general biology of adenosine A2A signaling," *Progress in Neurobiology*, vol. 83, no. 5, pp. 263–276, 2007.
- [3] M. Idzko, D. Ferrari, and H. K. Eltzschig, "Nucleotide signalling during inflammation," *Nature*, vol. 509, no. 7500, pp. 310–317, 2014.
- [4] G. H. Möser, J. Schrader, and A. Deussen, "Turnover of adenosine in plasma of human and dog blood," *American Journal of Physiology*, vol. 256, no. 4 Pt 1, pp. C799–C806, 1989.
- [5] S. V. Da Silva, M. G. Haberl, P. Zhang et al., "Early synaptic deficits in the APP/PS1 mouse model of Alzheimer's disease involve neuronal adenosine A2A receptors," *Nature Communications*, vol. 7, Article ID 11915, 2016.
- [6] B. M. Fontinha, J. M. Delgado-García, N. Madroñal, J. A. Ribeiro, A. M. Sebastião, and A. Gruart, "Adenosine A(2A) receptor modulation of hippocampal CA3-CA1 synapse plasticity during associative learning in behaving mice," *Neuropsychopharmacology*, vol. 34, no. 7, pp. 1865–1874, 2009.
- [7] D. Boison, "Adenosine dysfunction in epilepsy," *Glia*, vol. 60, no. 8, pp. 1234–1243, 2012.
- [8] M. H. O'Regan, R. E. Simpson, L. M. Perkins, and J. W. Phillis, "The selective A2 adenosine receptor agonist CGS 21680 enhances excitatory transmitter amino acid release from the ischemic rat cerebral cortex," *Neuroscience Letters*, vol. 138, no. 1, pp. 169–172, 1992.
- [9] F. Ciruela, V. Casadó, R. J. Rodrigues et al., "Presynaptic control of striatal glutamatergic neurotransmission by adenosine A1-A2A receptor heteromers," *The Journal of Neuroscience*, vol. 26, no. 7, pp. 2080–2087, 2006.
- [10] V. Ralevic and W. R. Dunn, "Purinergetic transmission in blood vessels," *Autonomic Neuroscience: Basic and Clinical*, vol. 191, pp. 48–66, 2015.
- [11] C. Cekic and J. Linden, "Purinergetic regulation of the immune system," *Nature Reviews Immunology*, vol. 16, no. 3, pp. 177–192, 2016.
- [12] A. Ohta and M. Sitkovsky, "Role of G-protein-coupled adenosine receptors in downregulation of inflammation and protection from tissue damage," *Nature*, vol. 414, no. 6866, pp. 916–920, 2001.
- [13] E. Rissanen, J. R. Virta, T. Paavilainen et al., "Adenosine A2A receptors in secondary progressive multiple sclerosis: a [11C]TMSX brain PET study," *Journal of Cerebral Blood Flow & Metabolism*, vol. 33, no. 9, pp. 1394–1401, 2013.
- [14] J. Chen, P. K. Sonsalla, F. Pedata et al., "Adenosine A2A receptors and brain injury: broad spectrum of neuroprotection, multifaceted actions and "fine tuning" modulation," *Progress in Neurobiology*, vol. 83, no. 5, pp. 310–331, 2007.
- [15] A. F. Ramlackhansingh, S. K. Bose, I. Ahmed, F. E. Turkheimer, N. Pavese, and D. J. Brooks, "Adenosine 2A receptor availability in dyskinetic and nondyskinetic patients with Parkinson disease," *Neurology*, vol. 76, no. 21, pp. 1811–1816, 2011.
- [16] M. Mishina, K. Ishiwata, M. Naganawa et al., "Adenosine A2A receptors measured with [11C]TMSX pet in the striata of parkinson's disease patients," *PLoS ONE*, vol. 6, no. 2, Article ID e17338, 2011.
- [17] R. A. Cunha, "Adenosine Neuromodulation and Neuroprotection," in *Handbook of Neurochemistry and Molecular Neurobiology*, A. Lajtha and E. S. Vizi, Eds., pp. 255–273, Springer, Boston, Mass, USA, 2008.
- [18] P. Svenningsson, H. Hall, G. Sedvall, and B. B. Fredholm, "Distribution of adenosine receptors in the postmortem human brain: An extended autoradiographic study," *Synapse*, vol. 27, no. 4, pp. 322–335, 1997.
- [19] M. Mishina, K. Ishiwata, Y. Kimura et al., "Evaluation of distribution of adenosine A2A receptors in normal human brain measured with [11C]TMSX PET," *Synapse*, vol. 61, no. 9, pp. 778–784, 2007.
- [20] L. V. Lopes, L. Halldner, N. Rebola et al., "Binding of the prototypical adenosine A 2A receptor agonist CGS 21680 to the cerebral cortex of adenosine A 1 and A 2A receptor knockout mice," *British Journal of Pharmacology*, vol. 141, no. 6, pp. 1006–1014, 2004.
- [21] N. Rebola, C. R. Oliveira, and R. A. Cunha, "Transducing system operated by adenosine A2A receptors to facilitate acetylcholine release in the rat hippocampus," *European Journal of Pharmacology*, vol. 454, no. 1, pp. 31–38, 2002.
- [22] N. Rebola, A. M. Sebastião, A. De Mendonca, C. R. Oliveira, J. A. Ribeiro, and R. A. Cunha, "Enhanced adenosine A2A receptor facilitation of synaptic transmission in the hippocampus of aged rats," *Journal of Neurophysiology*, vol. 90, no. 2, pp. 1295–1303, 2003.
- [23] M. I. Martinez-Mir, A. Probst, and J. M. Palacios, "Adenosine A2 receptors: Selective localization in the human basal ganglia and alterations with disease," *Neuroscience*, vol. 42, no. 3, pp. 697–706, 1991.
- [24] S. N. Schiffmann, F. Libert, G. Vassart, and J.-J. Vanderhaeghen, "Distribution of adenosine A2 receptor mRNA in the human brain," *Neuroscience Letters*, vol. 130, no. 2, pp. 177–181, 1991.
- [25] S. N. Schiffmann, O. Jacobs, and J. J. Vanderhaeghen, "Striatal restricted adenosine A2 receptor (RDC8) is expressed by enkephalin but not by substance P neurons: an in situ hybridization histochemistry study," *Journal of Neurochemistry*, vol. 57, no. 3, pp. 1062–1067, 1991.
- [26] B. D. Hettinger, A. Lee, J. Linden, and D. L. Rosin, "Ultrastructural localization of adenosine A2A receptors suggests multiple cellular sites for modulation of GABAergic neurons in rat striatum," *Journal of Comparative Neurology*, vol. 431, no. 3, pp. 331–346, 2001.
- [27] C. Quiroz, R. Luján, M. Uchigashima et al., "Key modulatory role of presynaptic adenosine A2A receptors in cortical neurotransmission to the striatal direct pathway," *The Scientific World Journal*, vol. 9, pp. 1321–1344, 2009.
- [28] A. Martire, A. Ferrante, R. L. Potenza et al., "Remodeling of striatal NMDA receptors by chronic A(2A) receptor blockade in Huntington's disease mice," *Neurobiology of Disease*, vol. 37, no. 1, pp. 99–105, 2010.
- [29] M. Marchi, L. Raiteri, F. Risso et al., "Effects of adenosine A1 and A2A receptor activation on the evoked release of glutamate from rat cerebrocortical synaptosomes," *British Journal of Pharmacology*, vol. 136, no. 3, pp. 434–440, 2002.
- [30] M. Marcoli, L. Raiteri, A. Bonfanti et al., "Sensitivity to selective adenosine A1 and A2A receptor antagonists of the release of

- glutamate induced by ischemia in rat cerebocortical slices," *Neuropharmacology*, vol. 45, no. 2, pp. 201–210, 2003.
- [31] M.-R. Nikbakht and T. W. Stone, "Suppression of presynaptic responses to adenosine by activation of NMDA receptors," *European Journal of Pharmacology*, vol. 427, no. 1, pp. 13–25, 2001.
- [32] R. J. Rodrigues, T. M. Alfaro, N. Rebola, C. R. Oliveira, and R. A. Cunha, "Co-localization and functional interaction between adenosine A(2A) and metabotropic group 5 receptors in glutamatergic nerve terminals of the rat striatum," *Journal of Neurochemistry*, vol. 92, no. 3, pp. 433–441, 2005.
- [33] M. T. Tebano, M. R. Domenici, and P. Popoli, "SCH 58261 differentially influences quinolinic acid-induced effects in striatal and in hippocampal slices," *European Journal of Pharmacology*, vol. 450, no. 3, pp. 253–257, 2002.
- [34] C. Corsi, A. Melani, L. Bianchi, G. Pepeu, and F. Pedata, "Striatal A2A adenosine receptors differentially regulate spontaneous and K⁺-evoked glutamate release in vivo in young and aged rats," *NeuroReport*, vol. 10, no. 4, pp. 687–691, 1999.
- [35] C. Corsi, A. Melani, L. Bianchi, and F. Pedata, "Striatal A2A adenosine receptor antagonism differentially modifies striatal glutamate outflow in vivo in young and aged rats," *NeuroReport*, vol. 11, no. 11, pp. 2591–2595, 2000.
- [36] A. Pintor, D. Quarta, A. Pèzzola, R. Reggio, and P. Popoli, "SCH 58261 (an adenosine A2A receptor antagonist) reduces, only at low doses, K⁺-evoked glutamate release in the striatum," *European Journal of Pharmacology*, vol. 421, no. 3, pp. 177–180, 2001.
- [37] M. Gianfriddo, C. Corsi, A. Melani et al., "Adenosine A2A antagonism increases striatal glutamate outflow in the quinolinic acid rat model of Huntington's disease," *Brain Research*, vol. 979, no. 1–2, pp. 225–229, 2003.
- [38] M. T. Tebano, A. Pintor, C. Frank et al., "Adenosine A_{2A} receptor blockade differentially influences excitotoxic mechanisms at pre- and postsynaptic sites in the rat striatum," *Journal of Neuroscience Research*, vol. 77, no. 1, pp. 100–107, 2004.
- [39] P. Popoli, A. Pintor, M. R. Domenici et al., "Blockade of striatal adenosine A2A receptor reduces, through a presynaptic mechanism, quinolinic acid-induced excitotoxicity: possible relevance to neuroprotective interventions in neurodegenerative diseases of the striatum," *The Journal of Neuroscience*, vol. 22, no. 5, pp. 1967–1975, 2002.
- [40] P. Popoli, C. Frank, M. T. Tebano et al., "Modulation of glutamate release and excitotoxicity by adenosine A_{2A} receptors," *Neurology*, vol. 61, no. 11, pp. S69–S71, 2003.
- [41] N. J. Abbott, L. Rönnbäck, and E. Hansson, "Astrocyte-endothelial interactions at the blood-brain barrier," *Nature Reviews Neuroscience*, vol. 7, no. 1, pp. 41–53, 2006.
- [42] J. Keaney and M. Campbell, "The dynamic blood-brain barrier," *FEBS Journal*, vol. 282, no. 21, pp. 4067–4079, 2015.
- [43] C. Larochelle, J. I. Alvarez, and A. Prat, "How do immune cells overcome the blood-brain barrier in multiple sclerosis?" *FEBS Letters*, vol. 585, no. 23, pp. 3770–3780, 2011.
- [44] M. S. Bynoe, C. Viret, A. Yan, and D.-G. Kim, "Adenosine receptor signaling: A key to opening the blood-brain door," *Fluids and Barriers of the CNS*, vol. 12, no. 1, article no. 20, 2015.
- [45] D.-G. Kim and M. S. Bynoe, "A2A Adenosine Receptor Regulates the Human Blood-Brain Barrier Permeability," *Molecular Neurobiology*, vol. 52, no. 1, pp. 664–678, 2015.
- [46] L. Airas, J. Niemelä, G. Yegutkin, and S. Jalkanen, "Mechanism of action of IFN-beta in the treatment of multiple sclerosis: a special reference to CD73 and adenosine," *Annals of the New York Academy of Sciences*, vol. 1110, pp. 641–648, 2007.
- [47] J. H. Mills, L. Alabanza, B. B. Weksler, P.-O. Couraud, I. A. Romero, and M. S. Bynoe, "Human brain endothelial cells are responsive to adenosine receptor activation," *Purinergic Signalling*, vol. 7, no. 2, pp. 265–273, 2011.
- [48] A. J. Carman, J. H. Mills, A. Krenz, D.-G. Kim, and M. S. Bynoe, "Adenosine receptor signaling modulates permeability of the blood-brain barrier," *The Journal of Neuroscience*, vol. 31, no. 37, pp. 13272–13280, 2011.
- [49] J. Niemelä, I. Ifergan, G. G. Yegutkin, S. Jalkanen, A. Prat, and L. Airas, "IFN- β regulates CD73 and adenosine expression at the blood-brain barrier," *European Journal of Immunology*, vol. 38, no. 10, pp. 2718–2726, 2008.
- [50] H. Watanabe, W. Kuhne, P. Schwartz, and H. M. Piper, "A₂-adenosine receptor stimulation increases macromolecule permeability of coronary endothelial cells," *American Journal of Physiology-Heart and Circulatory Physiology*, vol. 262, no. 4, pp. H1174–H1181, 1992.
- [51] A. Hempel, T. Noll, A. Muhs, and H. M. Piper, "Functional antagonism between cAMP and cGMP on permeability of coronary endothelial monolayers," *American Journal of Physiology-Heart and Circulatory Physiology*, vol. 270, no. 4, pp. H1264–H1271, 1996.
- [52] Q. Lu, E. O. Harrington, J. Newton et al., "Adenosine protected against pulmonary edema through transporter- and receptor A₂-mediated endothelial barrier enhancement," *American Journal of Physiology-Lung Cellular and Molecular Physiology*, vol. 298, no. 6, pp. L755–L767, 2010.
- [53] F. R. Haselton, J. S. Alexander, and S. N. Mueller, "Adenosine decreases permeability of in vitro endothelial monolayers," *Journal of Applied Physiology*, vol. 74, no. 4, pp. 1581–1590, 1985.
- [54] L. F. Richard, T. E. Dahms, and R. O. Webster, "Adenosine prevents permeability increase in oxidant-injured endothelial monolayers," *American Journal of Physiology*, vol. 274, no. 1, pp. H35–H42, 1998.
- [55] R. M. Ransohoff and B. Engelhardt, "The anatomical and cellular basis of immune surveillance in the central nervous system," *Nature Reviews Immunology*, vol. 12, no. 9, pp. 623–635, 2012.
- [56] M. A. Lopes Pinheiro, G. Kooij, M. R. Mizze et al., "Immune cell trafficking across the barriers of the central nervous system in multiple sclerosis and stroke," *Biochimica et Biophysica Acta (BBA) - Molecular Basis of Disease*, vol. 1862, no. 3, pp. 461–471, 2016.
- [57] J. H. Mills, D.-G. Kim, A. Krenz, J.-F. Chen, and M. S. Bynoe, "A2A adenosine receptor signaling in lymphocytes and the central nervous system regulates inflammation during experimental autoimmune encephalomyelitis," *The Journal of Immunology*, vol. 188, no. 11, pp. 5713–5722, 2012.
- [58] J. H. Mills, L. F. Thompson, C. Mueller et al., "CD73 is required for efficient entry of lymphocytes into the central nervous system during experimental autoimmune encephalomyelitis," *Proceedings of the National Academy of Sciences of the United States of America*, vol. 105, no. 27, pp. 9325–9330, 2008.
- [59] J. H. Mills, L. M. Alabanza, D. A. Mahamed, and M. S. Bynoe, "Extracellular adenosine signaling induces CX3CL1 expression in the brain to promote experimental autoimmune encephalomyelitis," *Journal of Neuroinflammation*, vol. 9, article no. 193, 2012.
- [60] B. Stevens, S. Porta, L. L. Haak, V. Gallo, and R. D. Fields, "Adenosine: a neuron-glia transmitter promoting myelination

- in the CNS in response to action potentials," *Neuron*, vol. 36, no. 5, pp. 855–868, 2002.
- [61] E. Coppi, L. Cellai, G. Maraula et al., "Role of adenosine in oligodendrocyte precursor maturation," *Frontiers in Cellular Neuroscience*, vol. 9, 2015.
- [62] E. Coppi, L. Cellai, G. Maraula, A. M. Pugliese, and F. Pedata, "Adenosine A2A receptors inhibit delayed rectifier potassium currents and cell differentiation in primary purified oligodendrocyte cultures," *Neuropharmacology*, vol. 73, pp. 301–310, 2013.
- [63] A. G. Orr, A. L. Orr, X. Li, R. E. Gross, and S. F. Traynelis, "Adenosine A2A receptor mediates microglial process retraction," *Nature Neuroscience*, vol. 12, no. 7, pp. 872–878, 2009.
- [64] M. C. Wittendorp, H. W. G. M. Boddeke, and K. Biber, "Adenosine A3 receptor-induced CCL2 synthesis in cultured mouse astrocytes," *Glia*, vol. 46, no. 4, pp. 410–418, 2004.
- [65] A. G. Orr, E. C. Hsiao, M. M. Wang et al., "Astrocytic adenosine receptor A2A and Gs-coupled signaling regulate memory," *Nature Neuroscience*, vol. 18, no. 3, pp. 423–439, 2015.
- [66] R. Brambilla, L. Cottini, M. Fumagalli, S. Ceruti, and M. P. Abbracchio, "Blockade of A2A adenosine receptors prevents basic fibroblast growth factor-induced reactive astrogliosis in rat striatal primary astrocytes," *Glia*, vol. 43, no. 2, pp. 190–194, 2003.
- [67] J. S. Fink, D. R. Weaver, S. A. Rivkees et al., "Molecular cloning of the rat A₂ adenosine receptor: selective co-expression with D₂ dopamine receptors in rat striatum," *Brain Research*, vol. 14, no. 3, pp. 186–195, 1992.
- [68] P. Calabresi, B. Picconi, A. Tozzi, V. Ghiglieri, and M. Di Filippo, "Direct and indirect pathways of basal ganglia: a critical reappraisal," *Nature Neuroscience*, vol. 17, no. 8, pp. 1022–1030, 2014.
- [69] A. Mori, "Mode of action of adenosine A2A receptor antagonists as symptomatic treatment for Parkinson's disease," *International Review of Neurobiology*, vol. 119, pp. 87–116, 2014.
- [70] M. Canals, D. Marcellino, F. Fanelli et al., "Adenosine A2A-dopamine D2 receptor-receptor heteromerization: Qualitative and quantitative assessment by fluorescence and bioluminescence energy transfer," *The Journal of Biological Chemistry*, vol. 278, no. 47, pp. 46741–46749, 2003.
- [71] P. Calabresi, M. D. Filippo, V. Ghiglieri, N. Tambasco, and B. Picconi, "Levodopa-induced dyskinesias in patients with Parkinson's disease: filling the bench-to-bedside gap," *The Lancet Neurology*, vol. 9, no. 11, pp. 1106–1117, 2010.
- [72] P. Jenner, "An Overview of adenosine A2A receptor antagonists in Parkinson's disease," *International Review of Neurobiology*, vol. 119, pp. 71–86, 2014.
- [73] G. A. Graveland, R. S. Williams, and M. DiFiglia, "Evidence for degenerative and regenerative changes in neostriatal spiny neurons in Huntington's disease," *Science*, vol. 227, no. 4688, pp. 770–773, 1985.
- [74] M. Glass, M. Dragunow, and R. L. M. Faull, "The pattern of neurodegeneration in Huntington's disease: a comparative study of cannabinoid, dopamine, adenosine and GABA(A) receptor alterations in the human basal ganglia in Huntington's disease," *Neuroscience*, vol. 97, no. 3, pp. 505–519, 2000.
- [75] J.-H. J. Cha, A. S. Frey, S. A. Alsdorf et al., "Altered neurotransmitter receptor expression in transgenic mouse models of Huntington's disease," *Philosophical Transactions of the Royal Society B: Biological Sciences*, vol. 354, no. 1386, pp. 981–989, 1999.
- [76] S. Mievius, D. Blum, and C. Ledent, "A2A receptor knockout worsens survival and motor behaviour in a transgenic mouse model of Huntington's disease," *Neurobiology of Disease*, vol. 41, no. 2, pp. 570–576, 2011.
- [77] S.-Y. Chou, Y.-C. Lee, H.-M. Chen et al., "CGS21680 attenuates symptoms of Huntington's disease in a transgenic mouse model," *Journal of Neurochemistry*, vol. 93, no. 2, pp. 310–320, 2005.
- [78] M.-C. Chiang, Y.-C. Lee, C.-L. Huang, and Y. Chern, "cAMP-response element-binding protein contributes to suppression of the A2A adenosine receptor promoter by mutant huntingtin with expanded polyglutamine residues," *The Journal of Biological Chemistry*, vol. 280, no. 14, pp. 14331–14340, 2005.
- [79] C.-M. Dhaenens, S. Burnouf, C. Simonin et al., "A genetic variation in the ADORA2A gene modifies age at onset in Huntington's disease," *Neurobiology of Disease*, vol. 35, no. 3, pp. 474–476, 2009.
- [80] S. Tyebji, A. Saavedra, P. M. Canas et al., "Hyperactivation of D1 and A2A receptors contributes to cognitive dysfunction in Huntington's disease," *Neurobiology of Disease*, vol. 74, pp. 41–57, 2015.
- [81] W. Li, H. B. Silva, J. Real et al., "Inactivation of adenosine A2A receptors reverses working memory deficits at early stages of Huntington's disease models," *Neurobiology of Disease*, vol. 79, pp. 70–80, 2015.
- [82] M. R. Domenici, M. L. Scattoni, A. Martire et al., "Behavioral and electrophysiological effects of the adenosine A2A receptor antagonist SCH 58261 in R6/2 Huntington's disease mice," *Neurobiology of Disease*, vol. 28, no. 2, pp. 197–205, 2007.
- [83] K. Ishiwata, N. Ogi, N. Hayakawa et al., "Adenosine A2A receptor imaging with [¹¹C]KF18446 PET in the rat brain after quinolinic acid lesion: Comparison with the dopamine receptor imaging," *Annals of Nuclear Medicine*, vol. 16, no. 7, pp. 467–475, 2002.
- [84] J. L. Albasanz, S. Perez, M. Barrachina, I. Ferrer, and M. Martín, "Up-regulation of adenosine receptors in the frontal cortex in Alzheimer's disease," *Brain Pathology*, vol. 18, no. 2, pp. 211–219, 2008.
- [85] G. W. Arendash, W. Schleich, K. Rezai-Zadeh et al., "Caffeine protects Alzheimer's mice against cognitive impairment and reduces brain β -amyloid production," *Neuroscience*, vol. 142, no. 4, pp. 941–952, 2006.
- [86] O. P. Dall'Igna, L. O. Porciúncula, D. O. Souza, R. A. Cunha, and D. R. Lara, "Neuroprotection by caffeine and adenosine A_{2A} receptor blockade of β -amyloid neurotoxicity," *British Journal of Pharmacology*, vol. 138, no. 7, pp. 1207–1209, 2003.
- [87] S. Giunta, V. Andriolo, and A. Castorina, "Dual blockade of the A1 and A_{2A} adenosine receptor prevents amyloid beta toxicity in neuroblastoma cells exposed to aluminum chloride," *The International Journal of Biochemistry & Cell Biology*, vol. 54, pp. 122–136, 2014.
- [88] P. M. Canas, L. O. Porciúncula, G. M. A. Cunha et al., "Adenosine A2A receptor blockade prevents synaptotoxicity and memory dysfunction caused by β -amyloid peptides via p38 mitogen-activated protein kinase pathway," *The Journal of Neuroscience*, vol. 29, no. 47, pp. 14741–14751, 2009.
- [89] B. V. Nagpure, J. Bian, and S. Strack, "Hydrogen Sulfide Inhibits A2A Adenosine Receptor Agonist Induced β -Amyloid Production in SH-SY5Y Neuroblastoma Cells via a cAMP Dependent Pathway," *PLoS ONE*, vol. 9, no. 2, p. e88508, 2014.

- [90] O. P. Dall'Igna, P. Fett, M. W. Gomes, D. O. Souza, R. A. Cunha, and D. R. Lara, "Caffeine and adenosine A_{2a} receptor antagonists prevent β -amyloid (25–35)-induced cognitive deficits in mice," *Experimental Neurology*, vol. 203, no. 1, pp. 241–245, 2007.
- [91] G. M. A. Cunha, P. M. Canas, C. S. Melo et al., "Adenosine A_{2A} receptor blockade prevents memory dysfunction caused by β -amyloid peptides but not by scopolamine or MK-801," *Experimental Neurology*, vol. 210, no. 2, pp. 776–781, 2008.
- [92] C. Laurent, S. Burnouf, B. Ferry et al., "Erratum: A_{2A} adenosine receptor deletion is protective in a mouse model of Tauopathy (Molecular Psychiatry (2016) 21 149 (doi:10.1038/mp.2015.115))," *Molecular Psychiatry*, vol. 21, no. 1, p. 149, 2016.
- [93] N. Pagnussat, A. S. Almeida, D. M. Marques et al., "Adenosine A(2A) receptors are necessary and sufficient to trigger memory impairment in adult mice," *British Journal of Pharmacology*, vol. 172, no. 15, pp. 3831–3845, 2015.
- [94] P. Li, D. Rial, P. M. Canas et al., "Optogenetic activation of intracellular adenosine A_{2A} receptor signaling in the hippocampus is sufficient to trigger CREB phosphorylation and impair memory," *Molecular Psychiatry*, vol. 20, no. 11, pp. 1481–1481, 2015.
- [95] J. Lu, J. Cui, X. Li et al., "An Anti-Parkinson's Disease Drug via Targeting Adenosine A_{2A} Receptor Enhances Amyloid- β Generation and γ -Secretase Activity," *PLoS One*, vol. 11, no. 11, Article ID e0166415, 2016.
- [96] R. M. Ransohoff, D. A. Hafler, and C. F. Lucchinetti, "Multiple sclerosis - A quiet revolution," *Nature Reviews Neurology*, vol. 11, no. 3, pp. 134–142, 2015.
- [97] B. F. G. Popescu and C. F. Lucchinetti, "Meningeal and cortical grey matter pathology in multiple sclerosis," *BMC Neurology*, vol. 12, article 11, 2012.
- [98] J. M. Frischer, S. Bramow, A. Dal-Bianco et al., "The relation between inflammation and neurodegeneration in multiple sclerosis brains," *Brain*, vol. 132, no. 5, pp. 1175–1189, 2009.
- [99] E. Rissanen, J. Tuisku, J. Rokka et al., "In vivo detection of diffuse inflammation in secondary progressive multiple sclerosis using PET imaging and the radioligand ¹¹C-PK11195," *Journal of Nuclear Medicine*, vol. 55, no. 6, pp. 939–944, 2014.
- [100] L. Airas, E. Rissanen, and J. O. Rinne, "Imaging neuroinflammation in multiple sclerosis using TSPO-PET," *Clinical and Translational Imaging*, vol. 3, no. 6, pp. 461–473, 2015.
- [101] A. J. Thompson, "Challenge of progressive multiple sclerosis therapy," *Current Opinion in Neurology*, vol. 30, no. 3, pp. 237–240, 2017.
- [102] J. Ingwersen, B. Wingerath, J. Graf et al., "Dual roles of the adenosine A_{2a} receptor in autoimmune neuroinflammation," *Journal of Neuroinflammation*, vol. 13, no. 1, article no. 48, 2016.
- [103] A. M. Amorini, A. Petzold, B. Tavazzi et al., "Increase of uric acid and purine compounds in biological fluids of multiple sclerosis patients," *Clinical Biochemistry*, vol. 42, no. 10–11, pp. 1001–1006, 2009.
- [104] C. R. N. Polachini, R. M. Spanevello, E. A. Casali et al., "Alterations in the cholinesterase and adenosine deaminase activities and inflammation biomarker levels in patients with multiple sclerosis," *Neuroscience*, vol. 266, pp. 266–274, 2014.
- [105] A. K. Hedström, E. M. Mowry, M. A. Gianfrancesco et al., "High consumption of coffee is associated with decreased multiple sclerosis risk; results from two independent studies," *Journal of Neurology, Neurosurgery & Psychiatry*, vol. 87, no. 5, pp. 454–460, 2016.
- [106] M. B. D'hooghe, P. Haentjens, G. Nagels, and J. De Keyser, "Alcohol, coffee, fish, smoking and disease progression in multiple sclerosis," *European Journal of Neurology*, vol. 19, no. 4, pp. 616–624, 2012.
- [107] G. Q. Chen, Y. Y. Chen, X. S. Wang et al., "Chronic caffeine treatment attenuates experimental autoimmune encephalomyelitis induced by guinea pig spinal cord homogenates in Wistar rats," *Brain Research*, vol. 1309, pp. 116–125, 2010.
- [108] S. Tsutsui, J. Schnermann, F. Noorbakhsh et al., "A₁ adenosine receptor upregulation and activation attenuates neuroinflammation and demyelination in a model of multiple sclerosis," *The Journal of Neuroscience*, vol. 24, no. 6, pp. 1521–1529, 2004.
- [109] T. Wang, N.-N. Xi, Y. Chen et al., "Chronic caffeine treatment protects against experimental autoimmune encephalomyelitis in mice: therapeutic window and receptor subtype mechanism," *Neuropharmacology*, vol. 86, pp. 203–211, 2014.
- [110] S. Yao, Z. Li, Q. Huang et al., "Genetic inactivation of the adenosine A(2A) receptor exacerbates brain damage in mice with experimental autoimmune encephalomyelitis," *Journal of Neurochemistry*, vol. 123, no. 1, pp. 100–112, 2012.
- [111] Y. Liu, H. Zou, P. Zhao et al., "Activation of the adenosine A_{2A} receptor attenuates experimental autoimmune encephalomyelitis and is associated with increased intracellular calcium levels," *Neuroscience*, vol. 330, pp. 150–161, 2016.
- [112] M. L. Trincavelli, A. Melani, S. Guidi et al., "Regulation of A(2A) adenosine receptor expression and functioning following permanent focal ischemia in rat brain," *Journal of Neurochemistry*, vol. 104, no. 2, pp. 479–490, 2008.
- [113] J. W. Phillis, "The effects of selective A₁ and A_{2a} adenosine receptor antagonists on cerebral ischemic injury in the gerbil," *Brain Research*, vol. 705, no. 1–2, pp. 79–84, 1995.
- [114] Y. Gao and J. W. Phillis, "CGS 15943, An adenosine A₂ receptor antagonist, reduces cerebral ischemic injury in the mongolian gerbil," *Life Sciences*, vol. 55, no. 3, pp. PL61–PL65, 1994.
- [115] A. Monopoli, G. Lozza, A. Forlani, A. Mattavelli, and E. Ongini, "Blockade of adenosine A_{2A} receptors by SCH 58261 results in neuroprotective effects in cerebral ischaemia in rats," *NeuroReport*, vol. 9, no. 17, pp. 3955–3959, 1998.
- [116] K. Jo, R. Derin, M. Li, and D. S. Bredt, "Characterization of MALS/Vel-1, -2, and -3: a family of mammalian LIN-7 homologs enriched at brain synapses in association with the postsynaptic density-95/NMDA receptor postsynaptic complex," *The Journal of Neuroscience*, vol. 19, no. 11, pp. 4189–4199, 1999.
- [117] H. Higashi, J. R. Meno, A. S. Marwaha, and H. R. Winn, "Hippocampal injury and neurobehavioral deficits following hyperglycemic cerebral ischemia: effect of theophylline and ZM 241385," *Journal of Neurosurgery*, vol. 96, no. 1, pp. 117–126, 2002.
- [118] A. Melani, S. Cipriani, M. G. Vannucchi et al., "Selective adenosine A_{2a} receptor antagonism reduces JNK activation in oligodendrocytes after cerebral ischaemia," *Brain*, vol. 132, no. 6, pp. 1480–1495, 2009.
- [119] L. Gui, W. Duan, H. Tian et al., "Adenosine A_{2A} receptor deficiency reduces striatal glutamate outflow and attenuates brain injury induced by transient focal cerebral ischemia in mice," *Brain Research*, vol. 1297, pp. 185–193, 2009.
- [120] R. A. Mohamed, A. M. Agha, and N. N. Nassar, "SCH58261 the selective adenosine A_{2A} receptor blocker modulates ischemia reperfusion injury following bilateral carotid occlusion: Role of inflammatory mediators," *Neurochemical Research*, vol. 37, no. 3, pp. 538–547, 2012.

- [121] Z. J. Yang, B. Wang, H. Kwansa et al., "Adenosine A2A receptor contributes to ischemic brain damage in newborn piglet," *Journal of Cerebral Blood Flow & Metabolism*, vol. 33, pp. 1612–1620, 2013.
- [122] A. Melani, M. Gianfriddo, M. G. Vannucchi et al., "The selective A2A receptor antagonist SCH 58261 protects from neurological deficit, brain damage and activation of p38 MAPK in rat focal cerebral ischemia," *Brain Research*, vol. 1073–1074, no. 1, pp. 470–480, 2006.
- [123] A. Melani, L. Pantoni, F. Bordoni et al., "The selective A2A receptor antagonist SCH 58261 reduces striatal transmitter outflow, turning behavior and ischemic brain damage induced by permanent focal ischemia in the rat," *Brain Research*, vol. 959, no. 2, pp. 243–250, 2003.
- [124] L. Yu, Z. Huang, J. F. Mariani, Y. Wang, M. Moskowitz, and J. Chen, "Selective inactivation or reconstitution of adenosine A2A receptors in bone marrow cells reveals their significant contribution to the development of ischemic brain injury," *Nature Medicine*, vol. 10, no. 10, pp. 1081–1087, 2004.
- [125] A. Melani, I. Dettori, F. Corti, L. Cellai, and F. Pedata, "Time-course of protection by the selective A2A receptor antagonist SCH58261 after transient focal cerebral ischemia," *Neurological Sciences*, vol. 36, no. 8, pp. 1441–1448, 2015.
- [126] U. Fronz, A. Deten, F. Baumann et al., "Continuous adenosine A2A receptor antagonism after focal cerebral ischemia in spontaneously hypertensive rats," *Naunyn-Schmiedeberg's Archives of Pharmacology*, vol. 387, no. 2, pp. 165–173, 2014.
- [127] U. Ådén, L. Halldner, H. Lagercrantz, I. Dalmau, C. Ledent, and B. B. Fredholm, "Aggravated brain damage after hypoxic ischemia in immature adenosine A2A knockout mice," *Stroke*, vol. 34, no. 3, pp. 739–744, 2003.
- [128] A. Melani, F. Corti, L. Cellai, M. Giuliana Vannucchi, and F. Pedata, "Low doses of the selective adenosine A2A receptor agonist CGS21680 are protective in a rat model of transient cerebral ischemia," *Brain Research*, vol. 1551, pp. 59–72, 2014.
- [129] M. Sakata, K. Ishibashi, and M. Imai, "Initial Evaluation of a Novel Adenosine A2A Receptor Ligand, (11)C-Preladenant, in Healthy Human Subjects," *Journal of Nuclear Medicine*, 2017.
- [130] O. Barret, J. Hannestad, C. Vala et al., "Characterization in humans of ¹⁸F-MNI-444, a PET radiotracer for brain adenosine 2A receptors," *Journal of Nuclear Medicine*, vol. 56, no. 4, pp. 586–591, 2015.
- [131] I. Grachev, M. Doder, D. Brooks, and R. Hinz, "Quantitative in vivo Imaging of Adenosine A2A Receptors in the Human Brain Using 11C-SCH442416 PET: A Pilot Study," *Journal of Diagnostic Imaging in Therapy*, vol. 1, no. 1, pp. 1–19, 2014.
- [132] M. Mishina, Y. Kimura, M. Naganawa et al., "Differential effects of age on human striatal adenosine A1 and A2A receptors," *Synapse*, vol. 66, no. 9, pp. 832–839, 2012.
- [133] K. Varani, F. Vincenzi, A. Tosi et al., "A_{2A} adenosine receptor overexpression and functionality, as well as TNF- α levels, correlate with motor symptoms in Parkinson's disease," *The FASEB Journal*, vol. 24, no. 2, pp. 587–598, 2010.
- [134] K. Ishiwata, M. Mishina, Y. Kimura, K. Oda, T. Sasaki, and K. Ishii, "First visualization of adenosine A2A receptors in the human brain by positron emission tomography with [11C]TMSX," *Synapse*, vol. 55, no. 2, pp. 133–136, 2005.
- [135] I. Heinonen, S. V. Nesterov, K. Liukko et al., "Myocardial blood flow and adenosine A2A receptor density in endurance athletes and untrained men," *The Journal of Physiology*, vol. 586, no. 21, pp. 5193–5202, 2008.
- [136] K. Ishiwata, K. Kawamura, Y. Kimura, K. Oda, and K. Ishii, "Potential of an adenosine A2A receptor antagonist [11C]TMSX for myocardial imaging by positron emission tomography: A first human study," *Annals of Nuclear Medicine*, vol. 17, no. 6, pp. 457–462, 2003.
- [137] K. Ishiwata, M. Mizuno, Y. Kimura et al., "Potential of [11C]TMSX for the evaluation of adenosine A2A receptors in the skeletal muscle by positron emission tomography," *Nuclear Medicine and Biology*, vol. 31, no. 7, pp. 949–956, 2004.
- [138] M. Mizuno, Y. Kimura, K. Tokizawa et al., "Greater adenosine A2A receptor densities in cardiac and skeletal muscle in endurance-trained men: A [11C]TMSX PET study," *Nuclear Medicine and Biology*, vol. 32, no. 8, pp. 831–836, 2005.
- [139] K. Ishiwata, J. Noguchi, and S. Wakabayashi, "11C-labeled KF18446: a potential central nervous system adenosine A2A receptor ligand," *Journal of Nuclear Medicine*, vol. 41, no. 2, pp. 345–354, 2000.
- [140] S. Stone-Elander, J.-O. Thorell, L. Eriksson, B. B. Fredholm, and M. Ingvar, "In vivo biodistribution of [N-11C-methyl]KF 17837 using 3-D-PET: Evaluation as a ligand for the study of adenosine A(2A) receptors," *Nuclear Medicine and Biology*, vol. 24, no. 2, pp. 187–191, 1997.
- [141] E. Rissanen, J. Tuisku, P. Luoto et al., "Automated reference region extraction and population-based input function for brain [11C]TMSX PET image analyses," *Journal of Cerebral Blood Flow & Metabolism*, vol. 35, no. 1, pp. 157–165, 2015.
- [142] M. Naganawa, Y. Kimura, M. Mishina et al., "Quantification of adenosine A2A receptors in the human brain using [11C]TMSX and positron emission tomography," *European Journal of Nuclear Medicine and Molecular Imaging*, vol. 34, no. 5, pp. 679–687, 2007.
- [143] B. R. Neustadt and e. a. et al., "Potent, Selective, and Orally Active Adenosine A2A Receptor Antagonists: Arylpiperazine Derivatives of Pyrazolo[4,3-e]-1,2,4-triazolo[1,5-c]pyrimidines," *ChemInform*, vol. 38, no. 29, 2007.
- [144] X. Zhou, R. Boellaard, K. Ishiwata et al., "In Vivo Evaluation of," *Journal of Nuclear Medicine*, vol. 58, no. 5, pp. 762–767, 2017.
- [145] C. Vala, T. J. Morley, X. Zhang et al., "Synthesis and in vivo Evaluation of Fluorine-18 and Iodine-123 Pyrazolo[4,3-e]-1,2,4-triazolo[1,5-c]pyrimidine Derivatives as PET and SPECT Radiotracers for Mapping A2A Receptors," *ChemMedChem*, pp. 1936–1943, 2016.
- [146] O. Barret, J. Hannestad, D. Alagille et al., "Adenosine 2A receptor occupancy by tozadenant and preladenant in rhesus monkeys," *Journal of Nuclear Medicine*, vol. 55, no. 10, pp. 1712–1718, 2014.
- [147] S. Todde, R. M. Moresco, P. Simonelli et al., "Design, radiosynthesis, and biodistribution of a new potent and selective ligand for in vivo imaging of the adenosine A2A receptor system using positron emission tomography [2]," *Journal of Medicinal Chemistry*, vol. 43, no. 23, pp. 4359–4362, 2000.
- [148] I. Grachev, M. Doder, D. Brooks, and R. Hinz, "An in vivo Positron Emission Tomography Study of Adenosine 2A Receptor Occupancy by Preladenant using 11C-SCH442416 in Healthy Subjects," *Journal of Diagnostic Imaging in Therapy*, vol. 1, no. 1, pp. 20–48, 2014.
- [149] D. J. Brooks, S. Papapetropoulos, F. Vandenhende et al., "An open-label, positron emission tomography study to assess adenosine A2A brain receptor occupancy of vipadenant (BIIB014) at steady-state levels in healthy male volunteers," *Clinical Neuropharmacology*, vol. 33, no. 2, pp. 55–60, 2010.

- [150] M. Naganawa, Y. Kimura, J. Yano et al., "Robust estimation of the arterial input function for Logan plots using an intersectional searching algorithm and clustering in positron emission tomography for neuroreceptor imaging," *NeuroImage*, vol. 40, no. 1, pp. 26–34, 2008.
- [151] X. Zhou, S. Khanapur, J. R. De Jong et al., "In vivo evaluation of [11C]preladenant positron emission tomography for quantification of adenosine A2A receptors in the rat brain," *Journal of Cerebral Blood Flow & Metabolism*, vol. 37, no. 2, pp. 577–589, 2016.
- [152] E. Hirani, J. Gillies, A. Karasawa et al., "Evaluation of [4-O-methyl-11C]KW-6002 as a potential PET ligand for mapping central adenosine A2A receptors in rats," *Synapse*, vol. 42, no. 3, pp. 164–176, 2001.
- [153] D. J. Brooks, M. Doder, S. Osman et al., "Positron emission tomography analysis of [11C]KW-6002 binding to human and rat adenosine A2A receptors in the brain," *Synapse*, vol. 62, no. 9, pp. 671–681, 2008.
- [154] D. A. Mankoff, "A definition of molecular imaging," *Journal of Nuclear Medicine*, vol. 48, no. 6, pp. 18N–21N, 2007.

Research Article

Integrating a ¹⁹F MRI Tracer Agent into the Clinical Scale Manufacturing of a T-Cell Immunotherapy

Charles F. O'Hanlon,¹ Tamara Fedczyna,² Shannon Eaker,²
William D. Shingleton,³ and Brooke M. Helfer¹

¹Celsense Inc., 603 Stanwix Street Suite 390, Pittsburgh, PA 15222, USA

²GE Healthcare, 100 Results Way, Marlborough, MA 01752, USA

³GE Healthcare, The Grove Center, White Lion Road, Amersham, Buckinghamshire HP7 9LL, UK

Correspondence should be addressed to Brooke M. Helfer; brooke@celsense.com

Received 10 July 2017; Revised 19 September 2017; Accepted 2 October 2017; Published 2 November 2017

Academic Editor: Anne Roivainen

Copyright © 2017 Charles F. O'Hanlon et al. This is an open access article distributed under the Creative Commons Attribution License, which permits unrestricted use, distribution, and reproduction in any medium, provided the original work is properly cited.

Leukocyte immunotherapies have made great progress in the treatment of cancer. Recent reports on the treatment of B-cell malignancies using Chimeric Antigen Receptor and affinity enhanced T-Cell Receptor therapies have demonstrated encouraging clinical results. As investigators begin to explore the treatment of solid tumors with these cells, the hurdle of evaluating T-cell homing to and persistence at the site of disease remain. Significant challenges regarding the GMP manufacture and administration of a therapeutic dose of millions to billions of transduced T-cells remain. Here we report on the application of a clinically authorized ¹⁹F MRI tracer agent to human T-cells, employing state-of-the-art methods and equipment in the manufacture of a cellular therapy. Using a general T-cell expansion protocol and clinical scale industrial bioreactors, we show ¹⁹F labeling without detriment to the product +/- cryopreservation. While the incorporation of the ¹⁹F tracer is not trivial, it is just one of the many steps that can aid in progression of a therapeutic to and through the clinic. Combining the MRI tracking capabilities, safety profiles, and clinical sensitivity of this method, this application demonstrates the ability of ¹⁹F MRI to be used in industrial scale applications to visualize the spatial fate of cellular therapeutics.

1. Introduction

In the past 5 years, the successful treatment of cancer patients with autologous T-cells that have been engineered to recognize and kill tumors has been reported in the academic literature [1–8]. Although the total number of patients treated is relatively small, the unexpectedly high rates of complete response have provoked global reaction by other academic investigators, large pharmaceutical companies, and financial markets to allocate significant resources to translate these therapies into commercial products that can be economically delivered to patients.

The enabling breakthrough for these new therapies is the targeting of tumor cells with aberrant patterns of gene expression versus the originating tissue type [9]. These therapies are typically referred to as CAR T-cells (Chimeric Antigen Receptor-T-cells) or TCR cells (T-Cell Receptor cells) but may

involve NK cells, mixed lymphocytes, and T-cells and NK cells derived from allogenic cell lines. In this study, we refer to them generically as engineered T-cell therapies. The engineered aspect of these cells typically involves genetically modifying immune cells in culture to express a receptor with an affinity for a target expressed by the tumor cells [10].

A second engineering aspect is large scale processes to genetically modify tens of millions of cells in culture, extracting the “unused” proteins and virus used in the transduction process, expanding the population of modified cells, and testing the cell product to verify that it meets predetermined release criteria. Integrating manufacturing of complex proteins and virus particles, traditional tissue culture, large scale transduction, and quality assurance on an industrial scale in a patient-centric process is a daunting undertaking that is currently being developed in real-time on a global basis [10, 11]. This process involves many empirical

steps: testing a particular technology on a stand-alone basis and retesting the technology integrated in the putative large scale process.

The rich market valuations for companies specializing in engineered T-cell therapies indicate that investors expect therapeutic developers to rapidly overcome the many manufacturing challenges for these treatments and advance beyond the treatment of blood cancers to solid tumors. Of the 1.7 million new cases of cancer in the US each year, less than 1% involve Acute Lymphoblastic Leukemia (ALL), the most successful treatment to date, and less than 10% involve leukemia, lymphoma, and myeloma [12].

Investigators and developers of engineered T-cell therapies are currently considering a large number of receptors and targets to treat solid tumors. Unfortunately, there is no high throughput *in vitro* method or data demonstrating the relevancy of preclinical models involving xenograft human tumors and engineered human immune cells. Like the work in ALL, the path forward will involve multiple early clinical studies. To accelerate the process, developers must embrace new technologies that answer fundamental questions regarding migration, persistence, and tumor killing for new receptor and target combinations. Definitive pharmacokinetic (PK) data for engineered T-cells will rapidly identify promising therapies and may provide further guidance for dosing strategies, different routes of administration, the ablation of endogenous immune cells, and the simultaneous administration of check point inhibitors or other immunotherapies.

The ideal cellular imaging technology for the development of PK data meets several criteria including being a quantitative, sensitive, biocompatible (viability preserving and nongenetically modifying), long lived, and nondilutive [13]. Most imaging technologies meet some but not all of these characteristics, with varying pros and cons of each modality, requiring a balance of wants and needs in examining cellular migration and persistence. Common imaging modalities for clinical cell tracking include MRI, PET, and SPECT. Ultrasound has also been used but is less common (imaging modalities reviewed extensively elsewhere, [13–17]). Here we will examine a nonradioactive perfluorocarbon based imaging agent that has been used clinically and is able to be visualized and quantified by fluorine MRI [18, 19].

Incorporation of fluorine labeling has been well demonstrated in the literature [18–24] but only on a small scale, cultures involving small volume flasks and not liters of media. In this paper we describe one of the empirical steps in the process of evaluating a new therapeutic component, namely, cell labeling. Here we report on a set of experiments that demonstrate that Cell Sense (CS-1000), a 19F MRI cell tracking agent used to develop clinical pharmacokinetic data for cell therapies, can be integrated into an industrial process for manufacturing an engineered T-cell therapy.

2. Methods

2.1. T-Cell Generation. Lymphocytes were isolated from buffy coats (Central Blood Bank, Pittsburgh PA) by Ficoll (GE Healthcare) and gradient separation (Percoll, GE Healthcare)

as described previously [25]. Lymphocytes were stimulated with 2.5 ug/mL PHA (Roche) and cultured in Iscove's Modified Dulbecco's Medium (IMDM, Gibco) containing 10% human AB serum (Sigma), 200 IU/mL IL-2 (GE Healthcare), 0.5% Penicillin, Streptomycin, Glutamine mix (PSG, Gibco), and 600 mg/L glucose (Gibco).

2.2. Cellular Expansion. Cells were expanded in 2 L Perfusion Cellbags in Wave 2/10 (Xuri W5) bioreactors with perfusion capability (GE Healthcare). Cells were initially seeded at $2.5\text{--}5 \times 10^5$ cells/mL with 5% CO₂ and 6 RPM (rock per minute). Culture volume was increased, keeping cells at 5×10^5 cells/mL until 1 L of media is reached. Once the culture volume was above 750 mL, rock was increased to 8 RPM. Perfusion was started once culture volume reaches 1 L and the rock rate was increased to 10 RPM. Days 1-2 were set for 250 mL of perfusion. Days 3-5 were set at 500 mL. Cultures were grown for 7 days reaching up to 2×10^6 cells/mL.

2.3. 19F Labeling of Human T-Cells. Cell Sense (CS-1000 ATM, Celsense Inc.) was infused via a vented vial spike (ICU Medical) into the bioreactor. Reagent was either pumped in via the bioreactor pump or fed by gravity. Vials are filled with 27 mL of reagent, with the spike 25 mL being delivered per vial. Cells were labeled at 10 mg/mL CS-1000 ATM for the final 24 hours of culture.

2.4. Cellular Viability. Cellular viability was determined by Trypan Blue exclusion.

2.5. Cellular Phenotype. Cell surface immunostaining analysis was performed using a BD FACS Caliber flow cytometer. Fluorescein isothiocyanate (FITC) CD3 and CD4 (Beckman Coulter Immunotech) and phycoerythrin (PE) CD8 (Beckman Coulter Immunotech) and CD32 (Biolegend) conjugated antibodies were used with their associated control antibodies (Beckman Coulter Immunotech and Biolegend) to assess the cellular population. Before staining, cells were washed in phosphate buffered saline (PBS) and blocked in 20% human AB serum for 10 minutes. Samples were then incubated with fluorescent antibodies at suggested concentrations for 20 minutes. After washing with PBS, samples were analyzed. Data analysis was performed using BD CellQuest Pro Software.

2.6. Nuclear Magnetic Resonance (NMR) Analysis of Labeled Cells. To assay the fluorine content of the cells after labeling, cell pellets of a known number of cells ($\geq 3 \times 10^6$ cells) were lysed with 1% Triton-X 100 (Sigma Aldrich) and a fluorine reference solution (trifluoroacetic acid, TFA) for a final concentration of 0.05% TFA. The lysed solution was placed in a 5 mm quartz NMR tube and read using a Bruker AVANCE spectrometer (Bruker, Billerica MA) operating at 282 MHz. 19F NMR spectra with both PFPE and TFA peaks were obtained and the ratios of the integrated areas under the peaks were used to calculate the mean 19F/cell or F/c as described previously [24, 26].

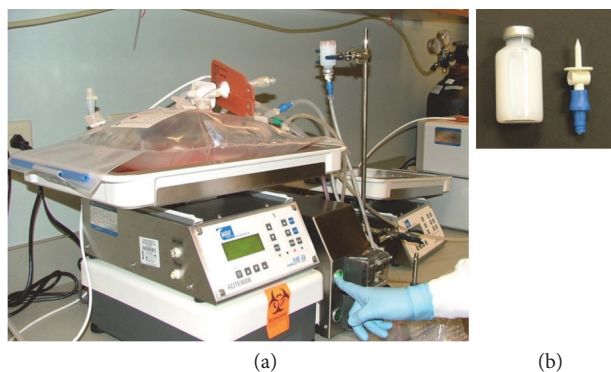


FIGURE 1: *Incorporation of cellular labeling.* Human T-cells were expanded to 1L of culture in a GE Wave 2/10 bioreactor. (a) By adding CS-1000 ATM through a vented spike, a closed sterile system was able to be maintained. Vials containing 27 mL of CS-1000 ATM were fed either by gravity (not shown) or by peristaltic pump through a vented vial spike. With this method of delivery, 25 mL of reagent is delivered per vial. (b) 27 mL vial imaged with the vented spike.

2.7. Determination of Labeled Population. Cells were labeled with Cell Sense CS-ATM DM Green (CS-DM), a preclinical grade, fluorescent green conjugated version of CS-1000 ATM as performed above. Cells were washed of excess reagent and label uptake assessed by flow cytometry. Percentage of labeled population was determined by comparing the histograms for the 488 emission channel between unlabeled and CS-DM labeled cells.

2.8. Cryopreservation. Cells were pelleted and resuspended in 20% serum (Sigma Aldrich) 10% dimethyl sulfoxide (DMSO, brand) containing media which is slowly brought down to -80°C before transferring to liquid nitrogen.

3. Results

3.1. The Logistics of Labeling at Industrial Scale. Introducing an imaging agent into clinical preparations requires the properties of the therapeutic and the manufacturing protocol for cellular preparation be unaltered by its addition. Preclinical studies have shown the efficacy of the reagent at experimental levels and in the clinic at cellular doses of 10^6 cells [18, 20–24]. In the area of T-cell therapies, higher doses of cells and large volumes are often required for cellular expansion. Scale, in this context, takes into consideration billions of cells and its relationship to the volume of label, along with the ability to maintain sterility within the system. These parameters at a small scale were not an obstacle when compared to larger clinical scale preparations. The issue of scale was addressed by taking product packaging volume from 4 mL to 27 mL. The 27 mL packaging resulted in 25 mL of delivered reagent with 2 mL of hold-up volume when administered by vented spike (Figure 1). Small scale preparations involved the addition of reagent to a flask in a tissue culture hood, while large scale preparations are often performed in a clean room, where a closed system is preferred. The addition of the larger

packaging size and vented spike delivery allows for larger volume administration without the transfer of the bioreactor to a culture hood. Using this method, reagent can be pumped in via the bioreactors peristaltic pump or simply gravity fed. Adding to the adaptability of the process, cellular labeling was performed in the final 24 hours of cellular expansion as not to increase the time or complexity of product preparation.

3.2. Uptake and Viability. Cellular viability is a common release criterion for therapeutic cells. Keeping the requirements for an imaging reagent in mind, cells were examined under two categories: normal healthy donor expanded T-cells and cryopreserved T-cells. The two categories of cells were used to examine clinical scale labeling and expansion as well as the storage of labeled cells to assess labeling properties for stored and/or shipped cells. Prior studies showed that T-cells are labeled effectively at 10 mg/mL, which is the constant dose used throughout the studies (data not shown). Cells were labeled at 10 mg/mL in 1L of media for 24 hours. The label possesses a single major spectral peak by NMR, which when compared to a trifluoroacetic acid standard (TFA) allows for the calculation of F/c (19F/cell, Figure 2(a)). All cell groups demonstrated labeling of 10^{11} 19F/cell (F/c). Using Trypan Blue exclusion, we clearly demonstrated that cellular viability was maintained (Figures 2(c) and 2(d)). Importantly, cryopreserved cells maintain cellular health and retain label after thaw (Figure 2(c)). Viability and F/c are summarized for each category of cells in Figure 2(d). Examining the degree of label retention in nonengineered cells, a fluorescently conjugated form of Cell Sense was used to show the distribution of cellular label (Figure 2(b)). Flow cytometry confirmed that $\sim 90\%$ of the T-cell preparation was labeled with reagent.

3.3. Cellular Characterization. A cellular therapeutic requires a clear definition and characterization of the cellular product. Before therapeutics is released for patient administration, a number of release criteria are assessed. A panel of surface markers was used to assess labeled and unlabeled cells in each of the previously mentioned categories (recently expanded and cryopreserved). Different immunotherapeutic T-cells have different release criteria; in this study we examined the cellular populations for the CD3 T-cell maker, CD8 cytotoxic T-cell marker, CD4 T helper cell marker, and CD32 myeloid and B-cell maker. The ratios of CD8 and CD4 cells were maintained with a limited number of CD32 (nonlymphocyte) cells present (Figure 3). Importantly, these ratios were maintained after cryopreservation. The composition of engineered cells will vary by the way in which they are generated, with the desired ratios of CD4 : CD8 cell varying by manufacture; based on the labeling performed here, we would not anticipate the ratios to change in other expansion protocols.

4. Discussion

Early Phase 1 trials primarily look for evidence of drug safety, but pharmacologic activity and early indications of efficacy are often explored. Early Phase 1 trials typically involve escalating dosage and a single route of administration.

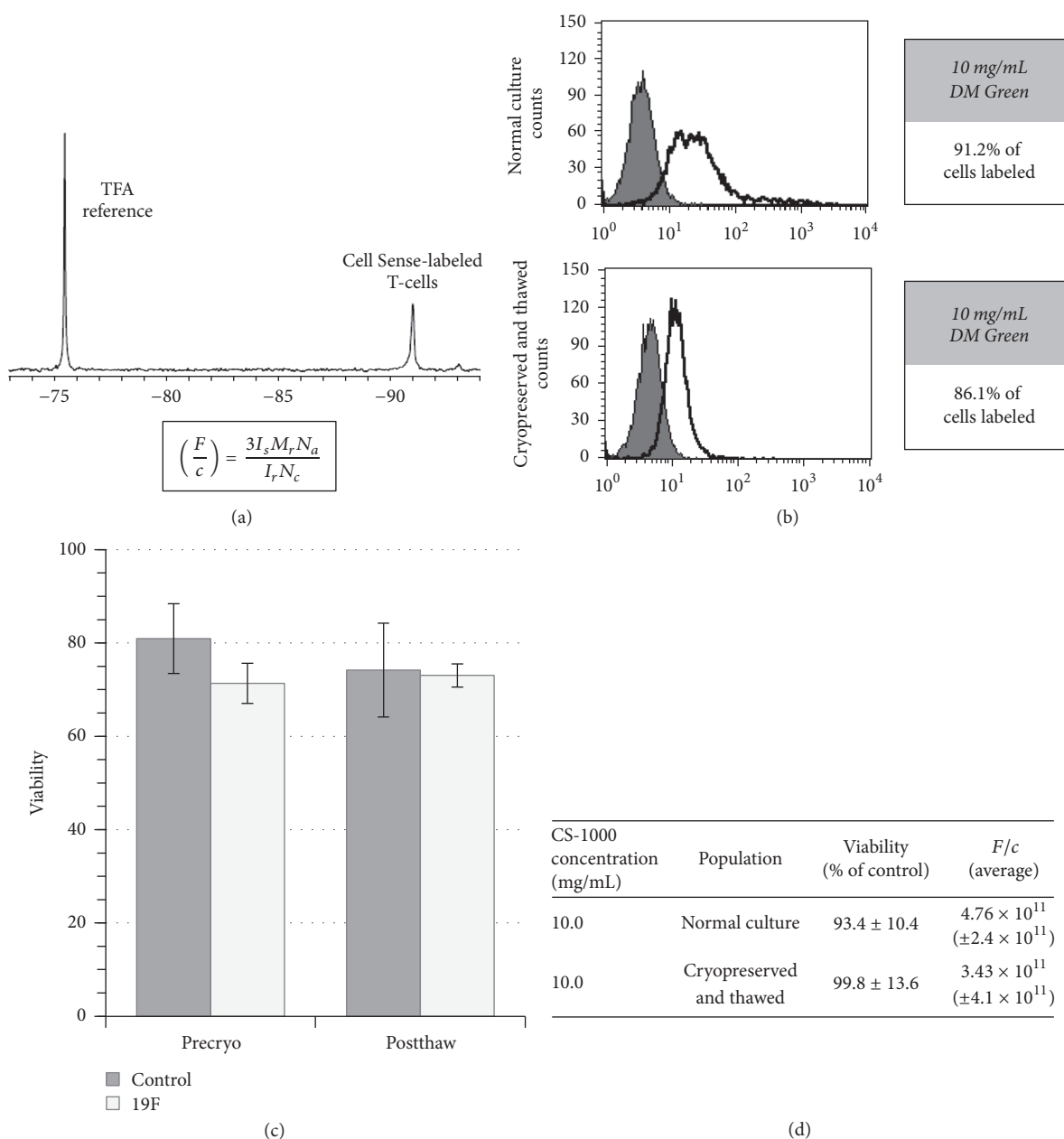


FIGURE 2: Label uptake and cellular viability after label. (a) CS-1000 ATM produces a single major spectral peak when detected by NMR. Using the integration values of the labeled cells and TFA reference, the ^{19}F atoms/cell (F/c) can be calculated. I_s = integrated area of major peak of the cell pellet, M_r = moles of TFA reference (three ^{19}F per TFA molecule already reflected in equation), N_a = Avogadro's number, I_r = integrated area under TFA reference peak, and N_c = number of cells in pellet. (b) Labeling with a green fluorescently conjugated version of the reagent, cellular uptake of the reagent was examined by flow cytometry (n2). (c) Comparison of the viability of labeled and unlabeled cells both before and after cryopreservation (precryo n5, postthaw n2). (d) Table summarizing the viability and label uptake of groups of cells.

In consideration of early Phase 1 trials, the FDA states in their guidance for Cellular and Gene Therapy Products that evidence of the cell therapy products persistence and activity should be monitored. Further, the guidance document suggests monitoring the point of administration and site of intended activity, as well as other potential migratory sites or abnormal cell behavior [27]. Pharmacokinetic (PK) data for a cell therapy product *in vivo* would help answer some of these unknowns. The cell therapy results to date are

promising [1–8]; however cellular therapies face a number of challenges before coming of a widely available treatment option. Manufacturing scale-up and obtaining pharmacokinetic data are two such challenges to be overcome, both obstacles considered throughout this manuscript.

Incorporation of an imaging agent into a clinical protocol requires that the imaging agent does not alter the cellular therapy, either in health or in function, and is capable of being imaged clinically [13]. Earlier experiments demonstrate

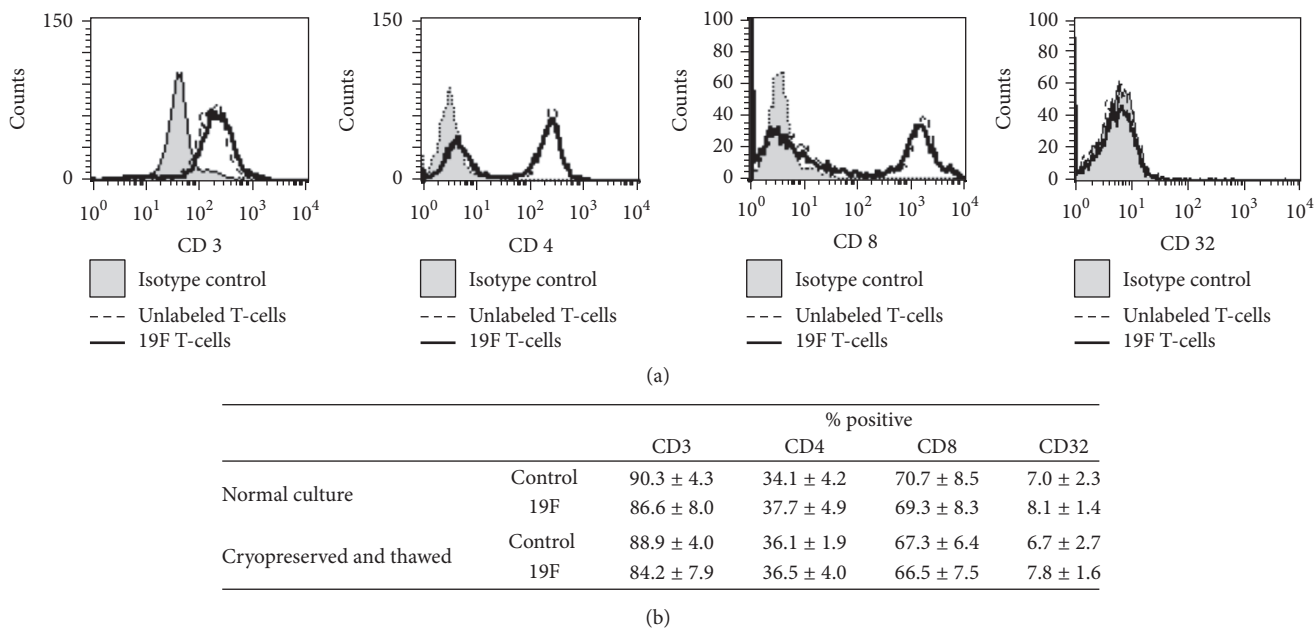


FIGURE 3: Phenotypic examination of labeled cells. Labeled and unlabeled T-cell populations are compared for the presence of the following phenotypic markers: CD3, CD4, CD8, and CD32. (a) Histograms comparing cellular populations labeled with conjugated antibodies for the depicted surface marker or isotype control. (b) Table summarizing the cellular populations (n2) presenting +/- CS-1000 ATM labeling and +/- cryopreservation.

the labels ability to maintain cellular health and function in multiple cell types [18, 20–24] and to be imaged at clinically relevant scan times [19]. For ease of use, having the label be easily incorporated into cellular processing was also important. CS-1000 ATM does not require the addition of transfection agents, which eases the incorporation process. Our studies demonstrate an additional simplification; by increasing the packaging and dose of deliverable reagent per vial, we were able to maintain the ease of use for large clinical scale manufacturing (Figure 1). A degree of the design of expansion protocols involve expansion of the culture in bioreactors in a clean room environment, factoring in the attachments (tubing) feeding into the bioreactors for the continued culture. Having a 25 mL dose of cellular label being administered to existing lines of a bioreactor via a vented spike eliminates the transfer of the culture to a biologic safety cabinet and lends itself to the industrial manufacturing process. Through the consideration of these scaling components, CS-1000 ATM was able to overcome previously undemonstrated questions of labeling cells at clinical scale.

The addition of the 19F imaging agent to the manufacturing process did not alter common release criteria, namely, the cellular health or phenotype of the culture (Figures 2 and 3, resp.). An important aspect of adding an internalized label for cellular trafficking is not to alter these criteria. Cells were labeled with an average of 3.7×10^{11} F/c. Cryopreservation of samples was also examined. When cells are being tested for release criteria, shipped, or stored for repeat dosing, cryopreservation may be necessary. Cellular phenotype, health, and cellular label were maintained upon thawing of cryopreserved samples (Figures 2 and 3). Other

imaging modalities may lack the ability to be cryopreserved and require labeling of the cellular population after thawing due to the nature of the imaging agent (i.e., half-life) or concerns regarding the extent of cellular labeling [28].

Incorporating a cellular imaging agent to the therapeutic process allows PK data to be achieved through *in vivo* imaging of cellular therapies. Imaging enables the examination of a therapy’s ability to reach its target (such as a solid tumor). Of equal importance, such methodology could account for potential off target delivery. In the selection of route of administration for cellular delivery, comparing various routes could help drive therapeutic outcome if one route demonstrates improved targeting. Furthermore, since therapeutic response may take 90 to 120 days, the possibility of using an imaging agent as a biomarker for efficacy when considering cancer treatment also holds great promise. Imaging also allows for the detection of cells failing to home/migrate; should a cellular therapy not reach the site of disease, readministration of the cellular therapy of alternative therapies could also be considered. Our goal by addressing the scalability of cellular labeling is that the technology can enable faster and more effective examination of cellular PK in man.

Imaging in clinical trials has the potential to strengthen safety and homing data. With one trial using 19F imaging completed [19] and another trial set to recruit (clinicaltrials.gov, NCT02035085) there are still steps being made in the implementation of this technology. Through the data developed in this manuscript, the concerns over clinical scale-up and incorporation of cellular labeling in clinical scale T-cell immunotherapy manufacturing have been addressed.

As engineered T-cells are developed to target solid tumors, the ability to image with an agent that can transition from preclinical to clinical studies can help develop the pharmacokinetic data to necessary to accelerate the therapeutic path forward.

Abbreviations

CAR:	Chimeric Antigen Receptor
TCR:	T-Cell Receptor
ALL:	Acute Lymphoblastic Leukemia
PK:	Pharmacokinetic
19F:	Fluorine 19
NK:	Natural Killer
MRI:	Magnetic Resonance Imaging
PET:	Positron emission tomography
SPECT:	Single photon emission computed tomography
CS:	Cell Sense.

Disclosure

Human buffy coats were obtained from the Central Blood Bank (Pittsburgh, PA) for research purposes, and all applicable consent was collected by Central Blood Bank.

Conflicts of Interest

Charles F. O'Hanlon is an employee and shareholder of Celsense Inc. Brooke M. Helfer is an employee of Celsense Inc. Tamara Fedczyna, Shannon Eaker, and William D. Shingleton are employees of GE Healthcare. Cell Sense, the 19F MRI tracer agent described in the article, is manufactured by Celsense Inc. The Wave Bioreactor described in the article is manufactured by GE Healthcare. Celsense Inc. and GE Healthcare jointly provided fund and in-kind support for this research project.

Authors' Contributions

Charles F. O'Hanlon, Tamara Fedczyna, Shannon Eaker, William D. Shingleton, and Brooke M. Helfer participated in the composition, review, and editing of the manuscript. Brooke M. Helfer compiled the data and was responsible for the composition of the figures.

Acknowledgments

Funding for this work was provided by Celsense Inc. and a grant from GE Healthcare.

References

- [1] S. A. Grupp, M. Kalos, D. Barrett et al., "Chimeric antigen receptor-modified T cells for acute lymphoid leukemia," *The New England Journal of Medicine*, vol. 368, no. 16, pp. 1509–1518, 2013.
- [2] S. L. Maude, N. Frey, and P. A. Shaw, "Chimeric antigen receptor T cells for sustained remissions in leukemia," *The New England Journal of Medicine*, vol. 371, no. 16, pp. 1507–1517, 2014.
- [3] A. L. Garfall, M. V. Maus, W.-T. Hwang et al., "Chimeric antigen receptor T cells against CD19 for multiple myeloma," *The New England Journal of Medicine*, vol. 373, no. 11, pp. 1040–1047, 2015.
- [4] A. P. Rapoport, E. A. Stadtmauer, G. K. Binder-Scholl, O. Goloubeva, D. T. Vogl, and S. F. Lacey, "NY-ESO-1-specific TCR-engineered T cells mediate sustained antigen-specific antitumor effects in myeloma," *Nature Medicine*, vol. 21, pp. 914–921, 2015.
- [5] P. Kebriaei, H. Singh, M. H. Huls, M. J. Figliola, R. Bassett, S. Olivares et al., "Phase I trials using Sleeping Beauty to generate CD19-specific CAR T cells," *The Journal of clinical investigation*, vol. 126, no. 9, Article ID 5004935, pp. 3363–3376, 2016.
- [6] X. Wang, L. L. Popplewell, J. R. Wagner et al., "Phase 1 studies of central memory-derived CD19 CAR T-cell therapy following autologous HSCT in patients with B-cell NHL," *Blood*, vol. 127, no. 24, pp. 2980–2990, 2016.
- [7] J. N. Kochenderfer, M. E. Dudley, R. O. Carpenter et al., "Donor-derived CD19-targeted T cells cause regression of malignancy persisting after allogeneic hematopoietic stem cell transplantation," *Blood*, vol. 122, no. 25, pp. 4129–4139, 2013.
- [8] C. J. Turtle, L.-A. Hanafi, C. Berger et al., "CD19 CAR-T cells of defined CD4+:CD8+ composition in adult B cell ALL patients," *The Journal of Clinical Investigation*, vol. 126, no. 6, pp. 2123–2138, 2016.
- [9] A. Bot, J. E. Brewer, Z. Eshhar et al., "Target discovery for T cell therapy: Next steps to advance Immunotherapies," *Journal for ImmunoTherapy of Cancer*, vol. 3, no. 1, article no. 31, 2015.
- [10] B. L. Levine, J. Miskin, K. Wonnacott, and C. Keir, "Global Manufacturing of CAR T Cell Therapy," *Molecular Therapy - Methods and Clinical Development*, vol. 4, pp. 92–101, 2017.
- [11] S. Eaker, E. Abraham, J. Allickson et al., "Bioreactors for cell therapies: Current status and future advances," *Cytotherapy*, vol. 19, no. 1, pp. 9–18, 2017.
- [12] Society AC, "Facts and Figures 2016," Atlanta, American Cancer Society, 2016.
- [13] J. V. Frangioni and R. J. Hajjar, "In vivo tracking of stem cells for clinical trials in cardiovascular disease," *Circulation*, vol. 110, no. 21, pp. 3378–3383, 2004.
- [14] E. T. Ahrens and J. W. M. Bulte, "Tracking immune cells in vivo using magnetic resonance imaging," *Nature Reviews Immunology*, vol. 13, no. 10, pp. 755–763, 2013.
- [15] A. V. Naumova, M. Modo, A. Moore, C. E. Murry, and J. A. Frank, "Clinical imaging in regenerative medicine," *Nature Biotechnology*, vol. 32, no. 8, pp. 804–818, 2014.
- [16] M. Srinivas, A. Heerschap, E. T. Ahrens, C. G. Figdor, and I. J. M. de Vries, "19F MRI for quantitative in vivo cell tracking," *Trends in Biotechnology*, vol. 28, no. 7, pp. 363–370, 2010.
- [17] C. M. Long and J. W. M. Bulte, "In vivo tracking of cellular therapeutics using magnetic resonance imaging," *Expert Opinion on Biological Therapy*, vol. 9, no. 3, pp. 293–306, 2009.
- [18] E. T. Ahrens, R. Flores, H. Xu, and P. A. Morel, "In vivo imaging platform for tracking immunotherapeutic cells," *Nature Biotechnology*, vol. 23, no. 8, pp. 983–987, 2005.
- [19] E. T. Ahrens, B. M. Helfer, C. F. O'Hanlon, and C. Schirda, "Clinical cell therapy imaging using a perfluorocarbon tracer and fluorine-19 MRI," *Magnetic Resonance in Medicine*, vol. 72, no. 6, pp. 1696–1701, 2014.
- [20] P. Boehm-Sturm, L. Mengler, S. Wecker, M. Hoehn, and T. Kallur, "In vivo tracking of human neural stem cells with 19F magnetic resonance imaging," *PLoS ONE*, vol. 6, no. 12, Article ID e29040, 2011.

- [21] M. N. Bouchlaka, K. D. Ludwig, J. W. Gordon et al., "19F-MRI for monitoring human NK cells in vivo," *OncolImmunology*, vol. 5, no. 5, Article ID e1143996, 2016.
- [22] B. M. Helfer, A. Balducci, A. D. Nelson et al., "Functional assessment of human dendritic cells labeled for in vivo 19F magnetic resonance imaging cell tracking," *Cytotherapy*, vol. 12, no. 2, pp. 238–250, 2010.
- [23] B. M. Helfer, A. Balducci, Z. Sadeghi et al., "19F MRI tracer preserves in vitro and in vivo properties of hematopoietic stem cells," *Cell Transplantation*, vol. 22, no. 1, pp. 87–97, 2013.
- [24] M. Srinivas, P. A. Morel, L. A. Ernst, D. H. Laidlaw, and E. T. Ahrens, "Fluorine-19 MRI for visualization and quantification of cell migration in a diabetes model," *Magnetic Resonance in Medicine*, vol. 58, no. 4, pp. 725–734, 2007.
- [25] P. Kaliński, C. M. U. Hilkens, A. Snijders, F. G. M. Snijdwint, and M. L. Kapsenberg, "IL-12-Deficient Dendritic Cells, Generated in the Presence of Prostaglandin E2, Promote Type 2 Cytokine Production in Maturing Human Naive T Helper Cells," *The Journal of Immunology*, vol. 159, no. 1, pp. 28–35, 1997.
- [26] J. M. Janjic, M. Srinivas, D. K. K. Kadayakkara, and E. T. Ahrens, "Self-delivering nanoemulsions for dual fluorine-19 MRI and fluorescence detection," *Journal of the American Chemical Society*, vol. 130, no. 9, pp. 2832–2841, 2008.
- [27] Guidance for Industry, "Preclinical Assessment of Investigational Cellular and Gene Therapy Products (DRAFT GUIDANCE)," in *U.S. Department of Health and Human Services FDA, Center for Biologics Evaluation and Research*, 2012.
- [28] G. M. van Buul, G. Kotek, P. A. Wielopolski et al., "Clinically translatable cell tracking and quantification by MRI in cartilage repair using superparamagnetic iron oxides," *PLoS ONE*, vol. 6, no. 2, Article ID e17001, 2011.

Clinical Study

Head-to-Head Comparison of ^{68}Ga -Citrate and ^{18}F -FDG PET/CT for Detection of Infectious Foci in Patients with *Staphylococcus aureus* Bacteraemia

Soile P. Salomäki,^{1,2,3} Jukka Kemppainen,^{2,4,5} Ulla Hohenthal,^{1,3}
Pauliina Luoto,² Olli Eskola,² Pirjo Nuutila,^{2,3,6} Marko Seppänen,^{2,4,5} Laura Pirilä,^{3,7}
Jarmo Oksi,^{1,3} and Anne Roivainen^{2,4}

¹Department of Infectious Diseases, Division of Medicine, Turku University Hospital, Turku, Finland

²Turku PET Centre, University of Turku, Turku, Finland

³Faculty of Medicine, University of Turku, Turku, Finland

⁴Turku PET Centre, Turku University Hospital, Turku, Finland

⁵Department of Clinical Physiology and Nuclear Medicine, Turku University Hospital, Turku, Finland

⁶Department of Endocrinology, Division of Medicine, Turku University Hospital, Turku, Finland

⁷Department of Rheumatology, Division of Medicine, Turku University Hospital, Turku, Finland

Correspondence should be addressed to Anne Roivainen; anne.roivainen@utu.fi

Received 14 June 2017; Revised 13 August 2017; Accepted 29 August 2017; Published 17 October 2017

Academic Editor: Frank Rösch

Copyright © 2017 Soile P. Salomäki et al. This is an open access article distributed under the Creative Commons Attribution License, which permits unrestricted use, distribution, and reproduction in any medium, provided the original work is properly cited.

Purpose. This study evaluated the potential of ^{68}Ga -citrate positron emission tomography/computed tomography (PET/CT) for the detection of infectious foci in patients with *Staphylococcus aureus* bacteraemia by comparing it with 2- ^{18}F fluoro-2-deoxy-*D*-glucose (^{18}F -FDG) PET/CT. **Methods.** Four patients admitted to hospital due to *S. aureus* bacteraemia underwent both ^{18}F -FDG and ^{68}Ga -citrate whole-body PET/CT scans to detect infectious foci. **Results.** The time from hospital admission and the initiation of antibiotic treatment to the first PET/CT was 4–10 days. The time interval between ^{18}F -FDG and ^{68}Ga -citrate PET/CT was 1–4 days. Three patients had vertebral osteomyelitis (spondylodiscitis) and one had osteomyelitis in the toe; these were detected by both ^{18}F -FDG (maximum standardised uptake value [SUV_{max}] 6.0 ± 1.0) and ^{68}Ga -citrate (SUV_{max} 6.8 ± 3.5 , $P = 0.61$). Three patients had soft tissue infectious foci, with more intense ^{18}F -FDG uptake (SUV_{max} 6.5 ± 2.5) than ^{68}Ga -citrate uptake (SUV_{max} 3.9 ± 1.2 , $P = 0.0033$). **Conclusions.** Our small cohort of patients with *S. aureus* bacteraemia revealed that ^{68}Ga -citrate PET/CT is comparable to ^{18}F -FDG PET/CT for detection of osteomyelitis, whereas ^{18}F -FDG resulted in a higher signal for the detection of soft tissue infectious foci.

1. Introduction

Positron emission tomography (PET) with the radiolabelled glucose analogue 2- ^{18}F fluoro-2-deoxy-*D*-glucose (^{18}F -FDG) is a sensitive and widely used method to detect inflammation and infection according to the high glucose uptake of activated inflammatory cells. It has an important role in the diagnosis of fever of unknown origin when conventional imaging has failed [1]. *Staphylococcus aureus* bacteraemia is a life-threatening condition, and detection and eradication

of deep infectious foci are crucial for successful treatment [2]. In previous studies, ^{18}F -FDG PET/CT has proven to be a sensitive method for the detection of infectious foci in patients with gram-positive bacteraemia [2, 3].

^{68}Ga -citrate has also been shown to be a sensitive and specific tracer for the detection of infectious lesions [4, 5], although only a few human studies using ^{68}Ga -citrate PET/CT exist. The biological mechanism of ^{68}Ga -citrate accumulation in infectious foci is not fully understood. Once injected the Ga-citrate complex is quickly dissociated into

Ga^{3+} and citrate $^{3-}$ within the blood. Then, 99% of the gallium ions are attached to transferrin [6, 7], which accumulates in inflammatory lesions. In addition, it is assumed that some ^{68}Ga may attach to bacterial siderophores, lactoferrin inside neutrophils, and free lactoferrin at the site of infection [8]. According to previous studies, ^{68}Ga -citrate PET/CT appears to be a sensitive tool for the detection of bone infections [4, 9], although until now it has not been studied in patients with *S. aureus* bacteraemia.

The purpose of this study was to evaluate the potential of ^{68}Ga -citrate PET/CT for the detection of infectious foci in patients with *S. aureus* bacteraemia by comparing it with ^{18}F -FDG in a head-to-head setting.

2. Materials and Methods

2.1. Subjects. This study evaluates four consecutive patients who were admitted to hospital due to *S. aureus* bacteraemia. All patients underwent both ^{18}F -FDG and ^{68}Ga -citrate whole-body PET/CT to detect infectious foci. The study was approved by the institutional ethical review board and all participants signed informed consent. The study was registered as a clinical trial (NCT01878721).

2.2. PET/CT. The synthesis of ^{68}Ga -citrate was performed with automated synthesis device (Modular Lab, Eckert & Ziegler Eurotope GmbH, Berlin, Germany). ^{68}Ga was obtained from a $^{68}\text{Ge}/^{68}\text{Ga}$ generator (IGG-100, 1850 MBq, Eckert & Ziegler Isotope Products, Valencia, CA, USA) by eluting the generator with 6 ml of 0.1 M hydrogen chloride (HCl). ^{68}Ga was prepurified through a cationic exchanger (Strata X-C, Phenomenex Inc., Torrance, CA) by eluting with HCl/acetone-solution (800 μl). Acetone was then evaporated by heating at 110°C for 240 s and after cooling of $^{68}\text{GaCl}_3$, the sterile isotonic sodium citrate solution (4 ml) was added to the reaction vial followed by 240 s reaction time. The product was transferred to the end product vial through a nonpyrogenic 0.22 μm sterile filter and diluted with saline (9 mg/ml, 6 ml). The radiochemical purity of the ^{68}Ga -citrate was evaluated by instant thin layer chromatography-silica-gel technique using methanol/acetic acid (9 : 1) as a mobile phase. pH of the product was tested with indicator strips (pH range 2.0–9.0) and sterile filter integrity was assessed by a bubble point test.

Whole-body ^{18}F -FDG and ^{68}Ga -citrate PET/CT (Discovery VCT, GE Medical Systems) were performed in all patients within 1–4 days. All patients fasted before the ^{18}F -FDG scan. The injected radioactivity doses of ^{18}F -FDG and ^{68}Ga -citrate were 292 ± 68 MBq (range: 227–387 MBq) and 196 ± 37 MBq (range: 158–245 MBq), respectively. PET scanning started at 58 ± 7 min (range: 52–67 min) after ^{18}F -FDG injection and 81 ± 23 min (range: 48–100 min) after ^{68}Ga -citrate injection. The whole-body PET acquisition (3 min/bed position) was performed following a low dose CT for anatomical reference and attenuation correction. PET images were reconstructed using a 3D maximum-likelihood reconstruction with an ordered-subsets expectation maximization algorithm (VUE Point, GE Healthcare). Visual analysis of the images was

performed by an experienced nuclear medicine specialist (J. K.), with the results being reevaluated by the research team for consensus. A positive finding was defined as an abnormal accumulation of ^{18}F -FDG or ^{68}Ga -citrate indicating infectious foci. ^{18}F -FDG and ^{68}Ga -citrate uptake in the volumes of interest were quantified and expressed as maximum standardised uptake values (SUV_{max}) by normalising the tissue radioactivity concentration for the injected radioactivity dose and the patient's weight. The blood background radioactivity concentration was determined from the left ventricle cavity as SUV_{mean} , and the target-to-background ratio (TBR) was calculated as $\text{SUV}_{\text{max, infection}} / \text{SUV}_{\text{mean, blood}}$.

2.3. Statistical Analysis. Results are expressed as mean \pm SD and range. A paired *t*-test was used to compare ^{18}F -FDG and ^{68}Ga -citrate uptake. A *P* value of <0.05 was considered statistically significant.

3. Results

^{68}Ga -citrate was prepared with high radiochemical purity ($\geq 95\%$) with pH of 3.0–7.0.

Patient characteristics are presented in Table 1. All patients had a condition predisposing them to infection. In addition, Patient #3 had a cardiac pacemaker. The time interval from hospital admission and initiation of antibiotic treatment to the first PET/CT was 4–10 days, with the second PET/CT scan performed within another 1–4 days. The order of the ^{18}F -FDG and ^{68}Ga -citrate scans depended on the availability of tracers, with both being performed first in two cases. The mean C-reactive protein (CRP) levels were 89 ± 55 mg/l on the day of ^{18}F -FDG PET/CT and 124 ± 118 mg/l on the day of ^{68}Ga -citrate PET/CT ($P = 0.56$). The blood background ($n = 4$) SUV_{mean} was 1.4 ± 0.05 for ^{18}F -FDG and 2.9 ± 0.88 for ^{68}Ga -citrate ($P = 0.043$).

Three patients had vertebral osteomyelitis (spondylodiscitis) and one patient had osteomyelitis of the toe. The osteomyelitic foci were detected by both PET/CT methods (Table 2, Figures 1 and 2) and magnetic resonance imaging (MRI) in the cases of vertebral osteomyelitis and X-ray in the case of osteomyelitis of the toe. In the areas of osteomyelitis ($n = 4$), the SUV_{max} of ^{18}F -FDG was 6.0 ± 1.0 (range: 5.3–7.4) and the SUV_{max} of ^{68}Ga -citrate was 6.8 ± 3.5 (range: 2.7–11.1, $P = 0.61$). The corresponding TBRs of ^{18}F -FDG and ^{68}Ga -citrate were 4.4 ± 0.90 and 2.5 ± 1.4 , respectively ($P = 0.015$). Three patients had multiple infectious lesions and abscesses in soft tissue (Patients #1, #3, and #4). In these soft tissue infectious foci and abscesses ($n = 8$), the SUV_{max} of ^{18}F -FDG (6.5 ± 2.5 , range: 3.7–10.6) was significantly higher than that of ^{68}Ga -citrate (3.9 ± 1.2 , range: 2.1–6.1, $P = 0.0033$; Figure 1). The corresponding TBRs of ^{18}F -FDG and ^{68}Ga -citrate were 4.6 ± 1.8 and 1.7 ± 0.7 , respectively ($P = 0.00021$).

In addition to infectious foci, all of the patients also had other metabolic findings. Three patients (Patients #2, #3, and #4) demonstrated strong uptake of ^{68}Ga -citrate in the larger arteries, coincidental to visible atherosclerosis on CT. In the ascending aorta ($n = 4$), the SUV_{max} of ^{68}Ga -citrate was 4.7 ± 1.9 (range: 2.0–6.6), whereas the SUV_{max} of ^{18}F -FDG

TABLE 1: Characteristics of the study patients.

Patient number	Age (years)	Gender	Comorbidities	Time from starting antibiotics to ¹⁸ F-FDG PET/CT (days)	Time from starting antibiotics to ⁶⁸ Ga-citrate PET/CT (days)	CRP on ¹⁸ F-FDG PET/CT (mg/l)	CRP on ⁶⁸ Ga-citrate PET/CT (mg/l)	Complications from <i>S. aureus</i> bacteraemia based on routine exams, PET/CTs, and follow-up
(1)	66	F	Atopic eczema	10	11	92	109	Meningitis, vertebral osteomyelitis, paravertebral abscesses, multiple infectious foci in soft tissues
(2)	70	F	Liver cirrhosis, type 2 diabetes, generalised atherosclerosis, HTN	6	5	14	14	Vertebral osteomyelitis, pneumonia
(3)	66	M	Cardiomyopathy, HTN, asthma, cardiac pacemaker	5	4	105	291	Osteomyelitis in toe and feet
(4)	86	M	COPD, immunosuppressive medication due to chronic dermatology disease	8	12	146	83	Vertebral osteomyelitis, septic arthritis, multiple infectious foci in soft tissues

F, female; M, male; HTN, hypertension; COPD, chronic obstructive pulmonary disease; CRP, C-reactive protein.

TABLE 2: Quantitative ^{18}F -FDG and ^{68}Ga -citrate PET/CT findings.

Patient number	Visually active findings	^{18}F -FDG		^{68}Ga -citrate	
		SUV _{max}	TBR	SUV _{max}	TBR
	<i>Infectious foci</i>				
	Blood background ^a	1.4	—	2.1	—
	Vertebral osteomyelitis	6.1	4.4	7.3	3.5
(1)	Psoas/paravertebral abscess	10.6	7.6	6.1	2.9
	Left elbow abscess	9.4	6.7	4.0	1.9
	Three soft tissue infectious foci in left arm	7.3; 6.3; 5.4	5.2; 4.5; 3.9	5.0; 3.6; 3.5	2.4; 1.7; 1.7
	Soft tissue infectious focus in left gluteus	3.7	2.6	2.1	0.8
	Blood background ^a	1.3	—	2.9	—
(2)	Vertebral osteomyelitis	7.4	5.7	11.1	3.8
	Pneumonia, right lung	2.7	2.1	3.7	1.3
	Pneumonia, left lung	3.9	3.0	3.1	1.1
	Blood background ^a	1.4	—	2.4	—
(3)	Septic arthritis and osteomyelitis, I toe	5.3	3.8	2.7	1.1
	Soft tissue infectious focus, I toe	4.6	3.3	2.9	1.2
	Blood background ^a	1.4	—	4.1	—
	Vertebral osteomyelitis	5.3	3.8	5.9	1.4
(4)	Shoulder abscess	4.5	3.2	4.2	1.0
	Septic arthritis, glenohumeral joint	5.0	3.6	2.5	0.6
	Septic arthritis, sternoclavicular joint	7.7	5.5	6.2	1.5
	<i>Other metabolic findings</i>				
(1)	Active spleen	2.9	2.1	2.7	1.3
	Ascending aorta	1.6	1.1	2.0	1.0
	Parotid, unexplained	1.8	1.4	9.4	3.2
(2)	Reactive lymph nodes, neck right side	2.5	1.9	5.6	1.9
	Inferior vena cava, thrombosis	2.5	1.9	8.6	3.0
	Ascending aorta	1.6	1.2	6.6	2.3
	Caecum, unspecific uptake	12.6	9.0	1.7	0.7
(3)	Descending colon, tubular adenoma	9.7	6.9	7.8	3.3
	Ascending aorta	2.1	1.5	5.4	2.3
	Reactive lymph nodes, neck right side	6.8	4.9	4.6	1.1
(4)	Reactive lymph nodes, neck left side	6.6	4.7	3.7	0.9
	Ascending aorta	1.2	0.9	4.6	1.1

^aDetermined from heart left ventricle cavity, SUV_{mean}; TBR, target-to-background ratio (SUV_{max,infection}/SUV_{mean,blood}).

was 1.6 ± 0.37 (range: 1.2–2.1, $P = 0.051$). The corresponding TBRs were 1.7 ± 0.72 for ^{68}Ga -citrate and 1.2 ± 0.25 for ^{18}F -FDG ($P = 0.17$). Patient #1 showed increased splenic uptake of both tracers, which was interpreted as a normal reaction in a septic condition. Patient #2 demonstrated high uptake of ^{68}Ga -citrate in an enlarged parotid gland and lymph nodes in the neck (Figure 2(a)), which were not detected on ^{18}F -FDG PET/CT. In the absence of clinical symptoms, the enlarged parotid gland was not further studied by MRI or ultrasound, so the observed ^{68}Ga -citrate uptake remained unexplained. Patient #2 also demonstrated ^{68}Ga -citrate uptake in the inferior vena cava, but not ^{18}F -FDG uptake, with thrombosis being confirmed by ultrasonography. Patient #3 had a clear focal accumulation of both ^{68}Ga -citrate and ^{18}F -FDG in

the descending colon, which was subsequently confirmed as a tubular adenoma in a colonoscopy with biopsies. The same patient also demonstrated ^{18}F -FDG but not ^{68}Ga -citrate accumulation in the caecum without specific findings on colonoscopy or biopsy. Patient #4 had reactive lymph nodes in the neck, which were indicated as being metabolically active by both imaging methods.

4. Discussion

We believe that this is the first study to compare ^{68}Ga -citrate and ^{18}F -FDG PET/CT imaging of infectious foci in patients with *S. aureus* bacteraemia. Our results revealed that ^{68}Ga -citrate and ^{18}F -FDG are comparable PET tracers for the

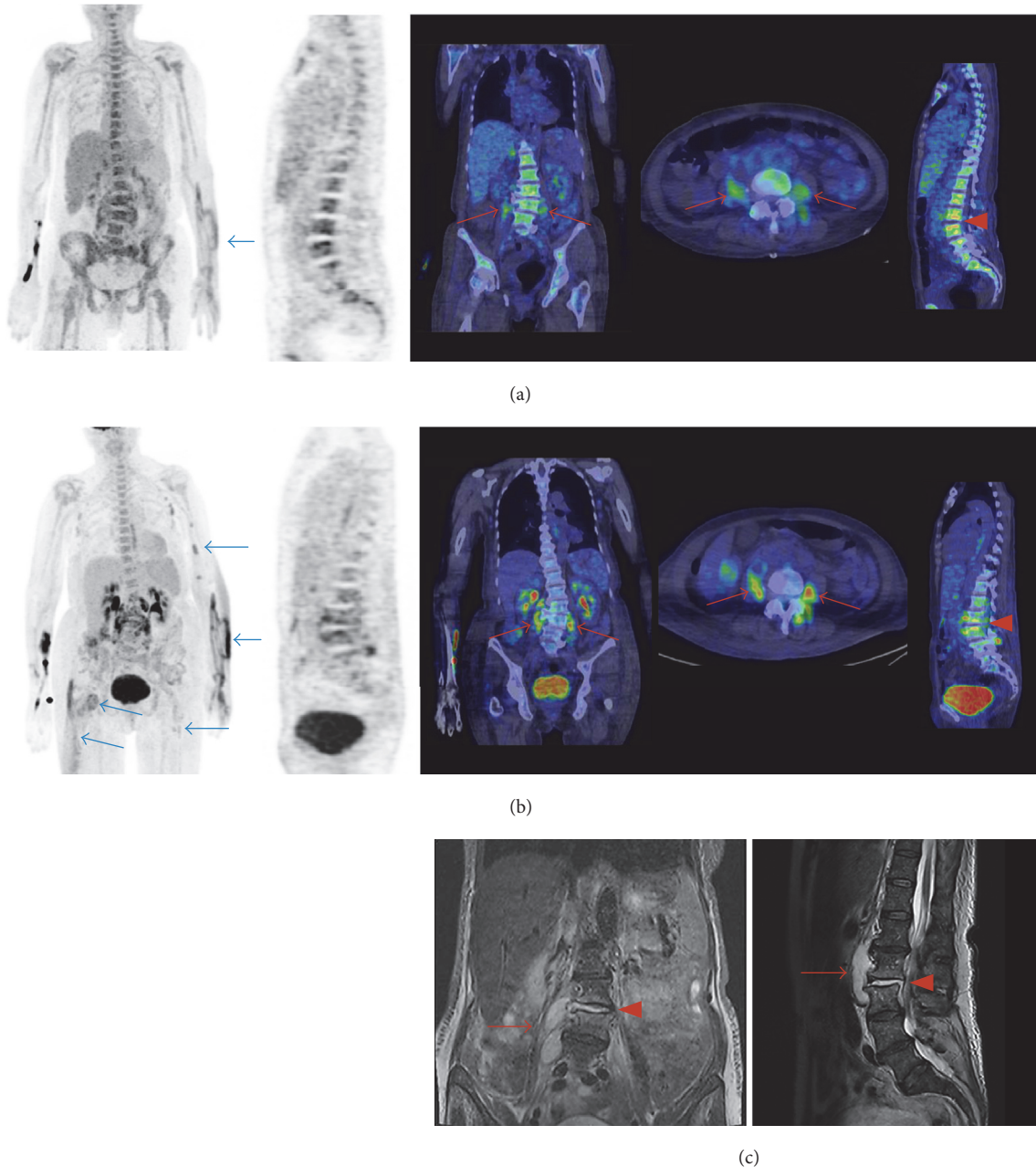


FIGURE 1: Patient #1 was a 66-year-old woman (weight: 65 kg) who presented at the hospital because of back pain and general symptoms. Both ^{68}Ga -citrate (a) and ^{18}F -FDG PET/CT (b) showed vertebral osteomyelitis (spondylodiscitis; red arrowheads) and abscesses in the iliopsoas and paravertebral area (red arrows). These were confirmed by MRI (c). ^{18}F -FDG PET/CT also showed other multiple soft tissue infectious foci ((b), blue arrows), some of which were not detectable on ^{68}Ga -citrate PET/CT ((a), blue arrow). The injected radioactivity dose of ^{18}F -FDG was 227 MBq and the PET acquisition started 54 min after injection. The injected radioactivity dose of ^{68}Ga -citrate was 245 MBq and the PET acquisition started 88 min after injection. MRI sequences were as follows: T2-weighted short inversion time inversion recovery (STIR) on the coronal view image (left) and T2-weighted on the sagittal view image (right).

detection of osteomyelitis. However, the soft tissue infectious foci were clearly better visualized with ^{18}F -FDG than ^{68}Ga -citrate.

In general, two different tracers must be compared with caution and taking into account their potentially different properties, such as uptake mechanisms and flow/diffusion

dependency. In animal models, both ^{18}F -FDG and ^{68}Ga -citrate have shown increased accumulation in *S. aureus* osteomyelitis, whereas, in healing bones without infection, only ^{18}F -FDG accumulation was observed [9]. Our results are in line with the animal studies, in that accumulation of these tracers in patients with osteomyelitis does not differ in the

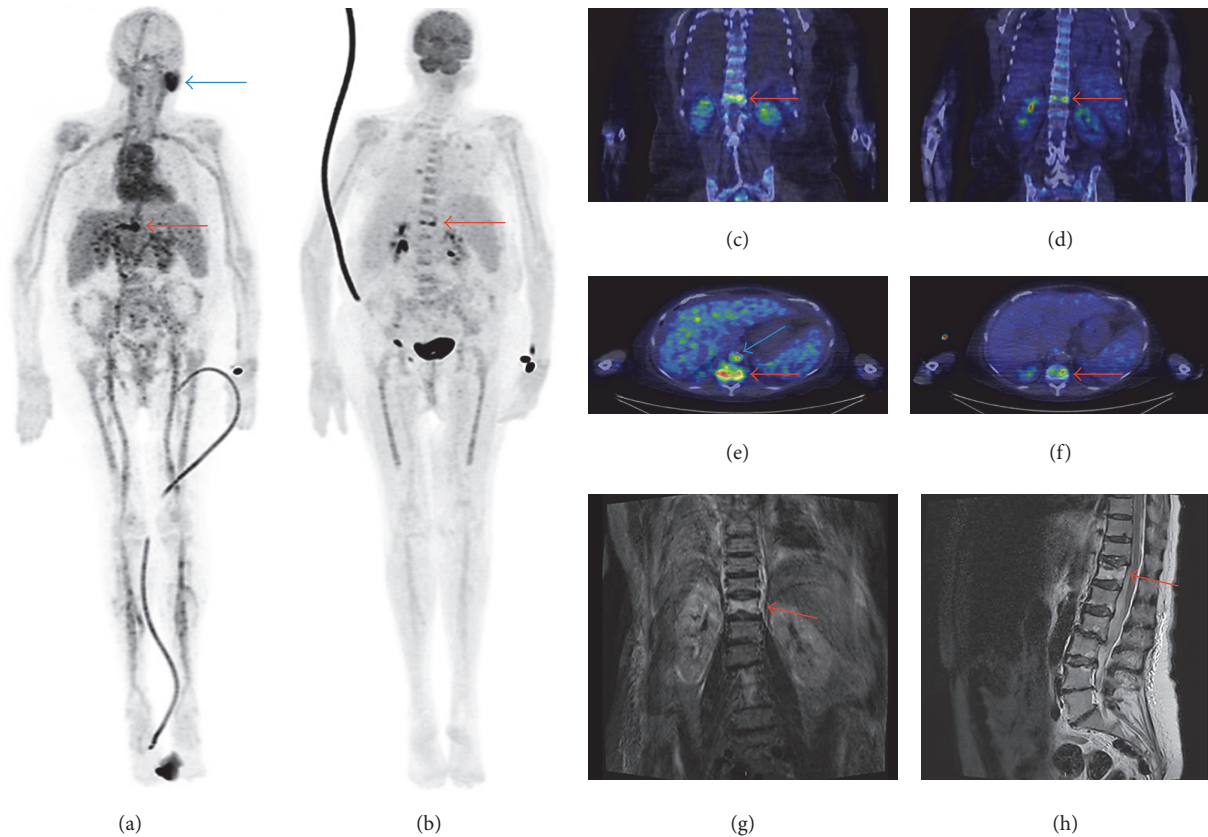


FIGURE 2: Patient #2 was a 70-year-old woman (weight: 69 kg), with multiple background diseases, who was admitted to hospital because of back pain and high fever. Both ^{68}Ga -citrate (a, c, e) and ^{18}F -FDG PET/CT (b, d, f) showed vertebral osteomyelitis (spondylodiscitis) in Th12 (red arrows) and pneumonia in both lungs. MRI showed oedema in Th12 (g, h). ^{68}Ga -citrate PET/CT also revealed uptake in the left parotid gland (unspecific; (a), blue arrow), neck lymph nodes (reactive), and inferior vena cava (thrombosis; (e), blue arrow). There was no ^{18}F -FDG uptake in these areas. The injected radioactivity dose of ^{18}F -FDG was 279 MBq and the PET acquisition started 50 min after injection. The injected radioactivity dose of ^{68}Ga -citrate was 199 MBq and the PET acquisition started 100 min after injection. MRI sequences were as follows: T2-weighted short inversion time inversion recovery (STIR) on the coronal view image (left) and T2-weighted on the sagittal view image (right).

acute phase of *S. aureus* infection. Further studies are warranted to clarify whether ^{68}Ga -citrate PET/CT can confirm the healing of osteomyelitis and whether it is superior to ^{18}F -FDG for the differentiation of infection from sterile bone inflammation.

We found a difference between ^{18}F -FDG and ^{68}Ga -citrate PET/CT in the detection of soft tissue infection. Contrary to the clear findings of multiple small infectious foci without abscess formation in ^{18}F -FDG PET/CT, such lesions were only slightly visible or not visible at all on ^{68}Ga -citrate PET/CT (Patient #1). The difference in SUV_{max} between ^{18}F -FDG and ^{68}Ga -citrate was also statistically significant. These findings were not controlled by other imaging modalities, but some were also detectable in clinical status (e.g., multiple infectious foci in Patient #1's arm). In this study we used 196 ± 37 MBq for ^{68}Ga -citrate PET and started imaging after 81 ± 23 minutes. The observed blood background $\text{SUV}_{\text{mean}} 2.9 + 0.88$ may be a strong contributing factor for not visualizing soft tissue infections with ^{68}Ga -citrate. It can be hypothesized that lowering of injected radioactivity dose to 100 MBq would reduce blood pool radioactivity and cause less background

noise. In order to confirm the effect of a lower ^{68}Ga -citrate dose, further studies are warranted. A recent study comparing ^{18}F -FDG, ^{68}Ga -citrate, and other tracers in a pig-model of haematogenously disseminated *S. aureus* infection reported slightly different results [10]. These findings may be due to the higher blood background radioactivity of ^{68}Ga -citrate (Table 2). The slight differences in the production of ^{68}Ga -citrate might reflect different results, too.

Owing to its high sensitivity, specificity, and accuracy in the detection of osteomyelitis, MRI is the recommended imaging modality when spondylodiscitis is suspected [11]. MRI provides higher spatial resolution of the spinal cord than PET/CT, which is important if an operation is considered. However, sometimes MRI cannot be obtained because of patient-related reasons (e.g., implanted cardiac devices, claustrophobia). In such cases, ^{18}F -FDG PET/CT is the recommended imaging modality [11]. Traditionally, MRI is targeted to the part of the body where the patient has signs or symptoms; however, a previous study [12] showed that around one-third of infectious foci in *S. aureus* bacteraemia are asymptomatic. Thus, these silent infectious foci may

pass unnoticed with traditional imaging, while PET/CT scanning provides information on the whole body, and as demonstrated in our cases, multiple infectious foci can be detected simultaneously.

In addition to infectious foci, both ^{18}F -FDG and ^{68}Ga -citrate PET/CT also revealed other clinically significant findings. In Patient #3, PET/CT findings in the colon led to colonoscopy and the finding of a tubular adenoma. Patient #2 demonstrated an uptake of ^{68}Ga -citrate (but not ^{18}F -FDG) in the inferior vena cava where thrombosis was later confirmed by ultrasound. This can be related to pooling tracer just proximal to the narrowing caused by the thrombus. More comprehensive studies are needed to explain the differences in the findings of ^{68}Ga -citrate and ^{18}F -FDG, for example, whether they are ascribed due to infection versus sterile inflammation.

The accumulation of ^{68}Ga -citrate in atherosclerotic arteries warrants further studies to determine its importance. Previously, ^{68}Ga -chloride uptake has been demonstrated in atherosclerotic lesions in mice [13]. Instead, in the papers presented by Nanni and coworkers [4] as well as Vorster and coworkers [14], the relatively high vascular radioactivity was regarded as a normal biodistribution of ^{68}Ga -citrate. The identification of atherosclerosis in 3 patients by ^{68}Ga -citrate may be coincidental. One advantage of ^{68}Ga -citrate over ^{18}F -FDG is that patients are not required to fast before the scan. However, for detection of metastatic endovascular infection the accumulation of ^{68}Ga -citrate in atherosclerotic arteries can be regarded as a limitation of ^{68}Ga -citrate PET/CT in patients with *S. aureus* bacteraemia.

In the current study, the time intervals between ^{18}F -FDG and ^{68}Ga -citrate scans were short (1–4 days), and CRP remained at the same levels over these intervals. Neither surgical procedures nor changes to the antimicrobial treatment were made between the two scans. We thus consider that the infectious status of the patients did not differ markedly between ^{18}F -FDG and ^{68}Ga -citrate studies. However, time interval from commencement of antibiotic treatment to the first PET/CT was 4–10 days and we are not able to exclude the possibility that due to this delay some of the infectious lesions were not detected. We also determined the TBRs, which revealed that the blood radioactivity concentration of ^{68}Ga -citrate was higher than that of ^{18}F -FDG. Thus, in many foci, the TBRs of ^{68}Ga -citrate PET/CT were lower than in ^{18}F -FDG PET/CT. In general, the number of patients is small, which can be regarded as a limitation of this study.

5. Conclusion

^{68}Ga -citrate and ^{18}F -FDG are comparable PET tracers for the imaging of osteomyelitis in patients with *S. aureus* bacteraemia. Further studies are warranted to clarify whether ^{68}Ga -citrate PET/CT can detect osteomyelitis caused by other pathogens and whether it can assess the healing of infectious osteomyelitis. For the detection of soft tissue infectious foci, ^{18}F -FDG PET/CT shows higher intensity than ^{68}Ga -citrate PET/CT but the effect of lower ^{68}Ga -citrate dose should be verified by further studies.

Conflicts of Interest

The authors declare that they have no conflicts of interest.

Acknowledgments

The authors thank Mia Koutu and Laura Kontto for helping with PET/CT imaging and Timo Kattelus for helping with the images. This study was conducted in the Finnish Centre of Excellence in Cardiovascular and Metabolic Diseases supported by the Academy of Finland, University of Turku, Turku University Hospital, and Åbo Akademi University. This study was also funded by Turku University Foundation and the Foundation of Rauno and Anne Puolimatka.

References

- [1] N. Ergül, M. Halac, T.F. Cermik et al., “The diagnostic role of FDG PET/CT in patients with fever of unknown origin,” *Molecular Imaging and Radionuclide Therapy*, vol. 20, pp. 19–25, 2011.
- [2] F. J. Vos, B. J. Kullberg, P. D. Sturm et al., “Metastatic infectious disease and clinical outcome in *Staphylococcus aureus* and *Streptococcus species* bacteremia,” *Medicine*, vol. 91, no. 2, pp. 86–94, 2012.
- [3] F. J. Vos, C. P. Bleeker-Rovers, and P. D. Sturm, “ ^{18}F -FDG PET/CT for detection of metastatic infection in gram-positive bacteremia,” *Journal of Nuclear Medicine*, vol. 51, no. 8, pp. 1234–1240, 2010.
- [4] C. Nanni, C. Errani, and L. Boriani, “ ^{68}Ga -citrate PET/CT for evaluating patients with infections of the bone: preliminary results,” *Journal of Nuclear Medicine*, vol. 51, no. 12, pp. 1932–1936, 2010.
- [5] V. Kumar, D. K. Boddeti, S. G. Evans, and S. Angelides, “ ^{68}Ga -citrate-PET for diagnostic imaging of infection in rats and for intra-abdominal infection in a patient,” *Current Radiopharmaceuticals*, vol. 5, no. 1, pp. 71–75, 2012.
- [6] M-F. Tsan, “Mechanism of gallium-67 accumulation in inflammatory lesions,” *Journal of Nuclear Medicine*, vol. 26, pp. 88–92, 1985.
- [7] V. Kumar, D. K. Boddeti, S. G. Evans, F. Roesch, and R. Howman-Giles, “Potential use of ^{68}Ga -apo-transferrin as a PET imaging agent for detecting *Staphylococcus aureus* infection,” *Nuclear Medicine and Biology*, vol. 38, no. 3, pp. 393–398, 2011.
- [8] P. Hoffer, “Gallium Mechanisms,” *Journal of Nuclear Medicine*, vol. 21, pp. 282–285, 1980.
- [9] T. J. Mäkinen, P. Lankinen, T. Pöyhönen, J. Jalava, H. T. Aro, and A. Roivainen, “Comparison of ^{18}F -FDG and ^{68}Ga PET imaging in the assessment of experimental osteomyelitis due to *Staphylococcus aureus*,” *European Journal of Nuclear Medicine and Molecular Imaging*, vol. 32, no. 11, pp. 1259–1268, 2005.
- [10] O. L. Nielsen, P. Afzelius, D. Bender et al., “Comparison of autologous ^{111}In -leukocytes, ^{18}F -FDG, ^{11}C -methionine, ^{11}C -PK11195 and ^{68}Ga -citrate for diagnostic nuclear imaging in a juvenile porcine haematogenous *Staphylococcus aureus* osteomyelitis model,” *American Journal of Nuclear Medicine and Molecular Imaging*, vol. 5, pp. 169–182, 2015.
- [11] E. F. Berbari, S. S. Kanj, T. J. Kowalski et al., “2015 Infectious Diseases Society of America (IDSA) Clinical practice guidelines for the diagnosis and treatment of native vertebral osteomyelitis in adults,” *Clinical Infectious Diseases*, vol. 61, no. 6, pp. e26–e46, 2015.

- [12] M. L. Cuijpers, F. J. Vos, C. P. Bleeker-Rovers et al., "Complicating infectious foci in patients with *Staphylococcus aureus* or *Streptococcus* species bacteraemia," in *European Journal of Clinical Microbiology and Infectious Disease*, vol. 26, pp. 105–113, 2007.
- [13] J. M. U. Silvola, I. Laitinen, H. J. Sipilä et al., "Uptake of ^{68}Ga gallium in atherosclerotic plaques in $\text{LDLR}^{-/-}\text{ApoB}^{100/100}$ mice," *EJN-MMI Research*, vol. 1, no. 1, pp. 1–8, 2011.
- [14] M. Vorster, A. Maes, A. Jacobs et al., "Evaluating the possible role of ^{68}Ga -citrate PET/CT in the characterization of indeterminate lung lesions," *Annals of Nuclear Medicine*, vol. 28, pp. 523–530, 2014.

Research Article

Intensity of ^{18}F -FDG PET Uptake in Culture-Negative and Culture-Positive Cases of Chronic Osteomyelitis

Petteri Lankinen,¹ Marko Seppänen,² Kimmo Mattila,³ Markku Kallajoki,⁴
Juhani Knuuti,² and Hannu T. Aro¹

¹Orthopaedic Research Unit, Department of Orthopaedic Surgery and Traumatology, Turku University Hospital, University of Turku, Turku, Finland

²Turku PET Centre, Turku University Hospital, Turku, Finland

³Medical Imaging Centre of Southwest Finland, Turku University Hospital, University of Turku, Turku, Finland

⁴Department of Pathology, Turku University Hospital, Turku, Finland

Correspondence should be addressed to Hannu T. Aro; hannu.aro@utu.fi

Received 22 June 2017; Accepted 7 September 2017; Published 11 October 2017

Academic Editor: Cristina Nanni

Copyright © 2017 Petteri Lankinen et al. This is an open access article distributed under the Creative Commons Attribution License, which permits unrestricted use, distribution, and reproduction in any medium, provided the original work is properly cited.

Microbiologic cultures are not infrequently negative in patients with a histopathologic diagnosis of chronic osteomyelitis. Culture-negative cases may represent low-grade infections with a lower metabolic activity than culture-positive cases. ^{18}F -FDG PET could potentially detect such a difference. We determined whether the level of ^{18}F -FDG PET uptake differs in patients with culture-negative and culture-positive osteomyelitis. We reviewed the clinical charts of 40 consecutive patients, who had diagnostic ^{18}F -FDG PET for a suspected bone infection. Twenty-six patients were eligible with a confirmed diagnosis based on microbiologic cultures and/or histopathologic examination. Sixteen of 26 patients had chronic osteomyelitis. Eight of them had positive cultures, seven had negative cultures, and one patient had no cultures of the biopsy specimen. The patients with histologically and/or microbiologically proven osteomyelitis were correctly interpreted as true positive in the routine clinical reading of ^{18}F -FDG PET images. There was no relationship between the level of ^{18}F -FDG PET uptake and the presence of positive or negative bacterial cultures. The result favors the concept that culture-negative cases of osteomyelitis are false-negative infections due to nonculturable microbes. ^{18}F -FDG PET may help to confirm the presence of metabolically active infection in these patients and guide their appropriate treatment.

1. Introduction

Osteomyelitis, especially its less common hematogenous forms, is a remarkably difficult diagnostic problem. Based on recent meta-analyses [1–3], fluorodeoxyglucose positron emission tomography (^{18}F -FDG PET) is the most sensitive radiographic technique for detecting chronic osteomyelitis and it has a greater specificity than leukocyte scintigraphy, bone scintigraphy, or magnetic resonance imaging. ^{18}F -FDG PET is less accurate in the diagnosis of periprosthetic joint infections [4]. One of the contributing factors may be the virulence of the causative bone pathogen and the severity of the subsequent infection [5], which appear to contribute to the intensity of local ^{18}F -FDG uptake in infected tissues. In a standardized animal model, localized subacute/chronic

osteomyelitis caused by *S. epidermidis* has been characterized by a low ^{18}F -FDG uptake [6], while acute suppurative osteomyelitis caused by *S. aureus* results in a high uptake [7, 8].

The definitive diagnosis of osteomyelitis is made by culturing the pathogen from the site of infection. Unfortunately, biopsy cultures are not infrequently negative emphasizing the importance of both histologic and microbiologic samples of tissue samples [9]. In children, the rate of culture-negative osteomyelitis has been reported to be up to 47% [10]. The rate of negative cultures in histologically proven cases of osteomyelitis obtained from imaging-guided bone biopsies (excluding spine biopsies) was even higher (66%) [11]. In recent studies of vertebral osteomyelitis, the negative culture rate of image-guided biopsy was also high (68–70%) [12, 13]. The factors that predict positive or negative culture results

TABLE 1: PET-imaged patients with definite histopathologic and/or microbiologic diagnosis ($n = 26$).

Case #	Age/sex	Anatomic location	Implant	Analysis of biopsy sample	Microbiologic culture	Definite diagnosis
1	64/F	Sternoclavicular joint	No	Histology, microbiology	Negative	Osteoarthritis
2	21/M	Femur	No	Histology, microbiology	Negative	Brodie's abscess
3	59/F	Medial clavicle	No	Histology, microbiology	Negative	Chronic osteomyelitis
4	61/F	Sacrum	No	Histology	Not done	Chronic osteomyelitis
5	60/F	Femur	No	Histology, microbiology	Negative	Recurrent chronic osteomyelitis
6	17/F	Humerus	No	Histology, microbiology	Positive	Recurrent chronic osteomyelitis
7	70/M	Pelvis	No	Histology, microbiology	Positive	Chronic osteomyelitis
8	25/M	Tibia	No	Histology, microbiology	Positive	Brodie's abscess
9	67/F	Lumbar region	Yes	Microbiology	Positive	Spinal implant infection
12	21/F	Hip region	No	Histology, microbiology	Positive	Soft tissue infection
13	59/M	Thoracic spine	No	Histology, microbiology	Negative	Vertebral osteomyelitis
15	59/M	Symphysis	No	Histology, microbiology	Positive	Postoperative osteomyelitis
16	52/F	Tibia	No	Microbiology	Positive	Recurrent Brodie's abscess
18	18/M	Thoracic spine	Yes	Microbiology	Positive	Spinal implant infection
20	73/F	Thoracic spine	No	Histology, microbiology	Negative	Vertebral osteomyelitis
25	68/M	Sternum	No	Histology, microbiology	Positive	Soft tissue infection
26	73/F	Thoracic spine	No	Histology, microbiology	Negative	Plasmacytoma
27	19/M	Femur	No	Histology, microbiology	Negative	Recurrent chronic osteomyelitis
29	73/F	Lumbar spine	No	Histology, microbiology	Positive	Vertebral osteomyelitis
30	17/F	Tibia	No	Histology, microbiology	Negative	Brodie's abscess
32	73/F	Elbow region	No	Microbiology	Positive	Soft tissue infection
33	22/F	Ankle region	No	Histology, microbiology	Negative	Soft tissue infection
34	19/F	Tibia	Yes	Histology, microbiology	Positive	Postoperative osteomyelitis
36	42/M	Lumbar spine	No	Histology, microbiology	Negative	Transient bone marrow oedema
39	28/M	Femur	No	Histology, microbiology	Negative	Osteoblastoma
40	42/M	Radius	No	Histology, microbiology	Positive	Chronic osteomyelitis

are largely unknown [11, 14]. One reason is inappropriate culture conditions. Technical errors of biopsies and starting of antibiotic treatment before biopsy may also affect culture results. There are cases in which even repeated open biopsies fail to recover the underlying pathogen. Sequestra of chronic osteomyelitis are known to be covered by metabolically quiescent bacteria within adherent biofilms [15] and it has been suggested that false-negative infections are due to viable but nonculturable biofilm organisms [14].

Based on this knowledge, certain cases of culture-negative, histologically low-grade osteomyelitis may represent clinical conditions with an inherent difference in metabolic activity compared with culture-positive cases. We assumed that ^{18}F -FDG PET could potentially detect such a difference, because intracellular accumulation of the tracer reflects metabolic rate of cells at sites of infection and inflammation [16]. Thus, the purpose of this study was to determine whether the level of ^{18}F -FDG uptake differs in culture-negative and culture-positive cases of histologically and/or microbiologically proven osteomyelitis.

2. Methods

2.1. Patients. A part of this study has been published in a Ph.D. work [17]. The patient population represents 40 consecutive orthopaedic patients who had ^{18}F -FDG PET in a five-year period (ending December 2004) with minimum 4-year follow-up data as an adjunct imaging modality for evaluation

of a clinically suspected bone infection. The suspicion of bone infection was based on clinical symptoms, laboratory findings, and results of other imaging modalities. The study cases were retrieved from the hospital database based on the reference number of the PET imaging. The clinical charts of the patients were retrospectively reviewed. There was no contact with patients, and according to the national law the study did not require approval of the ethical board. The investigation was approved by the hospital administration and was conducted in accordance with the principles of Declaration of Helsinki.

Fourteen of the original 40 patients were excluded from the current analysis. Seven cases were excluded because no histopathologic or microbiologic verification of the diagnosis was made. Five cases were excluded because ^{18}F -FDG PET was applied only to evaluate of antimicrobial treatment response. Two additional cases were excluded because the primary indication for PET imaging was not suspected infection.

Twenty-six (65%) of the 40 patients had definite histopathologic and/or microbiologic diagnosis based on the examination of samples (Table 1). Biopsy samples were obtained during neurosurgical decompression of the spinal canal, during an open biopsy performed by an orthopaedic surgeon, or by CT/MRI guided needle biopsy performed by a musculoskeletal radiologist. The definite diagnosis was osteomyelitis in 16 patients (62%), soft tissue infection in four patients (15%), and spinal implant infections in two patients

(8%). The histologic diagnoses for the four remaining cases were plasmacytoma, osteoblastoma, transient bone marrow oedema, and degenerative sternoclavicular osteoarthritis.

A microbiologic culture was considered positive, if any relevant organism grew based on the judgment of a microbiologist. Of the 16 cases with proven osteomyelitis, eight (50%) had positive cultures and seven (44%) had negative cultures (Table 2). One patient with low-grade sacral osteomyelitis (case #4) had no cultures done of the biopsy specimen. The culture-negative cases were predominantly rare forms of hematogenous osteomyelitis, including two indolent Brodie's abscesses, two cases of recurrent chronic osteomyelitis of the femur, one case of chronic osteomyelitis of the medial clavicle (possible synovitis, acne, pustulosis, hyperostosis, and osteitis (SAPHO) syndrome), and two cases of vertebral osteomyelitis (Table 2).

None of the patients with negative cultures had antibiotic therapy before sampling (Table 2). Three patients with negative cultures had repeated biopsies because of failures in recovering the pathogen (Table 2). Three other patients with culture-negative osteomyelitis had multiple tissue samples taken at surgery (laminectomy) or during open biopsies. Only one case of culture-negative vertebral osteomyelitis was based on a single procedure of CT-guided biopsy. Routine microbiologic analysis of bone specimens included extended culture times and specific cultures for the diagnosis of tuberculosis, if indicated. Molecular diagnostic technology of polymerase chain reactions (PCRs) was applied in four patients with repeated biopsies (in three culture-negative patients and one culture-positive patient). None of universal PCRs were positive.

There were three patients with a past history of a skeletal infection with fever in both groups (culture-negative cases #2, #5, and #30 and culture-positive cases #6, #16, and #40). Two of these cases had history of osteomyelitis treatment as a child. One additional culture-positive case (case #8) had been hospitalized for an unexplained skeletal pain as a 15-year-old. The current diagnostic studies were most commonly started due to local pain or night aching. None of the patients had fever or draining sinus as a sign of acute exacerbation of chronic osteomyelitis. Pain had lasted \leq one month in six patients and for 3–12 months in the remaining 10 patients. Aside from pain, one patient had recognized a local resistance (case #3). One patient was symptomless (case #8). One patient (case #20) suffered from radiating back pain for a month and developed acute paraparesis before spinal decompression.

Patient groups of culture-negative and culture-positive osteomyelitis both had normal or slightly elevated blood levels of C-reactive protein (median 6 mg/L, range 1–73 mg/L, respective to median 6 mg/L, range 1–49 mg/L). All patients with culture-negative osteomyelitis, except one, had slightly elevated erythrocyte sedimentation rate (median 18 mm/hour, range 7–27 mm/hour). There was a trend for higher erythrocyte sedimentation rate (median 28 mm/hour, range 2–82 mm/hour) in culture-positive cases.

2.2. ^{18}F -FDG PET. ^{18}F -FDG PET imaging was performed as an adjunct part of routine work-up in the differential diagnostics of osteomyelitis. The clinical reviewers of the

PET images had access to all patient charts, including the results of conventional imaging modalities. Based on the interpretation of the reviewers, the result of ^{18}F -FDG PET was recorded as true positive or false negative (Table 3). The patients were instructed to fast for 6 hours prior to PET. ^{18}F -FDG PET imaging was performed with an Advance PET scanner (General Electric Medical Systems, Milwaukee, WI, USA) operated in 2-dimensional mode (high resolution). The scanner had 18 rings of bismuth germanate detectors, and the axial length of the imaging field of view (FOV) was 152 mm. Whole body acquisition was started 60 minutes after the injection of ^{18}F -FDG (5 minutes per bed position). The mean dose of intravenous bolus injection of ^{18}F -FDG was 297 MBq (SD 71 MBq; range, 160–384 MBq). A standard transmission scan for attenuation correction was obtained after the emission imaging using two rod sources containing germanium-68. All 35 transaxial image slices were reconstructed with an ordered subsets expectation maximization algorithm (OSEM) and the central 200 mm-diameter transaxial FOV and 128×128 matrix leading to pixel size 1.56×1.56 mm were used. Random counts and dead time were corrected by the system and scatter correction was incorporated into the reconstruction algorithm. Quantitative analysis of the ^{18}F -FDG uptake was performed on standardized circular regions of interest (ROIs, diameter of 15 mm) at the site of visually detected increased tracer accumulation from background using transaxial slices. Tracer accumulation was reported as the standardized uptake value (SUV), which was calculated as the radioactivity of the ROI divided by the relative injected dose expressed per patient's body weight. Both SUV_{mean} , representing the average uptake on the selected ROI, and the maximum SUV value (SUV_{max}), representing the highest pixel uptake in the ROI, were analyzed. In addition, $\text{SUV}_{\text{ratio}}$, that is, the ratio between the site of suspected infection and the ROI of the corresponding healthy anatomic site, was calculated for SUV_{mean} and SUV_{max} [7, 18].

2.3. MRI, Bone Scintigraphy, and Infection Scans. The decision to perform other imaging modalities (MRI, three-phase bone scintigraphy, infection scan with labeled leukocytes or antigranulocyte antibodies, and occasionally CT) (Table 3) was based on the judgment of clinical indications in each case. The three-phase bone scintigraphy (bone scan) was performed with $^{99\text{m}}\text{Tc}$ -HDP or DPD (mean dose 670 MBq). Infection scans were performed using either $^{99\text{m}}\text{Tc}$ -white blood cell scanning (HMPAO, Ceretec, GE Healthcare, Amersham Place, United Kingdom, mean dose 209 MBq) or $^{99\text{m}}\text{Tc}$ -antigranulocyte scintigraphy (LeukoScan®, Immunomedics GmbH, Darmstadt, Germany, mean dose 1000 MBq) technique. Based on the interpretation of the clinical reviewers, the results were recorded as true positive or false negative (Table 3).

2.4. Statistical Analysis. Data are expressed as mean \pm standard deviation (SD). Nonparametric Mann–Whitney U test was applied in the comparison of SUV_{mean} and SUV_{max} values between patients with culture-positive and culture-negative osteomyelitis. $p < 0.05$ was considered significant. All

TABLE 2: Patients with histologically and/or microbiologically proven osteomyelitis ($n = 16$).

Case	Age/sex	Definite diagnosis	Microbiologic culture	Method of biopsy	Antimicrobial therapy before biopsy	Antimicrobial therapy started before PET
6	17/F	Recurrent chronic osteomyelitis of humerus	Coagulase-negative <i>Staphylococcus</i>	Open biopsy	No	No
7	70/M	Chronic osteomyelitis of pelvis	<i>P. aeruginosa</i> , <i>Enterococcus</i> , <i>S. epidermidis</i>	Open biopsy	Yes, interrupted before biopsy	Yes
8	25/M	Brodie's abscess of tibia	<i>S. aureus</i>	Percutaneous biopsy under fluoroscopy	No	No
15	59/M	Postoperative osteomyelitis of symphysis	<i>S. epidermidis</i>	MRI-guided biopsy	No	No
16	52/F	Recurrent Brodie's abscess of tibia	<i>S. aureus</i>	Open biopsy	No	No
29	73/F	Vertebral osteomyelitis	<i>S. epidermidis</i>	Biopsy during laminectomy	No	Yes
34	19/F	Postoperative osteomyelitis of tibia	<i>S. epidermidis</i>	Open biopsy and removal of bone screw	No	No
40	42/M	Chronic osteomyelitis of radius	<i>Bacillus</i> species	MRI-guided biopsy and repeated open biopsy	Yes, interrupted before biopsy	No
2	21/M	Brodie's abscess of femur	Negative	Repeated open and CT-guided biopsy	No	No
3	59/F	Chronic osteomyelitis of medial clavicle	Negative	Open biopsy	No	No
5	60/F	Recurrent chronic osteomyelitis of femur	Negative	Open biopsy	No	No
13	59/M	Vertebral osteomyelitis	Negative	Biopsy during laminectomy	No	Yes
20	73/F	Vertebral osteomyelitis	Negative	CT-guided biopsy	No	No
27	19/M	Recurrent chronic osteomyelitis of femur	Negative	Repeated MRI-guided and open biopsy	No	Yes
30	17/F	Brodie's abscess of tibia	Negative	MRI-guided and open biopsy	No	No
4	61/F	Chronic osteomyelitis of sacrum	Not done	CT-guided biopsy	No	No

TABLE 3: Results of ^{18}F -FDG PET and additional imaging modalities in patients with proven osteomyelitis ($n = 16$).

Case #	Microbiologic culture	PET	MRI	Bone scan	Infection scan	CT	SUV		SUV _{ratio}	
							SUV _{mean}	SUV _{max}	SUV _{mean}	SUV _{max}
6	Culture-positive	TP	TP	TP	—	—	1.19	1.98	2.25	2.89
7	Culture-positive	TP	FN	TP	FN	—	3.93	5.53	5.44	4.78
8	Culture-positive	TP	TP	TP	TP	TP	0.99	2.86	10.1	20.51
15	Culture-positive	TP	TP	TP	—	TP	4.62	7.59	3.79	5.56
16	Culture-positive	TP	TP	TP	TP	TP	0.90	2.81	3.60	4.36
29	Culture-positive	TP	TP	TP	TP	—	2.54	4.11	2.42	2.83
34	Culture-positive	TP	—	—	TP	FN	1.72	2.59	9.72	11.28
40	Culture-positive	TP	TP	TP	FN	—	1.55	2.37	2.48	2.47
2	Culture-negative	TP	TP	TP	TP	—	0.74	1.16	4.90	2.57
3	Culture-negative	TP	—	TP	—	FN	1.95	2.50	2.30	2.14
5	Culture-negative	TP	TP	TP	TP	—	2.34	2.79	16.10	14.28
13	Culture-negative	TP	TP	—	—	—	3.08	4.43	3.47	3.61
20	Culture-negative	TP	FN	TP	TP	TP	1.80	3.05	2.12	2.77
27	Culture-negative	TP	TP	—	—	—	1.96	2.91	11.44	12.47
30	Culture-negative	TP	TP	TP	TP	—	2.60	2.86	13.20	7.72
4	Not done	TP	FN	TP	TP	FN	2.57	2.80	1.36	1.89

PET = positron emission tomography; MRI = magnetic resonance imaging; Bone scan = three-phase bone scintigraphy; Infection scan = labeled leukocyte scintigraphy; CT = computerized tomography; TP = true positive; FN = false negative; — = not done.

statistical analyses were performed using IBM SPSS Statistics software (International Business Machines Corp., Armonk, New York, USA).

3. Results

SUV_{mean} values of culture-negative (mean ± SD, 2.07 ± 0.74) and culture-positive cases of chronic osteomyelitis (2.18 ± 1.31) did not differ significantly. The SUV_{max} values of culture-negative (2.81 ± 0.96) and culture-positive cases (3.73 ± 1.70) neither showed significant intergroup differences (Figure 1).

There was a clear visual difference in the uptake of ^{18}F -FDG at the infection site and at the corresponding ROI of the contralateral healthy bone (Figure 2). Both in culture-negative and culture-positive cases, the calculations of SUV_{ratio} confirmed high mean values for SUV_{mean} (7.65 versus 4.98, resp.) and for SUV_{max} (6.51 versus 6.84, resp.) (Figure 1).

The patients with histologically and/or microbiologically proven osteomyelitis ($n = 16$) were all correctly interpreted as true positive in the routine clinical reading of ^{18}F -FDG PET images (Table 3). Four patients (25%) out of 16 (cases #4, #7, #20, and #40) had false-negative MRI or labeled leukocyte scintigraphy (Table 3). In the retrospective view, in these cases ^{18}F -FDG PET brought a significant diagnostic help compared with the results of other imaging modalities.

Among the whole group of patients ($n = 26$) (Table 1), ^{18}F -FDG PET gave no false-negative cases and three false positive cases. The three false positive cases were due to periarticular soft tissue infections (cases #12 and #33) and vertebral plasmacytoma (case #26).

4. Discussion

The present retrospective analysis was focused on the diagnostic imaging and microbiologic challenges in a special

subgroup of patients with predominantly rare forms of hematogenous chronic osteomyelitis, including four cases of Brodie’s abscesses. The rate of positive cultures was 47%, which is similar to the reported rates of 30%–42% in previous studies on imaging-guided biopsies with combined histologic and microbiologic evaluation [9, 11–13]. Thus, our patient population resembles the previously published series and was subsequently appropriate for evaluation of ^{18}F -FDG PET imaging in the characterization of culture-negative cases. The culture-negative cases may be incorrectly described as negative because the infecting microbe(s) may be nonculturable [14]. If true, we assumed that culture-negative cases might have a lower metabolic activity than culture-positive cases measured by ^{18}F -FDG PET imaging. Against our hypothesis, there was no relationship between the level of ^{18}F -FDG PET uptake and the presence of positive or negative bacterial cultures among these patients with histologically and/or microbiologically proven chronic osteomyelitis.

Reflecting the rarity of the cases, it is evident that a multicenter prospective study is needed to get definitive answers to the open questions. Previously Wu and coworkers [11] have already paid attention to the small number of requests for imaging-guided core bone biopsies for suspected osteomyelitis. They found that two large US centers had only 3–7 such cases per year. The number of cases enrolled in our study closely resembles the experience of Wu and coworkers. Twenty-six patients, who had ^{18}F -FDG PET imaging for suspected osteomyelitis and underwent the necessary microbiologic and/or histologic examinations of biopsies during a five-year period, represented about 5 referred cases per year in our university hospital district of about 800.000 inhabitants. Most of these cases were primarily scrutinized by the sarcoma treatment group for exclusion of a bone tumor. Overall, it is important to emphasize two facts. First, the majority of osteomyelitis patients (like posttraumatic

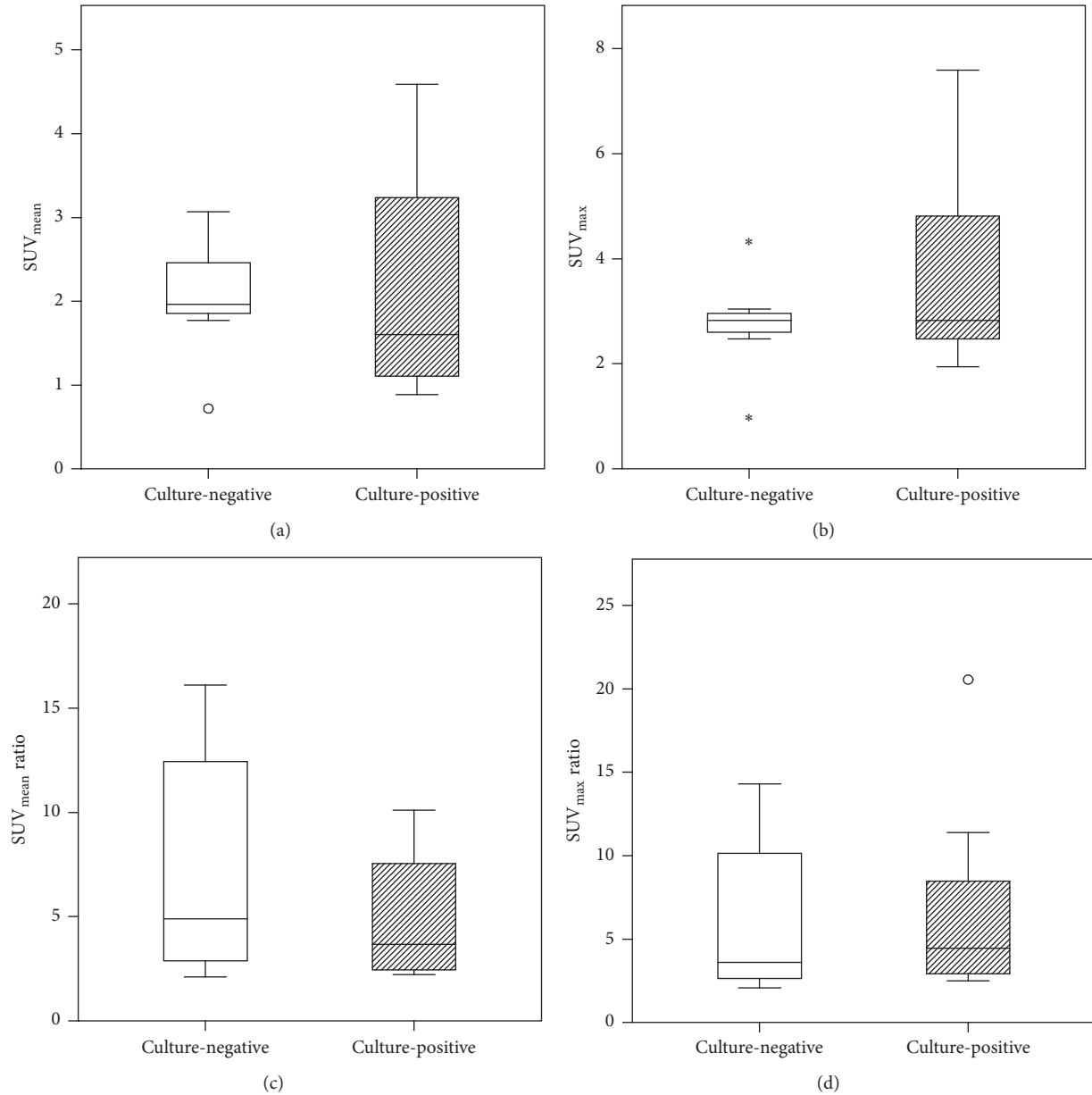


FIGURE 1: Comparison of SUV_{mean} (a), SUV_{max} (b), SUV_{mean} ratio (c), and SUV_{max} ratio (d) values measured in ^{18}F -FDG PET imaging of osteomyelitis patients. The differences between culture-negative ($n = 7$) and culture-positive ($n = 8$) cases were not statistically significant. Box plots are showing median, 1st and 3rd quartiles, minimum and maximum values, and outliers (white circles and asterisks).

cases) have an undisputed clinical history with clear-cut laboratory/radiographic data suggesting osteomyelitis and do not require advanced noninvasive differential diagnostics like ^{18}F -FDG PET imaging and a histologic proof of the diagnosis. Secondly, the microbiologic isolation of the causative bone pathogen(s) yields positive results in most cases (78%) of posttraumatic osteomyelitis [19] and, for example, virtually in all cases with recurrent infection of open tibial fractures [20]. As shown in the previous studies [9, 11–13] and in the current study, the situation is different in subgroups of patients who are referred to ^{18}F -FDG PET imaging and/or imaging-guided biopsy for suspected chronic osteomyelitis.

Based on previous studies, a negative ^{18}F -FDG PET scan can virtually rule out chronic osteomyelitis [18]. The high accuracy of ^{18}F -FDG PET for excluding chronic osteomyelitis may be related to the high uptake of ^{18}F -FDG by activated macrophages, which are among the predominant cells in chronic infections [16]. The false positive case of vertebral plasmacytoma demonstrates the inability of ^{18}F -FDG PET imaging in the differentiation of chronic osteomyelitis and a malignant bone tumor. Both of these conditions result in the high accumulation of ^{18}F -FDG and may even share the macrophage-related mechanism of the tracer uptake. ^{18}F -FDG accumulates not only in tumor cells, but also in

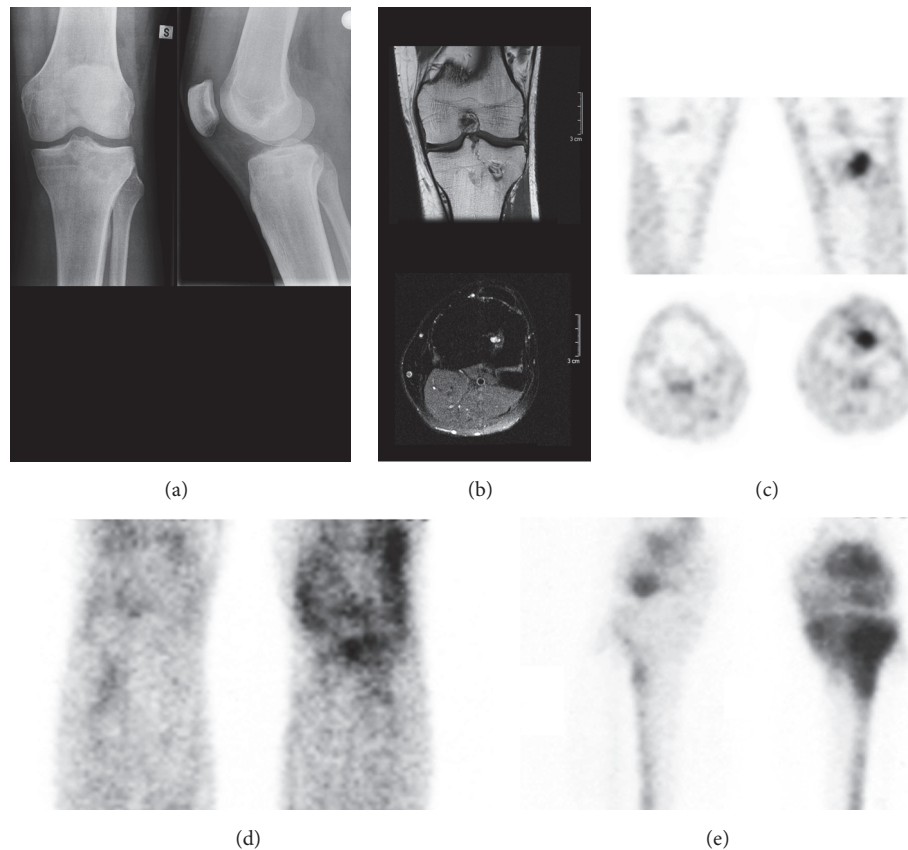


FIGURE 2: A 25-year-old man with an indolent Brodie's abscess in the proximal tibia (case #8). The patient had been hospitalized for knee pain 10 years earlier, but no specific diagnosis was made. He now suffered a sports related ACL ligament rupture of his left knee. As an incidental finding, anterior-posterior and lateral radiographs (a) showed cystic lesion with surrounding sclerosis in the proximal tibia. Coronal and transaxial MR-images (b) demonstrated a 2 cm sclerotic osseous lesion with contrast medium enhancement and oedema of the surrounding tissues. Coronal and transaxial ^{18}F -FDG PET images (c) showed an increased local uptake of the tracer. Compared with the corresponding ROI of the contralateral tibia, SUV_{mean} ratio was 10.1 and SUV_{max} ratio 20.51. The lesion was correctly characterized with infection scintigraphy with labeled antibody fragments (LeukoScan) (d) and three-phase bone scintigraphy (e). Based on percutaneous biopsy samples taken under fluoroscopy, the final histological diagnosis was Brodie's abscess and the microbiologic culture revealed *S. aureus* as the causative pathogen.

macrophages and newly formed granulation tissues, which are infiltrating the marginal areas of tumor necrosis [21].

This study had limitations. Data of the small patient population were retrospectively extracted from medical records of a single university hospital. There were no definite indications for the use of ^{18}F -FDG PET imaging in the diagnostic armamentarium of suspected osteomyelitis. Thus, seven of the original 40 patients had PET imaging but never had definite histopathologic or microbiologic verification of the diagnosis probably due to mild symptoms and negative imaging results. The execution of other imaging modalities was not determined but was solely based on the clinical judgment. As a result, imaging studies were not performed in a constant manner for the comparison with ^{18}F -FDG PET imaging and the variation could affect the interpretation of ^{18}F -FDG PET images. We cannot exclude occasional errors in the sampling of the biopsies as well as in the performance of microbiologic analyses. However, a special attention had been placed to repeat biopsies in culture-negative cases minimizing the risk of errors in surgical sampling. In addition, the

microbiologic culture techniques were based on the notion that detection of low-virulent slow-growing bacteria requires extended culture times. Molecular assays, such as polymerase chain reaction (PCR), have been developed to aid in bacterial detection and identification [22, 23]. These techniques were applied, but not in all culture-negative cases. The applied PET imaging technique was constant in all patients and the clinical follow-up time of all patients was long enough, but as a result the imaging was not performed with the current models of PET scanners with a low-dose or full-dose diagnostic CT, which provide means to acquire more precise anatomic and physiologic data improving foremost specificity but also sensitivity [24, 25]. This technical limitation seemed to have only a minor impact, because the interpretation of the PET images of both culture-positive and culture-negative cases was unquestionable and showed high $\text{SUV}_{\text{ratio}}$ values. Only the two false positive cases due to periarticular soft tissue infections could have been avoided by using ^{18}F -FDG PET/CT, because it provides exact anatomic localization of ^{18}F -FDG uptake. As a potential technical limitation, a

standard circular ROI (15 mm in diameter) was applied in the SUV analyses of FDG tracer accumulation. Certainly, the infected bone regions varied in size and most of them were larger than the selected ROI. The small diameter of the ROI carried a risk for partial-volume effect (PVE) meaning that the apparent pixel values in PET images were influenced by the surrounding high pixel values [26]. If the measured SUV_{mean} values were under the possible influence of PVE, the current analysis included also the comparison of SUV_{max} values based on the maximum uptake of ^{18}F -FDG in a single pixel (size of 1.56×1.56 mm).

5. Conclusion

We conclude that there is no relationship between the level of ^{18}F -FDG PET uptake and the presence of positive or negative bacterial cultures in patients with histologically proven osteomyelitis. The result favors the concept that culture-negative cases are false-negative infections due to nonculturable microbes. Thus, ^{18}F -FDG PET may help to confirm the presence of active infection in patients with culture-negative low-grade osteomyelitis and guide their appropriate treatment.

Conflicts of Interest

The authors declare that there are no conflicts of interest regarding the publication of this paper.

Acknowledgments

This research was financially supported by the Sigrid Jusélius Foundation.

References

- [1] M. F. Termaat, P. G. H. M. Raijmakers, H. J. Scholten, F. C. Barker, P. Patka, and H. J. T. M. Haarman, "The accuracy of diagnostic imaging for the assessment of chronic osteomyelitis: a systematic review and meta-analysis," *The Journal of Bone and Joint Surgery—American Volume*, vol. 87, no. 11, pp. 2464–2471, 2005.
- [2] N. Prandini, E. Lazzeri, B. Rossi, P. Erba, M. G. Parisella, and A. Signore, "Nuclear medicine imaging of bone infections," *Nuclear Medicine Communications*, vol. 27, no. 8, pp. 633–644, 2006.
- [3] G.-L. Wang, K. Zhao, Z.-F. Liu, M.-J. Dong, and S.-Y. Yang, "A meta-analysis of fluorodeoxyglucose-positron emission tomography versus scintigraphy in the evaluation of suspected osteomyelitis," *Nuclear Medicine Communications*, vol. 32, no. 12, pp. 1134–1142, 2011.
- [4] C. D. Valle, J. Parvizi, T. W. Bauer et al., "Diagnosis of periprosthetic joint infections of the hip and knee," *Journal of the American Academy of Orthopaedic Surgeons*, vol. 18, no. 12, pp. 760–770, 2010.
- [5] D. Teterycz, T. Ferry, D. Lew et al., "Outcome of orthopedic implant infections due to different staphylococci," *International Journal of Infectious Diseases*, vol. 14, no. 10, pp. e913–e918, 2010.
- [6] P. Lankinen, K. Lehtimäki, A. J. Hakanen, A. Roivainen, and H. T. Aro, "A comparative ^{18}F -FDG PET/CT imaging of experimental *Staphylococcus aureus* osteomyelitis and *Staphylococcus epidermidis* foreign-body-associated infection in the rabbit tibia," *EJNMMI Research*, vol. 2, no. 1, pp. 1–10, 2012.
- [7] J. K. Koort, T. J. Mäkinen, J. Knuuti, J. Jalava, and H. T. Aro, "Comparative ^{18}F -FDG PET of experimental *Staphylococcus aureus* osteomyelitis and normal bone healing," *Journal of Nuclear Medicine*, vol. 45, no. 8, pp. 1406–1411, 2004.
- [8] L. Jones-Jackson, R. Walker, G. Purnell et al., "Early detection of bone infection and differentiation from post-surgical inflammation using 2-deoxy-2-[^{18}F]-fluoro-D-glucose positron emission tomography (FDG-PET) in an animal model," *Journal of Orthopaedic Research*, vol. 23, no. 6, pp. 1484–1489, 2005.
- [9] L. M. White, M. E. Schweitzer, D. M. Deely, and F. Gannon, "Study of osteomyelitis: Utility of combined histologic and microbiologic evaluation of percutaneous biopsy samples," *Radiology*, vol. 197, no. 3, pp. 840–842, 1995.
- [10] R. L. Floyed and R. W. Steele, "Culture-negative osteomyelitis," *Pediatric Infectious Disease Journal*, vol. 22, no. 8, pp. 731–735, 2003.
- [11] J. S. Wu, T. Gorbachova, W. B. Morrison, and A. H. Haims, "Imaging-guided bone biopsy for osteomyelitis: Are there factors associated with positive or negative cultures?" *American Journal of Roentgenology*, vol. 188, no. 6, pp. 1529–1534, 2007.
- [12] C. M. Heyer, L.-J. Brus, S. A. Peters, and S. P. Lemburg, "Efficacy of CT-guided biopsies of the spine in patients with spondylitis - An analysis of 164 procedures," *European Journal of Radiology*, vol. 81, no. 3, pp. e244–e249, 2012.
- [13] J. K. Sehn and L. A. Gilula, "Percutaneous needle biopsy in diagnosis and identification of causative organisms in cases of suspected vertebral osteomyelitis," *European Journal of Radiology*, vol. 81, no. 5, pp. 940–946, 2012.
- [14] J. H. Calhoun, M. M. Manring, and M. Shirtliff, "Osteomyelitis of the long bones," *Seminars in Plastic Surgery*, vol. 23, no. 2, pp. 59–72, 2009.
- [15] A. G. Gristina, M. Oga, L. X. Webb, and C. D. Hobgood, "Adherent bacterial colonization in the pathogenesis of osteomyelitis," *Science*, vol. 228, no. 4702, pp. 990–993, 1985.
- [16] A. H. Kaim, B. Weber, M. O. Kurrer, J. Gottschalk, G. K. Von Schulthess, and A. Buck, "Autoradiographic quantification of ^{18}F -FDG uptake in experimental soft-tissue abscesses in rats," *Radiology*, vol. 223, no. 2, pp. 446–451, 2002.
- [17] P. Lankinen, "PET imaging of osteomyelitis—Feasibility of ^{18}F -FDG, ^{68}Ga -chloride, and ^{68}Ga -DOTAVAP-P1 tracers in staphylococcal bone infections," *Annales Universitatis Turkuensis Ser D: Medica Odontologica*, vol. 1076, 2013.
- [18] F. De Winter, C. Van De Wiele, D. Vogelaers, K. De Smet, R. Verdonk, and R. A. Dierckx, "Fluorine-18 fluorodeoxyglucose-positron emission tomography: A highly accurate imaging modality for the diagnosis of chronic musculoskeletal infections," *Journal of Bone and Joint Surgery - Series A*, vol. 83, no. 5, pp. 651–24, 2001.
- [19] R. A. Murphy, J.-B. Ronat, R. M. Fakhri et al., "Multidrug-resistant chronic osteomyelitis complicating war injury in Iraqi civilians," *Journal of Trauma - Injury, Infection and Critical Care*, vol. 71, no. 1, pp. 252–254, 2011.
- [20] E. N. Johnson, T. C. Burns, R. A. Hayda, D. R. Hospenthal, and C. K. Murray, "Infectious complications of open type III tibial fractures among combat casualties," *Clinical Infectious Diseases*, vol. 45, no. 4, pp. 409–415, 2007.

- [21] R. Kubota, S. Yamada, K. Kubota, K. Ishiwata, N. Tamahashi, and T. Ido, "Intratumoral distribution of fluorine-18-fluorodeoxyglucose in vivo: High accumulation in macrophages and granulation tissues studied by microautoradiography," *Journal of Nuclear Medicine*, vol. 33, no. 11, pp. 1972–1980, 1992.
- [22] F. Fenollar, V. Roux, A. Stein, M. Drancourt, and D. Raoult, "Analysis of 525 samples to determine the usefulness of PCR amplification and sequencing of the 16S rRNA gene for diagnosis of bone and joint infections," *Journal of Clinical Microbiology*, vol. 44, no. 3, pp. 1018–1028, 2006.
- [23] V. Fihman, D. Hannouche, V. Bousson et al., "Improved diagnosis specificity in bone and joint infections using molecular techniques," *Journal of Infection*, vol. 55, no. 6, pp. 510–517, 2007.
- [24] G. K. Von Schulthess, H. C. Steinert, and T. F. Hany, "Integrated PET/CT: Current applications and future directions," *Radiology*, vol. 238, no. 2, pp. 405–422, 2006.
- [25] K. Strobel and K. D. M. Stumpe, "PET/CT in musculoskeletal infection," *Seminars in Musculoskeletal Radiology*, vol. 11, no. 4, pp. 353–364, 2007.
- [26] E. J. Hoffman, S.-C. Huang, and M. E. Phelps, "Quantitation in positron emission computed tomography: 1. effect of object size," *Journal of Computer Assisted Tomography*, vol. 3, no. 3, pp. 299–308, 1979.

Research Article

Kinetic Modelling of Infection Tracers [^{18}F]FDG, [^{68}Ga]Ga-Citrate, [^{11}C]Methionine, and [^{11}C]Donepezil in a Porcine Osteomyelitis Model

Lars Jødal,^{1,2,3} Svend B. Jensen,^{3,4} Ole L. Nielsen,¹ Pia Afzelius,⁵ Per Borghammer,² Aage K. O. Alstrup,² and Søren B. Hansen²

¹Department of Veterinary and Animal Sciences, University of Copenhagen, Copenhagen, Denmark

²Department of Nuclear Medicine and PET Centre, Aarhus University Hospital, Aarhus, Denmark

³Department of Nuclear Medicine, Aalborg University Hospital, Aalborg, Denmark

⁴Department of Chemistry and Biosciences, Aalborg University, Aalborg, Denmark

⁵Department of Diagnostic Imaging, North Zealand Hospital, Copenhagen University Hospital, Hillerød, Denmark

Correspondence should be addressed to Lars Jødal; lajo@rn.dk

Received 1 June 2017; Accepted 24 August 2017; Published 9 October 2017

Academic Editor: Xiang-Guo Li

Copyright © 2017 Lars Jødal et al. This is an open access article distributed under the Creative Commons Attribution License, which permits unrestricted use, distribution, and reproduction in any medium, provided the original work is properly cited.

Introduction. Positron emission tomography (PET) is increasingly applied for infection imaging using [^{18}F]FDG as tracer, but uptake is unspecific. The present study compares the kinetics of [^{18}F]FDG and three other PET tracers with relevance for infection imaging. **Methods.** A juvenile porcine osteomyelitis model was used. Eleven pigs underwent PET/CT with 60-minute dynamic PET imaging of [^{18}F]FDG, [^{68}Ga]Ga-citrate, [^{11}C]methionine, and/or [^{11}C]donepezil, along with blood sampling. For infectious lesions, kinetic modelling with one- and two-tissue-compartment models was conducted for each tracer. **Results.** Irreversible uptake was found for [^{18}F]FDG and [^{68}Ga]Ga-citrate; reversible uptake was found for [^{11}C]methionine (two-tissue model) and [^{11}C]donepezil (one-tissue model). The uptake rate for [^{68}Ga]Ga-citrate was slow and diffusion-limited. For the other tracers, the uptake rate was primarily determined by perfusion (flow-limited uptake). Net uptake rate for [^{18}F]FDG and distribution volume for [^{11}C]methionine were significantly higher for infectious lesions than for correspondingly noninfected tissue. For [^{11}C]donepezil in pigs, labelled metabolite products appeared to be important for the analysis. **Conclusions.** The kinetics of the four studied tracers in infection was characterized. For clinical applications, [^{18}F]FDG remains the first-choice PET tracer. [^{11}C]methionine may have a potential for detecting soft tissue infections. [^{68}Ga]Ga-citrate and [^{11}C]donepezil were not found useful for imaging of osteomyelitis.

1. Introduction

Positron emission tomography (PET) allows imaging of molecular uptake but is dependent on the availability of tracers with uptake related to the investigated disease. For infection imaging, [^{18}F]FDG is useful [1], but a drawback is the nonspecific uptake of [^{18}F]FDG in metabolically active tissues (brain, muscles, etc.) [2].

We previously reported on static PET imaging in a porcine osteomyelitis model with a series of tracers that have been proposed for infection imaging [3–5]. In those reports, we concluded that the performance of [^{18}F]FDG for locating

infection was superior to the other tracers studied. However, our static imaging shows only the uptake at a given (typically late) time interval.

In the present paper, we elaborate on those studies [3–5] by including data from *dynamic* PET imaging of the same animals (based on the same tracer injections), using kinetic analysis to compare [^{18}F]FDG with [^{68}Ga]Ga-citrate, [^{11}C]methionine (L-[^{11}C -methyl]methionine), and [^{11}C]donepezil ([5- ^{11}C -methoxy]donepezil) as infection tracers. Dynamic imaging allows for a more detailed study of the uptake and release of tracers, which may contribute to a better understanding of the underlying physiology and also help

in determining the optimal time for static imaging. Blood perfusion results from dynamic imaging of [^{15}O]water in the same animals have already been reported [6].

Gamma-camera imaging (scintigraphy or SPECT) of infection is sometimes performed with [^{67}Ga]Ga-citrate. However, image quality is suboptimal and the radiation dose from ^{67}Ga is high. The positron-emitter ^{68}Ga allows PET imaging, which has a better spatial resolution and a higher detection efficiency than standard gamma-camera imaging. Furthermore, the shorter half-life of ^{68}Ga (67.7 min versus 78 hours for ^{67}Ga) reduces the radiation dose. In the body, the Ga^{3+} ion acts as an analogue of iron (Fe^{3+}), associating with transferrin; for more details, see [7]. Preliminary studies on [^{68}Ga]Ga-citrate in rats [8] and patients [9, 10] reported promising results.

Methionine is a naturally occurring essential amino acid. It can be labelled with the positron-emitter ^{11}C to obtain the chemically identical PET tracer [^{11}C]methionine. Methionine (natural or labelled) is transported into cells via the L-type amino acid transporter 1. It is crucial for the formation of proteins and is involved in the synthesis of phospholipids. The accumulation of methionine therefore reflects amino acid transport and protein synthesis. During cell replication, the demand for essential amino acids increases, as do protein and phospholipid synthesis. Although primarily used to detect malignant tumours [11], methionine is known from brain studies to accumulate in inflammatory tissue [12, 13]. Furthermore, a high uptake of [^{11}C]methionine has been observed after acute myocardial infarction, indicating that this tracer may be a good marker of inflammatory reactions during the phase of tissue repair [14].

Donepezil is a reversible inhibitor of acetylcholinesterase (AChE), the break-down enzyme of acetylcholine (ACh) [15]. ACh and AChE are primarily known as constituents in cholinergic neuronal signalling pathways, but immune cells have been shown to use ACh as a paracrine signalling molecule [16], and AChE and cholinergic receptors are upregulated in immune cells when exposed to phytohaemagglutinin [17]. It was recently shown that the AChE ligand [^{11}C]donepezil accumulates at sites of bacterial infection, suggesting that cholinergic PET imaging may have potential in the detection of inflammation and infections [18].

Therefore, we investigated the uptake processes of these PET tracers in order to determine their clinical potential in infection imaging in relation to both osteomyelitis and soft tissue infection. We hypothesized that (1) categorization of tracers into those having either reversible or irreversible uptake in infectious lesions is possible and (2) perfusion effects on tracer accumulation can be estimated. Finally, we wanted to estimate the optimal time points for static imaging of the tracers.

2. Materials and Methods

2.1. Porcine Osteomyelitis Protocol. The protocol for inducing osteomyelitis in domestic pigs has been described in detail elsewhere [3, 19–21]. Briefly, osteomyelitis was induced in the right hind limb of juvenile Danish Landrace \times Yorkshire

female pigs by intra-arterial injection of *S. aureus* (porcine strain S54F9). The injection was performed into the right femoral artery, allowing for selective infection of this hind limb while leaving the contralateral left hind limb as a noninfected control. Osteomyelitis was allowed to develop for one week, after which the pig was scanned and then euthanized. If a pig reached predefined humane endpoints, it was then euthanized (and not scanned). A refinement of the model, combining reduced body weight of the pigs (from 40 kg to 20 kg) with administration of penicillin at the onset of the first clinical signs of disease, proved effective in reducing systemic infection [21].

We attempted to prolong the infection period from one to two weeks, for the purpose of developing more chronic lesions, and managed to scan one pig two weeks after inoculation (pig number 5 of the 11 scanned pigs described below). However, 4 out of 5 pigs planned for scanning with the prolonged protocol had to be prematurely euthanized due to humane endpoints, so we returned to the subacute one-week pig protocol.

The animal protocol was approved by the Danish Animal Experimental Board, journal number 2012-15-2934-00123, and all procedures followed the European Directive 2010/63/EU on the protection of animals used for scientific purposes.

2.2. Animals and Lesions. Eleven juvenile female domestic pigs were scanned. Pigs number 1–4 had body weights of 39–42 kg (initial model) and pigs number 5–11 had body weights of 19–23 kg (refined model). Blood perfusion in the lesions in these pigs has been described previously [6], including 17 osteomyelitic (OM) lesions and 8 soft tissue (ST) lesions, with volume of interest (VOI) drawing primarily based on computed tomography (CT) scans. Other OM lesions were also found in pedal bones but were too small for robust volume of interest (VOI) drawing.

In the present paper, the kinetics of [^{18}F]FDG, [^{68}Ga]Ga-citrate, [^{11}C]methionine, and [^{11}C]donepezil were studied and modelled in the same 17 OM lesions and 8 ST lesions, with VOIs redrawn on the CTs from the dynamic PET/CT scans of these tracers. Not all tracers were used in all pigs, and the limitations set by the PET scanner field of view (FOV, further described below) resulted in not all lesions being dynamically scanned in all pigs. An overview is given in Table 1.

We have previously reported some data on the characterization of the lesions evolving from *S. aureus* inoculation in these pigs, including the methods used for bacteriological and immunohistochemical (IHC) identification of bacteria [3–5]. Generally, the lesions observed in the pigs were considered to be caused by infection associated with the inoculated *S. aureus* if the bacterial culture and/or *S. aureus* specific IHC staining confirmed the presence of *S. aureus* in one or several of the lesions within each individual pig (results not shown).

2.3. Dynamic PET Scans. PET scans were carried out at the Department of Nuclear Medicine & PET Centre (Aarhus University Hospital), and at Department of Nuclear Medicine (Aalborg University Hospital), with the pigs transported from

TABLE 1: Pig ID numbers (1–11) for different tracers and lesions^a.

Tracer	Dynamic data available	Osteomyelitic (OM) lesions ^b				Soft tissue (ST) lesions ^b
		Proximal femur	Distal femur	Proximal tibia	Distal tibia	
[¹⁵ O]water [6]	1–11	1	1, 5–10	1, 6–10	7, 8, 10	1, 2, 4 ^c , 8–11
[¹⁸ F]FDG	1–7, 9, 11	1	5–7	6, 7, 9	7	1, 4, 9, 11
[⁶⁸ Ga]Ga-citrate	1–5	1	5	—	—	1, 2, 4
[¹¹ C]methionine	1–10	1	1, 5–10	1, 6–10	7, 8, 10	1, 2, 4 ^c , 8–10
[¹¹ C]donepezil	5–7, 9, 10	—	5–7, 9, 10	6, 7, 9, 10	7, 10	9, 10

^aNumbering as presented in the [¹⁵O]water paper [6]. ^bThe [¹⁵O]water paper presents an exhaustive list of the lesions studied. In pig number 3, inoculation failed to produce infection [3]. ^cTwo soft tissue lesions within the FOV (pig number 4).

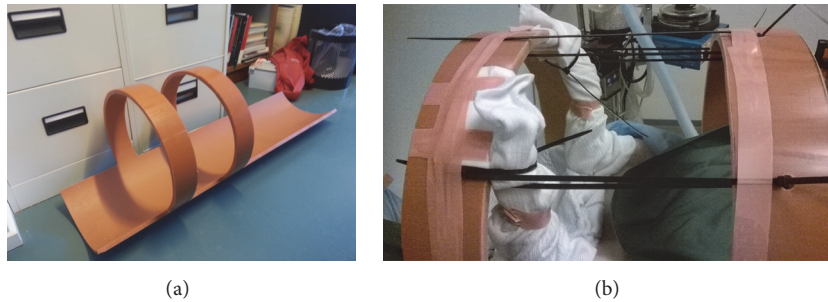


FIGURE 1: Two fixation devices for the pigs were produced from large plastic tubes, with a distance between the arches of either 15 or 21 cm, corresponding to the scanner FOVs. Assuming correct positioning of the device in the scanner, the arches made it visually clear where the FOV of the PET scan was located, thereby facilitating optimal positioning in the scanner. The fixation device also facilitated symmetric limb positioning and the avoidance of limb movement during the long scan sessions. (a) The 21 cm FOV fixation device. (b) Pig number 6 in the device.

one hospital to the other. The PET scans at Aarhus included the ¹¹C-labelled tracers in pigs number 1–10 and [¹⁸F]FDG in pig number 11. The PET scans at Aalborg included [⁶⁸Ga]Ga-citrate in pigs number 1–5 and [¹⁸F]FDG in pigs number 1–10.

At Aarhus, the PET data were acquired on a Biograph TruePoint 64 PET/CT scanner (Siemens, Erlangen, Germany). The scan field covered 21 cm in the axial direction and was positioned over the pelvic region and the hind limbs. The images were reconstructed with an OSEM algorithm with resolution recovery (TrueX, Siemens). The reconstruction parameters were 6 iterations, 21 subsets, 336 × 336 matrix in 109 slices, voxel size 2 × 2 × 2 mm³, and a 2 mm Gaussian filter. The spatial resolution of the reconstructed images was approximately 4 mm.

At Aalborg, the PET data were acquired on a GE VCT Discovery 64 PET/CT scanner (GE Healthcare, USA). The scan field covered 15 cm in the axial direction and was positioned over the pelvic region and the hind limbs. The images were reconstructed with an OSEM algorithm without resolution recovery (3D Vue Point, GE). The reconstruction parameters were 2 iterations, 28 subsets, 128 × 128 matrix in 47 slices, voxel size 5.5 × 5.5 × 3.3 mm³, and a 6 mm Gaussian filter.

On both scanners, image reconstruction included decay-correction to the start of scanning and attenuation-correction based on CT scanning.

For all tracers, the pigs were dynamically PET scanned for 60 minutes in 23 frames: 8 × 15 s, 4 × 30 s, 2 × 60 s, 2 × 120 s, 4

× 300 s, and 3 × 600 s. For [⁶⁸Ga]Ga-citrate, the animals were scanned for an additional 6 × 600 s (i.e., 120 minutes total scan time in 29 frames). After each of the dynamic scans, the pigs were statically scanned; the static PET/CT scans have been described in previous papers [3–5] and will not be further discussed here.

The pigs were scanned in dorsal recumbency (supine position). The hind limbs were positioned for the entire hind limbs and pelvis to be within the axial field of view (FOV) of the scanner. This was, however, not always possible; in particular, the 15 cm FOV at the Aalborg scanner (versus 21 cm FOV at the Aarhus scanner) was a limitation. To optimize the fixation position to the scanner FOV, custom-made fixation devices were used for pigs number 6–11 (Figure 1).

2.4. Blood Samples. Blood samples were drawn from the carotid artery at predetermined time points as listed below. The samples were manually drawn, and small variations occurred; the actual time of each sample was recorded. The samples were centrifuged to obtain plasma samples, which were counted in calibrated gamma-counters.

At Aarhus, plasma samples were counted in a Packard Cobra gamma counter. An energy window from 400 to 1400 keV was used. No signs of interference between consecutively administered radionuclides were seen in the plasma curves.

At Aalborg, plasma samples and full-blood samples were counted in a Wizard 2480 gamma counter (PerkinElmer,

Turku, Finland). To avoid interference from remnants of ^{111}In from ^{111}In -leukocytes (used in the same animals [3]), an energy window from 450 to 1200 keV was used [22].

In the 40 kg pigs (pigs number 1–4), 37 blood samples were drawn per tracer: every 5 seconds for 1 minute (12 samples), at 70, 80, 90, 100, 120, 140, 160, 180, 210, 240, 270, and 300 seconds (12 samples), and at 6, 7, 8, 9, 10, 15, 20, 25, 30, 35, 40, 50, and 60 minutes (13 samples). For ^{68}Ga Galactate, blood samples were also drawn at 75, 90, 105, and 120 minutes (four samples), for a total of 41 blood samples.

In the 20 kg pigs (pigs number 5–11), the number of blood samples was reduced to 26 samples per tracer: every 5 seconds for 50 seconds (10 samples), at 60, 80, 100, 120, 150, 180, 240, and 300 seconds (8 samples), and at 6, 8, 10, 15, 20, 30, 40, and 55 minutes (8 samples).

For ^{11}C methionine and ^{11}C donepezil, additional blood samples were drawn for metabolite analysis: at 2, 5, 10, 15, 25, and 40 minutes in the 40 kg pigs, and at 2, 5, 10, 20, 30, 40, and 55 minutes in the 20 kg pigs.

2.5. Input Function. The blood plasma rather than full blood was considered to be the reference fluid for tracer delivery (corresponding to equilibration between blood cells and plasma being slow compared to single-passage time of blood in the tissue). Accordingly, all input functions were based on plasma samples.

For both ^{18}F FDG and ^{68}Ga Galactate, the decay-corrected plasma sample data were used as the input function. No metabolite correction was performed for these two tracers because metabolite products are not expected to be found in the blood. ^{18}F FDG is phosphorylated within the cells, but the resulting (radioactive) metabolite is trapped within the cells [23]. Regarding ^{68}Ga Galactate, the Galactate complex quickly dissociates into Ga^{3+} and citrate $^{3-}$ within the blood, but the gallium ion attaches to transferrin (making ^{68}Ga Galactate-transferrin the actual tracer). Therefore, free gallium is not found in the blood [24].

For ^{11}C methionine and ^{11}C donepezil, metabolite correction was performed. A fractionated HPLC analysis was used to separate the metabolites from the parent tracer, and counting was used to determine the fraction of activity representing the parent tracer. Based on the obtained data points, Hill-type fraction curves were fitted:

$$f(t) = 1 - \frac{(1-a)t^b}{c+t^b}, \quad (1)$$

where t is the sampling time (seconds postinjection). The function starts at $f(0) = 1$ (thus assuming no metabolism before injection) and has an asymptotic value $f(\infty) = a$. The parameters a , b , and c were fitted for both tracers in the individual pigs.

In the following text, the *uncorrected input function* will denote the activity concentration (decay-corrected Bq/mL) from plasma samples and the *metabolite-corrected input function* will denote $f(t)$ times the uncorrected input function.

2.6. Determination of the Delay-Correction. The measured input function can be biased by delay and dispersion effects

due to the differences in distance between the blood sampling site (carotid artery) and the infection sites in the hind limbs. Such a delay can be determined by applying a series of possible delay-correction values, fitting the data with each value, and selecting the delay-correction resulting in the best fit [25].

We applied this procedure for each tracer in each animal, using input function offsets from -60 s to $+60$ s in 1-second steps. This was done using the uncorrected plasma data for the input function, and fitting a reversible two-tissue compartment model (rev2TCM in Figure 2; the models are further discussed below) to the first 300 s of the full field-of-view data. Using full FOV data ensures that the statistical noise is low. Restricting this fit to the early data has several advantages. First, this focuses on the part of the study where the input function changes fast and the delay therefore is important. Second, this means that physiological differences in uptake (e.g., bladder versus nonbladder, infection versus noninfection) will only have had little time to manifest; thus the full FOV data will be dominated by the bolus passage in this anatomical part of the animal, rather than by a mix of physiologies. Third, the possible metabolism effects will not yet dominate the input function, for which reason the uncorrected input function can be considered representative, even if the tracer over time is metabolized.

2.7. Kinetic Models. Relatively little literature exists on tracer kinetics in infections for the tracers investigated in this work. Rather than imposing a specific model on these tracers, we examined the applicability of three different models for each tracer (Figure 2).

Physiologically, the ITCM corresponds to the tracer entering and leaving the tissue with no binding or other specific uptake. The irr2TCM describes uptake and irreversible trapping of the tracer or metabolites (e.g., phosphorylated ^{18}F FDG). The rev2TCM corresponds to uptake in the tissue followed by reversible binding (or reversible metabolism) of the tracer.

In all of the models, the K_1 rate constant describes the first-pass uptake of tracer, equal to the product of perfusion and the first-pass extraction fraction. We report K_1 in units of $\text{mL}/\text{min}/100\text{ cm}^3$, that is, mL uptake per minute per 100 cm^3 of tissue. The other rate constants (k_2 , k_3 , and k_4 , all with unit min^{-1}) describe how rapid the concentration in a compartment changes due to a given process (excretion, binding, and metabolism in the tissue). The blood fraction V_b is the fraction of measured PET signal that originates from the blood in the vascular bed.

For models with irreversible uptake, the net uptake rate K_i (same unit as K_1) represents the effective irreversible uptake from the input. Whereas K_1 represents the rate of immediate (first-pass) uptake of tracer, K_i can similarly be interpreted as the rate of long-term uptake. For the irr2TCM, the theoretical net uptake rate is

$$K_i = \frac{K_1 \cdot k_3}{k_2 + k_3} \quad (\text{for irr2TCM}). \quad (2)$$

The net uptake rate may also be determined as the slope of a Patlak plot [26, 27].

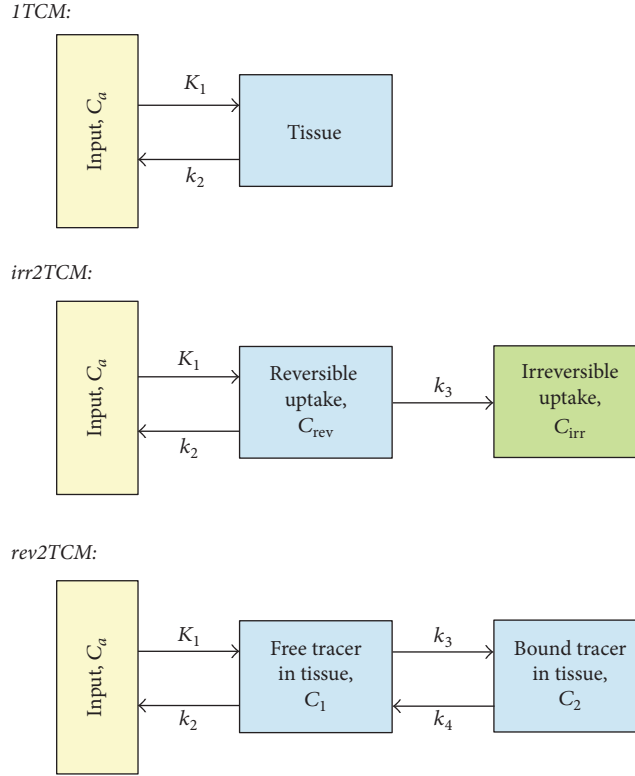


FIGURE 2: Kinetic models. From top to bottom: 1-tissue compartment model (1TCM), 2-tissue compartment model with irreversible uptake (irr2TCM), and 2TCM with reversible uptake (rev2TCM). The rate constants were fitted as K_1 (unit mL/min/cm³ or mL/min/100 cm³), the ratio K_1/k_2 (unit mL/cm³), k_3 (unit min⁻¹), and the ratio k_3/k_4 (no unit). Also the blood fraction V_b was fitted.

For models with reversible uptake, the distribution volume (DV, unit mL/cm³) is the ratio of the tissue concentration to the “input” concentration, once a steady-state has been reached, that is, the volume of “input” needed to account for the activity in 1 cm³ of tissue [28]. Although not being an uptake rate, DV may be used as an indicator of the degree of long-term uptake. For the 1TCM and rev2TCM, the theoretical distribution volumes are

$$DV = \frac{K_1}{k_2} \quad (\text{for 1TCM}) \quad (3)$$

$$DV = \frac{K_1}{k_2} \cdot \left(1 + \frac{k_3}{k_4}\right) \quad (\text{for rev2TCM}). \quad (4)$$

The distribution volume of reversible uptake may also be determined as the slope of a Logan plot [29, 30].

2.8. Weighting of the PET Data in Modelling. Theoretically, least-squares fitting is optimal with weights proportional to $1/\sigma^2$ where σ^2 is the variance of the noise. With N counts (Poisson distributed) during a frame length L , the count rate $R = N/L$ has variance:

$$\sigma^2(R) = \frac{N}{L^2} = \frac{R}{L}. \quad (5)$$

After decay-correction:

$$R_{dc} = dcf \times R$$

$$\sigma^2(R_{dc}) = dcf^2 \times \frac{R}{L} = dcf \times \frac{R_{dc}}{L}, \quad (6)$$

where dcf is the decay-correction factor, calculated from the radionuclide half-life and frame time interval. For weighting purposes, it can be well approximated by using the mid-time of the frame:

$$dcf = 2^{t/T_{1/2}} = \exp(\lambda t). \quad (7)$$

Seemingly, optimal weighting should be $1/\sigma^2 = L/R$ for non-decay-corrected data and $1/\sigma^2 = L/(dcf \times R_{dc})$ for decay-corrected data.

However, the count rate (or the activity concentration) is known only from a measurement that includes noise. In a simulation study, Thiele and Buchert [31] found that noise in the weighting factors can severely degrade parameter estimation and should therefore be avoided. Consistent with the weighting that gave the best results in that study, we used the following noise-free weighting factors for the decay-corrected PET data:

$$w = \frac{L}{dcf} = L \times \exp(-\lambda t). \quad (8)$$

These weights correctly include the effects of decay and the large differences in frame length (from 15 to 600 seconds). The weights are noise-free, at the cost of ignoring the statistical effects from variation in tracer concentration due to kinetics.

This approximation (weights not fully reflecting $1/\sigma^2$) is unlikely to be a problem. A simulation study by Yaqub et al. [32] found that kinetic modelling of PET data was reasonably robust against some misrepresentation of the variance in (noise-free) weighting, with only severe misrepresentation being a problem.

2.9. Modelling. For each tracer in each model (1TCM, irr2TCM, and rev2TCM), the fitted parameters were determined using least-squares fitting with the weighting described above. Additionally, Patlak plots and Logan plots were computed, based on the data from 10 minutes postinjection (p.i.) and onwards.

For [^{11}C]methionine and [^{11}C]donepezil, this procedure was performed twice: using an uncorrected input function and using a metabolite-corrected input function. For these two tracers, modelling was restricted to data from the first 40 minutes (out of 60 minutes), as metabolite data were in many cases incomplete for later frames.

Modelling was performed using software acquired from the Turku PET Centre website [33]. The parameter k_2 was fitted as the ratio K_1/k_2 (corresponding to the distribution volume of the first compartment). In the rev2TCM, the parameter k_4 was fitted as the ratio k_3/k_4 (corresponding to the binding potential BP if the first and second compartments are considered to represent unspecific and specific uptake, resp.).

2.10. Evaluation. In addition to visual inspection of the fits, the three models were compared with the corrected Akaike Information Criterion (AIC_c), which rewards a good fit but punishes the use of a model with many fitting parameters. For a given data set, AIC_c favours the model resulting in the lowest AIC_c value [34, 35].

For the determination of uptake as reversible or irreversible, the Patlak plot also was considered. If the uptake is reversible (i.e., not irreversible), the Patlak plot will eventually approach a constant value. Therefore, the linearity of the Patlak plot with a nonzero slope can be used as a test for irreversible uptake.

All these results are based on plasma input functions. To compare with perfusion, previously published results for blood perfusion in the same animals [6] were transformed into plasma perfusion by the formula

$$\begin{aligned} \text{plasma perfusion} &= (1 - \text{haematocrit}) \\ &\quad \times \text{blood perfusion}, \end{aligned} \quad (9)$$

with haematocrit being measured at a time roughly corresponding to the time of the [^{15}O]water PET.

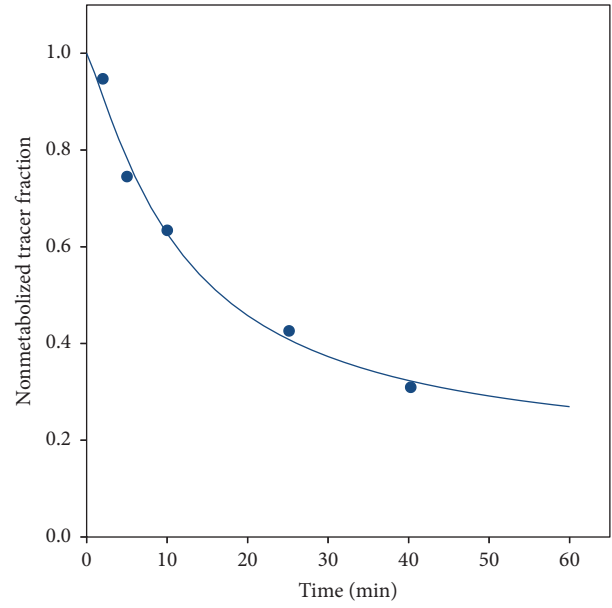


FIGURE 3: Representative data and curve fit (see (1)) for the fraction of nonmetabolized [^{11}C]methionine (from pig number 1).

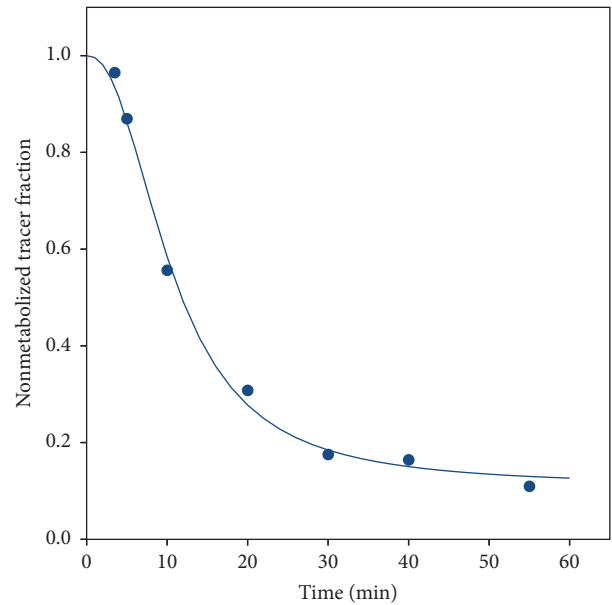


FIGURE 4: Representative data and curve fit (see (1)) for the fraction of nonmetabolized [^{11}C]donepezil (from pig number 10).

3. Results

3.1. Metabolite Correction. The fraction curves indicated considerable metabolism of both [^{11}C]methionine (Figure 3) and [^{11}C]donepezil (Figure 4).

For both [^{11}C]methionine and [^{11}C]donepezil, the “uncorrected” (i.e., not corrected for metabolism, but corrected for physical decay) plasma curves showed an unexpected tendency of slightly rising values after typically 20 minutes. As an example, see the data for [^{11}C]methionine

TABLE 2: Evaluation of the fitting models for the investigated tracers and input functions.

Tracer	Number of OM + ST foci modelled	Plasma input function	Visual impression of fit	Linear Patlak plot	Lowest AIC _c
[¹⁸ F]FDG	8 + 7	Uncorrected	Good fit of both 2TCM, with rev2TCM giving only minor improvement over irr2TCM. Poor fit of 1TCM.	Yes	rev2TCM
[⁶⁸ Ga]Ga-citrate	2 + 3	Uncorrected	Good fit of both 2TCM, with 1TCM reasonable for some curves.	Yes	irr2TCM or rev2TCM
[¹¹ C]methionine	17 + 7	Uncorrected	Good fits of rev2TCM. Cases with good irr2TCM fit (generally low-lying curves). For irr2TCM, the fit was improved over the uncorrected input function. Overall, rev2TCM appeared best.	No	See main text
		Metab. corr.		Almost	
[¹¹ C]donepezil	11 + 2	Uncorrected	Poor fits for all models.	No	See main text
		Metab. corr.	Good fits with 1TCM, only slightly improved by 2TCM (irr or rev).	Generally not	

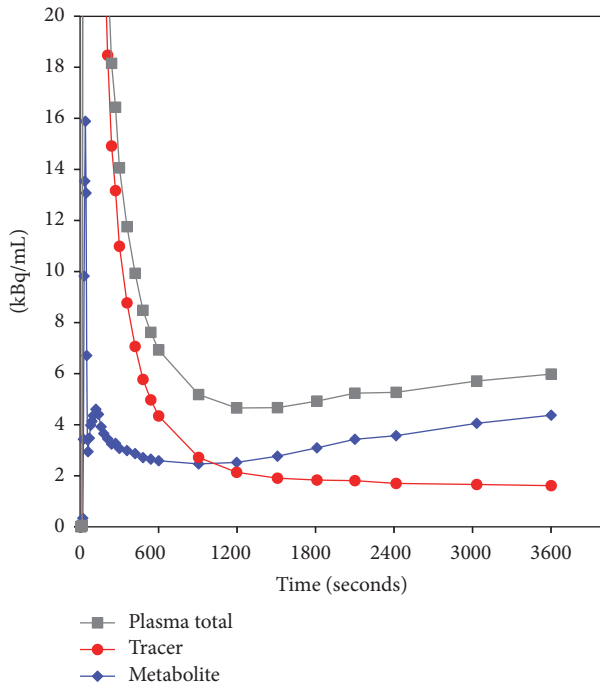


FIGURE 5: Representative sample plasma activity curves for [¹¹C]methionine (decay-corrected, from pig number 1). The scale of the vertical axis has been chosen to emphasize the curve tails, at the cost of truncating the bolus peak (maximum value ~600 kBq/mL). Uncorrected input function is the total plasma activity concentration (grey curve). Metabolite-corrected input function (red curve) originates as the product of the total plasma activity curve and the fraction curve (Figure 3). Also shown is the metabolite activity concentration (blue curve), that is, the difference between the other two curves. Similar curves were seen for [¹¹C]donepezil (not shown).

in Figure 5 (the data for [¹¹C]donepezil were similar). Possible reasons like unresolved background counts, either from other tracers in the multitracer study or from the surroundings, were investigated, but no sign of any such

problems was found; for example, blood samples taken before the arrival of the bolus injection were far below the level that would cause this background. Therefore, we conclude that the curves correctly represent the activity concentration in the plasma. After metabolite correction, the curves decreased as expected (Figure 5).

3.2. *Delay-Correction of Input Function.* Each input function ($n = 26$) was individually delay-corrected (but with a common delay for all lesions in the same scan). The mean \pm SD of the corrections was -4.5 ± 4.1 seconds. A negative correction corresponds to the tracer arriving earlier to the scanned tissue (PET data) than to the site of blood sampling (plasma input data). All individual corrections were numerically smaller than the initial PET frame length (15 seconds).

3.3. *Modelling.* The overall results for the different models are summarized in Table 2, with elaborating comments given here.

3.3.1. [¹⁸F]FDG. Despite the lowest AIC_c values having been found for rev2TCM, the irr2TCM appeared visually to give a reasonable fit for the investigated time range. Example fits are shown in Figure 6. The Patlak plots (not shown) were linear with nonzero slopes, indicating the presence of irreversible uptake. Also, the majority of fitted ratios k_3/k_4 were above 2 (median value ~4 for all VOIs, ~5 if restricted to infected side); that is, overall k_4 was considerably lower than k_3 . For these reasons and because irr2TCM has fewer parameters than rev2TCM, we pragmatically chose to base the further analysis of [¹⁸F]FDG uptake on the *irr2TCM*. The values of K_1 were overall very similar for irr2TCM and rev2TCM.

3.3.2. [⁶⁸Ga]Ga-Citrate. Overall, the AIC_c values indicated nearly equal quality of fits for irr2TCM and rev2TCM. Example fits are shown in Figure 7. The Patlak plots were linear with nonzero slopes. Further analysis will assume the simplest model: *irr2TCM*.

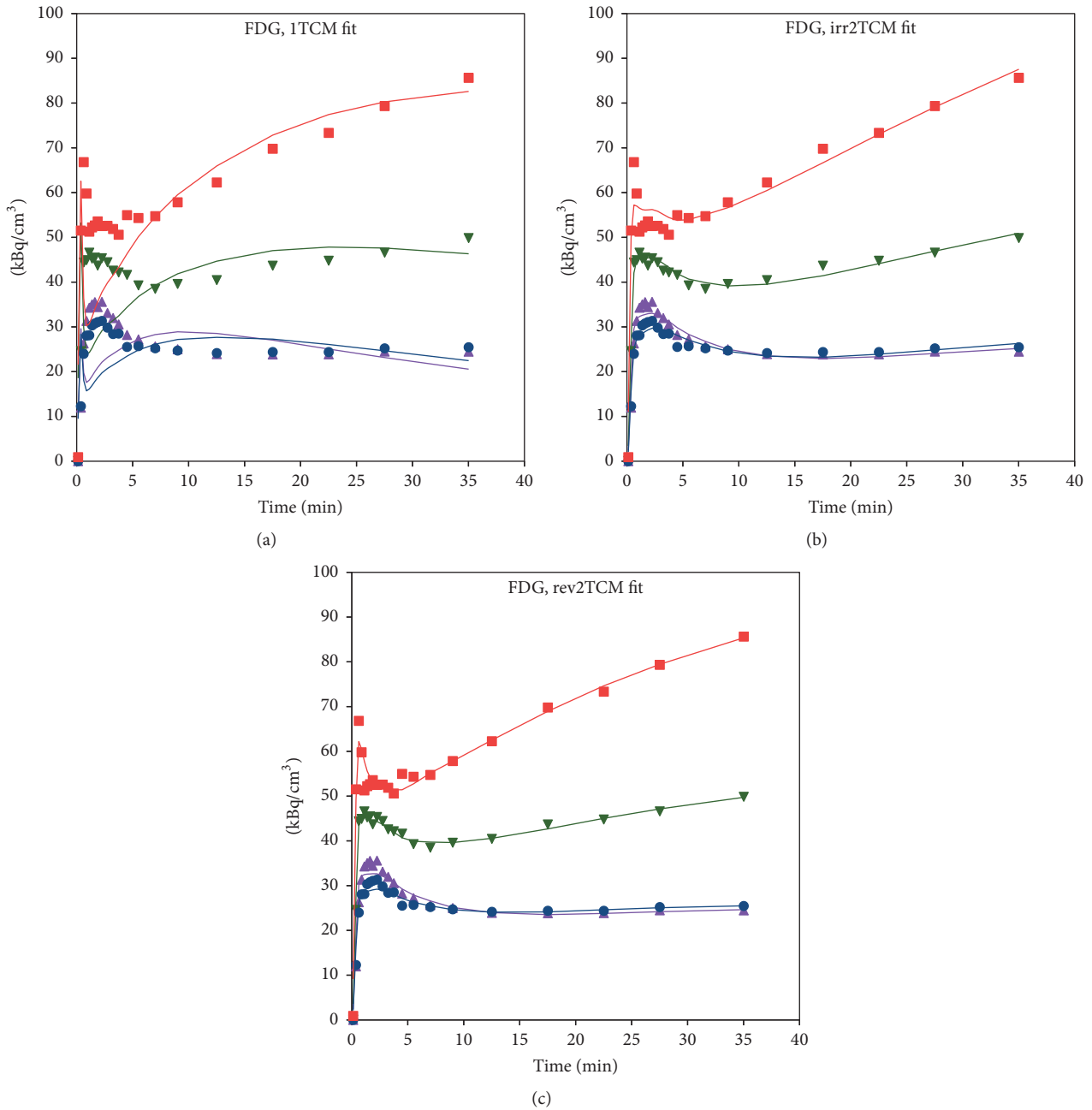


FIGURE 6: Model fits for $[^{18}\text{F}]$ FDG in pig number 6, using 1TCM (a), irr2TCM (b), and rev2TCM (c) models. Red and blue: OM lesion in the distal femur and the corresponding noninfected bone. Green and mauve: OM lesion in the proximal tibia and the corresponding noninfected tissue. In this case, modelling was restricted to 0–40 minutes because movement of the right limb occurred in the following frame.

For both $[^{18}\text{F}]$ FDG and $[^{68}\text{Ga}]$ Ga-citrate, good correspondence was observed between the slope of the Patlak plot and K_i calculated from the irr2TCM parameters.

3.3.3. $[^{11}\text{C}]$ Methionine. The AIC_c values sometimes favoured rev2TCM and sometimes favoured irr2TCM, but, from mean and median values, rev2TCM was favoured. Visually, the irr2TCM fit showed a problematic upward trend in the late part of the fits (Figure 8). Despite the extent of metabolism during the study (Figure 3), only a small difference was

observed between using the uncorrected or the metabolite-corrected input function with the rev2TCM: the AIC_c values were comparable, the fits were visually very similar, and the fitted rate parameters K_1 , K_1/k_2 , and k_3 were very similar. Only the k_3/k_4 values differed markedly, being lower for the corrected than the uncorrected input function. However, the k_3/k_4 ratio is important for the distribution volume (see (4)), and the further analysis of the $[^{11}\text{C}]$ methionine data will assume the rev2TCM model with a metabolite-corrected input function.

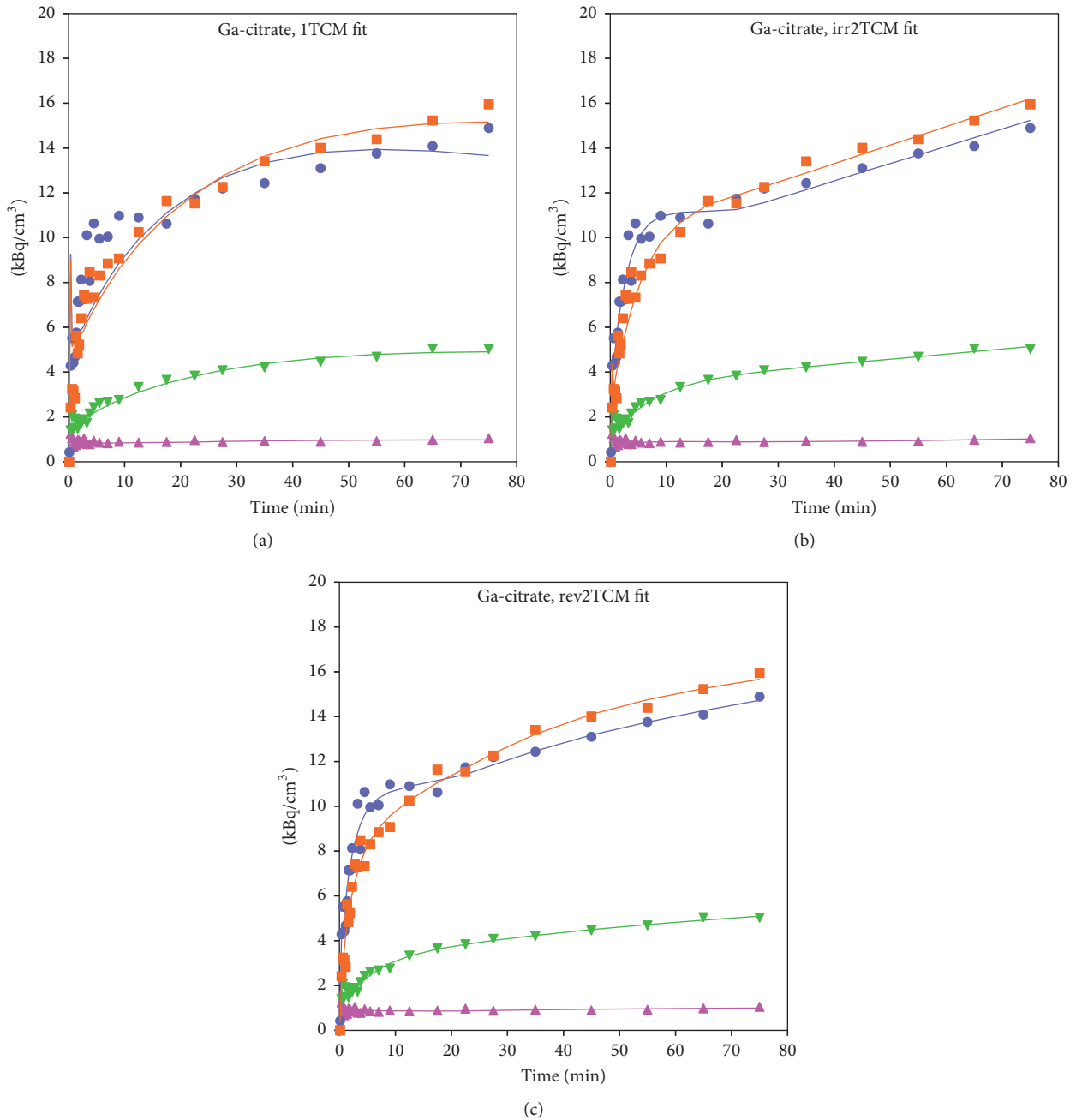


FIGURE 7: Model fits for $[^{68}\text{Ga}]\text{Ga-citrate}$ in pig no. 1, using ITCM (a), irr2TCM (b), and rev2TCM (c) models. Orange and light blue: OM lesion in the proximal femur and the corresponding noninfected bone. Light green and cyan: ST lesion near the metatarsal bone and the corresponding noninfected tissue.

3.3.4. $[^{11}\text{C}]\text{Donepezil}$. Both the plots and the AIC_c values unequivocally favoured fits with a metabolite-corrected input function (Figure 9). Within these, the AIC_c values variably favoured each of the three models but with no obvious pattern (e.g., not distinguishing infected versus noninfected tissue, bone versus soft tissue, or high versus low K_1). Visually, however, the ITCM (with metabolite-corrected input) fits well in all cases. A typical fit for the ITCM is seen in

Figure 9(b). Further analysis of $[^{11}\text{C}]\text{donepezil}$ will be based on the ITCM with a metabolite-corrected input function.

3.4. Perfusion and First-Pass Uptake Rate (K_1). The K_1 parameter represents the product of perfusion and the extraction fraction for the tracer. Thus, plotting K_1 as a function of perfusion gives a measure of extraction; if the extraction fraction is independent of perfusion, the plot will

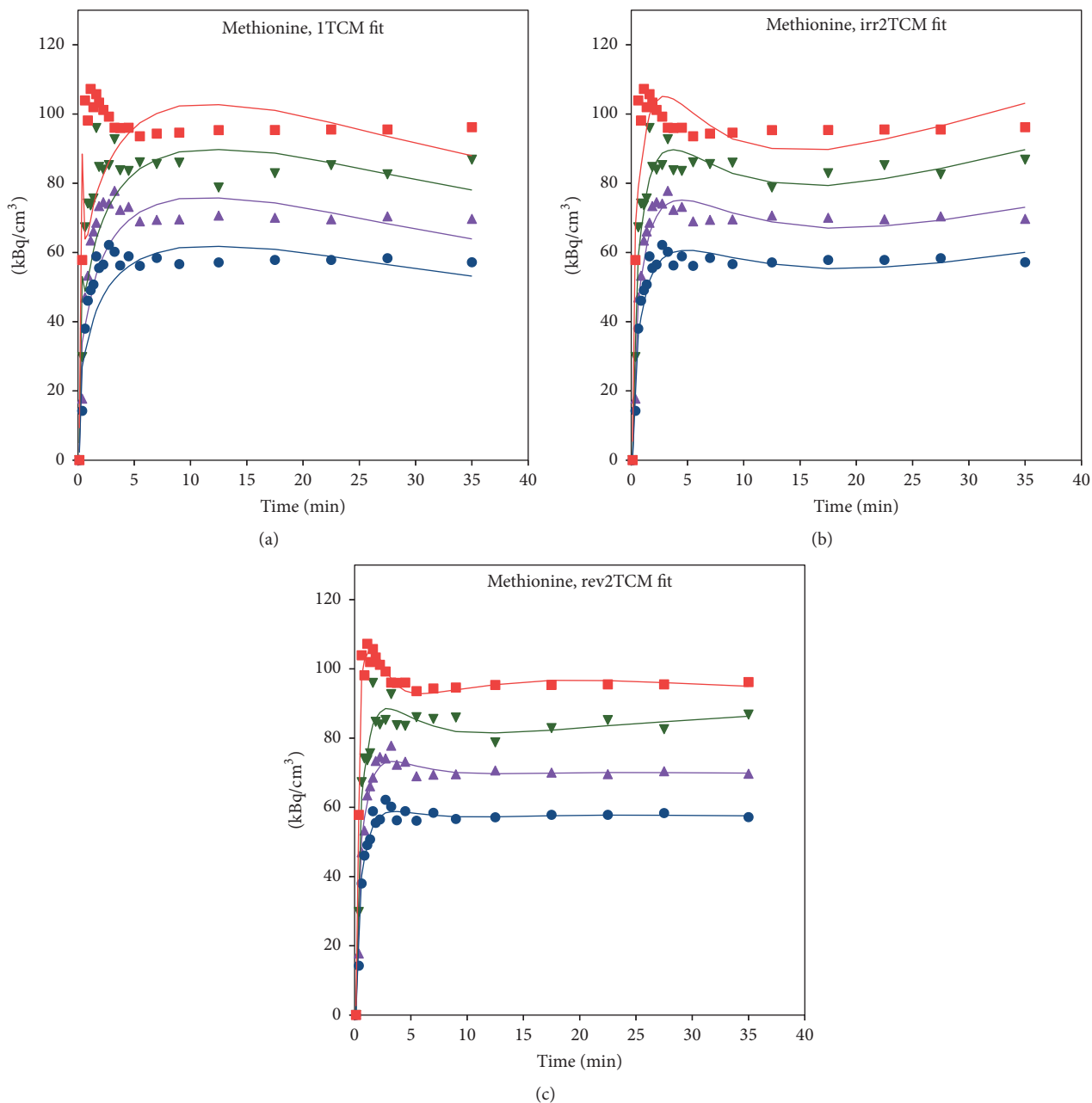


FIGURE 8: Model fits for $[^{11}\text{C}]$ methionine in pig number 6 (same animal as in Figure 6), using uncorrected plasma data as the input function. Legend as in Figure 6. Fits with a metabolite-corrected input function (not shown) were visually very similar to the shown fits, although with a reduced upward trend in the irreversible model (b).

show proportionality between K_1 and perfusion. The blood perfusion of these lesions in these animals has been described previously, based on $[^{15}\text{O}]$ water PET scans [6]. These data were transformed into plasma perfusion according to (9).

Figure 10 shows the values of K_1 plotted as a function of plasma perfusion. Notably, $[^{68}\text{Ga}]$ Ga-citrate shows only small uptake compared to perfusion, that is, a small extraction fraction.

The paradoxical plot for $[^{11}\text{C}]$ donepezil, showing K_1 values that are significantly higher than perfusion (corresponding to $>100\%$ extraction), is not a result of using

the simple 1TCM rather than one of the 2TCM models. Overall, the K_1 data from these models (not shown) were very similar, in some cases even higher, resulting in very similar plots (not shown). For further explanations, see Discussion.

For $[^{18}\text{F}]$ FDG, $[^{11}\text{C}]$ methionine, and $[^{11}\text{C}]$ donepezil, a paired t -test showed a higher K_1 in the infected (right) side than in the noninfected (left) side ($p \leq 0.0001$). For $[^{68}\text{Ga}]$ Ga-citrate, no significant difference was found ($p > 0.05$).

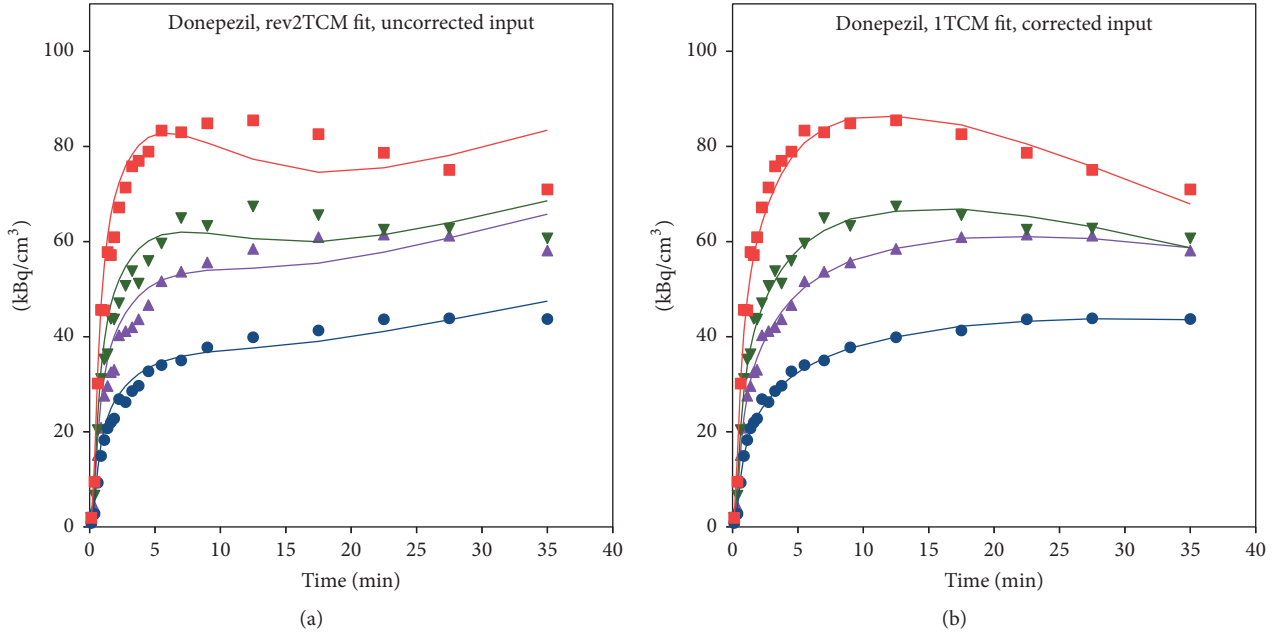


FIGURE 9: Model fits for $[^{11}\text{C}]$ donepezil in pig number 6 (same animal as in Figures 6 and 8). Legend as in Figure 6. (a) Using the *uncorrected* input function, even the model with the most parameters (rev2TCM) gives a poor fit. (b) Using the *metabolite-corrected* input function, the model with the least parameters (1TCM) gives a good fit.

3.5. *Irreversible Net Uptake Rate (K_i) for $[^{18}\text{F}]$ FDG and $[^{68}\text{Ga}]$ Ga-Citrate.* For both $[^{18}\text{F}]$ FDG and $[^{68}\text{Ga}]$ Ga-citrate, good agreement was observed between K_i calculated from the Patlak plots and from the irr2TCM model (data not shown).

Figure 11 shows K_i as a function of plasma perfusion. Figure 12 compares K_i in the infected versus corresponding noninfected positions. For $[^{18}\text{F}]$ FDG, K_i values were significantly higher in the infected lesions than in the corresponding noninfected positions ($p < 0.002$, paired t -test). For $[^{68}\text{Ga}]$ Ga-citrate, the difference was not statistically significant ($p > 0.05$).

3.6. *Distribution Volume (DV) of Reversible Tracers.* For $[^{11}\text{C}]$ donepezil fitted with the 1TCM, good agreement was observed between DV calculated from the Logan plots and from (3). For $[^{11}\text{C}]$ methionine fitted with the rev2TCM, the agreement was not as good between DV from the Logan plots and from (4); however, the lack of agreement was due to the rev2TCM giving unrealistically high values in some cases (e.g., $>100 \text{ mL/cm}^3$), corresponding to cases with high values of k_3/k_4 . Excluding these cases, good agreement was observed in the DV calculations.

Overall, the slope of the Logan plot was used as a robust measure of DV. Figure 13 shows DV as a function of plasma perfusion. Figure 14 compares DV in the infected and corresponding noninfected locations. For $[^{11}\text{C}]$ methionine, DV was significantly higher in the infected locations ($p = 0.0005$), while the minor difference seen for $[^{11}\text{C}]$ donepezil was not significant ($p > 0.05$).

4. Discussion

Four very different PET tracers were studied for their potential as markers of infection in a porcine model of osteomyelitis (including associated soft tissue lesions). As noted, the results from static imaging have been reported earlier [3–5], but dynamic imaging can provide more information on the uptake processes, which is not available when the tracer concentration is measured at only one time interval.

The modelling of PET data is restricted by the length of the acquisition, the number of data points, and statistical noise. Therefore, some level of pragmatism is needed when setting up or choosing a model. Strictly irreversible uptake (in the sense of the molecules staying in the body for life) is rare, but the efflux level from a compartment may be practically zero relative to the length of the PET acquisition. In the present study, we attempted to find a level that makes the models useful for providing information about the uptake process while accepting a level of pragmatism to distinguish “practically irreversible” from “practically reversible” uptake.

4.1. *$[^{18}\text{F}]$ FDG.* For the kinetic modelling of $[^{18}\text{F}]$ FDG, the two classical models are the irr2TCM by Sokoloff et al. [36] and the rev2TCM by Phelps et al. [37]. In both models, the second tissue compartment represents the metabolite product $[^{18}\text{F}]$ FDG-6-phosphate, and in the latter model $k_4 > 0$ represents dephosphorylation back to $[^{18}\text{F}]$ FDG. Relative to infection, the kinetic modelling of $[^{18}\text{F}]$ FDG uptake appears only to have been performed in lung studies (reviewed in [38]) and in a single study of an acute viral infection [39]. All

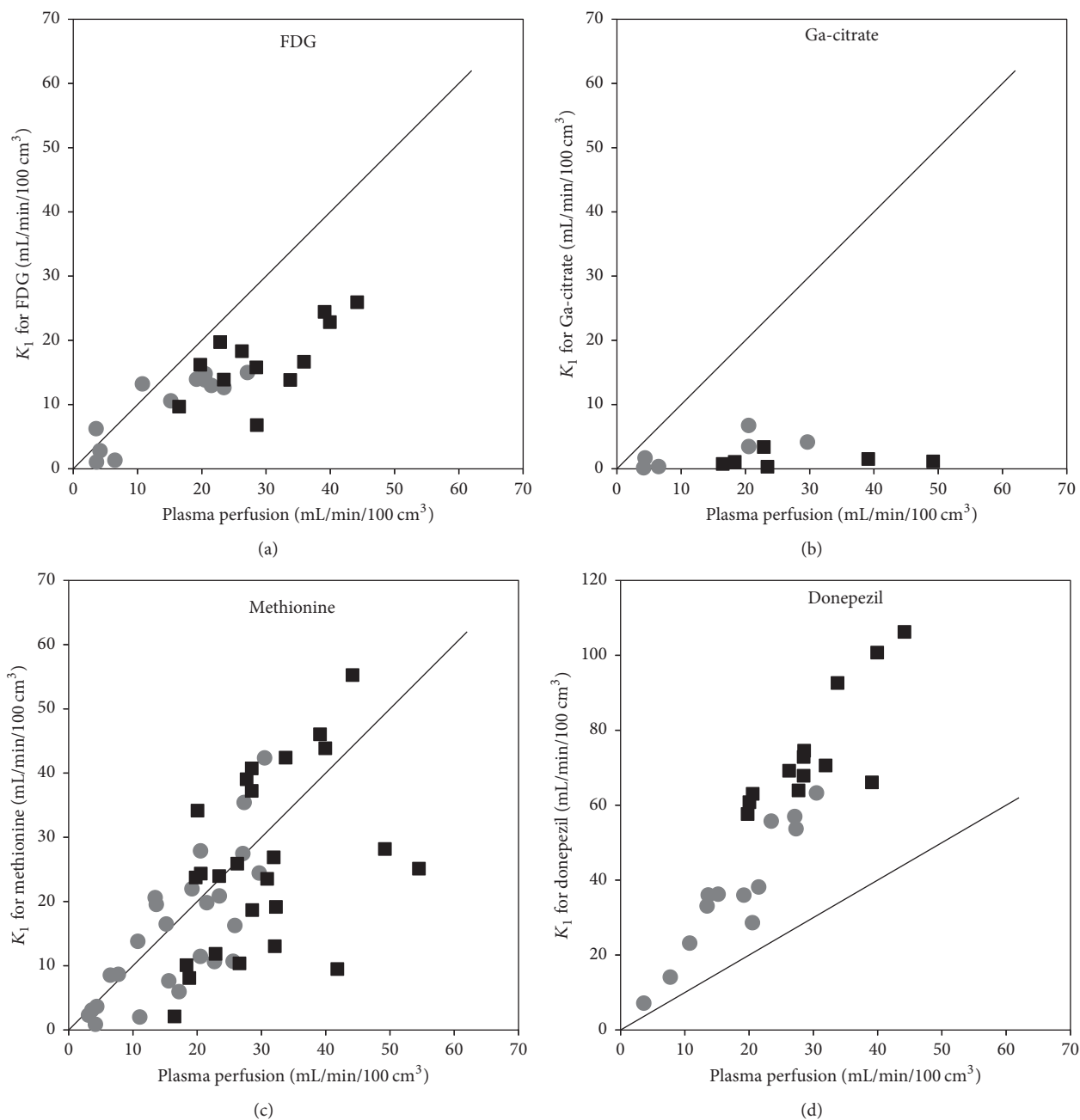


FIGURE 10: First-pass uptake K_1 as a function of plasma perfusion, shown along with the identity line ($y = x$). The black squares represent infection foci and the grey circles represent the corresponding noninfected positions. The plots include both bone and soft tissue data. The data for $[^{68}\text{Ga}]\text{Ga-citrate}$ did not correlate with perfusion ($R^2 = 0.03$). For $[^{11}\text{C}]\text{donepezil}$, all data points are above the identity line, paradoxically corresponding to an extraction fraction above 100%. See Discussion.

of these studies focus on irreversible uptake models, generally the irr2TCM, although some lung studies included a separate reversible compartment for uptake in pulmonary oedema [38, 40].

In our porcine osteomyelitis model, the uptake of $[^{18}\text{F}]\text{FDG}$ was found to be (practically) irreversible, with a reasonable fit by the irr2TCM. Accordingly, the level of uptake was evaluated based on the irreversible net uptake rate, K_i , in almost all cases showing elevated uptake in lesions

compared to healthy tissue, for both OM and ST lesions (Figure 12). The correlation with perfusion seen for both first-pass uptake (Figure 10) and net uptake (Figure 11) indicates uptake of $[^{18}\text{F}]\text{FDG}$ to be more flow-limited than diffusion-limited.

4.2. $[^{68}\text{Ga}]\text{Ga-Citrate}$. Dynamic PET studies of $[^{68}\text{Ga}]\text{Ga-citrate}$ and $[^{68}\text{Ga}]\text{Ga-transferrin}$ have been published before [8, 41, 42], but the present study appears to be the first to

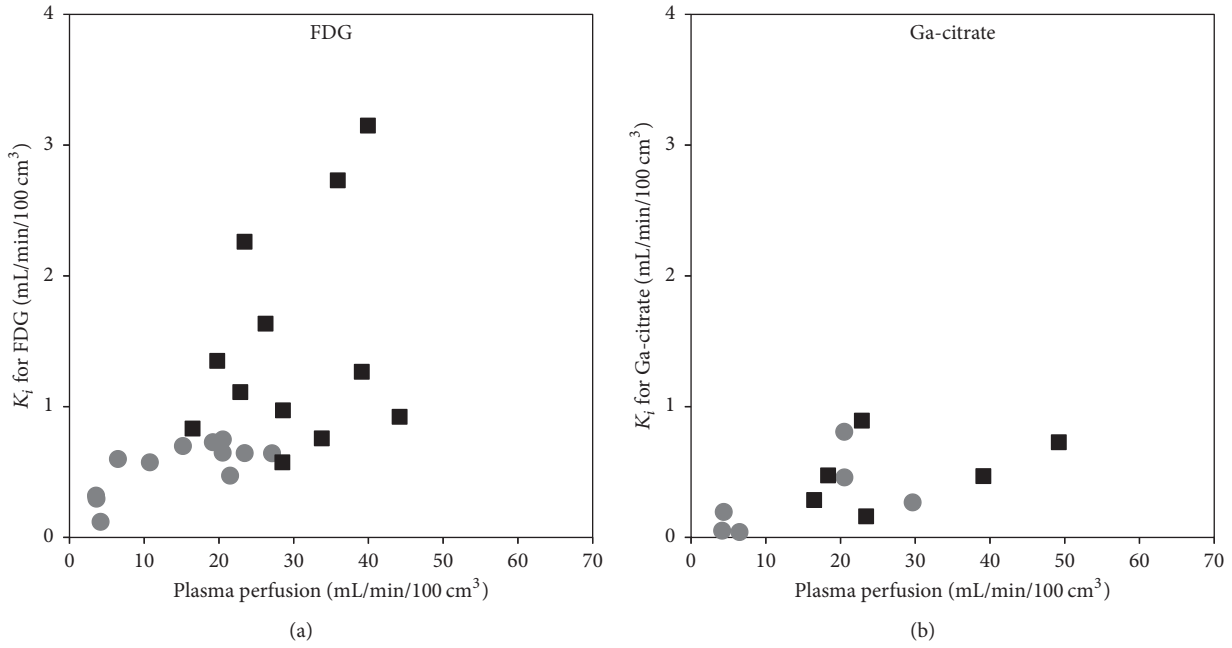


FIGURE 11: Irreversible uptake K_i as a function of plasma perfusion, for the tracers showing irreversible uptake: [¹⁸F]FDG (a) and [⁶⁸Ga]Ga-citrate (b). Black squares represent infection foci and grey circles corresponding to noninfected positions (compare with Figure 10).

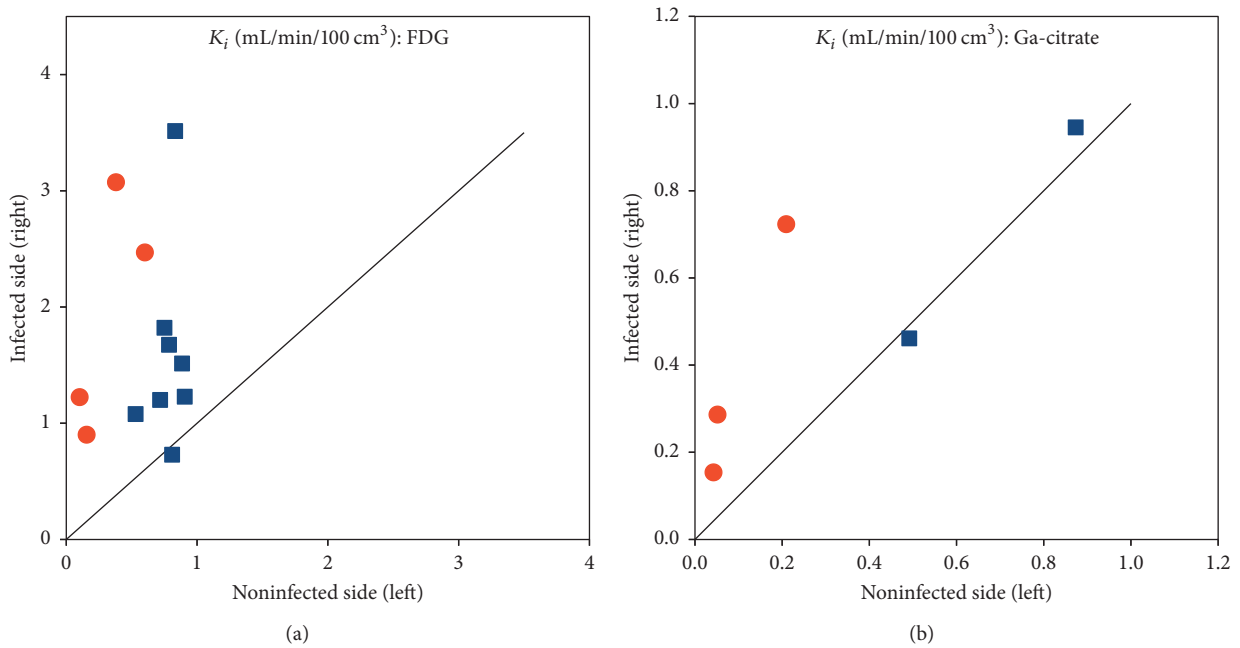


FIGURE 12: Comparison of irreversible net uptake rate K_i in infected (right hind limb) versus noninfected (left hind limb) positions. Bone is represented by blue squares and soft tissue by red circles. The line is the identity line ($y = x$). (a) shows [¹⁸F]FDG and (b) shows [⁶⁸Ga]Ga-citrate; note the difference in scales.

include kinetic modelling. As noted by Kumar and Boddeti [43], no literature is available on the early imaging times of [⁶⁷Ga]Ga-citrate SPECT. We found the uptake of ⁶⁸Ga to be well described by the irr2TCM (Figure 7). However, first-pass uptake (K_1) of ⁶⁸Ga was small compared to that of the

other tracers, indicating a very small extraction fraction with little dependence on perfusion (Figures 10 and 11), that is, diffusion-limited.

The physiological reason for the slow uptake of ⁶⁸Ga may be related to the binding of gallium to a large protein

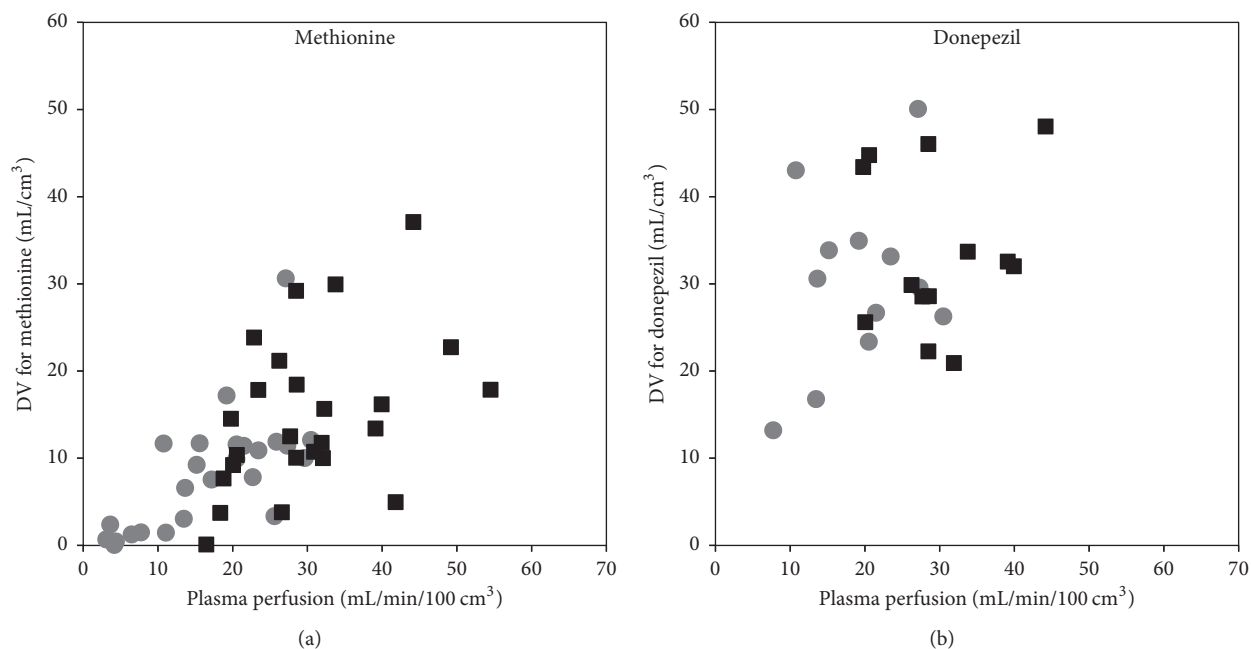


FIGURE 13: Distribution volume DV as a function of plasma perfusion, for the tracers showing reversible uptake: $[^{11}\text{C}]$ methionine (a) and $[^{11}\text{C}]$ donepezil (b). Legend as in Figure 11.

(transferrin). Uptake will either require extravasation of the large $[^{68}\text{Ga}]\text{Ga}$ -transferrin complex or require a two-step process, such as the release of ^{68}Ga from the protein before the uptake or the uptake of $[^{68}\text{Ga}]\text{Ga}$ -transferrin by leukocytes which then enter tissue [44]. Therefore, even though bacteria may show increased uptake of gallium due to its chemical similarities with iron [43], the overall uptake mechanism appears to be quite slow.

For static imaging, slow uptake favours late imaging. Physically, the half-life of ^{68}Ga restricts imaging to a few hours after injection. In a study of lung lesions, Vorster et al. [10] recommended imaging to start no later than 120 minutes p.i.

Compared to other ^{68}Ga infection studies [8–10, 41], the results in the porcine osteomyelitis model (present paper and [3, 4]) appear disappointing. At the basic level, the tracer is a Ga^{3+} ion (with chemical similarities to the Fe^{3+} ion), which makes a species difference unlikely. A different reason may be indicated by Figure 12: maybe the tracer is able to differentiate infected *soft tissue* from healthy tissue (despite the slow uptake rate) but is not suitable for bone infections. Mäkinen et al. [8] did find uptake in bone lesions in a rat model, but noted as a limitation of the study that their model “perhaps best simulates osteomyelitis arising from grossly contaminated long-bone fractures.” In contrast, the porcine osteomyelitis model represents haematogenous osteomyelitis without bone trauma.

4.3. $[^{11}\text{C}]\text{Methionine}$. The modelling of $[^{11}\text{C}]\text{methionine}$ uptake required a rev2TCM. For comparison, Fischman et

al. [45] described the muscle uptake of $[^{11}\text{C}]\text{methionine}$ with a 2TCM, where the second compartment represented the incorporation of $[^{11}\text{C}]\text{methionine}$ in tissue proteins, and they assumed that the degradation rate of labelled protein could be ignored (corresponding to $k_4 = 0$ in our notation). That is, they suggested an irr2TCM rather than rev2TCM. Our finding of rev2TCM as preferable thus corresponds to protein degradation being nonnegligible.

Despite the considerable metabolism of $[^{11}\text{C}]\text{methionine}$ during the acquisition time (Figure 3), practically only the k_4 rate constant depended on whether modelling was based on the uncorrected or the metabolite-corrected input function (with higher k_4 values in the latter case). It appears that the metabolite products have kinetics quite similar to the original molecule. The correlation with perfusion seen for both first-pass uptake (Figure 10) and distribution volume (Figure 13) indicates uptake of $[^{11}\text{C}]\text{methionine}$ to be flow-limited.

The unexpected rise in the plasma activity curves after ~20 minutes (Figure 5) might be explained by a heavy uptake by metabolizing organs (the liver), followed by a later release of radioactive metabolite products to the blood pool.

Generally, the distribution volume (DV) for $[^{11}\text{C}]\text{methionine}$ was higher in the infected tissue than in the noninfected tissue (Figure 14). This difference between infected and noninfected tissue could point to $[^{11}\text{C}]\text{methionine}$ having a role in infection imaging (regardless of the role of perfusion in causing the distinction). In line with the results from static imaging [3, 5], the distinction between infected and noninfected tissue appeared more clear for soft tissue than for bone (Figure 14). As indicated by the two already mentioned

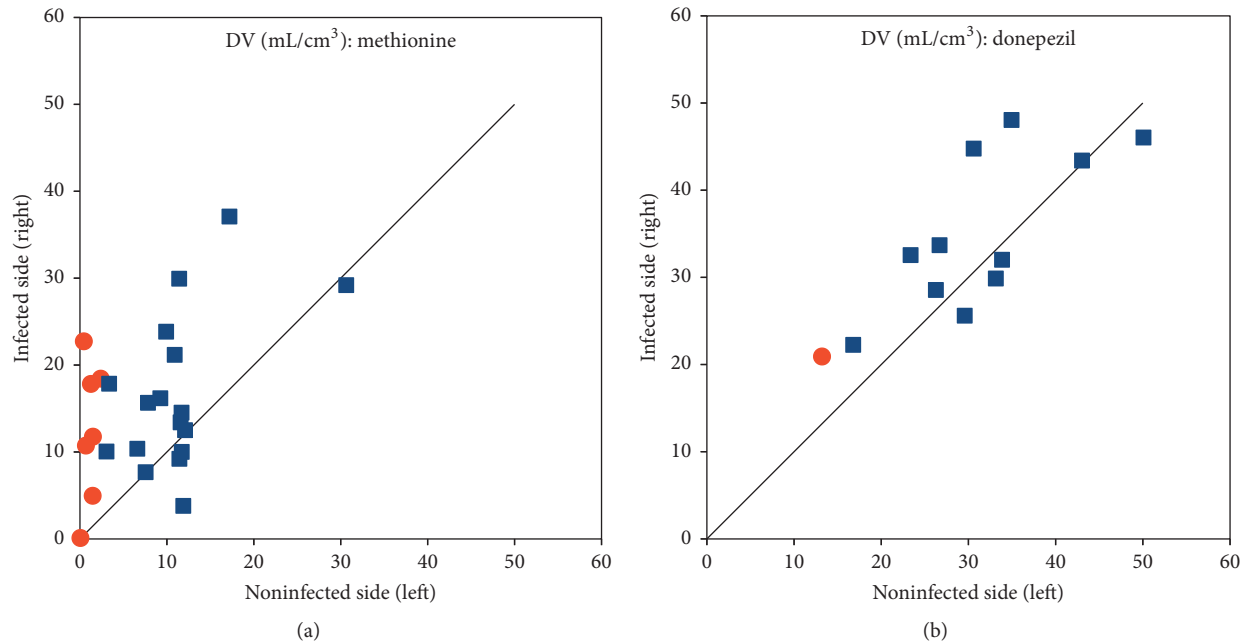


FIGURE 14: Comparison of the distribution volume DV in infected (right) and noninfected (left) limbs. Bone is represented by blue squares and soft tissue by red circles. The line is the identity line ($y = x$). (a) shows $[^{11}\text{C}]$ methionine, and (b) shows $[^{11}\text{C}]$ donepezil.

case reports [12, 13], $[^{11}\text{C}]$ methionine could be useful for brain infection imaging, where $[^{18}\text{F}]$ FDG suffers from the high physiological uptake in healthy brain tissue.

The uptake curves in both infected and noninfected tissues appear quite stable after approximately 10–15 minutes (Figure 8), indicating that static imaging could be performed starting at this time.

4.4. $[^{11}\text{C}]$ Donepezil. Metabolite-corrected $[^{11}\text{C}]$ donepezil could be modelled with the ITCM model. However, the K_1 parameter was systematically higher than plasma (and blood) perfusion, paradoxically indicating an extraction fraction above 100% (Figure 10). We consider this to be an indication that at least one of the radioactive metabolite products of $[^{11}\text{C}]$ donepezil has marked uptake along with the main tracer. Indeed, Funaki et al. [46] reported that affinity of the M1 metabolite for AChE is almost as high as the affinity of donepezil for AChE; the M1 metabolite is radioactive when the parent tracer is $[5\text{-}^{11}\text{C}\text{-methoxy}]$ donepezil. In a steady-state study with a regular administration of donepezil, Meier-Davis et al. [47] found M1 to be relatively more prominent in minipigs than in humans and rats.

Meier-Davis et al. [47] also found the overall level of metabolites to be higher in the pigs. This species difference may explain why we found relatively fast metabolization of $[^{11}\text{C}]$ donepezil (Figure 4), in contrast to the human study by Hiraoka et al. [48] who saw only minor metabolism of $[^{11}\text{C}]$ donepezil (>85% remaining after 30 minutes) and therefore did not need metabolite correction. Also, Hiraoka et al. found the rev2TCM to be unequivocally better than the ITCM, while our study finds the distinction less clear. As noted, however, their input functions were not corrected for metabolites.

The strong correlation between first-pass uptake and perfusion (Figure 10) indicates flow-limited uptake of $[^{11}\text{C}]$ donepezil, although the effect is less evident for distribution volume (Figure 13).

Regarding $[^{11}\text{C}]$ donepezil as an infection tracer, our data did show an overall higher first-pass uptake in the infected lesions and a strong correlation with perfusion (Figure 10), while the DV was only slightly higher in the infected sites than in the corresponding noninfected locations (Figure 14), and the difference was not statistically significant.

4.5. Limitations. The pig model was developed as a model for osteomyelitis, for which reason only relatively few soft tissue lesions were available, limiting the scope of the study as a general infection study. For $[^{68}\text{Ga}]$ Ga-citrate, only relatively limited data were available.

5. Conclusion

$[^{18}\text{F}]$ FDG was reasonably well described by the irr2TCM (irreversible uptake, three rate constants) for the 60-minute length studied, and, for both bone and soft tissue, $[^{18}\text{F}]$ FDG showed increased uptake in infected tissue (Figure 12). The correlation with perfusion indicated that the tracer is mainly flow-limited.

$[^{68}\text{Ga}]$ Ga-citrate was also well described by irrTCM but showed very little or very slow uptake, which was a limitation for infection imaging. The difference between infected and noninfected sites appeared to be higher in soft tissue rather than bone lesions, but too little data were available to draw a conclusion (Figure 12). Uptake was slow and diffusion-limited. To allow time for uptake, “late” imaging is preferable,

but not so late that the radionuclide has decayed. Imaging at 120 minutes p.i. appears a good compromise.

[¹¹C]methionine needed a rev2TCM (reversible uptake, four rate constants) for modelling. Despite considerable metabolism during the 40 minutes modelled, the K_1 , k_2 , and k_3 rate constants were only slightly affected if an uncorrected input function was used, that is, only k_4 was markedly affected. In a majority of cases, the uptake (measured as the distribution volume) was elevated in the infected tissue compared to the noninfected tissue (Figure 14), but the difference was less than for [¹⁸F]FDG (measured as the net uptake rate, Figure 12). Uptake appeared flow-limited. Based on the activity curves, imaging at ~15 minutes p.i. appears favourable.

[¹¹C]donepezil could be modelled with a 1TCM (reversible uptake, two rate constants) but required metabolite correction—at least in this juvenile, porcine model. The uptake of labelled metabolite products appeared to be nonnegligible. Based on the present study, the uptake of [¹¹C]donepezil in osteomyelitis seems to depend more on perfusion (flow-limited) than on differences between infected and noninfected tissues. For soft tissue infection, too few data were available to draw a conclusion.

Overall, among the studied PET tracers [¹⁸F]FDG showed optimal characteristics for the detection of infectious foci. [⁶⁸Ga]Ga-citrate and [¹¹C]donepezil were not found to be useful for imaging of osteomyelitis. For soft tissue, [¹¹C]methionine and perhaps [⁶⁸Ga]Ga-citrate may be applicable to quantify different aspects of inflammatory or infectious processes, while too few soft tissue data on [¹¹C]donepezil were available to draw any conclusions.

Disclosure

The funder had no influence on the design, analysis, interpretation, or the writing of the manuscript.

Conflicts of Interest

The authors declare no conflicts of interest.

Acknowledgments

The authors are grateful for the support provided by the technical staff at Aarhus University Hospital, Aalborg University Hospital, and Copenhagen University. Vesa Oikonen is acknowledged for stimulating discussions and helping with the modelling software. This work was supported by the Danish Council for Independent Research, Technology and Production Sciences, Grant no. 0602-01911B (11-107077).

References

- [1] S. Basu, T. Chryssikos, S. Moghadam-Kia, H. Zhuang, D. A. Torigian, and A. Alavi, "Positron emission tomography as a diagnostic tool in infection: present role and future possibilities," *Seminars in Nuclear Medicine*, vol. 39, no. 1, pp. 36–51, 2009.
- [2] S. Ahmad Sarji, "Physiological uptake in FDG PET simulating disease," *Biomedical Imaging and Intervention Journal*, vol. 2, no. 4, 2006.
- [3] O. L. Nielsen, P. Afzelius, D. Bender et al., "Comparison of autologous ¹¹¹In-leukocytes, ¹⁸F-FDG, ¹¹C-methionine, ¹¹C-PK11195 and ⁶⁸Ga-citrate for diagnostic nuclear imaging in a juvenile porcine haematogenous staphylococcus aureus osteomyelitis model," *American Journal of Nuclear Medicine and Molecular Imaging*, vol. 5, no. 2, pp. 169–182, 2015.
- [4] P. Afzelius, O. L. Nielsen, A. K. O. Alstrup et al., "Biodistribution of the radionuclides ¹⁸F-FDG, ¹¹C-methionine, ¹¹C-PK11195, and ⁶⁸Ga-citrate in domestic juvenile female pigs and morphological and molecular imaging of the tracers in hematogenously disseminated *Staphylococcus aureus* lesions," *American Journal of Nuclear Medicine and Molecular Imaging*, vol. 6, no. 1, pp. 42–58, 2016.
- [5] P. Afzelius, A. K. O. Alstrup, H. C. Schönheyder et al., "Utility of ¹¹C-methionine and ¹¹C-donepezil for imaging of *Staphylococcus aureus* induced osteomyelitis in a juvenile porcine model: comparison to autologous ¹¹¹In-labelled leukocytes, ^{99m}Tc-DPD, and ¹⁸F-FDG," *American Journal of Nuclear Medicine and Molecular Imaging*, vol. 6, no. 6, pp. 286–300, 2016.
- [6] L. Jødal, O. L. Nielsen, P. Afzelius, A. K. O. Alstrup, and S. B. Hansen, "Blood perfusion in osteomyelitis studied with [¹⁵O]water PET in a juvenile porcine model," *EJNMMI Research*, vol. 7, no. 1, article no. 4, 2017.
- [7] S. B. Jensen, K. M. Nielsen, D. Mewis, and J. Kaufmann, "Fast and simple one-step preparation of ⁶⁸Ga citrate for routine clinical PET," *Nuclear Medicine Communications*, vol. 34, no. 8, pp. 806–812, 2013.
- [8] T. J. Mäkinen, P. Lankinen, T. Pöyhönen, J. Jalava, H. T. Aro, and A. Roivainen, "Comparison of ¹⁸F-FDG and ⁶⁸Ga PET imaging in the assessment of experimental osteomyelitis due to *Staphylococcus aureus*," *European Journal of Nuclear Medicine and Molecular Imaging*, vol. 32, no. 11, pp. 1259–1268, 2005.
- [9] C. Nanni, C. Errani, and L. Boriani, "⁶⁸Ga-citrate PET/CT for evaluating patients with infections of the bone: preliminary results," *Journal of Nuclear Medicine*, vol. 51, no. 12, pp. 1932–1936, 2010.
- [10] M. Vorster, A. Maes, A. Jacobs et al., "Evaluating the possible role of ⁶⁸Ga-citrate PET/CT in the characterization of indeterminate lung lesions," *Annals of Nuclear Medicine*, vol. 28, no. 6, pp. 523–530, 2014, <http://link.springer.com/10.1007/s12149-014-0842-9>.
- [11] S. Zhao, Y. Kuge, M. Kohanawa et al., "Usefulness of ¹¹C-methionine for differentiating tumors from granulomas in experimental rat models: a comparison with ¹⁸F-FDG and ¹⁸F-FLT," *Journal of Nuclear Medicine*, vol. 49, no. 1, pp. 135–141, 2008.
- [12] K. Hirata, T. Shiga, N. Fujima et al., "¹¹C-methionine positron emission tomography may monitor the activity of encephalitis," *Acta Radiologica*, vol. 53, no. 10, pp. 1155–1157, 2012.
- [13] Y. Maeda, H. Oguni, Y. Saitou et al., "Rasmussen syndrome: multifocal spread of inflammation suggested from MRI and PET findings," *Epilepsia*, vol. 44, no. 8, pp. 1118–1121, 2003.
- [14] M. Morooka, K. Kubota, H. Kadowaki et al., "¹¹C-methionine PET of acute myocardial infarction," *Journal of Nuclear Medicine*, vol. 50, no. 8, pp. 1283–1287, 2009.
- [15] H. Sugimoto, H. Ogura, Y. Arai, Y. Iimura, and Y. Yamanishi, "Research and development of donepezil hydrochloride, a

- new type of acetylcholinesterase inhibitor," *Japanese Journal of Pharmacology*, vol. 89, no. 1, pp. 7–20, 2002.
- [16] K. Kawashima, T. Fujii, Y. Moriwaki, and H. Misawa, "Critical roles of acetylcholine and the muscarinic and nicotinic acetylcholine receptors in the regulation of immune function," *Life Sciences*, vol. 91, no. 21–22, pp. 1027–1032, 2012.
- [17] T. Fujii, Y. Watanabe, K. Fujimoto, and K. Kawashima, "Expression of acetylcholine in lymphocytes and modulation of an independent lymphocytic cholinergic activity by immunological stimulation," *Biogenic Amines*, vol. 17, no. 4–6, pp. 373–386, 2003.
- [18] N. P. Jørgensen, A. K. O. Alstrup, F. V. Mortensen et al., "Cholinergic PET imaging in infections and inflammation using ^{11}C -donepezil and ^{18}F -FE0BV," *European Journal of Nuclear Medicine and Molecular Imaging*, vol. 44, no. 3, pp. 449–458, 2017.
- [19] L. K. Johansen, J. Koch, D. Frees et al., "Pathology and Biofilm Formation in a Porcine Model of Staphylococcal Osteomyelitis," *Journal of Comparative Pathology*, vol. 147, no. 2–3, pp. 343–353, 2012.
- [20] L. K. Johansen, E. L. Svalastoga, D. Frees et al., "A new technique for modeling of hematogenous osteomyelitis in pigs: Inoculation into femoral artery," *Journal of Investigative Surgery*, vol. 26, no. 3, pp. 149–153, 2013.
- [21] A. K. O. Alstrup, K. M. Nielsen, H. C. Schönheyder et al., "Refinement of a hematogenous localized osteomyelitis model in pigs," *Scandinavian Journal of Laboratory Animal Science*, vol. 42, no. 3, pp. 1–4, 2016.
- [22] L. Jødal, S. B. Hansen, and S. B. Jensen, "Impact of contamination with long-lived radionuclides on PET kinetics modelling in multitracer studies," *Nuclear Medicine Communications*, vol. 37, no. 8, pp. 818–824, 2016.
- [23] P. Som, H. L. Atkins, D. Bandyopadhyay et al., "A fluorinated glucose analog, 2-fluoro-2-deoxy-D-glucose (F-18): Nontoxic tracer for rapid tumor detection," *Journal of Nuclear Medicine*, vol. 21, no. 7, pp. 670–675, 1980.
- [24] M.-F. Tsan, "Mechanism of gallium-67 accumulation in inflammatory lesions," *Journal of Nuclear Medicine*, vol. 26, no. 1, pp. 88–92, 1985.
- [25] J. Van den Hoff, W. Burchert, W. Muller-Schauenburg, G.-J. Meyer, and H. Hundeshagen, "Accurate local blood flow measurements with dynamic PET: Fast determination of input function delay and dispersion by multilinear minimization," *Journal of Nuclear Medicine*, vol. 34, no. 10, pp. 1770–1777, 1993.
- [26] C. S. Patlak, R. G. Blasberg, and J. D. Fenstermacher, "Graphical evaluation of blood-to-brain transfer constants from multiple-time uptake data," *Journal of Cerebral Blood Flow and Metabolism*, vol. 3, no. 1, pp. 1–7, 1983.
- [27] C. S. Patlak and R. G. Blasberg, "Graphical Evaluation of Blood-to-Brain Transfer Constants from Multiple-Time Uptake Data. Generalizations," *Journal of Cerebral Blood Flow & Metabolism*, vol. 5, no. 4, pp. 584–590, 2016.
- [28] R. B. Innis, V. J. Cunningham, and J. Delforge, "Consensus nomenclature for *in vivo* imaging of reversibly binding radioligands," *Journal of Cerebral Blood Flow & Metabolism*, vol. 27, no. 9, pp. 1533–1539, 2007.
- [29] J. Logan, J. S. Fowler, N. D. Volkow et al., "Graphical analysis of reversible radioligand binding from time-activity measurements applied to [^{11}C -methyl]-(-)-cocaine PET studies in human subjects," *Journal of Cerebral Blood Flow & Metabolism*, vol. 10, no. 5, pp. 740–747, 1990.
- [30] J. Logan, "Graphical analysis of PET data applied to reversible and irreversible tracers," *Nuclear Medicine and Biology*, vol. 27, no. 7, pp. 661–670, 2000.
- [31] F. Thiele and R. Buchert, "Evaluation of non-uniform weighting in non-linear regression for pharmacokinetic neuroreceptor modelling," *Nuclear Medicine Communications*, vol. 29, no. 2, pp. 179–188, 2008.
- [32] M. Yaqub, R. Boellaard, M. A. Kroppholler, and A. A. Lammermsma, "Optimization algorithms and weighting factors for analysis of dynamic PET studies," *Physics in Medicine and Biology*, vol. 51, no. 17, article no. 007, pp. 4217–4232, 2006.
- [33] TPC. List of applications in TPCCLIB. *Turku PET Centre web site*. Available from: <http://www.turkupetcentre.net/programs/doc/index.html>.
- [34] H. Akaike, "A new look at the statistical model identification," *IEEE Transactions on Automatic Control*, vol. 19, pp. 716–723, 1974.
- [35] K. P. Burnham and D. R. Anderson, "Multimodel inference: understanding AIC and BIC in model selection," *Sociological Methods and Research*, vol. 33, no. 2, pp. 261–304, 2004.
- [36] L. Sokoloff, M. Reivich, and C. Kennedy, "The [^{14}C]deoxyglucose method for the measurement of local cerebral glucose utilization: theory, procedure, and normal values in the conscious and anesthetized albino rat," *Journal of Neurochemistry*, vol. 28, no. 5, pp. 897–916, 1977.
- [37] M. E. Phelps, S. C. Huang, E. J. Hoffman, C. Selin, L. Sokoloff, and D. E. Kuhl, "Tomographic measurement of local cerebral glucose metabolic rate in humans with (F-18)2-fluoro-2-deoxy-D-glucose: validation of method," *Annals of Neurology*, vol. 6, no. 5, pp. 371–388, 1979.
- [38] T. Schroeder, M. F. Vidal Melo, and J. G. Venegas, "Analysis of 2-[Fluorine-18]-Fluoro-2-deoxy-D-glucose uptake kinetics in PET studies of pulmonary inflammation," *Academic Radiology*, vol. 18, no. 4, pp. 418–423, 2011.
- [39] S. Chefer, D. Thomasson, J. Seidel et al., "Modeling [^{18}F]-FDG lymphoid tissue kinetics to characterize nonhuman primate immune response to Middle East respiratory syndrome-coronavirus aerosol challenge," *EJNMMI Research*, vol. 5, no. 1, article no. 65, pp. 1–11, 2015, <http://www.ejnmmires.com/content/5/1/65>.
- [40] T. Schroeder, M. F. Vidal Melo, G. Musch, R. S. Harris, J. G. Venegas, and T. Winkler, "Modeling Pulmonary Kinetics of 2-Deoxy-2- [^{18}F]fluoro-d-glucose During Acute Lung Injury," *Academic Radiology*, vol. 15, no. 6, pp. 763–775, 2008.
- [41] V. Kumar, D. K. Boddeti, S. G. Evans, F. Roesch, and R. Howman-Giles, "Potential use of ^{68}Ga -apo-transferrin as a PET imaging agent for detecting *Staphylococcus aureus* infection," *Nuclear Medicine and Biology*, vol. 38, no. 3, pp. 393–398, 2011.
- [42] J. T. Thackeray, J. P. Bankstahl, Y. Wang et al., "Targeting post-infarct inflammation by PET imaging: comparison of ^{68}Ga -citrate and ^{68}Ga -DOTATATE with ^{18}F -FDG in a mouse model," *European Journal of Nuclear Medicine and Molecular Imaging*, vol. 42, no. 2, pp. 317–327, 2014.
- [43] V. Kumar and D. K. Boddeti, " ^{68}Ga -radiopharmaceuticals for PET imaging of infection and inflammation," in *Theranostics, Gallium-68, and Other Radionuclides*, R. P. Baum and F. Rösch, Eds., pp. 189–219, Springer, Berlin, Heidelberg, 2013, <http://link.springer.com/10.1007/978-3-642-27994-2.11>.

- [44] E. K. J. Pauwels, V. R. McCready, J. H. M. B. Stoot, and D. F. P. Van Deurzen, "The mechanism of accumulation of tumour-localising radiopharmaceuticals," *European Journal of Nuclear Medicine*, vol. 25, no. 3, pp. 277–305, 1998.
- [45] A. J. Fischman, Y. M. Yu, E. Livni et al., "Muscle protein synthesis by positron-emission tomography with L-[methyl-¹¹C]methionine in adult humans," *Proceedings of the National Academy of Sciences of the United States of America*, vol. 95, no. 22, pp. 12793–12798, 1998.
- [46] Y. Funaki, M. Kato, R. Iwata et al., "Evaluation of the binding characteristics of [5-¹¹C-methoxy]donepezil in the rat brain for in vivo visualization of acetylcholinesterase," *Journal Pharmacological Sciences*, vol. 91, no. 2, pp. 105–112, 2003.
- [47] S. R. Davis and R. Murgasova, "Comparison of metabolism of donepezil in rat, mini-pig and human, following oral and transdermal administration, and in an in vitro model of human epidermis," *Journal of Drug Metabolism & Toxicology*, vol. 3, no. 4, 2012.
- [48] K. Hiraoka, N. Okamura, Y. Funaki et al., "Quantitative analysis of donepezil binding to acetylcholinesterase using positron emission tomography and [5-¹¹C-methoxy]donepezil," *NeuroImage*, vol. 46, no. 3, pp. 616–623, 2009.

Review Article

TSPO PET Imaging: From Microglial Activation to Peripheral Sterile Inflammatory Diseases?

Bérenger Largeau,¹ Anne-Claire Dupont,^{1,2} Denis Guilloteau,^{1,2}
Maria-João Santiago-Ribeiro,^{1,2} and Nicolas Arlicot^{1,2}

¹CHRU Tours, 2 Boulevard Tonnellé, 37044 Tours, France

²Institut National de la Santé et de la Recherche Médicale U930, 10 Boulevard Tonnellé, 37032 Tours, France

Correspondence should be addressed to Bérenger Largeau; berenger.largeau@etu.univ-tours.fr

Received 26 May 2017; Revised 1 August 2017; Accepted 7 August 2017; Published 25 September 2017

Academic Editor: Anne Roivainen

Copyright © 2017 Bérenger Largeau et al. This is an open access article distributed under the Creative Commons Attribution License, which permits unrestricted use, distribution, and reproduction in any medium, provided the original work is properly cited.

Peripheral sterile inflammatory diseases (PSIDs) are a heterogeneous group of disorders that gathers several chronic insults involving the cardiovascular, respiratory, gastrointestinal, or musculoskeletal system and wherein inflammation is the cornerstone of the pathophysiology. In PSID, timely characterization and localization of inflammatory *foci* are crucial for an adequate care for patients. In brain diseases, *in vivo* positron emission tomography (PET) exploration of inflammation has matured over the last 20 years, through the development of radiopharmaceuticals targeting the translocator protein-18 kDa (TSPO) as molecular biomarkers of activated microglia. Recently, TSPO has been introduced as a possible molecular target for PSIDs PET imaging, making this protein a potential biomarker to address disease heterogeneity, to assist in patient stratification, and to contribute to predicting treatment response. In this review, we summarized the major research advances recently made in the field of TSPO PET imaging in PSIDs. Promising preliminary results have been reported in bowel, cardiovascular, and rheumatic inflammatory diseases, consolidated by preclinical studies. Limitations of TSPO PET imaging in PSIDs, regarding both its large expression in healthy peripheral tissues, unlike in central nervous system, and the production of peripheral radiolabeled metabolites, are also discussed, regarding their possible consequences on TSPO PET signal's quantification.

1. The Sterile Inflammatory Response and PET Imaging of Inflammation

Inflammation and its protagonist, inflammatory cells, act as the initial host defense to struggle against infection and injury. Immune system diseases can be dichotomized into autoimmune disorders, in which several actors lead to intrinsic hyperactivity of sensor/pattern-recognition receptor function, causing exacerbate and dysregulated immune response [1] and immunodeficiency diseases (i.e., inherited/primary or acquired/secondary), characterized by an inability of immune system to contain infectious disease and cancer development [2]. In both cases, the inflammatory processes are unappropriated; this explains the paradoxical relationship between immunodeficiency diseases and autoimmunity [3]. In inflammatory conditions, following exposure to aseptic

stimulus involving physical chemical or metabolic signal such as burns, trauma, and dead cells, a cascade of response will be initiated by the release of local chemokines, interleukins, and prostaglandins, which are well-known proinflammatory mediators [4, 5]. Monocytes, macrophages, dendritic cells, and neutrophils are first-line immune effectors located in the interface between innate and adaptive immunity. Apart from autoimmunity disorders, noninfectious/sterile inflammatory diseases include various conditions where the leading cause of inflammation is acute and/or chronic exposure to irritant particles [5]. These sterile stimuli are different in nature and can be induced by drug therapy [6], alcohol consumption [7], exogenous particulates such as silica dioxide [8], asbestos [8], cigarette smoke [9], or endogenous particulates as well as monosodium urate [10], amyloid- β [11], and cholesterol [12]. Macrophages are a key player in the pathophysiology

of sterile etiology, autoimmunity disorders [13], and irritant particles mediated diseases [5]. Macrophage activation starts with a proinflammatory phase, called M1 state. Sterile injuries provoke inflammation similar to injury caused by pathogens but M1b macrophage phenotype predominantly develop, before being polarized into M2 phenotype which induce anti-inflammatory/profibrotic response [14]. Given the fact that macrophages play a crucial role in sterile inflammatory processes, macrophage imaging appears to be a promising approach to assess, better characterize, and improve the diagnosis of disorders related to sterile inflammation.

Diagnosis of most peripheral sterile inflammatory diseases (PSIDs) is based on history, clinical symptoms, biology, serology, and conventional imaging technique such as radiological analysis or magnetic resonance imaging (MRI). Concerning its signs and clinical features, the inflammatory process is very stereotypic and nonspecific [5] to such an extent that the only symptoms can be asthenia, arthralgia, and fever. Furthermore, in front of inflammatory syndrome, clinicians have to make a decision about an infectious or sterile etiology and, sometimes, practitioners in internal medicine have recourse to trial corticosteroid therapy or empiric antibiotic therapy to statute despite the risk of complicating ulterior diagnosis [15]. Indeed, corticosteroids or anti-infectious drug could conceal the pathogenic process and therefore make uninformative conventional imaging techniques due to a lack of sensitivity, so the residual disease remains inaccessible. Similarly, inflammatory *foci* cannot be detected in the early phase of development because of the lack of substantial anatomical changes at this time. In front of several conventional exam limitations (e.g., invasive, lack of repeatability) and in order to investigate PSIDs by a deeper approach and to access pathophysiology, the use of molecular imaging and especially PET imaging has increased significantly in recent years. PET is a molecular and functional imaging modality, which permits repeated and noninvasive determination and quantification of specific biological and pharmacological processes [16] whose interest is in early diagnosis and to monitor/follow up the residual disease is promising. ^{18}F -FDG represents the most widely used PET tracer and many authors have elucidated in detail relationship between inflammatory response, local hyperaemia, and hypervascularisation and uptake of ^{18}F -FDG [17, 18]. Various PSIDs have been investigated with ^{18}F -FDG including atherosclerosis [19], vasculitis [20], valvular inflammation [21], myocardial inflammation [22], rheumatoid arthritis [23], and Crohn's disease [24]. Nevertheless, ^{18}F -FDG is a glucose analog which indicates an increase of glucose consumption, which in itself can be indicative of other on-going processes such as cancer, cell regeneration, or muscle contraction as seen in peristalsis. Furthermore, another limitation concerning its pharmacokinetic, the renal pathway by which ^{18}F -FDG is eliminated, obstructs the image quantification [25].

Choline as an important precursor of membrane phospholipids has been labelled to image inflammatory diseases such as atherosclerosis [26–28] with a greater sensitivity in detecting atherosclerotic plaques than ^{18}F -FDG [28].

Besides metabolic PET tracers of inflammatory cells (i.e., ^{18}F -FDG and ^{18}F -Choline), radioligands have been developed to evaluate more accurately peripheral sterile inflammatory processes. Among these, membrane receptor such as 18 kDa translocator protein (TSPO) and B lymphocyte CD20 antigen [29], cytokines like cyclooxygenase subtype 2 [30], matrix metalloproteinase [31], interleukin-2 [32] or endothelial adhesion proteins such integrin $\alpha\text{v}\beta\text{3}$ [33], vascular adhesion protein-1 [34], and vascular cell adhesion molecule-1 [35] have been targeted. In this review, we focus on the most recent preclinical and clinical applications of TSPO PET imaging in PSIDs and discuss the potential added value in the clinical practice.

2. TSPO PET Tracers

TSPO is a highly hydrophobic five-transmembrane domain protein mainly situated in the outer mitochondrial membrane and is highly expressed in macrophages [36, 37]. TSPO is widely distributed in most peripheral organs including kidneys, nasal epithelium, adrenal glands, lungs, and heart, whilst the highest concentrations are in the steroid producing tissues, and is also minimally expressed in resting microglial cells in the healthy brain [38]. Numerous TSPO PET tracers have been developed and used mainly for the imaging of neuroinflammation [39].

In addition to many endogenous compounds like cholesterol or porphyrin, TSPO binds a range of synthetic ligands. Historically, the benzodiazepine ^{11}C -Ro5-4864 was the first ligand able to discriminate peripheral from central benzodiazepine receptors [40]. Over the past few years, several structure activity relationship studies have established that four main domains are necessary for a ligand to interact with the TSPO, three major lipophilic regions, and one hydrogen-bond donor group [41]. Thus, several classes of TSPO radioligands have been synthesized, with, for most of them, the availability of compounds radiolabelled with carbon-1 (^{11}C) or fluorine-18 (^{18}F). The most widely used TSPO PET radiopharmaceutical, namely, ^{11}C -(R)-PK11195, an isoquinoline carboxamide developed in the early 1980s, was the first nonbenzodiazepine type compound identified to bind to TSPO with high affinity (human dissociation constant, $K_d = 2 \text{ nM}$) [42]. Despite having been tagged as the gold standard of TSPO ligands, ^{11}C -(R)-PK11195 has several drawbacks including the short half-life of carbon-11, a low brain bioavailability, and a poor signal-to-noise ratio due to high nonspecific binding [43]. To counteract these limitations, there has been a great effort for the development of second-generation TSPO PET radiotracers. Among them, the derivatives of phenoxyarylacetamides (^{11}C -DAA1106, ^{11}C -PBR28, ^{11}C -PBR06, and ^{18}F -FEPPA) [44–47], designed from a chemical structure based on the opening of the diazepine ring of Ro5-4864, the derivatives of imidazopyridines (^{11}C -CLINME), and the derivatives of pyrazolopyrimidines (^{18}F -DPA-714) [48] are included.

Furthermore, a single nucleotide polymorphism in the TSPO gene (rs6971) leading to an amino-acid substitution (A147T) has been identified [49]. This polymorphism affects

TABLE 1

Applications	Population/Animal models	Radioligand	Main findings	Ref.
Preclinical	(i) TSPO PET on day 8 after DSS- and TNBS-induced IBD in rats (ii) 6 rats were followed up over 22 days	^{18}F -DPA-714	(i) Significantly increased tracer uptake in the rat colon in both groups, DSS and TNBS, compared to controls (ii) Increased tracer binding until day 8/10 then tracer uptake decreased slowly	Bernards et al. (2014) [25]

DSS, dextran sodium sulfate; IBD, inflammatory bowel disease; TNBS, trinitrobenzenesulfonic acid.

the binding affinity properties of the most of TSPO with a huge heterogeneity in PET images and their associated quantitative data. Three distinct binder statuses have been identified: HAB, high- (A/A; ~70%), MAB, mixed- (A/T; ~21%), and LAB, low-affinity binders (T/T; ~9%) [50]. The fact that the second-generation radiopharmaceuticals have been found to be sensitive to this polymorphism leads searchers to develop rs6971-insensitive radioligands. For this purpose, ^{18}F -GE180, a third-generation TSPO tracers, was evaluated and seemed to be less sensitive to the TSPO-binding affinity status than the second generation [51]. Unfortunately, the small sample size and the exclusion of the LAB from this preliminary study led do not allow concluding that ^{18}F -GE180 is insensitive to the polymorphism. Then, a new analog of ^{11}C -(R)-PK11195, called ^{11}C -ER176, showed little sensitivity to rs6971 when tested in vitro and had high specific binding in monkey brain [52]. Nonetheless, the clinical relevance of this third-generation compound remains to be confirmed.

3. TSPO PET Imaging of PSIDs

3.1. Inflammatory Bowel Diseases (See Table 1). Although the etiology of inflammatory bowel diseases (IBDs), including Crohn's disease (CD) and ulcerative colitis (UC), is still unclear, it is widely accepted that both result from a mucosal immune response dysregulation in genetically predisposed individuals, for which susceptibility to IBD is mainly determined by complex interactions of environmental and genetic factors [53–55]. IBDs are characterized by various aspects of the inflammatory response, ranging from acute to chronic stages, and, in many cases, describe a cyclic evolution where attacks are interspersed with gastrointestinal stable periods. The natural history of the IBDs usually progresses to include strictures, fistulas, and abscesses [56]. Whereas in CD the whole gastrointestinal tract can be affected even if there is a predilection for ileocolonic involvement, UC is reduced to the caecum, colon, and rectum [57]. Localizing accurately the inflamed tissues is one criteria permitting differential diagnosis between the different types of IBDs and other diseases [58, 59]. Presently, the diagnostic approach relies on various exams ranging from clinical symptoms, such as bloody diarrhea, abdominal pain, asthenia, and weight loss, to serology, endoscopic exploration, radiological analysis, and nuclear medical investigations [25]. Nevertheless, 10 to 15% of all colorectal IBDs cases cannot be classified as UC or CD [60]. In order to provide information concerning

the inflammatory processes in IBD, ^{18}F -FDG PET imaging has been used in preclinical studies [25, 61, 62] and clinical studies [61, 63–67], especially in pediatric populations [64, 65, 68], and exhibited good diagnostic performances in patients with suspected IBD [58, 69]. Despite the well-known TSPO overexpression in colon cancer [70] and the knowledge that TSPO regulates the growth of colorectal cancer cells [71] which is also an unfavorable prognostic factor in stage III colorectal cancer [72], the involvement of TSPO in IBDs and dysplasia has not yet been completely investigated. After 7 days of treatment by dextran sodium sulfate (DSS), in a way to induce IBD in a rat model, Ostuni and colleagues [73] reported a TSPO overexpression, assessed by immunohistochemistry, in the rat colon of treated animals. In DSS model, whereas the increase of ^{18}F -FDG colon uptake did not reach a significance level, ^{18}F -DPA-714 colon binding showed a significant increase, compared to healthy animals. In addition, the relationship between tissue expression of TSPO, objectified by immunohistochemistry, and ^{18}F -DPA-714 uptake provides the proof-of-concept that TSPO PET radioligand can be used to evaluate dynamically peripheral inflammation [25]. These findings lead us to think that TSPO PET imaging could serve as a more precocious biomarker than ^{18}F -FDG to highlight the inflammatory processes of IBDs. Regarding the inflammatory cascade of IBDs, a recent study established the responsibility of the interleukin-33 (IL-33) pathway by modulating macrophages phenotype in IBDs [74]. Indeed, the authors demonstrated that IL-33 is involved in M2 macrophage polarization in inflamed mucosal samples from patients with IBD. Moreover, serum IL-33 levels were significantly lower in IBD's patients than those in healthy volunteers. Serum soluble suppression of tumorigenicity-2 (sST2) levels and its soluble receptor were significantly correlated with the pMayo score in UC patients but not in CD, supporting evidences that UC is a disorder linked to Th2-hyperpolarization in contrast to CD, which is rather Th1-derived [75].

3.2. Liver Diseases (See Table 2). The expression of TSPO in the liver of healthy humans is usually low [76, 77]. Recent evidences suggest that TSPO might be contribute to the liver damage and alcoholic hepatitis progression. Indeed, TSPO gene is upregulated in alcohol hepatitis and appears to be involved in various biological processes which are determinant in the pathophysiology of alcoholic liver disease such as regulation of reactive oxygen species, response to alcohol, negative regulation of nitric oxide pathway, and regulation of

TABLE 2

Applications	Population/animal models	Radioligand	Main findings	Ref.
Preclinical	6 mice per each group 2-, 4-, and 8-week MCD-fed mice versus control mice	^{18}F -FEDAC	In 4-week MCD livers, higher binding of tracer was observed at some <i>loci</i> in the right lobe compared to the left liver lobe Significantly increased uptake ratios of liver to blood in 2-, 4-, and 8-week MCD-fed mice, compared to controls Strong correlation between uptake ratio of tracer binding and NAFLD activity score was found during NAFLD progression	Xie et al. (2012) [79]
Preclinical	4 rats per each group after 2, 4, 6, and 8 weeks of CCl_4 treatment versus control rats	^{18}F -FEDAC	Significantly higher liver tracer SUV in all treatment groups, compared to controls Tracer binding positively correlated with CCl_4 treatment duration and severity of liver damage	Hatori et al. (2015) [80]

MCD, methionine and choline deficient; NAFLD, nonalcoholic fatty liver disease; SUV, standardized uptake value.

necrotic cell death [78]. Tissue analysis revealed more serious steatotic aggregates and necroinflammatory infiltration in the higher uptake region of ^{18}F -FEDAC. Autoradiography experiments [79, 80] supported *in vivo* PET data where TSPO tracer binding was not homogeneously distributed in the livers with nonalcoholic fatty liver disease (NAFLD) [79] and in the fibrotic livers (induced by carbon tetrachloride treatment) [80]. Analysis association between ^{18}F -FEDAC binding and NAFLD activity score is in consonance with *in vitro* findings where TSPO overexpression was reported in activated hepatic stellate cells [81] and in the adipocytes of stressed rats with adipocytes aggregates and neoangiogenesis process [82]. TSPO PET tracer uptake increased in parallel with liver disease severity whether it is in NAFLD [79] or in fibrosis liver models [80]. Positively correlation between hepatic TSPO and (transforming growth factor) TGF- β 1/(tumor necrosis factor) TNF- α mRNA expression [80] suggests that macrophage M1 and M2 phenotypes intervene during liver fibrosis development [83]. Complementary clinical studies with various liver diseases characterized by inflammatory processes (e.g., viral hepatitis, cholestatic hepatitis, autoimmune hepatitis, and Wilson's disease) are required to evaluate the ability of differential diagnosis of TSPO PET imaging.

3.3. Inflammatory Lung Diseases (See Table 3). In contrast to nonspecific current methods (e.g., chest radiography and computed tomography), TSPO PET imaging could potentially give quantitative information about macrophage trafficking and kinetics, in order to evaluate treatment response and contribute to our understanding of the pathophysiology of lung noninfectious inflammatory processes [84]. Moreover, invasive methods (e.g., lung biopsy and bronchoalveolar lavage) are unacceptable for repeat measurement in the context of longitudinal assessment for lung diseases [85]. Concerning single photon emission computed tomography (SPECT) scanning, although gamma-scintigraphy with ^{111}In -labelled granulocytes has been used to monitor migration of polynuclear cells into the lungs [86, 87], its metabolic activation and phenotype remain inaccessible with this nuclear exam [88].

A major concern for the meaning of this TSPO PET imaging approach is the multicellular expression of TSPO in the human lungs. In addition to resident alveolar macrophages, submucosal glands, pneumocytes, and epithelial lining of the airways expression of TSPO have been reported [89, 90] but not neutrophilic expression [91]. Asthma and chronic obstructive pulmonary disease (COPD) are two obstructive respiratory conditions where an important accumulation of inflammatory cells in the respiratory tract takes place and leads to chronic symptoms with periodic acute exacerbations of both asthma and COPD. The pathophysiology of these lung inflammatory disorders is distinct, involving rather excessive formation of eosinophils, mast cells, and CD4⁺ T cells in airways of asthmatics whereas, in COPD, typically neutrophils, macrophages, and CD8⁺ T cells infiltrate the respiratory tract [92]. TSPO seems to play a pathogenic role in asthma and COPD. Indeed, TSPO exhibited downregulated expression in patients with acute exacerbations of COPD [93]

and a protein-protein interaction network analysis revealed that TSPO could be implicated in development and/or progression of asthma in children [94]. TSPO is involved in various complex cellular processes such as intracellular transportation, mitophagy, and apoptosis [95–97]. Among them, mitochondrial dysregulation and especially mitophagy represent a key player of signaling pathways relevant to remodeling in chronic remodeling lung pathologies like asthma [98] and COPD [99]. Quantitative analysis of the acquired emission TSPO PET data is in consonance with these findings where mean tracer uptake, objectified by plateau tissue/plasma, was higher in COPD patients and asthmatics than in healthy volunteers. Moreover, pulmonary TSPO PET imaging used in combination with ^{18}F -FDG indicated that metabolic activation of inflammatory cells was higher in COPD patients than in chronic asthmatics [100]. Furthermore, cigarette smoke exposure, which is the leading cause of COPD, altered directly TSPO expression, paving the way for lung cancerization [101]. It should be noted that no obvious differences are seen between patients and healthy subject in the emission images for either ^{18}F FDG or ^{11}C -PK11195, due to the low density of the lung (Figure 1). Significant differences are only revealed by quantitative analysis of the acquired emission data [100].

TSPO PET imaging has been used to assess, in humans, macrophages involvement in interstitial lung diseases [102]. Surprisingly, Branley et al. [85] demonstrated that TSPO expression is reduced in these lung inflammatory disorders. Given the fact that patients with interstitial lung disease showed an accumulation of intrapulmonary macrophages [103] and experimental models of pulmonary inflammation revealed to be associated with TSPO overexpression [104], authors hypothesized that macrophages phenotypically differed in these patients (i.e., macrophage with reduced TSPO expression) [102]. In parallel to the relationship between lung density and disease activity (i.e., between controls, patients treated, and drug-naive patients), ^{11}C -PK11195 binding would tend to decline according to the disease burden in fibrosing alveolitis due to systemic sclerosis (FASSc) patients [85]. As a result of these achievements, TSPO PET imaging could be a decision-support exam to initiate immunosuppressive treatment in FASSc.

TSPO PET imaging did not provide unequivocal results [85, 100] and in front of some limitations (e.g., multicellular expression of TSPO in human lungs [89, 90], high variability in radiotracer uptake between COPD and asthmatic patients, and wide overlap between patients and controls [100]), TSPO did not seem to be a timely biomarker to diagnose and even less to improve our knowledge in lung disease pathophysiology. In addition, the apparent TSPO downregulation in interstitial lung diseases [85] and acute exacerbations of BPCO [93] should not be construed as absolute finding; indeed TSPO expression is a dynamic process and highly context-dependent, which is probably integrated in a time-dependent fashion (acute versus chronic injury).

TABLE 3

Applications	Population/animal models	Radioligand	Main findings	Ref.
Preclinical	Unilateral instillation of fibrogenic (microcrystalline SiO ₂ , <i>n</i> = 12 rabbits), nonfibrogenic (amorphous SiO ₂ , <i>n</i> = 10 rabbits) 5 μm particles into rabbit lungs	¹¹ C-PK11195	Significantly increased tracer tissue/plasma ratios from day 3 after instillation in the challenged region, in both silica models, and remaining at least 2 weeks In the amorphous silica model, an extrapulmonary TSP0 PET signal appeared at 6 days In the microcrystalline silica model, this extrapulmonary signal is delayed until 3 weeks after instillation	Jones et al. (2002) [91]
Clinical	6 COPD patients, 6 chronic asthmatics, and 5 HC	¹¹ C-PK11195	Mean tracer uptake was higher in 4/6 COPD patients and 3/6 asthmatics than the maximum value in HC No statistical correlation was found between binding tracer and either the magnitude of the ¹⁸ F-EDG signal or the severity of the disease	Jones et al. (2003) [100]
Clinical	15 FASSc (10 drug-naive & 5 with immunosuppressive drugs) patients versus 7 HC	¹¹ C-PK11195	Tracer lung uptake was decreased in FASSc patients, compared to normal controls Strong negative correlation between tissue radioligand uptake and lung density in FASSc patients Pulmonary tracer binding showed a nonsignificant but progressive decrease from normal in FASSc drug-naive patients to those patients immunosuppressive-treated No significant correlation between tracer uptake and pulmonary function data	Branley et al. (2008) [85]

COPD, chronic obstructive pulmonary disease; FASSc, fibrosing alveolitis due to systemic sclerosis; HC, healthy control.

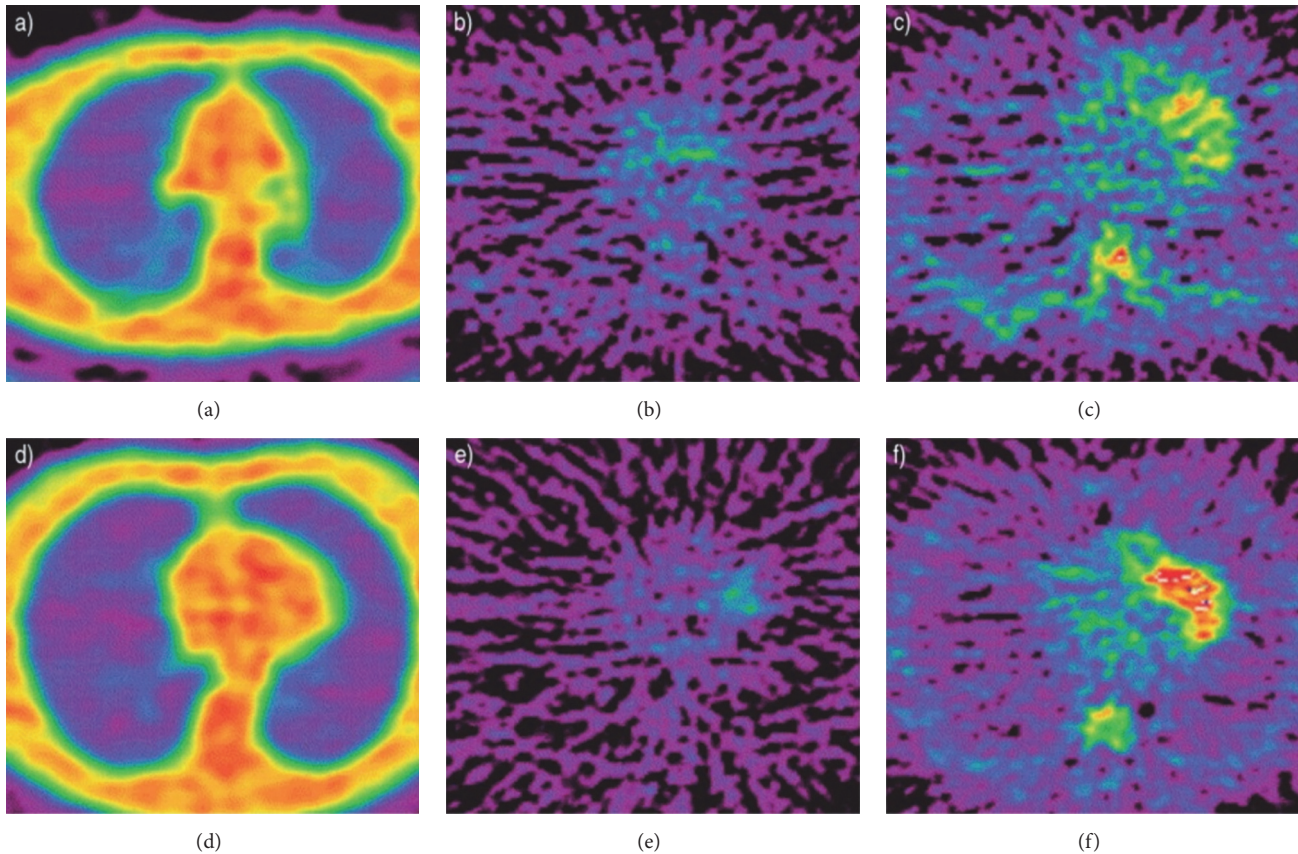


FIGURE 1: Transaxial thoracic images for transmission (a and d), ^{18}F -FDG emission (b and e) and ^{11}C -PK11195 (c and f) in a normal subject (a–c), and a patient with chronic obstructive pulmonary disease (d–f) from Jones et al. (2003) [100].

3.4. Inflammatory Vasculopathies (See Table 4). TSPO is involved in pathophysiology of various cardiovascular diseases, including arrhythmia, myocardial infarction, cardiac hypertrophy, atherosclerosis, myocarditis, and large vessel vasculitis (for review see Qi et al. 2012 [105]). Among these, large vessel vasculitis represents a heterogeneous group of complex disorders (e.g., giant cell arteritis, Takayasu's arteritis) in which chronic inflammatory lesions of the blood vessels are characterized by granulomatous pan-arteritis with focal leukocytic infiltration [106]. Typical clinical symptoms include the association of blindness, stroke, claudication according to the vascular territory affected/occluded, fever, night sweats, and arthralgia [107–109]. TSPO molecular imaging using ^{11}C -PK11195 provided valuable information such as presence, intensity, and localization of activated macrophages in large vessel vasculitis [36, 110]. In these studies, giant cell arteritis, Takayasu's arteritis, and lupus erythematosus patients fulfilling American College of Rheumatology diagnostic criteria [111] were enrolled. Authors defined active vasculitis as onset within the previous 3 months of any of the symptoms mentioned above and conversely asymptomatic patients' diagnosis based on absence of symptoms of active disease. The fact that TSPO PET signal was quantifiable even in some asymptomatic patients (Figure 2) paves the way of a preemptive therapeutic strategy, that is to say

prior the symptoms, whereas the inflammatory process is active [36, 110]. Although only one giant cell arteritis patient was enrolled for a longitudinal assessment of corticosteroids response, TSPO PET imaging could be a promising approach to monitor drug efficacy of immunosuppressive agents currently used and for drug development in vasculitis. Patients with large vessel vasculitis have an increased cardiovascular risk compared to the age-matched healthy population as a consequence of accelerated atherosclerosis [106].

Atherosclerosis is an inflammatory, chronic metabolic disorder of the arterial walls, in which intraplaque inflammation drives the progression and the destabilization of atheromatous lesions [112, 113]. It seems that atherosclerosis starts with the penetration of low-density lipoprotein (LDL) through a damaged endothelial wall, leading to their oxidation. These oxidized LDL particles act as autoantigens presented by macrophages which differentiate into foamy macrophages, promote the inflammation, and cause interleukins secretion [114–116]. According to its function as leader of cholesterol transport and steroidogenesis [97] and its dysregulation induced by smoke exposure [101], TSPO has been targeted in drug development of lipid-lowering therapy and “cardiovascular” anti-inflammatory/antioxidant treatment [117–119]. Autoradiography and immunostaining experiments highlighted that TSPO tracer binding concerned

TABLE 4

Applications	Population/animal models	Radioligand	Main findings	Ref.
			Vasculitis	
Clinical	(i) 15 patients with large vessel vasculitis (5 TA, 4 GCA, & 6 SLE) (ii) 1 GCA patient followed-up after 20-week course of oral CS	^{11}C -PK11195	(i) 3/5 patients whose tracer binding was found at the level of the aorta; maximal tracer uptake coincided with minimal calcification Tracer TBR was significantly higher in symptomatic, compared to asymptomatic patients (ii) Tracer uptake was markedly reduced in the wall of the aortic arch after CS treatment The reduction in radioligand binding was paralleled by a distinct improvement in symptoms and a decrease in his serum inflammatory markers	Pugliese et al. (2010) [36]
Clinical	7 patients (3 symptomatic & 4 asymptomatic) with large vessel vasculitis	^{11}C -PK11195	V_T was significantly greater in symptomatic than in asymptomatic patients	Lamare et al. (2010) [110]
			Atherosclerosis	
Preclinical	Constrictive cuff was placed on the right carotid artery of 6 mice	^{18}F -FEDA11106	Significantly increased tracer binding in the right carotid artery compared to left (unmanipulated) carotid artery TAC exhibited a significantly greater increase in binding at the downstream region when compared to the cuffed or upstream regions at 60 minutes after injection	Cuhlmann et al. (2014) [120]
Preclinical	10 atherosclerotic mice (LDLR ^{-/-} ApoB ^{100/100}) versus 9 healthy mice	^{18}F -FEMPA	There was visually detectable tracer uptake that colocalized with the aortic arch, but not significantly different between the animal groups Radioligand SUV was significantly higher in atherosclerotic aortas in muted mice than in healthy control mice	Hellberg et al. (2017) [121]
Clinical	32 patients with carotid stenosis (9 symptomatic & 27 asymptomatic)	^{11}C -PK11195	Tracer SUV and TBR were higher in carotid plaques of symptomatic than asymptomatic patients No significant correlation between radioligand TBR and plaque calcification ROC analysis of tracer TBR to identify patients with CVE showed sensitivity of 78%, specificity of 74%, NPV of 91%, and PPV of 50%	Gaemperli et al. (2012) [122]

CS, corticosteroids; CVE, cerebrovascular events; GCA, giant cell arteritis; HC, healthy control; NPV, negative predictive value; PPV, positive predictive value; ROC, receiver operating characteristic; SLE, systemic lupus erythematosus; SUV, standardized uptake value; TA, Takayasu's arteritis; TAC, time-activity curves; TBR, target-to-background ratio; V_T , total volume of distribution.

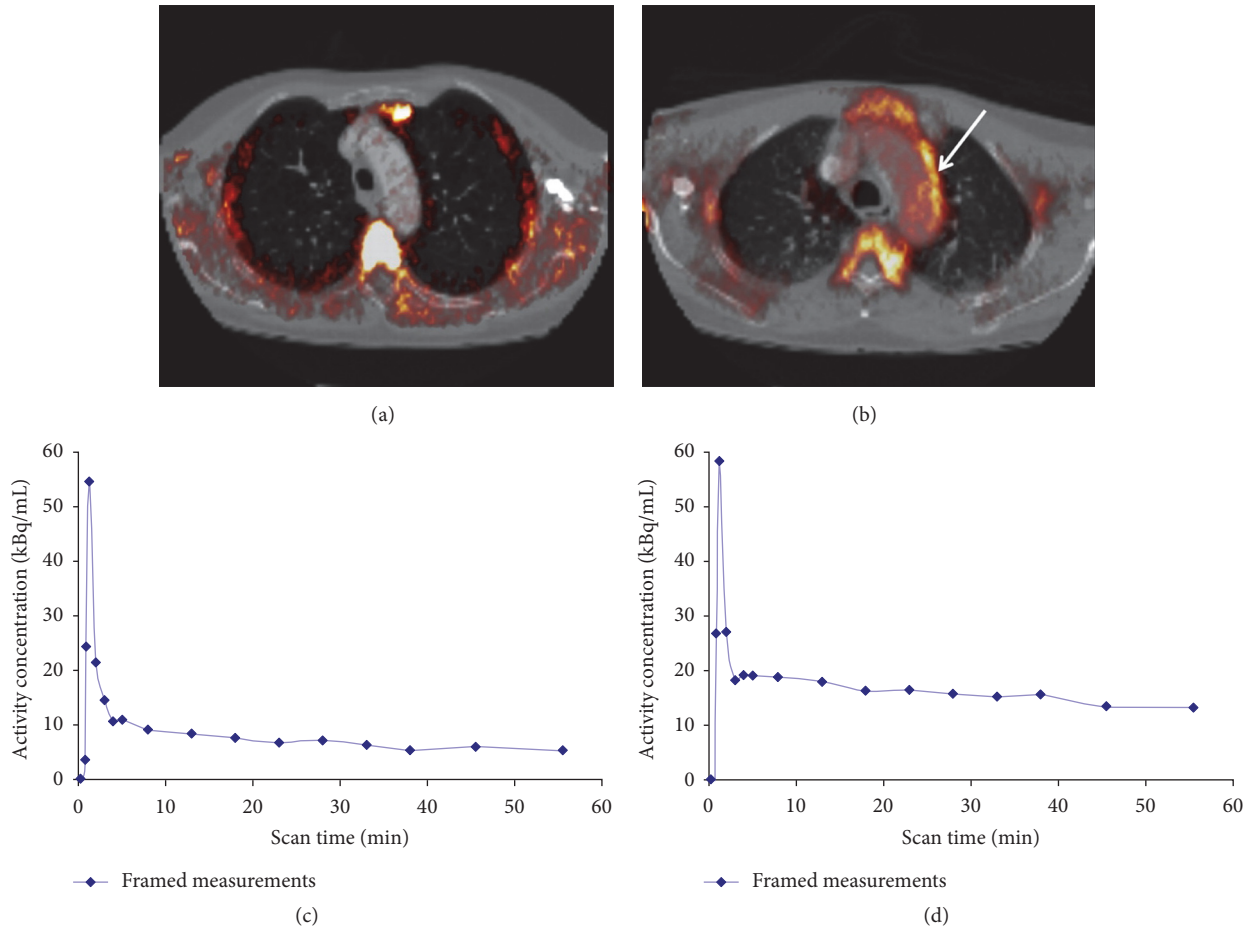


FIGURE 2: ^{11}C -PK11195 PET/CT angiography of asymptomatic (a) and symptomatic (b) patient with vasculitis. Each patient is shown in transverse view. Arrow indicates inflamed region of aortic arch. Respective time-activity curves (corrected for radioactive decay) derived from aortic vessel wall (c and d) from Lamare et al. (2010) [110].

predominantly CD68-positive areas of mice carotid sections [120] and human carotid endarterectomy samples [121, 122] which contained fibrotic and calcified tissue [121]. Recent research by Chinetti-Gbaguidi and colleagues [123] revealed that RANKL (receptor activator of nuclear factor κB (NF- κB) ligand) and MCSF (macrophage colony-stimulating factor), two major mediators of vascular calcification, are dysregulated by IL-4 polarization (i.e., M_1 to M_2 polarization), leading macrophages surrounding atherosclerotic plaques to be unable to resorb calcification. Therefore, the lack of association between plaque calcification score and ^{11}C -PK11195 target-to-background ratio (TBR) [122] could be explained by a different macrophage phenotype (i.e., M_2 polarized) which would be undetectable on PET images. Moreover, in the same clinical study TSPO PET imaging of patients with carotid stenosis revealed that ^{11}C -PK11195 standardized uptake value (SUV) and TBR were significantly higher in carotid atheromatous lesions of symptomatic patients (i.e., associated with stroke and transient ischemic attacks) compared to asymptomatic individuals. Surprisingly, no difference was found between the severity of carotid stenosis on CT angiography between symptomatic and asymptomatic patients [122]. Most

importantly, it appears that activated macrophages, assessed by TSPO PET, were detected at a disturbed flow site located downstream from the region of stenosis [120]. Finally, multi-modal imaging using ^{11}C -PK11195 PET in combination with CT plaque attenuation offers good diagnostic performances to improve risk stratification in patients with asymptomatic carotid stenosis in order to anticipate cerebrovascular events [122]. Beyond this potential diagnostic role of TSPO PET scanning for atherosclerosis, TSPO might be used as a therapeutic target for atherosclerosis. Indeed, the oxidative stress induced by high fat and high cholesterol atherogenic diet in rats has been associated with a reduction of TSPO-binding density [124].

3.5. Rheumatic and Musculoskeletal Disorders (See Table 5). Rheumatoid arthritis (RA) is a chronic autoimmune disease characterized by joint inflammation where the diagnosis is based on joint involvement, duration of symptoms, serology (i.e., rheumatoid factor, anticitrullinated protein antibody), and biology (i.e., erythrocyte sedimentation rate, C-reactive protein) [126, 127]. TSPO PET imaging in various animal models of noninfectious arthritis supported the fact that

TABLE 5

Applications	Population/animal models	Radioligand	Main findings	Ref.
			Rheumatic diseases	
Preclinical	6 rats were injected with 1% carrageenan solution into the paw 8 genetically susceptible rats were injected with inactivated <i>M. butyricum</i> into the nail	¹¹ C-PBR28	Significantly higher tracer SUV _{peak} in carrageenan-treated paws compared to paired contralateral controls Increased radioligand mean AUC _{SUV} of 60-minute time-activity data was found at the root of the tail, sacroiliac joints, and knees, compared to controls	Shao et al. (2013) [128]
Preclinical	18 rats (<i>n</i> = 7, 6, 5 for each tracer, resp.) were injected with mBSA to induce knee arthritis versus 5 untreated rats	¹¹ C-DPA-713/ ¹⁸ F-DPA-714/ ¹¹ C-PK11195	All three TSPO tracers clearly accumulated in arthritic knees Mean absolute SUV of the three radioligands was markedly higher than in contralateral knees	Gent et al. (2014) [129]
Preclinical	11 rats were injected with inactivated <i>M. tuberculosis</i> into the tail versus 6 rats nontreated	¹⁸ F-DPA-714	Increased tracer binding in ankles of treated rat, compared to control rat at 20 days The mean radioligand uptake value in treated animals was more than twice that of nontreated animals Association analysis exhibited a good relation between tracer uptake and the joint swelling	Pottier et al. (2014) [130]
Clinical	10 RA patients with active arthritis versus 8 HC	¹¹ C-PK11195	The mean <i>V_T</i> and the mean SUV ratios were significantly higher in knees with severe synovial swelling score than those in mild and absent synovial swelling SUV ratios in the contralateral uninflamed knee joints of RA patients were 50% higher than those in uninflamed knee joints of healthy volunteers	van der Laken et al. (2008) [125]
			Musculoskeletal disorders	
Preclinical	Mouse were injected with oil of turpentine into the left thigh muscle and then followed-up for 26 days after injection	¹⁸ F-DPA-714	The inflammatory muscles showed significantly increased local accumulation of tracer compared with collateral muscle The uptake peaked on day 6 and then dropped slowly along with the time till day 26, which was still higher than that in collateral muscle	Wu et al. (2014) [140]

AUC, area under the curve; HC, healthy controls; mBSA, methylated bovine serum albumin; RA, rheumatoid arthritis; SUV, standardized uptake value; *V_T*, total volume of distribution.

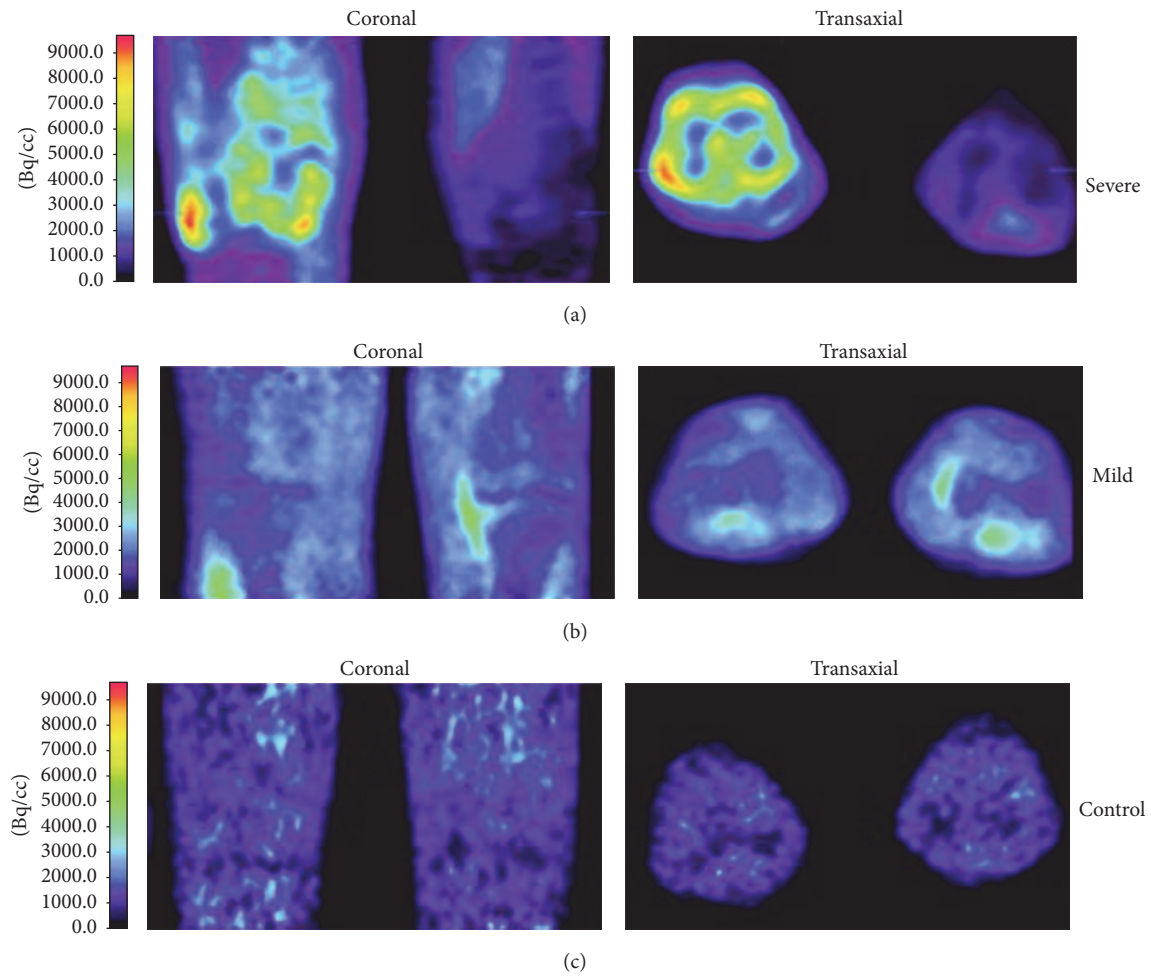


FIGURE 3: ^{11}C -PK11195 PET images in coronal and transaxial directions. (a) Images of severe clinical inflammation of the right knee (depicted at the left in both images) and no clinical inflammation of the left knee in a patient with rheumatoid arthritis (RA). (b) Images of mild inflammation of both knee joints in an RA patient. (c) Images of knees without joint disease in a control subject. The different levels of tracer uptake correspond to the colors in the color bar at the left, from van der Laken et al. (2008) [125].

nuclear-based approach provides quickly information on biological functions even before anatomical alterations of bone and cartilage [128–130]. TSPO PET imaging appears to be a promising approach to follow early events in the pathophysiology of RA, suggesting that a precocity medical care should be feasible even before the structural alterations, especially as the uninflamed knee joints of RA patients showed a significant greater TSPO tracer uptake than in healthy controls [125]. Moreover, association analysis showed a good correlation between tracer binding in joints and clinical synovial swelling or macrophage infiltration in synovial tissue in preclinical [130] and clinical study [125]. Figure 3 illustrates these findings. For imaging of RA, the key limitation of TSPO PET scanning is the tracer uptake in the inflamed synovium linked to binding in surrounding bone and bone marrow (e.g., periarticular bone of joints binding), keeping from quantifying accurately uptake in the synovium [129]. Nevertheless, this problem appears to be minimized when ^{18}F -DPA tracers have been used in rat model of rheumatoid

arthritis (i.e., better knee-to-bone ratios), compared to ^{11}C -PK11195 [129].

4. TSPO PET Imaging: Towards a Clinical Application for Pathologies with Both Central and Peripheral Inflammatory Component?

TSPO PET imaging has to date been used mainly to assess microglial activation in various neurologic diseases ranging from neurodegenerative disorders such as Huntington’s disease [131] and Alzheimer’s disease [132] to stroke [133] and psychiatric conditions like schizophrenia [134]. The promising results of TSPO PET imaging to diagnose and characterize some PSIDs and especially atherosclerosis [122] lead us to think that, as in some central nervous system disorders such as multiple sclerosis and amyotrophic lateral sclerosis [39], a clinical application of TSPO as a biomarker

of inflammation is possible. Nevertheless, as with neurologic disorders some limitations must be taken like spillover and partial volume effect (because of proximity of the blood pool and limited thickness of the arterial wall), a multicellular expression making mathematic model to quantify free and specific ligand binding more complex. Furthermore, in contrast to central conditions where tracer's radiolabeled metabolites are not sufficiently lipophilic to produce background noises, in PSIDs the pharmacokinetic of radiolabeled metabolites leads to hinder TSPO signal quantification. This is especially a limitation for IBDs where tracer elimination by the upper digestive tract (e.g., ^{18}F -DPA-714) compromised TSPO quantification [25].

The strength of TSPO PET imaging could rely on the ability to detect inflammatory changes in pathologies which have central and peripheral expression, for instance, to evaluate the relationship between neuroinflammation induced by stroke and TSPO expression of atherosclerotic plaques in patients with carotid stenosis. Indeed, it allows characterizing inflammation and establishing if interplay occurred between microglial activation and peripheral macrophages. In this sense, surprising findings have been found in liver fibrosis where TSPO are not overexpressed in patients with hepatic encephalopathy [135]. Likewise, in a preclinical study, inflammation in both the gut and the brain of rats with chemically induced colitis was observed by *ex vivo* biodistribution but these effects could not be detected by ^{11}C -PBR28 PET imaging which was likely due to insufficient resolution of the micro-PET camera [136]. Besides PSIDs, infectious diseases where TSPO PET imaging has already been investigated such as HIV infection [137] or sepsis [138] could benefit from this approach in order to know if central and peripheral inflammation is a continuum or acts independently.

5. Conclusion

The pathophysiologic involvement of TSPO in PSIDs is well-documented especially in cardiovascular conditions [105] at the opposite of microglial activation in neurologic disorders which remains controversial. Limitations of TSPO PET imaging in PSIDs concern the large expression of TSPO in peripheral tissues whereas, in central nervous system, TSPO expression is low in healthy brain [39]. A body of evidence gives a M1-phenotype biomarker status of microglial TSPO expression [139]. In line with these findings, the fact that TSPO PET imaging did not highlight significant signal in some PSIDs (e.g., atherosclerosis [122], interstitial lung disease [85]), where macrophage activation is now well-documented, seems to confirm that, also in peripheral disorders, TSPO may rather to be associated with harmful inflammatory state than regenerative environment. Nevertheless these *in vitro* findings need to be *in vivo* translated [139].

Conflicts of Interest

The authors declare no conflicts of interest.

Acknowledgments

This study was supported by the French National Agency for Research ("Investissements d'Avenir" no. ANR-11-LABX-0018-01), IRON, and the European Union's Seventh Framework Programme (FP7/2004–2013) under Grant Agreement no. 278850 (INMiND).

References

- [1] A. A. de Jesus, S. W. Canna, Y. Liu, and R. Goldbach-Mansky, "Molecular mechanisms in genetically defined autoinflammatory diseases: disorders of amplified danger signaling," *Annual Review of Immunology*, vol. 33, no. 1, pp. 823–874, 2015.
- [2] N. Raje and C. Dinakar, "Overview of immunodeficiency disorders," *Immunology and Allergy Clinics of North America*, vol. 35, no. 4, pp. 599–623, 2015.
- [3] J. Sleasman, "The association between immunodeficiency and the development of autoimmune disease," *Advances in Dental Research*, vol. 10, no. 1, pp. 57–61, 2016.
- [4] C.-J. Chen, H. Kono, D. Golenbock, G. Reed, S. Akira, and K. L. Rock, "Identification of a key pathway required for the sterile inflammatory response triggered by dying cells," *Nature Medicine*, vol. 13, no. 7, pp. 851–856, 2007.
- [5] K. L. Rock, E. Latz, F. Ontiveros, and H. Kono, "The sterile inflammatory response," *Annual Review of Immunology*, vol. 28, pp. 321–342, 2010.
- [6] C. Zhang, J. Feng, J. Du et al., "Macrophage-derived IL-1 α promotes sterile inflammation in a mouse model of acetaminophen hepatotoxicity," *Cellular & Molecular Immunology*, 2017.
- [7] C. Ju and P. Mandrekar, "Macrophages and Alcohol-Related Liver Inflammation," *Alcohol Research: Current Reviews*, vol. 37, pp. 251–262, 2015.
- [8] B. T. Mossman and A. Chung, "Mechanisms in the pathogenesis of asbestosis and silicosis," *The American Journal of Respiratory and Critical Care Medicine*, vol. 157, no. 5, pp. 1666–1680, 1998.
- [9] J. M. Craig, A. L. Scott, and W. Mitzner, "Immune-mediated inflammation in the pathogenesis of emphysema: insights from mouse models," *Cell and Tissue Research*, vol. 367, no. 3, pp. 591–605, 2017.
- [10] G. Nuki and P. A. Simkin, "A concise history of gout and hyperuricemia and their treatment," *Arthritis Research and Therapy*, vol. 8, supplement 1, article S1, 2006.
- [11] H. L. Weiner and D. Frenkel, "Immunology and immunotherapy of Alzheimer's disease," *Nature Reviews Immunology*, vol. 6, no. 5, pp. 404–416, 2006.
- [12] A. Gisterå and G. K. Hansson, "The immunology of atherosclerosis," *Nature Reviews Nephrology*, vol. 13, no. 6, pp. 368–380, 2017.
- [13] K. C. Navegantes, R. Souza Gomes, P. A. T. Pereira, P. G. Czaikoski, C. H. M. Azevedo, and M. C. Monteiro, "Immune modulation of some autoimmune diseases: The critical role of macrophages and neutrophils in the innate and adaptive immunity," *Journal of Translational Medicine*, vol. 15, no. 1, article 36, 2017.
- [14] M. Lech and H.-J. Anders, "Macrophages and fibrosis: how resident and infiltrating mononuclear phagocytes orchestrate all phases of tissue injury and repair," *Biochimica et Biophysica Acta: Molecular Basis of Disease*, vol. 1832, no. 7, pp. 989–997, 2013.
- [15] A. Freedman, J. Williams, and R. Bellamy, "Fever of unknown origin," *Clinical Medicine*, vol. 8, no. 5, pp. 526–530, 2008.

- [16] D. A. Mankoff, "A definition of molecular imaging," *Journal of Nuclear Medicine*, vol. 48, pp. 18N–21N, 2007.
- [17] R. Kubota, S. Yamada, and K. Kubota, "Intratumoral distribution of fluorine-18-fluorodeoxyglucose in vivo: high accumulation in macrophages and granulation tissues studied by microautoradiography," *Journal of Nuclear Medicine*, pp. 33–1972, 1992.
- [18] T. Mochizuki, E. Tsukamoto, and Y. Kuge, "FDG uptake and glucose transporter subtype expressions in experimental tumor and inflammation models," *Journal of Nuclear Medicine*, vol. 42, pp. 1551–1555, 2001.
- [19] S. Gogia, Y. Kaiser, and A. Tawakol, "Imaging High-Risk Atherosclerotic Plaques with PET," *Current Treatment Options in Cardiovascular Medicine*, vol. 18, no. 12, 2016.
- [20] J. Bucerius, "Monitoring Vasculitis with 18F-FDG PET," *The Quarterly Journal of Nuclear Medicine and Molecular Imaging*, vol. 60, pp. 219–235, 2016.
- [21] M. R. Dweck, C. Jones, N. V. Joshi et al., "Assessment of valvular calcification and inflammation by positron emission tomography in patients with aortic stenosis," *Circulation*, vol. 125, no. 1, pp. 76–86, 2012.
- [22] W. W. Lee, B. Marinelli, A. M. van der Laan et al., "PET/MRI of inflammation in myocardial infarction," *Journal of the American College of Cardiology*, vol. 59, no. 2, pp. 153–163, 2012.
- [23] S. Wang, Q. Xie, and W. LV, "Positron emission tomography/computed tomography imaging and rheumatoid arthritis," *International Journal of Rheumatic Diseases*, vol. 17, no. 3, pp. 248–255, 2014.
- [24] P. B. Shyn, "18F-FDG positron emission tomography: potential utility in the assessment of Crohn's disease," *Abdominal Imaging*, vol. 37, no. 3, pp. 377–386, 2012.
- [25] N. Bernards, G. Pottier, B. Thézé, F. Dollé, and R. Boisgard, "In vivo evaluation of inflammatory bowel disease with the aid of μ PET and the translocator protein 18 kDa radioligand [18 F]DPA-714," *Molecular Imaging and Biology*, vol. 17, pp. 67–75, 2014.
- [26] J. Bucerius, J. Schmaljohann, I. Böhm et al., "Feasibility of 18F-fluoromethylcholine PET/CT for imaging of vessel wall alterations in humans - First results," *European Journal of Nuclear Medicine and Molecular Imaging*, vol. 35, no. 4, pp. 815–820, 2008.
- [27] I. E. Laitinen, P. Luoto, K. Nagren et al., "Uptake of 11C-Choline in Mouse Atherosclerotic Plaques," *Journal of Nuclear Medicine*, vol. 51, no. 5, pp. 798–802, 2010.
- [28] C. M. Matter, "18F-Choline Images Murine Atherosclerotic Plaques Ex Vivo," *Arteriosclerosis, Thrombosis, and Vascular Biology*, vol. 26, no. 3, pp. 584–589, 2005.
- [29] L. Tran, A. D. R. Huitema, M. H. van Rijswijk et al., "CD20 antigen imaging with 124 I-rituximab PET/CT in patients with rheumatoid arthritis," *Human Antibodies*, vol. 20, pp. 29–35, 2011.
- [30] M. J. Uddin, B. C. Crews, K. Ghebreselasie et al., "Fluorinated COX-2 Inhibitors as Agents in PET Imaging of Inflammation and Cancer," *Cancer Prevention Research*, vol. 4, no. 10, pp. 1536–1545, 2011.
- [31] D. Hartung, M. Schäfers, S. Fujimoto et al., "Targeting of matrix metalloproteinase activation for noninvasive detection of vulnerable atherosclerotic lesions," *European Journal of Nuclear Medicine and Molecular Imaging*, vol. 34, supplement 1, pp. S1–S8, 2007.
- [32] V. di Galleonardo, A. Signore, A. W. J. M. Glaudemans, R. A. J. O. Dierckx, and E. F. J. de Vries, "*N*-(4- 18 F-fluorobenzoyl)interleukin-2 for PET of human-activated T lymphocytes," *Journal of Nuclear Medicine*, vol. 53, no. 5, pp. 679–686, 2012.
- [33] R. L. Wilder, "Integrin alpha V beta 3 as a target for treatment of rheumatoid arthritis and related rheumatic diseases," *Annals of the Rheumatic Diseases*, vol. 61, supplement 2, pp. 96ii–99, 2002.
- [34] P. Lankinen, T. J. Mäkinen, T. A. Pöyhönen et al., "68Ga-DOTAVAP-P1 PET imaging capable of demonstrating the phase of inflammation in healing bones and the progress of infection in osteomyelitic bones," *European Journal of Nuclear Medicine and Molecular Imaging*, vol. 35, no. 2, pp. 352–364, 2008.
- [35] M. Nahrendorf, E. Keliher, P. Panizzi et al., "18F-4V for PET-CT imaging of VCAM-1 expression in atherosclerosis," *JACC Cardiovascular Imaging*, vol. 2, no. 10, pp. 1213–1222, 2009.
- [36] F. Pugliese, O. Gaemperli, A. R. Kinderlerer et al., "Imaging of vascular inflammation with [11 C]-PK11195 and positron emission tomography/computed tomography angiography," *Journal of the American College of Cardiology*, vol. 56, no. 8, pp. 653–661, 2010.
- [37] F. Zavala, J. Haumont, and M. Lenfant, "Interaction of benzodiazepines with mouse macrophages," *European Journal of Pharmacology*, vol. 106, no. 3, pp. 561–566, 1984.
- [38] R. B. Banati, "Visualising microglial activation in vivo," *GLIA*, vol. 40, no. 2, pp. 206–217, 2002.
- [39] A.-C. Dupont, B. Largeau, M. J. S. Ribeiro, D. Guilloteau, C. Tronel, and N. Arlicot, "Translocator protein-18 kDa (TSPO) positron emission tomography (PET) imaging and its clinical impact in neurodegenerative diseases," *International Journal of Molecular Sciences*, vol. 18, no. 4, article no. 785, 2017.
- [40] M. Awad and M. Gavish, "Binding of [3 H]Ro 5–4864 and [3 H]PK 11195 to Cerebral Cortex and Peripheral Tissues of Various Species: Species Differences and Heterogeneity in Peripheral Benzodiazepine Binding Sites," *Journal of Neurochemistry*, vol. 49, no. 5, pp. 1407–1414, 1987.
- [41] M. Anzini, A. Cappelli, S. Vomero et al., "Molecular basis of peripheral vs central benzodiazepine receptor selectivity in a new class of peripheral benzodiazepine receptor ligands related to alpidem," *Journal of Medicinal Chemistry*, vol. 39, no. 21, pp. 4275–4284, 1996.
- [42] G. Le Fur, M. L. Perrier, N. Vaucher et al., "Peripheral benzodiazepine binding sites: Effect of PK 11195, 1-(2-chlorophenyl)-*n*-methyl-*n*-(1-methylpropyl)-3-isoquinolinecarboxamide. I. In vitro studies," *Life Sciences*, vol. 32, no. 16, pp. 1839–1847, 1983.
- [43] F. Chauveau, H. Boutin, N. van Camp, F. Dollé, and B. Tavitian, "Nuclear imaging of neuroinflammation: a comprehensive review of [11 C]PK11195 challengers," *European Journal of Nuclear Medicine and Molecular Imaging*, vol. 35, no. 12, pp. 2304–2319, 2008.
- [44] S. Chaki, T. Funakoshi, R. Yoshikawa et al., "Binding characteristics of [3 H]DAA1106, a novel and selective ligand for peripheral benzodiazepine receptors," *European Journal of Pharmacology*, vol. 371, no. 2–3, pp. 197–204, 1999.
- [45] M.-R. Zhang, J. Maeda, K. Furutsuka et al., "[18 F]FMDAA1106 and [18 F]FEDAA1106: two positron-emitter labeled ligands for peripheral benzodiazepine receptor (PBR)," *Bioorganic and Medicinal Chemistry Letters*, vol. 13, no. 2, pp. 201–204, 2003.
- [46] W. C. Kreisl, M. Fujita, Y. Fujimura et al., "Comparison of [11 C]-(R)-PK 11195 and [11 C]PBR28, two radioligands for translocator protein (18 kDa) in human and monkey: Implications for

- positron emission tomographic imaging of this inflammation biomarker," *NeuroImage*, vol. 49, no. 4, pp. 2924–2932, 2010.
- [47] A. A. Wilson, A. Garcia, J. Parkes et al., "Radiosynthesis and initial evaluation of [18F]-FEPPA for PET imaging of peripheral benzodiazepine receptors," *Nuclear Medicine and Biology*, vol. 35, no. 3, pp. 305–314, 2008.
- [48] S. Selleri, F. Bruni, C. Costagli et al., "2-Arylpyrazolo[1,5-a]pyrimidin-3-yl acetamides. New potent and selective peripheral benzodiazepine receptor ligands," *Bioorganic and Medicinal Chemistry*, vol. 9, no. 10, pp. 2661–2671, 2001.
- [49] D. R. Owen, A. J. Yeo, R. N. Gunn et al., "An 18-kDa translocator protein (TSPO) polymorphism explains differences in binding affinity of the PET radioligand PBR28," *Journal of Cerebral Blood Flow & Metabolism*, vol. 32, pp. 1–5, 2012.
- [50] K. K. Yoder, K. Nho, S. L. Risacher, S. Kim, L. Shen, and A. J. Saykin, "Influence of TSPO genotype on 11C-PBR28 standardized uptake values," *Journal of Nuclear Medicine*, vol. 54, no. 8, pp. 1320–1322, 2013.
- [51] Z. Fan, V. Calsolaro, R. A. Atkinson et al., "Flutriclamide (18F-GE180) PET: First-in-human PET study of novel third-generation in vivo marker of human translocator protein," *Journal of Nuclear Medicine*, vol. 57, no. 11, pp. 1753–1759, 2016.
- [52] M. Ikawa, T. G. Lohith, S. Shrestha et al., "11C-ER176, a radioligand for 18-kDa translocator protein, has adequate sensitivity to robustly image all three affinity genotypes in human brain," *Journal of Nuclear Medicine*, vol. 58, no. 2, pp. 320–325, 2017.
- [53] R. Desein, M. Chamailard, and S. Danese, "Innate immunity in Crohn's disease," *Journal of Clinical Gastroenterology*, vol. 42, pp. S144–S147, 2008.
- [54] D. Ellinghaus, J. Bethune, B.-S. Petersen, and A. Franke, "The genetics of Crohn's disease and ulcerative colitis—status quo and beyond," *Scandinavian Journal of Gastroenterology*, vol. 50, no. 1, pp. 13–23, 2015.
- [55] T. Stefanelli, A. Malesci, A. Repici, S. Vetrano, and S. Danese, "New insights into inflammatory bowel disease pathophysiology: paving the way for novel therapeutic targets," *Current Drug Targets*, vol. 9, no. 5, pp. 413–418, 2008.
- [56] G. Solina, S. Mandalà, C. La Barbera, and V. Mandalà, "Current management of intestinal bowel disease: the role of surgery," *Updates in Surgery*, vol. 68, no. 1, pp. 13–23, 2016.
- [57] A. M. McCombie, R. T. Mulder, and R. B. Geary, "How IBD patients cope with IBD: a systematic review," *Journal of Crohn's and Colitis*, vol. 7, no. 2, pp. 89–106, 2013.
- [58] F. Caobelli, L. Evangelista, N. Quartuccio et al., "Role of molecular imaging in the management of patients affected by inflammatory bowel disease: State-of-the-art," *World Journal of Radiology*, vol. 8, no. 10, p. 829, 2016.
- [59] K. A. Chachu and M. T. Osterman, "How to diagnose and treat IBD mimics in the refractory IBD patient who does not have IBD," *Inflammatory Bowel Diseases*, vol. 22, no. 5, pp. 1262–1274, 2016.
- [60] C. S. Gismera and B. S. Aladrén, "Inflammatory bowel diseases: a disease (s) of modern times? Is incidence still increasing?" *World Journal of Gastroenterology*, vol. 14, no. 36, pp. 5491–5498, 2008.
- [61] D. Bettenworth, S. Reuter, S. Hermann et al., "Translational 18F-FDG PET/CT Imaging to Monitor Lesion Activity in Intestinal Inflammation," *Journal of Nuclear Medicine*, vol. 54, no. 5, pp. 748–755, 2013.
- [62] P. Hindryckx, S. Staelens, L. Devisscher et al., "Longitudinal quantification of inflammation in the murine dextran sodium sulfate-induced colitis model using μ PET/CT," *Inflammatory Bowel Diseases*, vol. 17, no. 10, pp. 2058–2064, 2011.
- [63] R. T. Lapp, B. J. Spier, S. B. Perlman, C. J. Jaskowiak, and M. Reichelderfer, "Clinical Utility of Positron Emission Tomography/Computed Tomography in Inflammatory Bowel Disease," *Molecular Imaging and Biology*, vol. 13, no. 3, pp. 573–576, 2011.
- [64] D. A. Lemberg, R. M. Issenman, R. Cawdron et al., "Positron emission tomography in the investigation of pediatric inflammatory bowel disease," *Inflammatory Bowel Diseases*, vol. 11, no. 8, pp. 733–738, 2005.
- [65] M. Löffler, M. Weckesser, C. Franzius, O. Schober, and K.-P. Zimmer, "High diagnostic value of 18F-FDG-PET in pediatric patients with chronic inflammatory bowel disease," *Annals of the New York Academy of Sciences*, vol. 1072, pp. 379–385, 2006.
- [66] R. S. Meisner, B. J. Spier, S. Einarsson et al., "Pilot study using PET/CT as a novel, noninvasive assessment of disease activity in inflammatory bowel disease," *Inflammatory Bowel Diseases*, vol. 13, no. 8, pp. 993–1000, 2007.
- [67] M. Neurath, D. Vehling, K. Schunk et al., "Noninvasive assessment of Crohn's disease activity: a comparison of 18F-fluorodeoxyglucose positron emission tomography, hydromagnetic resonance imaging, and granulocyte scintigraphy with labeled antibodies," *The American Journal of Gastroenterology*, vol. 97, no. 8, pp. 1978–1985, 2002.
- [68] J. Däbritz, N. Jasper, M. Loeffler, M. Weckesser, and D. Foell, "Noninvasive assessment of pediatric inflammatory bowel disease with 18F-fluorodeoxyglucose-positron emission tomography and computed tomography," *European Journal of Gastroenterology and Hepatology*, vol. 23, no. 1, pp. 81–89, 2011.
- [69] G. Treglia, N. Quartuccio, R. Sadeghi et al., "Diagnostic performance of Fluorine-18-Fluorodeoxyglucose positron emission tomography in patients with chronic inflammatory bowel disease: a systematic review and a meta-analysis," *Journal of Crohn's and Colitis*, vol. 7, no. 5, pp. 345–354, 2013.
- [70] Y. Katz, A. Eitan, Z. Amiri, and M. Gavish, "Dramatic increase in peripheral benzodiazepine binding sites in human colonic adenocarcinoma as compared to normal colon," *European Journal of Pharmacology*, vol. 148, no. 3, pp. 483–484, 1988.
- [71] K. Maaser, "Up-Regulation of the Peripheral Benzodiazepine Receptor during Human Colorectal Carcinogenesis and Tumor Spread," *Clinical Cancer Research*, vol. 11, no. 5, pp. 1751–1756, 2005.
- [72] P. Grabowski, K. Maaser, and I. Schindler, "Overexpression of the peripheral benzodiazepine receptor is a relevant prognostic factor in stage III colorectal cancer," *Clinical Cancer Research*, vol. 8, no. 10, pp. 3205–3209, 2002.
- [73] M. A. Ostuni, L. Issop, G. Péranzi et al., "Overexpression of translocator protein in inflammatory bowel disease: potential diagnostic and treatment value," *Inflammatory Bowel Diseases*, vol. 16, no. 9, pp. 1476–1487, 2010.
- [74] D. H. Seo, X. Che, M. S. Kwak et al., "Interleukin-33 regulates intestinal inflammation by modulating macrophages in inflammatory bowel disease," *Scientific Reports*, vol. 7, no. 1, 2017.
- [75] C. J. Beltrán, L. E. Núñez, D. Díaz-Jiménez et al., "Characterization of the novel ST2/IL-33 system in patients with inflammatory bowel disease," *Inflammatory Bowel Diseases*, vol. 16, no. 7, pp. 1097–1107, 2010.
- [76] V. Papadopoulos, M. Baraldi, T. R. Guilarte et al., "Translocator protein (18 kDa): new nomenclature for the peripheral-type benzodiazepine receptor based on its structure and molecular function," *Trends in Pharmacological Sciences*, vol. 27, no. 8, pp. 402–409, 2006.

- [77] S. Savino, N. Denora, R. M. Iacobazzi et al., "Synthesis, Characterization, and Cytotoxicity of the First Oxaliplatin Pt(IV) Derivative Having a TSPO Ligand in the Axial Position," *International Journal of Molecular Sciences*, vol. 17, no. 7, 2016.
- [78] M. Liu, Y. Dou, R. Sun, Y. Zhang, and Y. Liu, "Molecular Mechanisms for Alcoholic Hepatitis Based on Analysis of Gene Expression Profile," *Hepatitis Monthly*, vol. 15, no. 5, p. e27336, 2015.
- [79] L. Xie, J. Yui, A. Hatori et al., "Translocator protein (18 kDa), a potential molecular imaging biomarker for non-invasively distinguishing non-alcoholic fatty liver disease," *Journal of Hepatology*, vol. 57, no. 5, pp. 1076–1082, 2012.
- [80] A. Hatori, J. Yui, L. Xie et al., "Utility of Translocator Protein (18 kDa) as a Molecular Imaging Biomarker to Monitor the Progression of Liver Fibrosis," *Scientific Reports*, vol. 5, no. 1, 2015.
- [81] R. Fischer, M. Schmitt, J. G. Bode, and D. Häussinger, "Expression of the peripheral-type benzodiazepine receptor and apoptosis induction in hepatic stellate cells," *Gastroenterology*, vol. 120, no. 5, pp. 1212–1226, 2001.
- [82] E. Campioli, G. Carnevale, R. Avallone, D. Guerra, and M. Baraldi, "Morphological and receptorial changes in the epididymal adipose tissue of rats subjected to a stressful stimulus," *Obesity*, vol. 19, no. 4, pp. 703–708, 2011.
- [83] N. Wang, H. Liang, and K. Zen, "Molecular mechanisms that influence the macrophage M1-M2 polarization balance," *Frontiers in Immunology*, vol. 5, article 614, 2014.
- [84] S. Capitanio, A. J. Nordin, A. R. Noraini, and C. Rossetti, "PET/CT in nononcological lung diseases: Current applications and future perspectives," *European Respiratory Review*, vol. 25, no. 141, pp. 247–258, 2016.
- [85] H. M. Branley, R. M. du Bois, A. U. Wells, and H. A. Jones, "PET scanning of macrophages in patients with scleroderma fibrosing alveolitis," *Nuclear Medicine and Biology*, vol. 35, no. 8, pp. 901–909, 2008.
- [86] S. Goel and R. Gadiraju, "Diffuse lung uptake of ¹¹¹In octreotide from chronic emphysema," *Journal of Nuclear Medicine Technology*, vol. 41, no. 2, pp. 117–118, 2013.
- [87] S. H. Saverymuttu, G. Phillips, A. M. Peters, and J. P. Lavender, "Indium ¹¹¹ autologous leucocyte scanning in lobar pneumonia and lung abscesses," *Thorax*, vol. 40, no. 12, pp. 925–930, 1985.
- [88] H. A. Jones, S. Sriskandan, A. M. Peters et al., "Dissociation of neutrophil emigration and metabolic activity in lobar pneumonia and bronchiectasis," *European Respiratory Journal*, vol. 10, no. 4, pp. 795–803, 1997.
- [89] E. Bribe, D. Carrière, C. Goubet, S. Galiègue, P. Casellas, and S. Joëlle, "Immunohistochemical Assessment of the Peripheral Benzodiazepine Receptor in Human Tissues," *Journal of Histochemistry & Cytochemistry*, vol. 52, no. 1, pp. 19–28, 2016.
- [90] J. C. Mak and P. J. Barnes, "Peripheral type benzodiazepine receptors in human and guinea pig lung: characterization and autoradiographic mapping," *Journal of Pharmacology and Experimental Therapeutics*, vol. 252, pp. 880–885, 1990.
- [91] H. A. Jones, S. O. Valind, I. C. Clark et al., "Kinetics of lung macrophages monitored in vivo following particulate challenge in rabbits," *Toxicology and Applied Pharmacology*, vol. 183, no. 1, pp. 46–54, 2002.
- [92] L. Zuo, K. Lucas, C. A. Fortuna, C. Chuang, and T. M. Best, "Molecular regulation of toll-like receptors in asthma and COPD," *Frontiers in Physiology*, vol. 6, article 312, 2015.
- [93] Y. Duan, M. Zhou, J. Xiao et al., "Prediction of key genes and miRNAs responsible for loss of muscle force in patients during an acute exacerbation of chronic obstructive pulmonary disease," *International Journal of Molecular Medicine*, vol. 38, no. 5, pp. 1450–1462, 2016.
- [94] Y. Chen and J. Qiao, "Protein-protein interaction network analysis and identifying regulation microRNAs in asthmatic children," *Allergologia et Immunopathologia*, vol. 43, no. 6, pp. 584–592, 2015.
- [95] T. Becker, F.-N. Vögtle, D. Stojanovski, and C. Meisinger, "Sorting and assembly of mitochondrial outer membrane proteins," *Biochimica et Biophysica Acta - Bioenergetics*, vol. 1777, no. 7–8, pp. 557–563, 2008.
- [96] J. Gatliff, D. East, J. Crosby et al., "TSPO interacts with VDAC1 and triggers a ROS-mediated inhibition of mitochondrial quality control," *Autophagy*, vol. 10, no. 12, pp. 2279–2296, 2015.
- [97] F. Li, J. Liu, N. Liu, L. A. Kuhn, R. M. Garavito, and S. Ferguson-Miller, "Translocator Protein 18 kDa (TSPO): An Old Protein with New Functions?" *Biochemistry*, vol. 55, no. 20, pp. 2821–2831, 2016.
- [98] O. A. Jaffer, A. B. Carter, P. N. Sanders et al., "Mitochondrial-Targeted Antioxidant Therapy Decreases Transforming Growth Factor- β -Mediated Collagen Production in a Murine Asthma Model," *American Journal of Respiratory Cell and Molecular Biology*, vol. 52, no. 1, pp. 106–115, 2015.
- [99] D. J. Rowlands, "Mitochondria dysfunction: a novel therapeutic target in pathological lung remodeling or bystander?" *Pharmacology and Therapeutics*, vol. 166, pp. 96–105, 2016.
- [100] H. A. Jones, P. S. Marino, B. H. Shakur, and N. W. Morrell, "In vivo assessment of lung inflammatory cell activity in patients with COPD and asthma," *European Respiratory Journal*, vol. 21, no. 4, pp. 567–573, 2003.
- [101] M. Gavish, S. Cohen, and R. Nagler, "Cigarette smoke effects on TSPO and VDAC expression in a cellular lung cancer model," *European Journal of Cancer Prevention*, vol. 25, no. 5, pp. 361–367, 2016.
- [102] H. M. Branley, R. M. du Bois, A. U. Wells, and H. A. Jones, "Peripheral-type benzodiazepine receptors in bronchoalveolar lavage cells of patients with interstitial lung disease," *Nuclear Medicine and Biology*, vol. 34, no. 5, pp. 553–558, 2007.
- [103] R. M. Silver, K. S. Miller, M. B. Kinsella, E. A. Smith, and S. I. Schabel, "Evaluation and management of scleroderma lung disease using bronchoalveolar lavage," *The American Journal of Medicine*, vol. 88, no. 5, pp. 470–476, 1990.
- [104] S. H. Audi, C. A. Dawson, S. B. Ahlf, and D. L. Roerig, "Lung tissue mitochondrial benzodiazepine receptors increase in a model of pulmonary inflammation," *Lung*, vol. 180, no. 5, pp. 241–250, 2002.
- [105] X. Qi, J. Xu, F. Wang, and J. Xiao, "Translocator protein (18 kDa): A promising therapeutic target and diagnostic tool for cardiovascular diseases," *Oxidative Medicine and Cellular Longevity*, Article ID 162934, 2012.
- [106] C. M. Weyand and J. J. Goronzy, "Medium- and Large-Vessel Vasculitis," *New England Journal of Medicine*, vol. 349, no. 2, pp. 160–169, 2003.
- [107] F. D. Carmona, P. Coit, G. Saruhan-Direskeneli et al., "Analysis of the common genetic component of large-vessel vasculitides through a meta-immunochip strategy," *Scientific Reports*, vol. 7, p. 43953, 2017.
- [108] F. D. Carmona, S. L. Mackie, J.-E. Martín et al., "A large-scale genetic analysis reveals a strong contribution of the HLA class

- II region to giant cell arteritis susceptibility," *American Journal of Human Genetics*, vol. 96, pp. 565–580, 2015.
- [109] G. Saruhan-Direskeneli, T. Hughes, K. Aksu et al., "Identification of Multiple Genetic Susceptibility Loci in Takayasu Arteritis," *American Journal of Human Genetics*, vol. 93, pp. 298–305, 2013.
- [110] F. Lamare, R. Hinz, O. Gaemperli et al., "Detection and Quantification of Large-Vessel Inflammation with ^{11}C -(R)-PK11195 PET/CT," *Journal of Nuclear Medicine*, vol. 52, no. 1, pp. 33–39, 2010.
- [111] B. Seeliger, J. Sznajd, J. C. Robson et al., "Are the 1990 American College of Rheumatology vasculitis classification criteria still valid?" *Rheumatology*, vol. 56, no. 7, pp. 1154–1161, 2017.
- [112] A. Lekic, Z. Brekalo, A. Kvesic et al., "Cross-talk Between Enzymes Matrix-metalloproteinase 2 and 9 and Regulatory T-cell Immunity in the Global Burden of Atherosclerosis," *Scandinavian Journal of Immunology*, vol. 86, no. 1, pp. 65–71, 2017.
- [113] P. Libby, "Inflammation in atherosclerosis," *Nature*, vol. 420, no. 6917, pp. 868–874, 2002.
- [114] Q. Li, Y. Wang, H. Li, G. Shen, and S. Hu, "Ox-LDL influences peripheral Th17/treg balance by modulating treg apoptosis and Th17 proliferation in atherosclerotic cerebral infarction," *Cellular Physiology and Biochemistry*, vol. 33, no. 6, pp. 1849–1862, 2014.
- [115] A. M. Lundberg and G. K. Hansson, "Innate immune signals in atherosclerosis," *Clinical Immunology*, vol. 134, no. 1, pp. 5–24, 2010.
- [116] N. Sasaki, T. Yamashita, M. Takeda, and K.-I. Hirata, "Regulatory T cells in atherogenesis," *Journal of Atherosclerosis and Thrombosis*, vol. 19, no. 6, pp. 503–515, 2012.
- [117] J. M. W. Taylor, A.-M. Allen, and A. Graham, "Targeting mitochondrial 18 kDa translocator protein (TSPO) regulates macrophage cholesterol efflux and lipid phenotype," *Clinical Science*, vol. 127, no. 10, pp. 603–613, 2014.
- [118] L. Veenman, V. Papadopoulos, and M. Gavish, "Channel-like functions of the 18-kDa translocator protein (TSPO): Regulation of apoptosis and steroidogenesis as part of the host-defense response," *Current Pharmaceutical Design*, vol. 13, no. 23, pp. 2385–2405, 2007.
- [119] L. Veenman and M. Gavish, "The peripheral-type benzodiazepine receptor and the cardiovascular system. Implications for drug development," *Pharmacology and Therapeutics*, vol. 110, no. 3, pp. 503–524, 2006.
- [120] S. Cuhlmann, W. Gsell, K. Van Der Heiden et al., "In vivo mapping of vascular inflammation using the translocator protein tracer 18F-FEDAA1106," *Molecular Imaging*, vol. 13, no. 6, 2014.
- [121] S. Hellberg, J. M. Silvola, M. Kiugel et al., "18-kDa translocator protein ligand 18F-FEMPA: biodistribution and uptake into atherosclerotic plaques in mice," *Journal of Nuclear Cardiology*, vol. 24, no. 3, pp. 862–871, 2017.
- [122] O. Gaemperli, J. Shalhoub, and D. R. J. Owen, "Imaging intraplaque inflammation in carotid atherosclerosis with ^{11}C -PK11195 positron emission tomography/computed tomography," *European Heart Journal*, vol. 33, no. 15, pp. 1902–1910, 2012.
- [123] G. Chinetti-Gbaguidi, M. Daoudi, M. Rosa et al., "Human Alternative Macrophages Populate Calcified Areas of Atherosclerotic Lesions and Display Impaired RANKL-Induced Osteoclastic Bone Resorption Activity Novelty and Significance," *Circulation Research*, vol. 121, no. 1, pp. 19–30, 2017.
- [124] J. Dimitrova-Shumkovska, L. Veenman, T. Ristoski, S. Leschiner, and M. Gavish, "Chronic high fat, high cholesterol supplementation decreases 18 kDa Translocator Protein binding capacity in association with increased oxidative stress in rat liver and aorta," *Food and Chemical Toxicology*, vol. 48, no. 3, pp. 910–921, 2010.
- [125] C. J. van der Laken, E. H. Elzinga, and M. A. Kroppholler, "Noninvasive imaging of macrophages in rheumatoid synovitis using ^{11}C -(R)-PK11195 and positron emission tomography," *Arthritis & Rheumatism*, vol. 58, no. 11, pp. 3350–3355, 2008.
- [126] V. F. Derksen, T. W. Huizinga, and D. van der Woude, "The role of autoantibodies in the pathophysiology of rheumatoid arthritis," *Seminars in Immunopathology*, vol. 39, no. 4, pp. 437–446, 2017.
- [127] E. S. Norli, G. H. Brinkmann, T. K. Kvien et al., "Self-limiting arthritis among patients fulfilling the 2010 ACR/EULAR classification criteria for rheumatoid arthritis in a very early arthritis cohort," *Seminars in Arthritis and Rheumatism*, vol. 46, no. 3, pp. 272–278, 2016.
- [128] X. Shao, X. Wang, S. J. English et al., "Imaging of carrageenan-induced local inflammation and adjuvant-induced systemic arthritis with ^{11}C PBR28 PET," *Nuclear Medicine and Biology*, vol. 40, no. 7, pp. 906–911, 2013.
- [129] Y. Y. J. Gent, K. Weijers, C. F. M. Molthoff et al., "Promising potential of new generation translocator protein tracers providing enhanced contrast of arthritis imaging by positron emission tomography in a rat model of arthritis," *Arthritis Research and Therapy*, vol. 16, no. 2, article R70, 2014.
- [130] G. Pottier, N. Bernards, F. Dollé, and R. Boisgard, " ^{18}F DPA-714 as a biomarker for positron emission tomography imaging of rheumatoid arthritis in an animal model," *Arthritis Research & Therapy*, vol. 16, no. 2, article R69, 2014.
- [131] M. Politis, N. Lahiri, F. Niccolini et al., "Increased central microglial activation associated with peripheral cytokine levels in premanifest Huntington's disease gene carriers," *Neurobiology of Disease*, vol. 83, pp. 115–121, 2015.
- [132] L. Hamelin, J. Lagarde, G. Dorothée et al., "Early and protective microglial activation in Alzheimer's disease: A prospective study using 18F-DPA-714 PET imaging," *Brain*, vol. 139, no. 4, pp. 1252–1264, 2016.
- [133] B. Zinnhardt, T. Viel, L. Wachsmuth et al., "Multimodal imaging reveals temporal and spatial microglia and matrix metalloproteinase activity after experimental stroke," *Journal of Cerebral Blood Flow & Metabolism*, 2015.
- [134] T. Notter, J. M. Coughlin, T. Gschwind et al., "Translational evaluation of translocator protein as a marker of neuroinflammation in schizophrenia," *Molecular Psychiatry*, 2017.
- [135] P. Iversen, D. A. Hansen, D. Bender et al., "Peripheral benzodiazepine receptors in the brain of cirrhosis patients with manifest hepatic encephalopathy," *European Journal of Nuclear Medicine and Molecular Imaging*, vol. 33, no. 7, pp. 810–816, 2006.
- [136] E. Kurtys, J. Doorduyn, U. L. M. Eisel, R. A. J. O. Dierckx, and E. F. J. de Vries, "Evaluating ^{11}C PBR28 PET for Monitoring Gut and Brain Inflammation in a Rat Model of Chemically Induced Colitis," *Molecular Imaging and Biology*, vol. 19, no. 1, pp. 68–76, 2017.
- [137] J. H. Vera, Q. Guo, J. H. Cole et al., "Neuroinflammation in treated HIV-positive individuals: A TSPO PET study," *Neurology*, vol. 86, no. 15, pp. 1425–1432, 2016.
- [138] J. Hannestad, J.-D. Gallezot, T. Schafbauer et al., "Endotoxin-induced systemic inflammation activates microglia: ^{11}C PBR28

positron emission tomography in nonhuman primates,” *NeuroImage*, vol. 63, no. 1, pp. 232–239, 2012.

- [139] L. Beckers, D. Ory, I. Geric et al., “Increased Expression of Translocator Protein (TSPO) Marks Pro-inflammatory Microglia but Does Not Predict Neurodegeneration,” *Molecular Imaging and Biology*.
- [140] C. Wu, X. Yue, L. Lang et al., “Longitudinal PET imaging of muscular inflammation using ¹⁸F-DPA-714 and ¹⁸F-alfatide II and differentiation with tumors,” *Theranostics*, vol. 4, no. 5, pp. 546–555, 2014.

Clinical Study

Correlation of 18F-FDG PET/MRE Metrics with Inflammatory Biomarkers in Patients with Crohn's Disease: A Pilot Study

Liran Domachevsky,¹ Haim Leibovitzh,² Irit Avni-Biron,²
Lev Lichtenstein,² Natalia Goldberg,¹ Meital Nidam,¹ David Groshar,¹
Hanna Bernstine,¹ and Ofer Ben-Bassat²

¹Department of Nuclear Medicine, Assuta Medical Centers and Sackler Faculty of Medicine, Tel Aviv University, Tel Aviv, Israel

²IBD Center, Division of Gastroenterology, Rabin Medical Center, Petah Tikva, Israel

Correspondence should be addressed to Liran Domachevsky; liranura@gmail.com

Received 25 May 2017; Accepted 3 August 2017; Published 19 September 2017

Academic Editor: Cristina Nanni

Copyright © 2017 Liran Domachevsky et al. This is an open access article distributed under the Creative Commons Attribution License, which permits unrestricted use, distribution, and reproduction in any medium, provided the original work is properly cited.

Background. To investigate the association between 18F-FDG (Fluorodeoxyglucose) PET (positron emission tomography)/MRE (magnetic resonance enterography) metrics with the inflammatory biomarkers fecal calprotectin and C-reactive protein (CRP) in patients with Crohn's disease (CD). **Methods.** This prospective pilot study was institutional review board (IRB) approved with informed consent obtained. Consecutive CD patients were referred to 18F-FDG PET/MRE. Patients in whom colonoscopy was performed and CRP and fecal calprotectin levels were measured were included. CRP and fecal calprotectin were regarded as positive for inflammation if they were greater than 0.5 mg/dl and 150 mcg/g, respectively. Correlation of quantitative variables was performed using the Pearson's correlation coefficient. Receiver operating characteristic (ROC) curves were drawn and the area under the curve (AUC) was calculated to evaluate the accuracy of PET and MRE metrics in determining the presence of inflammation evaluated by calprotectin and CRP levels. **Results.** Analysis of 21 patients (16 women and 5 men, 43 ± 18 years) was performed. Magnetic resonance index of activity (MaRIA) score had an AUC of 0.63 associated with fecal calprotectin and CRP. Adding apparent diffusion coefficient (ADC) and metabolic inflammatory volume (MIV) to MaRIA score resulted in an AUC of 0.92 with a cutoff value of 447 resulting in 83% and 100% sensitivity and specificity, respectively. **Conclusion.** The addition of ADC and MIV to the MaRIA score increases the accuracy for discrimination of disease activity in patients with CD. *Trial registration number* is 2015062.

1. Introduction

Crohn's disease (CD) is a chronic, relapsing, transmural inflammatory disease that can affect the entire gastrointestinal track [1]. Diagnosis and treatment assessment are based on clinical, endoscopic and cross-sectional imaging. However, clinical symptoms and clinical scores do not always correlate with endoscopic findings [2] and have not changed the long-term outcome in patients with CD [3]. Endoscopy on the other hand is very accurate in the assessment of early manifestations and enables histological evaluation of inflammation; however, it is an invasive tool that assesses the mucosal layer and only a short segment of the small bowel (i.e., terminal ileum).

The introduction of "treat to target" paradigm in CD with mucosal healing defined as the target, has led to search for convenient, reliable, and quantifiable variables to predict and assess the response to therapy and to monitor CD patients [3]. At present, C-reactive protein (CRP) and fecal calprotectin are the most widely used inflammatory biomarkers as a surrogate to endoscopy to monitor patients with CD [4]. Nevertheless, both tests have limitations and more objective tools are required.

Computerized tomography enterography (CTE) and Magnetic resonance enterography (MRE) are complementary diagnostic tools in the work-up of patients with CD as both can identify pathological processes in deeper layers of the

bowel and extraintestinal findings and evaluate the entire GI tract.

MRE has gained popularity given the lack of ionizing radiation [5], high contrast resolution, and the ability to perform dynamic contrast imaging. It was shown to have similar diagnostic accuracy as compared to CTE [6]. The addition of more advanced sequences such as diffusion weighted imaging (DWI) has increased the diagnostic accuracy [6]. Magnetic resonance index of activity (MaRIA) is MRE-based score that has been found to be reliable in quantifying the severity of the inflammatory processes in patients with CD and in assessing the response to therapy [7].

18-Fluorodeoxyglucose (18F-FDG) uptake is seen in metabolically active cells including inflammatory cells. Increased 18F-FDG uptake on PET/CTE was proven to be sensitive (54–98%) and specific (55–81%) in identifying active inflammatory segments of the small and large bowel in patients with CD. Uptake can be assessed qualitatively and semiquantitatively and therefore can be used to evaluate objectively the degree of inflammation and response to treatment [8]. However, given the high patient radiation dose, the study has not gained popularity, particularly as most patients with CD are young and repeated studies are necessary.

Simultaneous 18F-FDG PET/MRE might combine the advantages of both modalities. Several studies have recently demonstrated the feasibility of PET/MRE [9] and have shown the superiority of PET/MRE compared to PET/CT and MRE in the detection of extraluminal disease and in differentiating fibrotic from inflammatory components [10]. The aim of this prospective pilot study is to evaluate the association between 18F-FDG PET/MRE metrics with the inflammatory biomarkers fecal calprotectin and CRP.

2. Materials and Methods

This prospective study has been approved by the institutional review board. All subjects signed an informed consent form. Between December 2015 and December 2016, consecutive patients with newly diagnosed CD or patients with a known CD presenting with a flare-up were referred to 18F-FDG PET/MRE. All patients were off corticosteroid or biologic treatment. Patients were included in the study only if colonoscopy and laboratory work-up have been performed prior to or after 18F-FDG PET/MRE within 6 and 2 weeks, respectively. Laboratory work-up included fecal calprotectin, blood C-reactive protein (CRP) levels, white blood cell counts (WBC), platelets count, hemoglobin, hematocrit, creatinine, and albumin levels. CRP and fecal calprotectin were regarded as positive for inflammation if greater than 0.5 mg/dl and 150 mcg/g, respectively.

2.1. 18 F FDG PET/MRE Protocol. Patients were required to fast at least for 4 hours prior to arrival to the department. Upon arrival an intravenous catheter was placed for radiopharmaceutical administration, and for glucose level measurement. Patients received an intravenous injection of 3–4 mCi of 18F FDG (estimated effective dose of 1.87–2.5 mSv [11]). During the 18F FDG uptake phase of 45 minutes, patients were asked to drink a total volume of 2 ml/kg Avilac

syrup 66.7 g/100 ml–300 ml (Perrigo, IL) diluted in 1000 ml of water (i.e., a total of 1050–1200 ml, 175–200 ml every 7 minutes for 42 minutes) for optimal small bowel distention and to achieve high contrast resolution between bowel wall and lumen on T2 weighted and postcontrast imaging.

18F-FDG PET/MR was performed from the diaphragm to the mid-thigh on the Biograph mMR (Siemens AG, healthcare sector, Erlangen, Germany) simultaneous PET/MR system. Patients were positioned supine and multistep/multibed scanning was performed in caudocranial direction with two bed positions. We used a 24-channel spine RF coil integrated within the MR bed and 2 surface body coils (6 channel each) to cover the abdomen and pelvis. MR sequences included coronal thick slab T2-weighted image to determine that oral contrast has reached the right colon followed by intramuscular injection of 1 mg Glucagon is administered. Coronal and axial (with and without fat suppression) T2-weighted half-Fourier acquisition single shot turbo spin echo (HASTE) image, axial T1-weighted volumetric interpolated breath-hold examination (VIBE) (with and without fat suppression), DWI ($b = 50, 500, 1000, \text{ and } 1600 \text{ sec/mm}^2$), coronal T1-weighted nonenhanced VIBE image and gadolinium enhanced coronal T1-weighted VIBE image with 30 and 70 seconds delays, and axial T1-weighted VIBE image with 95 seconds delay. We used Gadoteric acid (Dotarem®, Guerbet, France) (0.2 ml/kg, 0.1 mmol/kg at 1–2 ml/s, 20 ml saline flush) as intravenous contrast media.

PET data was acquired in the list mode with the following reconstruction parameters: High definition PET + ordered subset expectation maximization (OSEM) iterative algorithm, three iteration and 21 subsets, Gaussian filter: FWHM 4 mm; relative scattered correction.

2.2. Image Analysis

2.2.1. PET Metrics. We used dedicated software for PET metric measurements (Syngo.via; Siemens AG, healthcare sector, Erlangen, Germany). A sphere VOI was drawn on bowel segments with pathological 18F FDG uptake (i.e., above physiological 18F FDG uptake in normal appearing bowel segments) and SUVmax was calculated. The metabolic inflammatory volume (MIV) was meticulously calculated using isocontour application with spheres drawn over bowel segments with increased FDG uptake using a fixed 40% threshold (Figure 1). To avoid false positive FDG uptake due to physiologic activity all segments were compared with MR images to confirm abnormal appearance on MR. All spherical VOI were visually evaluated on axial, sagittal, and coronal planes to be certain that the VOI is well located. In addition, the length of visually pathological FDG-avid segments was measured.

Normalization for body weight was performed using the patient weight in kg, measured before 18F FDG injection.

2.2.2. MRI Metrics. The following variables were evaluated [1]: Bowel wall thickness measured in mm, edema (i.e., high signal on T2-weighted imaged with fat suppression), bowel wall enhancement (i.e., higher than the enhancement of normal appearing segment), mesenteric vascularity (comb

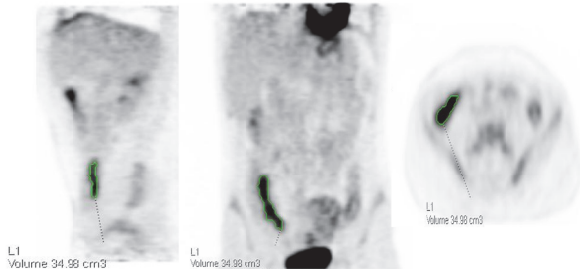


FIGURE 1: Metabolic inflammatory volume (MIV) calculation using isocontour application with spheres drawn over bowel segments with increased FDG uptake using a fixed 40% threshold.

sign) and edema, the presence of enlarged mesenteric lymph nodes, the presence of ulcer/fistula/fibrosis or abscess, and the length of the visually abnormal appearing segments measured on MRI and PET images. In case of skip lesions the sum of lengths was calculated.

DWI/ADC: region of interest (ROI) was placed over different locations in the affected segments with the highest signal intensity on DWI. The minimal ADC value was recorded.

MaRIA score [12]: $1.5 \times \text{wall thickness (mm)} + 0.02 \times \text{relative contrast enhancement (RCE)} + 5 \times \text{edema} + 10 \times \text{ulceration}$. $\text{RCE} = (\text{wall signal intensity (WSI)} \text{ after gadolinium} - \text{WSI before gadolinium}) / (\text{WSI before gadolinium}) \times 100 \times \text{SD noise before gadolinium} / \text{SD noise after gadolinium}$.

All measurements were conducted in consensus by a dual board-certified in radiology and nuclear medicine physician (LD, with 6 years of experience) and a board-certified nuclear medicine physician (HB, with 10 years of PET/CT experience).

2.3. *Statistical Analysis.* Correlation of quantitative variables was performed using the Pearson's correlation coefficient.

Receiver operating characteristic (ROC) curves were drawn and the area under the curve (AUC) was calculated to evaluate the accuracy of different PET and MRE metrics in determining the presence or lack of inflammation evaluated by calprotectin and CRP levels either separately or combined.

$p \leq 0.05$ was considered statistically significant. All data was analyzed using Medcalc (version 17.5.5, 2017).

3. Results

Twenty-seven consecutive patients (20 women and 7 men, 42 ± 15 years) were prospectively recruited to the study. All patients underwent 18F-FDG PET/MRE. Analysis was performed on 21 patients (16 women and 5 men, 43 ± 18 years) (three patients had no calprotectin levels available and three refused to undergo colonoscopy).

The length of the involved segments on PET attenuated corrected (AC) images correlated with the length as measured on MRI with R^2 of 0.99 (Figures 2 and 3).

MaRIA score had an AUC of 0.72 associated with fecal calprotectin. Adding ADC and MIV to MaRIA score (i.e., $\text{MaRIA} \times \text{ADC} \times \text{MIV}/1000$) resulted in an AUC of 0.88.

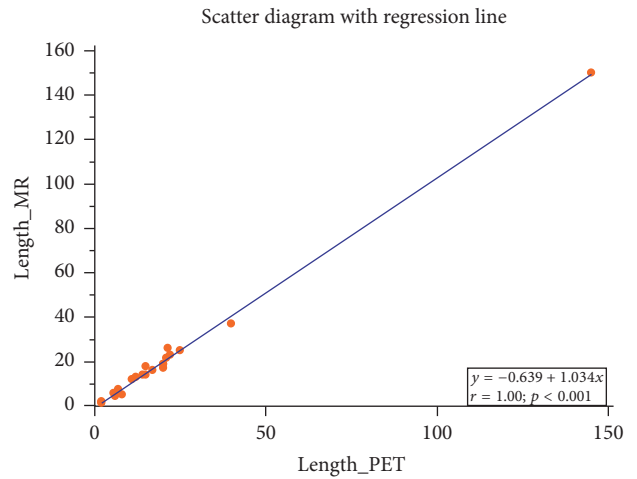


FIGURE 2: Scatter diagram with regression line demonstrating very high correlation between the length of the involved segments measured on PET and MR images.

MaRIA score had an AUC of 0.6 associated with CRP. Combining ADC and MIV to MaRIA score resulted in an AUC of 0.87. When fecal calprotectin and CRP were combined to differentiate active from nonactive disease (i.e., inflammation was determined only if both tests were abnormal), MaRIA score had an AUC of 0.63 associated with fecal calprotectin and CRP. Adding ADC and MIV to MaRIA score resulted in an AUC of 0.92 with a cutoff value of 447 resulting in 83% and 100% sensitivity and specificity, respectively (Figures 4–6). The AUC for SUVmax, SUVmax and MaRIA score and SUVmax, MaRIA score and MIV when fecal calprotectin and CRP were combined was 0.63, 0.6, and 0.8, respectively.

4. Discussion

The results of this pilot study imply that 18F-FDG PET/MRE metrics of MIV and ADC have an added value to MaRIA score in discriminating patients with active from nonactive Crohn's disease based on fecal calprotectin and CRP levels.

At present the diagnosis and treatment of patients with CD rely on clinical and laboratory evaluation, endoscopic assessment, and cross-sectional imaging [13]. However, the new concept of “treat to target” in CD patients, with mucosal healing gaining importance as the target aimed at, necessitates a noninvasive, reliable tool to monitor patients and to assess disease activity. Among several biomarkers that have been proposed to surrogate endoscopy in order to evaluate active inflammation and mucosal healing in CD, fecal calprotectin and CRP are currently the most widely used. Fecal calprotectin is released from human neutrophils and macrophages and reflects mucosal inflammation. It was found to be correlated with endoscopy in detecting disease activity and severity of intestinal inflammation. Abej et al. [14] have shown that stool calprotectin can differentiate active from nonactive disease and correlated with endoscopic findings. Calprotectin has been also used to monitor response to therapy and predict relapse [15]. Sipponen et al. [16]

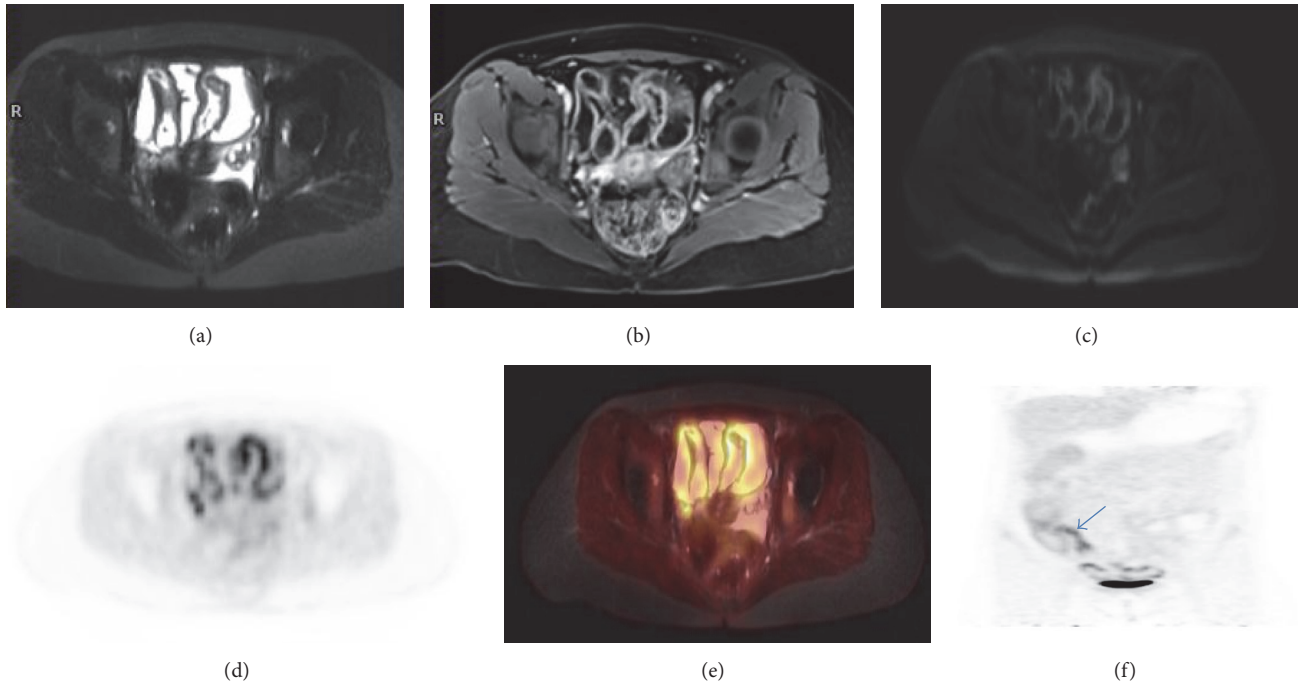


FIGURE 3: 29-year-old woman with CD. (a) Axial T2-weighted FS image demonstrating thickened wall of a long small bowel segment. (b), (c) There is increased enhancement and restricted diffusion of the involved small bowel mucosa seen on axial contrast enhanced T1-weighted and DWI images, respectively. (d) Axial PET attenuation correction image demonstrating FDG uptake along the involved small bowel segments. (e) Axial fused T2-weighted FS PET/MR image demonstrating FDG uptake correlating with thickened small bowel wall. (f) Coronal PET attenuation correction image showing increased FDG uptake in the terminal ileum (arrow) and several small bowel segments. Colonoscopy revealed terminal ileitis that was further confirmed by histology. However, colonoscopy did not reflect the true extent of disease as seen on 18F-FDG PET/MR.

showed that normalization of calprotectin values corresponds to response to therapy on endoscopy while for patients with sustained abnormal values no improvement was seen on endoscopy.

CRP has long become the biomarker of choice for assessment of inflammatory CD activity and was found to be more reliable in cases of transmural inflammation [4]. It is produced and released from hepatocytes and its synthesis is stimulated by interleukin 6 [17]. The relatively short half-life of 19 hours makes it sensitive to early changes in the status of inflammation. CRP has been shown to correlate with clinical activity [18] and endoscopic findings [19] to predict clinical relapse [20] and to assess the response to therapy [21]. However both biomarkers have their pros and cons in determining the status of CD. For example, single nucleotide polymorphism in CRP genes is known to affect the baseline and stimulated CRP levels resulting in false negative results [22]. Additionally, CRP might be less sensitive to mucosal inflammation and hence underestimate subtle inflammatory status. Although fecal calprotectin has proved to be more sensitive as compared to CRP in predicting disease activity on endoscopy [19], it is less reliable in limited ileal disease [23, 24]. The composite use of both biomarkers has been shown to be more specific in detecting the inflammatory status in CD patients [25].

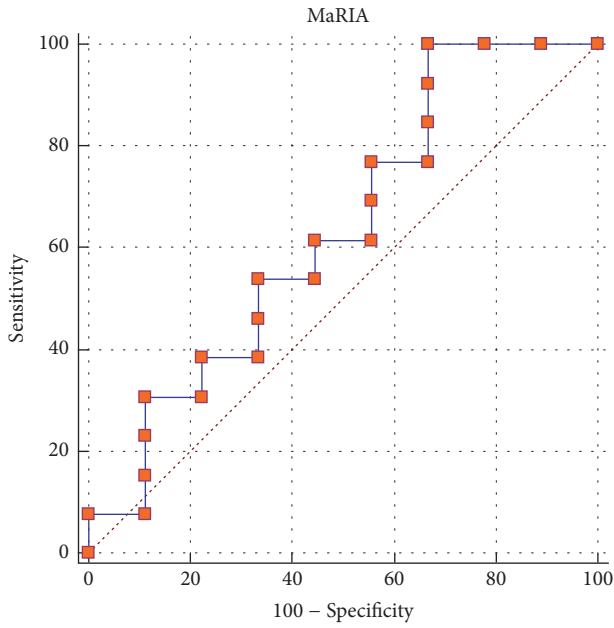
Several MRE severity indices have been proposed and evaluated from which the MaRIA score was found to have

the best overall operational characteristics regarding the detection of active disease and in assessing the severity of disease [12]. This score was correlated to CD endoscopic index of severity and found wall thickness, presence of bowel wall edema, ulcer, and relative contrast enhancement as independent predictors of inflammation activity.

There are conflicting data regarding the correlation of the MaRIA score and inflammatory biomarkers. For instance, Cerrillo et al. [26] found significant correlation between MaRIA index and fecal calprotectin levels with AUC in ROC analysis of 0.914 and a cutoff value of 166.5 mcg/g yielded a 90% sensitivity and 74% specificity for the diagnosis of intestinal inflammation. On the other hand, Abej et al. [14] have shown that fecal calprotectin cutoff level of 250 mcg/g is not correlated with the MaRIA score.

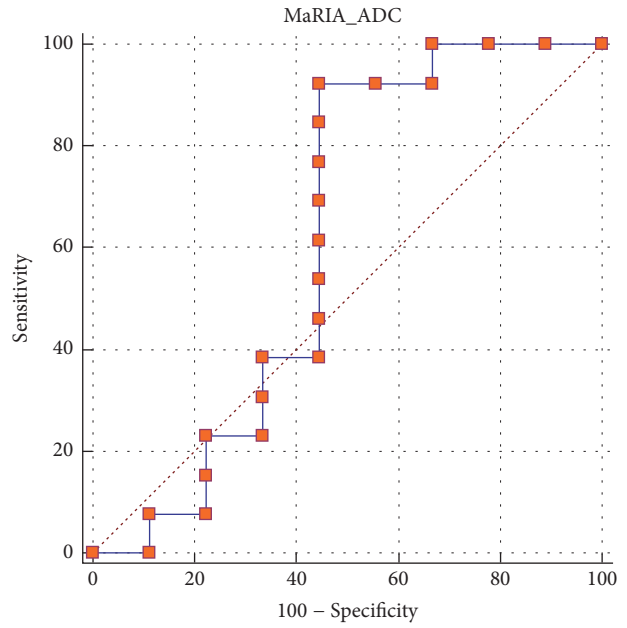
In this study the addition of ADC and MIV to the MaRIA score has increased significantly the accuracy in discriminating active from nonactive disease.

DWI has been correlated with CD inflamed segments and with clinical scores. Stanescu-Siegmund et al. [27] demonstrated in 131 patients that areas of inflammation had significantly lower ADC values compared to normal bowel ($p < 0.001$) with threshold of $1.56 \times 10^{-3} \text{ mm}^2/\text{s}$ having a sensitivity of 97.4% and specificity of 99.2% distinguishing normal and abnormal segments. Kim et al. [28] have shown that DWI increases the sensitivity in the detection of mild inflamed bowel segments with no obvious added value compared to



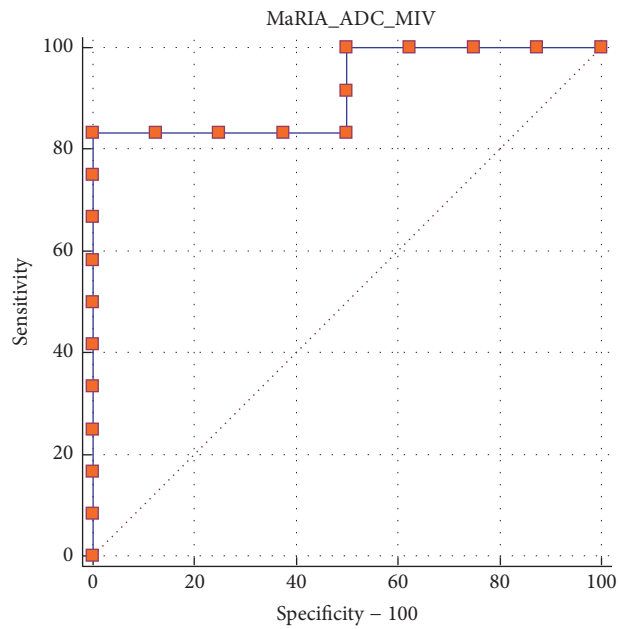
Calprotectin and CRP
AUC = 0.632
Associated criterion > 12.60
Sensitivity 100.00
Specificity 33.33

(a)



Calprotectin and CRP
AUC = 0.615
Associated criterion > 22.90
Sensitivity 92.31
Specificity 55.56

(b)



Calprotectin and CRP
AUC = 0.917
Associated criterion > 446.88
Sensitivity 83.33
Specificity 100.00

(c)

FIGURE 4: Receiver operating characteristic curves using calprotectin and CRP levels to determine active versus nonactive disease with MaRIA (a), MaRIA and ADC (b), and MaRIA, ADC, and MIV (c) as the variables. CRP: C-reactive protein; MaRIA: magnetic resonance index of activity; ADC: apparent diffusion coefficient; MIV: metabolic inflammatory volume.

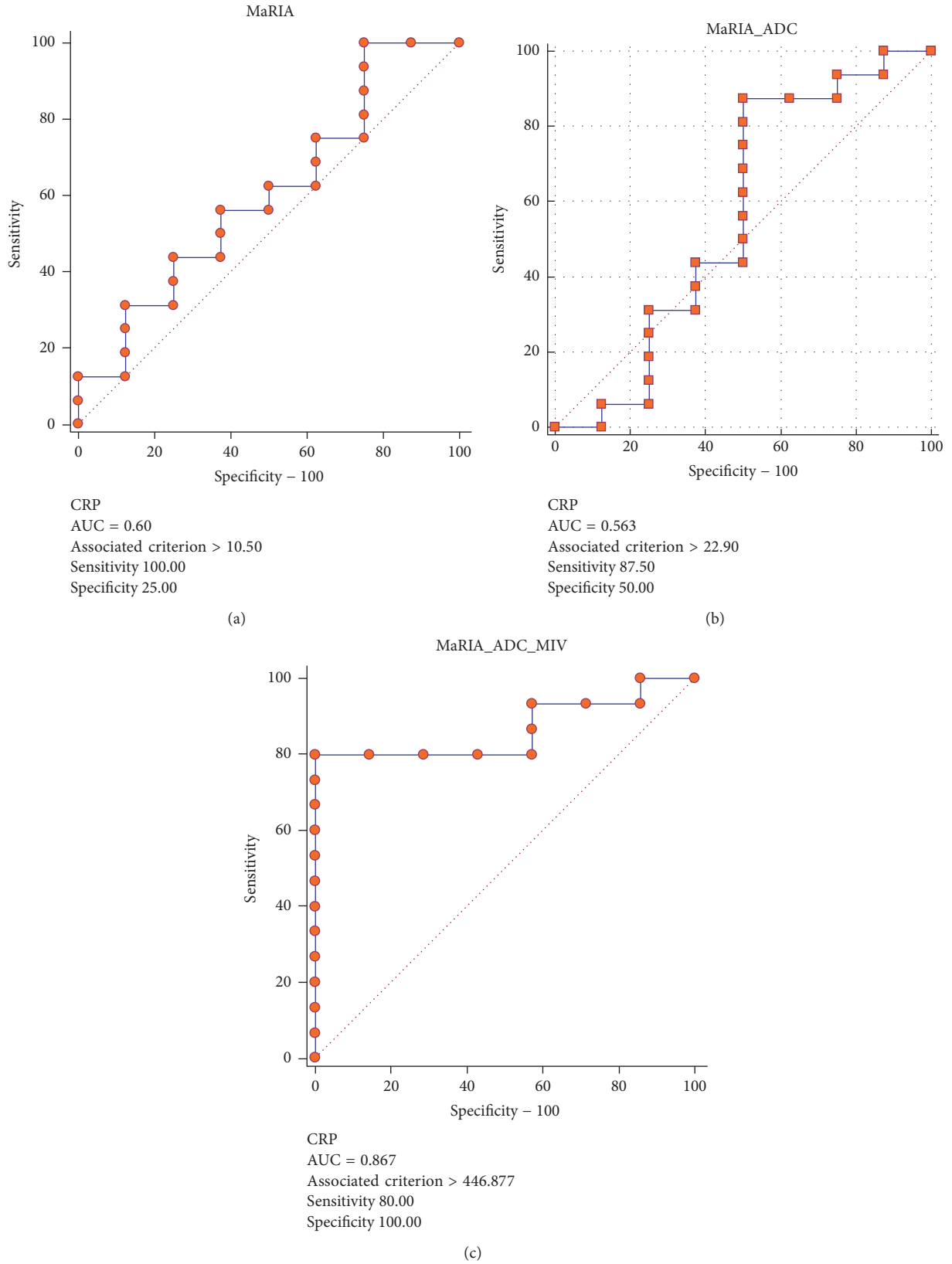


FIGURE 5: Receiver operating characteristic curves using CRP levels to determine active versus nonactive disease with MaRIA (a), MaRIA and ADC (b), and MaRIA, ADC, and MIV (c) as the variables. CRP: C-reactive protein; MaRIA: magnetic resonance index of activity; ADC: apparent diffusion coefficient; MIV: metabolic inflammatory volume.

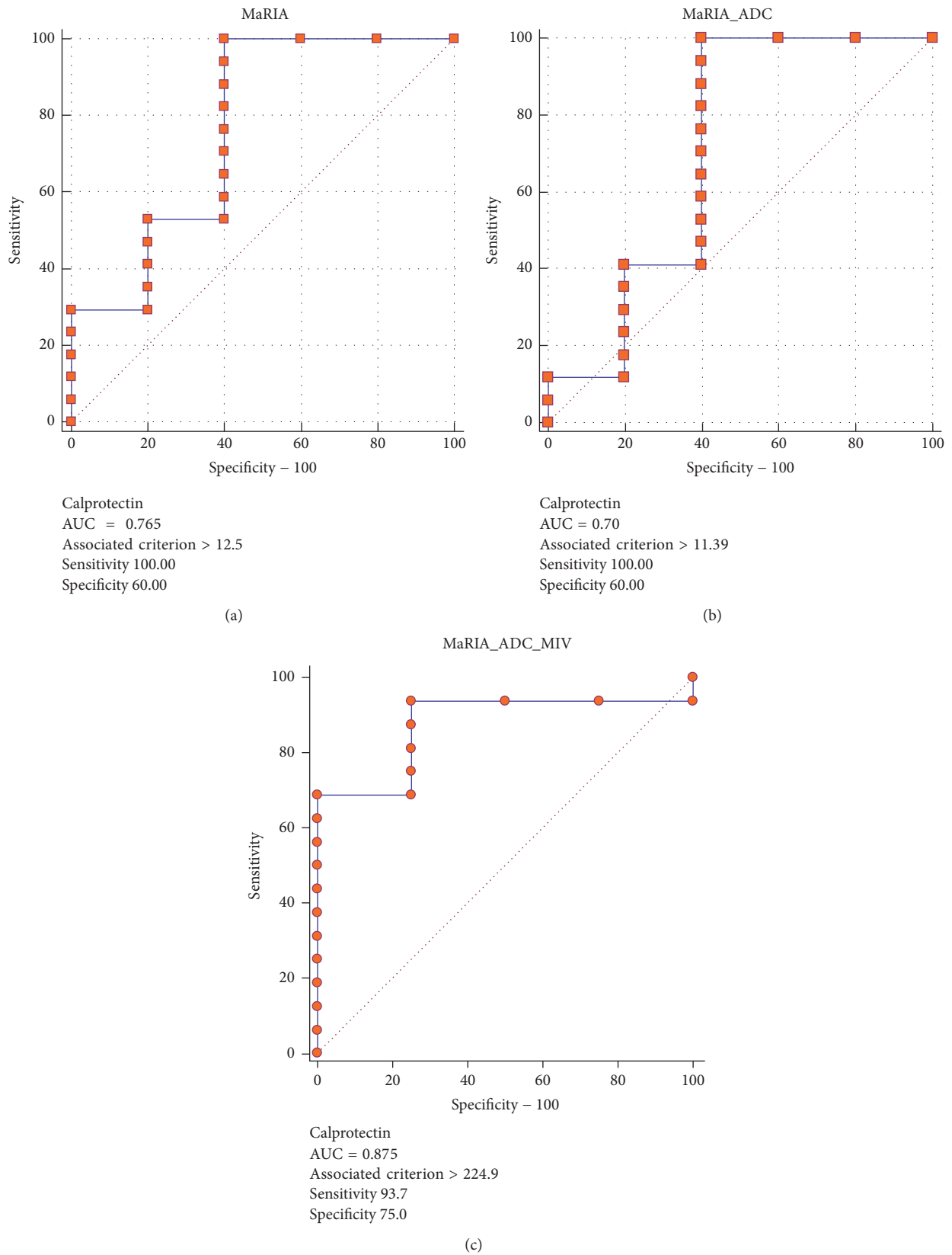


FIGURE 6: Receiver operating characteristic curves using calprotectin levels to determine active versus nonactive disease with MaRIA (a), MaRIA and ADC (b), and MaRIA, ADC, and MIV (c) as the variables. MaRIA: magnetic resonance index of activity; ADC: apparent diffusion coefficient. MIV: metabolic inflammatory volume.

conventional MR sequences in the detection of segments with ulcers. However, the addition of DWI to abnormal segments as seen on conventional MR sequences was correlated with higher endoscopy score (21 ± 10.1 versus 12.6 ± 8.4 ; $p = 0.021$) and the AUC in ROC analysis distinguishing segments with and without ulcers was significantly higher if DWI was added to conventional MR sequences (0.72 versus 0.661; $p = 0.029$). The specificity of DWI in detecting active disease was lower compared to conventional MR mainly due to false positive cases in the colorectal area.

The use of metabolic inflammatory volume in CD patients has been investigated in few studies. Jacene et al. [29] have shown on PET/CT that the product of metabolically active volume (corrected to background) and SUVmean is correlated with Crohn's disease endoscopy index of severity (CDEIS). Russo et al. [30] demonstrated that SUVmax corrected to body lean mass was superior to the total inflammatory volume in differentiating fibrotic from transmural inflammatory stenosis.

Cerrillo et al. [26] have shown that SUV-related metrics on 18F-FDG PET/CT correlated with CRP and recommended its use to monitor longitudinal changes of inflammation.

We found that the use of composite values of fecal calprotectin and CRP in combination to define active versus nonactive CD results in AUC 0.92 (83% sensitivity and 100% specificity using a cutoff value of 447) if MIV and ADC were added to the MaRIA score. This high association of 18F-FDG PET/MRE metrics with inflammatory biomarkers opens new opportunities for monitoring CD patients as both studies are noninvasive, quantifiable, and complementary.

Our study has several limitations: first, the number of patients is too small. Second, given the lack of standardization in DWI sequences and MIV measurements and for PET/MRE in general, a reliability study for these variables should be performed. Third, the low availability and high cost of PET/MR limit its use only to few academic centers.

In conclusion, in this pilot study, the addition of ADC and MIV to the MaRIA score increases the accuracy for discrimination of disease activity in patients with CD. Further larger studies are needed to validate these results and to evaluate if these variables can be used to monitor disease activity in patients with CD.

Disclosure

Liran Domachevsky and Haim Leibovitzh equally contributed as first authors to the manuscript. Hanna Bernstine and Ofer Ben-Bassat equally contributed as senior authors to the manuscript.

Conflicts of Interest

There are no conflicts of interest.

References

- [1] D. J. M. Tolan, R. Greenhalgh, I. A. Zealley, S. Halligan, and S. A. Taylor, "MR enterographic manifestations of small bowel Crohn disease," *Radiographics*, vol. 30, no. 2, pp. 367–384, 2010.
- [2] C. Cellier, T. Sahmoud, E. Froguel et al., "Correlations between clinical activity, endoscopic severity, and biological parameters in colonic or ileocolonic Crohn's disease. A prospective multi-centre study of 121 cases," *Gut*, vol. 35, no. 2, pp. 231–235, 1994.
- [3] G. Bouguen, B. G. Levesque, and B. G. Feagan, "Treat to target: a proposed new paradigm for the management of Crohn's disease," *Clinical Gastroenterology and Hepatology*, vol. 13, no. 6, pp. 1042.e2–1050.e2, 2015.
- [4] S. Chang, L. Malter, and D. Hudesman, "Disease monitoring in inflammatory bowel disease," *World Journal of Gastroenterology*, vol. 21, no. 40, pp. 11246–11259, 2015.
- [5] B. C. Allen and J. R. Leyendecker, "MR enterography for assessment and management of small bowel Crohn disease," *Radiologic Clinics of North America*, vol. 52, no. 4, pp. 799–810, 2014.
- [6] G. Masselli, M. Di Tola, E. Casciani et al., "Diagnosis of small-bowel diseases: Prospective comparison of multidetector row CT enterography with MR enterography," *Radiology*, vol. 279, no. 2, pp. 420–431, 2016.
- [7] D. H. Bruining, G. Bhatnagar, J. Rimola, S. Taylor, E. M. Zimmermann, and J. G. Fletcher, "CT and MR enterography in Crohn's disease: current and future applications," *Abdominal Imaging*, vol. 40, no. 5, pp. 965–974, 2015.
- [8] D. Groszhar, H. Bernstine, D. Stern et al., "PET/CT enterography in Crohn disease: correlation of disease activity on CT enterography with 18F-FDG uptake," *Journal of Nuclear Medicine*, vol. 51, no. 7, pp. 1009–1014, 2010.
- [9] K. Beiderwellen, S. Kinner, B. Gomez et al., "Hybrid imaging of the bowel using PET/MR enterography: Feasibility and first results," *European Journal of Radiology*, vol. 85, no. 2, pp. 414–421, 2016.
- [10] G. Pellino, E. Nicolai, O. A. Catalano et al., "PET/MR versus PET/CT imaging: Impact on the clinical management of small-bowel Crohn's disease," *Journal of Crohn's and Colitis*, vol. 10, no. 3, pp. 277–285, 2016.
- [11] B. Huang, M. W.-M. Law, and P.-L. Khong, "Whole-body PET/CT scanning: estimation of radiation dose and cancer risk," *Radiology*, vol. 251, no. 1, pp. 166–174, 2009.
- [12] J. Rimola, A. Alvarez-Cofiño, T. Pérez-Jeldres et al., "Comparison of three magnetic resonance enterography indices for grading activity in Crohn's disease," *Journal of Gastroenterology*, vol. 52, no. 5, pp. 585–593, 2016.
- [13] E. Iannicelli, I. Martini, C. Fantini et al., "Magnetic resonance enterography in Crohn's disease: New simple proposal to assess disease activity," *Clinical Imaging*, vol. 40, no. 3, pp. 492–497, 2016.
- [14] E. Abej, W. El-Matary, H. Singh, and C. N. Bernstein, "The Utility of Fecal Calprotectin in the Real-World Clinical Care of Patients with Inflammatory Bowel Disease," *Canadian Journal of Gastroenterology and Hepatology*, vol. 2016, Article ID 2483261, 2016.
- [15] R. D'Inca and R. Caccaro, "Measuring disease activity in Crohn's disease: what is currently available to the clinician," *Clinical and Experimental Gastroenterology*, vol. 7, no. 1, pp. 151–161, 2014.
- [16] T. Sipponen, C.-G. A. Björkstén, M. Färkkilä, H. Nuutinen, E. Savilahti, and K.-L. Kolho, "Faecal calprotectin and lactoferrin are reliable surrogate markers of endoscopic response during Crohn's disease treatment," *Scandinavian Journal of Gastroenterology*, vol. 45, no. 3, pp. 325–331, 2010.
- [17] S. Vermeire, G. Van Assche, and P. Rutgeerts, "The role of C-reactive protein as an inflammatory marker in gastrointestinal

- diseases," *Nature Clinical Practice Gastroenterology & Hepatology*, vol. 2, no. 12, pp. 580–586, 2005.
- [18] S. Karoui, S. Ouerdiane, M. Serghini et al., "Correlation between levels of C-reactive protein and clinical activity in Crohn's disease," *Digestive and Liver Disease*, vol. 39, no. 11, pp. 1006–1010, 2007.
- [19] M. H. Mosli, G. Zou, S. K. Garg et al., "C-reactive protein, fecal calprotectin, and stool lactoferrin for detection of endoscopic activity in symptomatic inflammatory bowel disease patients: A systematic review and meta-analysis," *American Journal of Gastroenterology*, vol. 110, no. 6, pp. 802–819, 2015.
- [20] A. Bitton, P. L. Dobkin, M. D. Edwardes et al., "Predicting relapse in Crohn's disease: A biopsychosocial model," *Gut*, vol. 57, no. 10, pp. 1386–1392, 2008.
- [21] M. Jürgens, J. M. M. John, I. Cleynen et al., "Levels of C-reactive protein are associated with response to infliximab therapy in patients with Crohn's disease," *Clinical Gastroenterology and Hepatology*, vol. 9, no. 5, pp. 421.e1–427.e1, 2011.
- [22] J. Jones, E. V. Loftus Jr., R. Panaccione et al., "Relationships Between Disease Activity and Serum and Fecal Biomarkers in Patients With Crohn's Disease," *Clinical Gastroenterology and Hepatology*, vol. 6, no. 11, pp. 1218–1224, 2008.
- [23] T. Lobatón, A. López-García, F. Rodríguez-Moranta, A. Ruiz, L. Rodríguez, and J. Guardiola, "A new rapid test for fecal calprotectin predicts endoscopic remission and postoperative recurrence in Crohn's disease," *Journal of Crohn's and Colitis*, vol. 7, no. 12, pp. e641–e651, 2013.
- [24] K. B. Gecse, J. F. Brandse, S. van Wilpe et al., "Impact of disease location on fecal calprotectin levels in Crohn's disease," *Scandinavian Journal of Gastroenterology*, vol. 50, no. 7, pp. 841–847, 2015.
- [25] J. D. Lewis, "The utility of biomarkers in the diagnosis and therapy of inflammatory bowel disease," *Gastroenterology*, vol. 140, no. 6, pp. 1817–1826, 2011.
- [26] E. Cerrillo, B. Beltrán, and S. Pous, "Fecal calprotectin in ileal Crohn's disease," *Inflammatory Bowel Diseases*, vol. 21, no. 7, pp. 1572–1579, 2015.
- [27] N. Stanescu-Siegmund, Y. Nimsch, A. P. Wunderlich et al., "Quantification of inflammatory activity in patients with Crohn's disease using diffusion weighted imaging (DWI) in MR enteroclysis and MR enterography," *Acta Radiologica*, vol. 58, no. 3, pp. 264–271, 2017.
- [28] K.-J. Kim, Y. Lee, S. H. Park et al., "Diffusion-weighted MR enterography for evaluating Crohn's disease: How does it add diagnostically to conventional MR enterography?" *Inflammatory Bowel Diseases*, vol. 21, no. 1, pp. 101–109, 2015.
- [29] H. A. Jacene, P. Ginsburg, J. Kwon et al., "Prediction of the need for surgical intervention in obstructive Crohn's disease by 18F-FDG PET/CT," *Journal of Nuclear Medicine*, vol. 50, no. 11, pp. 1751–1759, 2009.
- [30] E. A. Russo, S. Khan, R. Janisch et al., "Role of 18F-fluorodeoxyglucose Positron Emission Tomography in the Monitoring of Inflammatory Activity in Crohn's Disease," *Inflammatory Bowel Diseases*, vol. 22, no. 11, pp. 2619–2629, 2016.